Ultrafast Spectroscopy of Photochemical Processes in Specific Solvent Environments

Dissertation

zur Erlangung des Doktorgrades der Naturwissenschaften
(Dr. rer. nat.)
der Fakultät für Chemie und Pharmazie
der Universität Regensburg

vorgelegt von

Svenja Wortmann

aus Essen

2023

This work has been carried out between April 2019 and October 2023 under the supervision of Prof. Dr. Patrick Nürnberger at the Institute of Physical and Theoretical Chemistry at the University of Regensburg. Since April 2021 the research was funded by the DFG (Deutsche Forschungsgemeinschaft) within the RTG2620 focusing on 'Ion Pair Effects in Molecular Reactivity'.

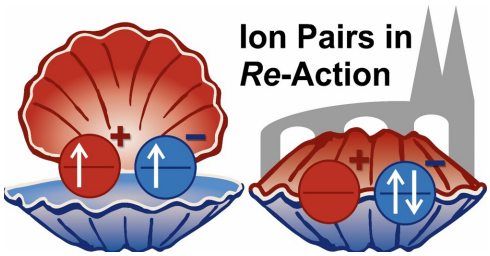

Supervisor: Prof. Dr. Patrick Nürnberger

Doctoral Committee:	Chair:	Prof. Dr. Oliver Tepner
	1st Referee:	Prof. Dr. Patrick Nürnberger
	2nd Referee:	Prof. Dr. Bernhard Dick
	3rd Referee:	Prof. Dr. Julia Rehbein

Universität Regensburg

Regensburg, November 7, 2023

Svenja Wortmann

Dedicated to my Family
for their continuous support and encouragement
during the entire years of study

"Fantasie ist wichtiger als Wissen,
denn Wissen ist begrenzt."
- Albert Einstein -

List of Publications

This thesis is based on the following publications:

Published:

[1] S. Wortmann, S. Schloeglmann, and P. Nuernberger. Sensitivity of Isomerization Kinetics of 1,3,5-Triphenylformazan on Cosolvents Added to Toluene. *J. Org. Chem.* **2021**, 87, 1745-1755, doi:10.1021/acs.joc.1c01928.

[2] S. Wortmann, R.J. Kutta, and P. Nuernberger. Monitoring the photochemistry of a formazan over 15 orders of magnitude in time. *Front. Chem.* **2022**, 10, 983342 doi: 10.3389/fchem.2022.983342.

To be submitted:

[3] S. Wortmann, R.J. Kutta, R.D. Crocker, F. Bergmeier, B. Geissler, D.J.M. Lyons, E. Riedle, T.V. Nguyen, and P. Nuernberger. Reversion of excited-state charge-transfer dynamics in dibenzotropylium-aniline compared to aryltropylium compounds.

In preparation:

[4] S. Wortmann, R.J. Kutta, R.D. Crocker, F. Bergmeier, J. Poll, D.J.M. Lyons, E. Riedle, T.V. Nguyen, and P. Nuernberger. Unveiling and influencing the photochemistry of a tropylium-aniline salt.

The publications, which are mentioned above, have been used in this dissertation. The permissions for reproducing the original articles were granted by the respective publishing company holding the copyright. For the corresponding documents see pp. XCIII.

Further publications which are not related to this thesis:

Published:

[5] I. M. Daubit, S. Wortmann, D. Siegmund, S. Hahn, P. Nuernberger, and N. Metzler-Nolte. Unveiling luminescent Ir(I) and Rh(I) NHC complexes: Structure, photophysical specifics, and cellular localization in the endoplasmatic reticulum, *Chemistry - A European Journal* **2021**, 27, 6783-6794, doi.org/10.1002/chem.202100375.

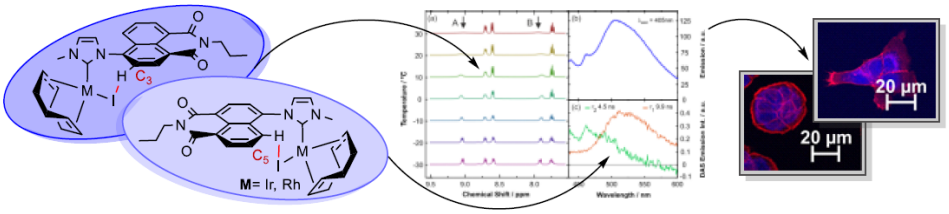

To be submitted:

[6] N. Schubert, M. Vázquez-Hernández, J. W. Southwell, S. Wortmann, S. Schloeglmann, A.-K. Duhme-Klair, P. Nuernberger, J. E. Bandow, and N. Metzler-Nolte, *Investigation of Ruthenium Catalysts and Coumarin Dyes for Bioorthogonal Uncaging Reactions within Gram-positive Bacteria.*

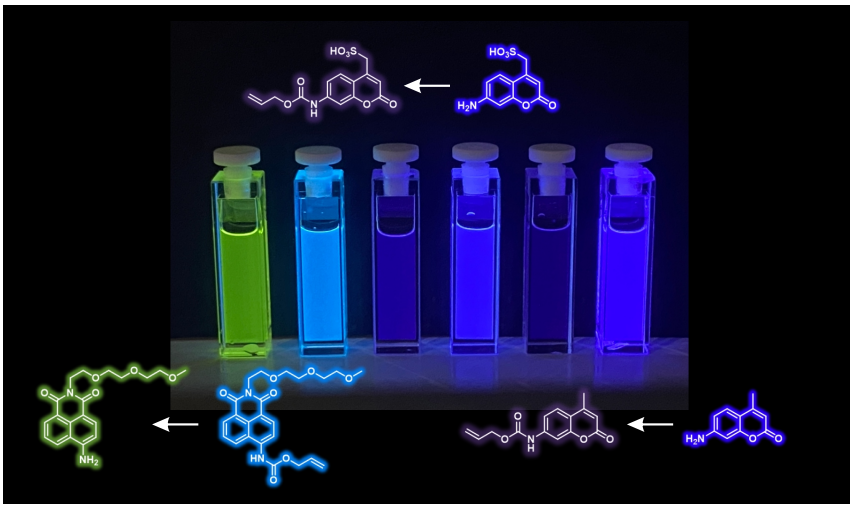

Contents

List of Publications **VII**

1 Motivation **1**

2 Theoretical Background **5**

2.1 Nonlinear Optical Processes 6

2.1.1 Nonlinear Polarization 6

2.1.2 Second-Order Nonlinear Optics 7

2.1.3 Phase-Matching Conditions 9

2.2 Time-Resolved Spectroscopy – Basic Concepts 12

2.2.1 Transient Absorption Spectroscopy 12

2.2.2 Fluorescence Upconversion 17

2.2.3 Time-Correlated Single Photon Counting 20

2.2.4 Streak Camera 22

2.3 Data Analysis 23

2.4 Quantum Chemical Calculations – Fundamentals 27

2.4.1 Hartee-Fock Approximation 28

2.4.2 Density Functional Theory 31

2.4.3 Møller–Plesset Perturbation Theory 37

3 1,3,5-Triphenylformazan 41

3.1 Introduction 42

3.2 Experimental and Theoretical Approaches 45

3.2.1 fs-ns Transient Absorption Spectroscopy 45

3.2.2 ns-ms Transient Absorption Spectroscopy 46

3.2.3 ms-min Transient Absorption Spectroscopy 47

3.2.4 Quantum Chemical Calculations 48

3.3 Results and Discussion 49

3.3.1 Photochemistry of TPF 49

3.3.2 Analysis of Reaction Pathways 61

3.3.3 Isomerization Kinetics in Solvent Admixtures 67

3.4 Conclusion and Outlook 75

4 Tropylium Salts 77

4.1 Introduction 78

4.2 Experimental and Theoretical Approaches 80

4.2.1 fs-ns Emission Experiments using Fluorescence Upconversion 80

4.2.2 ps-ns Emission Experiments using a Combination of Spectrograph and Streak Camera 83

4.2.3 ns Emission Experiments using TCSPC 84

4.2.4 Quantum Yield Determination using an Ulbricht Sphere 85

4.2.5 Transient Absorption 86

4.2.6 Quantum Chemical Calculations 87

4.3 Results and Discussion 88

4.3.1 DBTrop with Unsubstituted Dialkylanilines ($\mathbf{1}^+$ - $\mathbf{3}^+$) 88

4.3.2 DBTrop with Substituted Dimethylanilines ($\mathbf{4}^+$ and $\mathbf{5}^+$) 97

4.3.3 Unsubstituted Trop-DMA without the DB-Ring-System ($\mathbf{6}^+$) 103

4.4 Conclusion and Outlook 112

5 Chiral Phosphoric Acid-Imine Complexes 115

5.1 Introduction 116

5.2 Experimental and Theoretical Approaches 119

5.2.1 fs-ns Transient Absorption Spectroscopy 119

5.2.2 ms-min Transient Absorption Spectroscopy at Cryogenic Temperatures 120

5.2.3 Quantum Chemical Calculations 123

5.3 Results and Discussion 124

5.3.1 Ground-State Dynamics of the Pure Substrates 124

5.3.2 Ground-State Dynamics of Binary Mixtures 130

5.3.3 Excited-State Dynamics of the Pure Imine 135

5.3.4 Excited-State Dynamics of the Binary Mixture 138

5.4 Conclusion and Outlook 140

6 Summary 143

A 1,3,5-Triphenylformazan **XIII**

B Tropylium Salts **XXXIII**

C Chiral Phosphoric Acid-Imine Complexes **XLVII**

Glossary of Abbreviations and Acronyms **LI**

Bibliography **LVII**

Acknowledgment **LXXXIX**

Permissions **XCIII**

CHAPTER 1

Motivation

Isomerization is a process, where two molecular species with equivalent chemical formula but different physical configurations are converted into each other. It is a phenomenon which consistently occurs in our everyday life. The most popular example is retinal, which performs a cis/trans-isomerization process due to photon absorption. This molecular switching of retinal is the first step in the human eye leading to the process of vision.[7;8] A further biologically relevant example is the enzymatically triggered keto/enol-tautomerism of fructose into glucose, which is also an elementary step within our metabolism. However, it is not only observed in nature, instead this isomerization is also used in the food sector to synthesize fructose from glucose.[9–11] From this it follows that isomerizations are also an important process in different industry and research fields, like in catalysis,[12–14] medicine,[15;16] and nanotechnology,[17–22] to name a few.
As already obvious from the different application fields, isomerization can be induced by a variety of influences like enzymes, catalysts, light, temperature, pH changes, electrical voltages or the formation of chemical bonds to e.g. metals. Mostly, the distinct isomeric pairs are characterized by different chemical and physical properties, like the melting point, pK_a value, or absorption behavior.
In the last decades the application field of molecular switches especially in the technology sector is constantly growing. Typical molecular switches are for example azobenzene,[23–27] stilbene,[28–31] diphenylbutadiene,[32–35] and spiropyran.[36–40] All of the previously named molecular switches conglomerate an isomerization process triggered by the absorption of a photon, which exemplary indicates the huge potential of light. It can also be used to investigate or control chemical reactions. Since a lot of chemical processes, relaxations, structural rearrangements and vibrational motions are proceeding on a fs to ps time scale, the spectroscopic observation of such processes requires experimental approaches with a time resolution better than the char-

acteristic time scale of the process under investigation. The development of mode-locked laser systems in the 1960s,[41] which later formed the basis for the generation of pulse durations in the femtosecond range, enabled a new research field focusing on suitable measurement methods to study ultrafast processes. This research topic is summarized under the term 'femtochemistry' and was mainly advanced by the development of pump-probe spectroscopy by Ahmed Zewail for investigating molecular processes on a femtosecond time scale.[42;43]

Although the observation of several chemical, physical and biological processes requires ultrafast probing techniques, also a lot of mechanistic insights can be gained on time scales ranging from µs over ms and s up to min or even days. In those cases it is necessary to analyze the whole temporal range by combining the results of multiple time-resolved spectroscopic methods as represented in this work on the light-driven cis/trans-isomerization of the molecular system 1,3,5-triphenyl formazan (TPF) in different solvent environments.[1;2]

Chapter 3 focuses on the elucidation of the whole relaxation process of 1,3,5-triphenyl formazan after photoexcitation, which is accompanied by a color change of the solution due to isomerization. Since this molecular species comprises two double-bonds of which isomerization along both is possible, the reaction pathway becomes more complicated. However, during this work it was possible for the first time to monitor the early isomerization dynamics after excitation. Furthermore, we were able to derive a potential pathway of the full relaxation process proceeding over several conformeric species of TPF. Additionally, experimental indications were found to assume that some isomerization steps are assisted by a proton transfer, offering a new aspect within the discovery of the underlying isomerization mechanistics.

By combining photo-switchable derivatives with light-emitting substrates, it is possible to create a hybrid system comprising properties of organic field-effect transistors (OFETs)[44–46] and organic light-emitting diodes (OLEDs).[47–49] This class of organic light-emitting transistors (OLETs)[50;51] plays an important role for the development of optoelectronic devices, like displays, which became an essential part of our everyday life. Due to their high versatility and tunability regarding the absorption and emission properties by introducing diverse functional groups, the class of push-pull organic dyes are potential candidates for OLEDs.[52;53] Representatives of this molecular class are the here investigated tropylium dyes,[54] consisting of a tropylium backbone linked to an electron-rich aniline scaffold. Thus, Chapter 4 deals with the investigation of in total six differently substituted tropylium salts. Their photodynamics were characterized on their transient absorption and time-resolved emission behavior, combined with quantum chemical calculations. Five of the investigated molecules comprise a dibenzotropylium moiety with an aniline which is equipped with different substituents. For those species, theoretical calculations performed during this work unveiled the existence of two conformeric

structures for each tropylium cation. It could be shown that the preference which conformer is predominantly present in solution is dictated by the different functional groups, resulting in distinct spectral characteristics for the individual samples. In contrast, one of the investigated substrates only consists of the seven-membered tropylium ring bound to an aniline moiety, for which also only one stable conformeric structure was found within the calculations. Furthermore, it could be shown that reducing the conjugated π-system within the tropylium backbone yields even to completely different absorption and emission behavior in solution compared to those of the other cationic dyes comprising the dibenzotropylium framework. Moreover, we investigated the influence of additional ionic species in solution onto the spectroscopic properties of the tropylium cations by a systematic addition of an ammonium tetrafluoroborate as co-salt, indicating an increased ion pair formation at distinct salt concentrations. Thus, it is demonstrated within this thesis that tropylium salts show such a high tunability by varying the functional groups because of the structural reorientation in solution depending on the sterical effect of the substituents. Therefore, tropylium salts are used in a wide field of applications,[55–65] whereby also their ability to act as efficient organic Lewis acid catalyst[66] plays a crucial role for further applications summarized under the term 'green chemistry'. Hence, the development of metal-free catalysis cycles, which can replace the previously established metal-based methods, are of high interest.

The asymmetric transfer hydrogenation reaction of aldehydes using a chiral ammonium salt as catalyst instead of a metal-based substrate, honored in 2021 with the Nobel prize to David MacMillan and Benjamin List,[67–69] is also an example of a synthesis corresponding to the constantly growing field of 'green chemistry'. Especially in the pharmaceutical sector such asymmetric catalytic reactions are of great importance to produce enantiomerically pure drugs. Equivalent to cis/trans-isomers, the different enantiomers are characterized by variant properties that can cause a huge impact on the effect in the human body.

The development of such an enantioselective synthesis was also inspired by nature, more precisely by the enzymatically catalyzed imine reduction of living organisms utilizing organic dihydropyridine cofactors (e.g. NADH).[70;71] However, an effective enantioselective synthesis of imines was less advanced until the metal-free version of the asymmetric transfer hydrogenation was transferred onto imine substrates by Rueping and co-workers,[72–74] who reported for the first time a catalytic cycle for an effective and enantiomerically pure imine reduction using a Brønsted acid as catalyst[75] and a Hantzsch ester as hydrogen source.[67–69;76] Chapter 5 focuses on the investigation of the formed intermediates during this asymmetric catalysis. It is assumed that the ion-paired complexes play a key role during this reaction mechanism, acting as precatalytic compound.[72] Since experimental studies on the ion-paired complex formed within this

synthesis are rather underrepresented, but the formation of an ion pair might be the important step for the high enantioselectivity,[77;78] we started spectroscopic investigations on the photochemical behavior of these ion pairs. The cis/trans-isomerization was observable for all tested imine substrates, while the observation of the isomerization in substrate mixtures was much more challenging. However, an improved setup and cuvette design is presented in this thesis, which has the potential for future observations of the isomerization process in presence of the catalyst.

CHAPTER 2

Theoretical Background

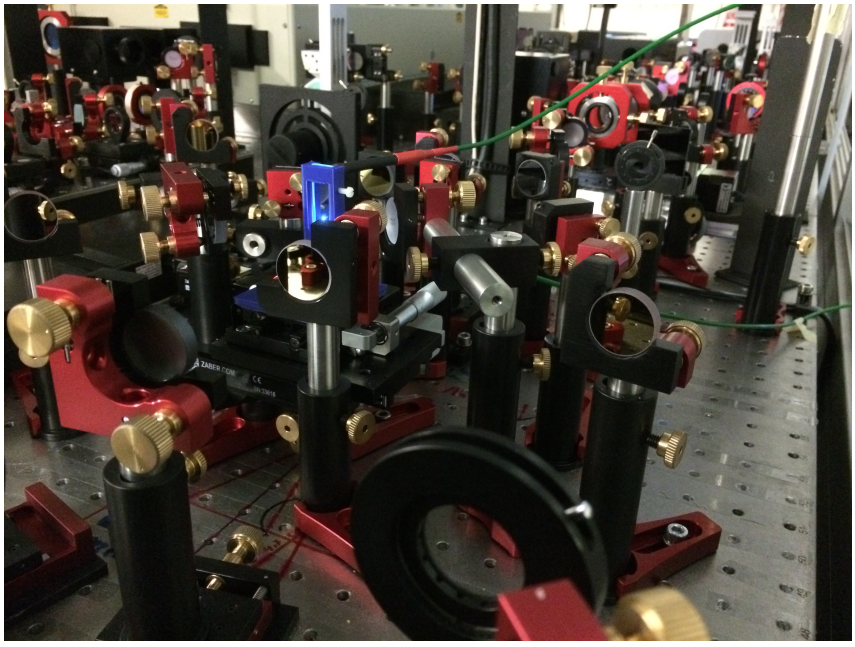

2.1 Nonlinear Optical Processes 6

2.2 Time-Resolved Spectroscopy – Basic Concepts 12

2.3 Data Analysis 23

2.4 Quantum Chemical Calculations – Fundamentals 27

2.1 Nonlinear Optical Processes

Since the development of the first laser system in 1960 by Theodore H. Maiman,[79] the field of nonlinear optics was discovered and further studied, creating new possibilities. High light intensities cause a nonlinear behavior by interaction with optical media. This results in an abolition of the typical laws related to linear optics. In nonlinear optics, the index of refraction and, by association, the velocity of light become dependent on the intensity of the incident electric field. Additionally, the superposition principle is no longer applicable in all situations, since electric fields with different frequencies can influence each other in nonlinear materials.

2.1.1 Nonlinear Polarization

The interaction of an incident electric field with a dielectric medium induces a deflection of the outer electrons of the atoms. The electrons start to oscillate with the frequency ω of the incoming electric field, resulting in an induced dipole moment in the dielectric medium. Note that in the following, non-dispersive, homogeneous, and isotropic media are assumed. In classical electrodynamics, the polarizability $\vec{P}$ depends linearly on the electromagnetic field $\vec{E}$ by

$$\vec{P} = \varepsilon_0 \chi \vec{E} \,, \tag{2.1}$$

whereby $\varepsilon_0 = 8.854 \cdot 10^{-12} \frac{\mathrm{F}}{\mathrm{m}}$ is defined as the vacuum permittivity. Moreover, χ describes the electric susceptibility of the medium, which is directly related to the index of refraction by

$$n^2 = \frac{\varepsilon}{\varepsilon_0} = 1 + \chi \,, \tag{2.2}$$

where ε is the permittivity of the dielectric material.[80] However, the relationship between the polarizability and the electric field in optical materials is characterized by a nearly linear behavior for small field strengths, but differs for intense electric fields, such as those of laser pulses (see Figure 2.1). The polarization, induced by high-intensity electric fields, can be mathematically described by the development of a Taylor series around $E = 0$.[81] Due to the assumption of a non-dispersive, homogeneous and isotropic medium, the polarization vector $\vec{P}$ and the electric field vector $\vec{E}$ are parallel at any point in space and time and thus, can be written as scalar

expression resulting in

$$\begin{aligned} P &= \varepsilon_0 \sum_n \chi^{(n)} E^n \\ &= \varepsilon_0 (\chi^{(1)} E + \chi^{(2)} E^2 + \chi^{(3)} E^3 + ... + \chi^{(n)} E^n) \, . \end{aligned} \tag{2.3}$$

Thereby, the first term describes the linear relation between the incident electric field and the induced polarization equivalent to Equation 2.1, while the subsequent parts denote higher-order nonlinearity. Their contribution decreases with increasing order, since $\chi^{(3)} \ll \chi^{(2)} \ll \chi^{(1)}$. For this reason, higher-order nonlinear polarizations are only relevant for intense electric fields.

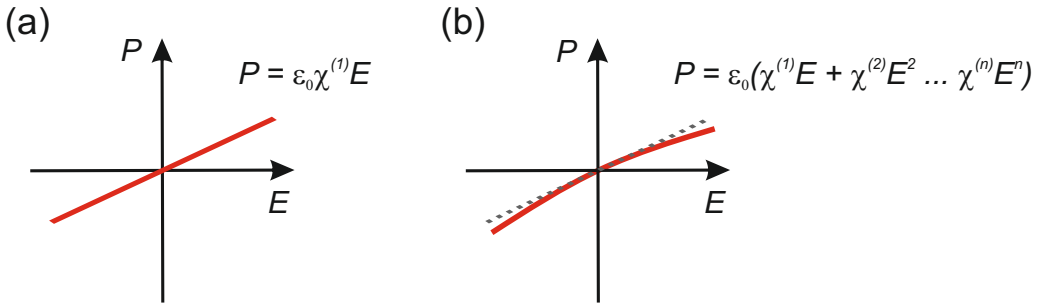

Figure 2.1: Relationship between the incoming electromagnetic field E and the induced polarization P for (a) linear dielectric media and (b) nonlinear media.

2.1.2 Second-Order Nonlinear Optics

In the case of second-order nonlinear processes, like second harmonic generation (SHG), sum-frequency generation (SFG) and difference-frequency generation (DFG), polarizations higher than second order are negligibly small,[82] resulting in the following term:

$$P \approx \varepsilon_0 (\chi^{(1)} E + \chi^{(2)} E^2) \, . \tag{2.4}$$

Let us assume an electric field of the form

$$E = E_0 \cdot \cos(\omega t) = \frac{1}{2} E_0 (e^{i\omega t} + e^{-i\omega t}) \, , \tag{2.5}$$

where the spatial dependence is omitted as if regarded at one point in space. E_0 describes the amplitude and ω characterizes the angular frequency of the electric field. The latter one is also

directly related to the wavelength λ_0 *via* the equation

$$\omega = 2\pi \cdot \nu = \frac{2\pi c_0}{\lambda_0} \,, \tag{2.6}$$

while $c_0 \approx 2.997 \cdot 10^8 \frac{\mathrm{m}}{\mathrm{s}}$ is the velocity of light in vacuum.
The induced polarization can now be obtained by substituting Equation 2.5 into Equation 2.4, yielding

$$P = \varepsilon_0 \chi^{(1)} E_0 \cos(\omega t) + \varepsilon_0 \chi^{(2)} E_0^2 \cos^2(\omega t) \,, \tag{2.7}$$

which can be rearranged due to the relation $\cos^2(\omega t) = \frac{1+\cos(2\omega t)}{2}$ into

$$\begin{aligned} P &= \varepsilon_0 \chi E_0 \cos(\omega t) + \varepsilon_0 \chi^{(2)} E_0^2 \Big(\frac{1+\cos(2\omega t)}{2} \Big) \\ &= \underbrace{\varepsilon_0 \chi E_0 \cos(\omega t)}_{P_L} + \underbrace{\frac{1}{2}\varepsilon_0 \chi^{(2)} E_0^2 + \frac{1}{2}\varepsilon_0 \chi^{(2)} E_0^2 \cos(2\omega t)}_{P_{NL}} \,. \end{aligned} \tag{2.8}$$

Equation 2.8 consists of three parts. The first one describes the linear polarization with a frequency ω equal to that of the incident electric field. The other two terms reflect the second-order nonlinear polarization, which is composed of a constant, time-independent part, named optical rectification, and a description of an electric field oscillating with the frequency 2ω, called second harmonic with a wavelength of $\lambda_0/2$.[83;84] Thus, the transmitted electric field contains an frequency-doubled optical component of the incident electric field, known as second harmonic (SH).
However, such second-order frequency conversion processes are only possible in nonlinear anisotropic media or crystals without point symmetry. The unit cell of centrosymmetric crystals has an inversion center, which means that the crystal's properties does not change by the transformation $\vec{r} \rightarrow$ -$\vec{r}$. Therefore, a reverse in direction of the incident electric field results only in a change of the sign, but does not influence the magnitude of the polarization. This means that both $P_2 = \varepsilon_0 \chi^{(2)} (+E)^2$ and $-P_2 = \varepsilon_0 \chi^{(2)} (-E)^2$ had to be fulfilled simultaneously, which is only possible if $\chi^{(2)} = 0$. In fact, all even polarization terms vanish in isotropic, centrosymmetric media. Thus, those media have to be anisotropic to generate second-order frequencies. Anisotropic media are characterized by an orientation-dependent relation between the polarization and the electric field. In this case, the vectors $\vec{P}$ and $\vec{E}$ are not necessarily parallel, for which reason each component of $\vec{P}$ can be described by a linear combination of the three spatial components of $\vec{E}$ by

$$P_i = \sum_j \varepsilon_0 \chi_{ij} E_j \tag{2.9}$$

with the indices i and j representing the three spatial directions x, y and z. The susceptibility χ_{ij} then is a tensor consisting of 3×3 constants. Similar to the relation in isotropic, homogeneous and non-dispersive media, the distinct polarization functions in nonlinear, anisotropic media can be mathematically described by a development of a Taylor series for each component of $\vec{E}$.[80;82;84] The susceptibility $\chi^{(n)}$ then generally is a tensor of rank $n+1$.
Ultimately, second harmonic generation is a special case of the sum-frequency generation (SFG), where two electric fields with different frequencies are interacting such that an electric field with the frequency $\omega_3 = \omega_1 + \omega_2$ is generated (see Figure 2.2). On the other hand, it is also possible that those two incident electric fields induce an oscillation with the difference frequency $\omega_3 = \omega_1 - \omega_2$ in the nonlinear medium, called difference-frequency generation (DFG). Those processes can be mathematically derived from Equation 2.4, where the electric field E consists of two harmonic components with the frequencies ω_1 and ω_2. Finally, the nonlinear polarization consists of five terms with the frequencies 0, $2\omega_1$, $2\omega_2$, $\omega_{3+} = \omega_1 + \omega_2$ and $\omega_{3-} = \omega_1 - \omega_2$. Although the generation of electric fields with all five frequencies is possible, only those that fulfill the phase-matching conditions are effectively created.[80;82]

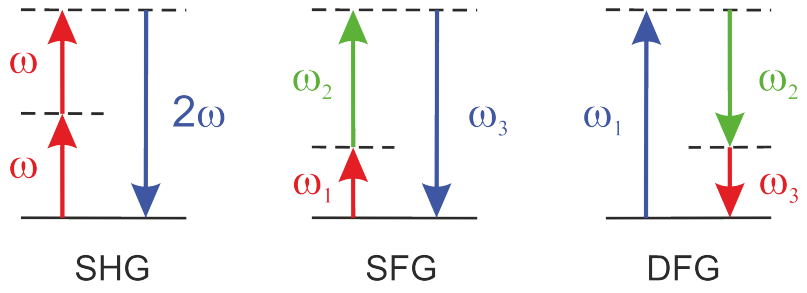

Figure 2.2: Schematic representation of the second-order nonlinear processes 'second harmonic generation' (SHG), 'sum-frequency generation' (SFG) and 'difference-frequency generation' (DFG).

2.1.3 Phase-Matching Conditions

To gain an efficient conversion process, all induced electric fields with the new frequency (for SHG: 2ω) have to interfere constructively. This is for example possible if the fundamental electric field propagates through the nonlinear medium with the same velocity as the generated waves ($c_\omega = c_{2\omega}$). The simplest expression of a propagating electric field with one clearly defined frequency ω is given by:

$$E(\vec{r},t) = E_0 \cdot e^{i(\vec{k}\vec{r}-\omega t)} = E_0 \cdot e^{i\phi} \tag{2.10}$$

with the wave vector $\vec{k}$ and the phase $\phi = \vec{k}\vec{r} - \omega t$, while the magnitude of the wave vector is related to the angular frequency *via*

$$|\vec{k}| = \frac{\omega \cdot n(\omega)}{c_0} \,. \tag{2.11}$$

Hence, for a maximal frequency conversion efficiency, both the energy conservation

$$\omega_3 = \omega_1 + \omega_2 \tag{2.12}$$

and the momentum conservation

$$\vec{k}_3 = \vec{k}_1 + \vec{k}_2 \tag{2.13}$$

have to be fulfilled.[85] Assuming collinearity, a perfect conversion efficiency is observed for

$$\Delta\vec{k} = \vec{k}_3 - \vec{k}_2 - \vec{k}_1 = 0 \,, \tag{2.14}$$

called phase-matching condition.[80] In non-dispersive media, the refractive index is independent of the frequency ω, which means that both phase-matching conditions are achieved, when Equation 2.12 is satisfied. In this case, the phase-velocities are equal, resulting in highly constructive interference. However, all media are dispersive, which results in different phase-velocities of the electric fields due to the frequency-dependent refractive index $n(\omega)$. Therefore, the conversion efficiency is reduced, since $\Delta\vec{k} \neq 0$, which is known as phase-mismatch.[80;84;86]
In order to achieve best possible phase-matching conditions, usually birefringent crystals are used, which are characterized by their polarization-dependent refractive index. Uniaxial birefringent media have one optical axis (o.A.), describing the propagation direction where no birefringence exists. Otherwise, it can be differentiated between ordinary and extraordinary beams. Electric fields with a polarization perpendicular to the plane, spanned by the propagation direction of the wave and the optical axis, or more precise the orientation of the wave vector $\vec{k}$ and the optic axis, are termed ordinary beam. Those waves are subjected to the ordinary refraction index $n_o(\omega)$, which follows Snell's law.[87] An electric field, that is parallelly polarized regarding the plane between the wave vector $\vec{k}$ and the optic axis, is denoted as extraordinary wave. The corresponding index of refraction $n(\theta,\omega)$ is additionally dependent on the angle θ, spanned by the wave vector $\vec{k}$ and the optical axis (see Figure 2.3). The refractive index of the extraordinary beam $n(\theta,\omega)$ can be described by a combination of the extraordinary $n_e(90°,\omega)$

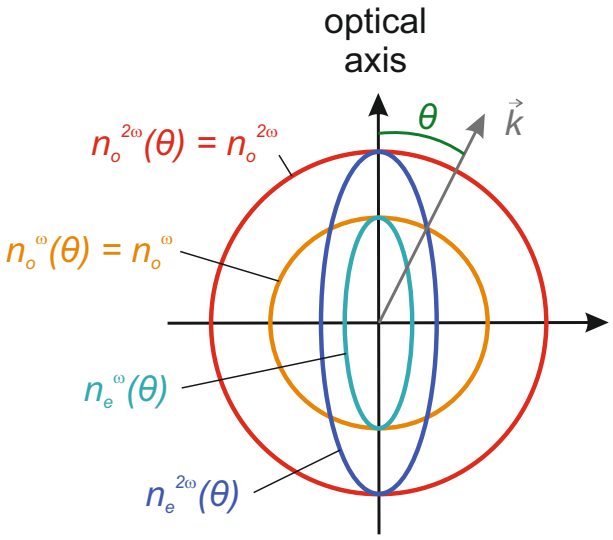

Figure 2.3: Index surfaces of the ordinary and extraordinary beams within a negative ($n_e < n_o$) uniaxial crystal. The phase-matching condition of an SHG process is fulfilled if $n_e^{2\omega}(\theta) = n_o^{\omega}$. The propagation direction of the generated second harmonic wave is indicated by the wave vector $\vec{k}$.

and the ordinary $n_o(\omega)$ refractive index by

$$n(\theta,\omega) = \frac{1}{\sqrt{\frac{\cos^2(\theta)}{n_o^2(\omega)} + \frac{\sin^2(\theta)}{n_e^2(90°,\omega)}}} \,. \tag{2.15}$$

This equation also illustrates that for a propagation along the optical axis ($\theta = 0°$), the refractive index depends only on the ordinary index n_o, for which reason the birefringence of the crystal vanishes along the optical axis.[80;84] Furthermore, one can distinguish between positive and negative uniaxial crystals. In the latter case, the ordinary refraction index is higher than the extraordinary one ($n_e < n_o$), which applies to the most common nonlinear crystals. In those crystals one can further differentiate between *Type I* and *Type II* phase-matching. In the example of SFG, *Type I* means, that the two fundamental waves have the same polarization direction, while the polarization of the sum-frequency beam is perpendicularly arranged to that of the fundamental (o + o → e as exemplarily shown in Figure 2.3 or e + e → o). Conversely, *Type II* is observed, when the two fundamentals have different polarizations (o + e → o or o + e → e).[80;84]

2.2 Time-Resolved Spectroscopy – Basic Concepts

The most commonly performed spectroscopy methods are steady-state experiments, which reflect in general only the average behavior of several individual time-dependent phenomena occurring during constant illumination of the molecular system. However, to resolve and monitor inter- and intramolecular dynamics, like molecular interactions, energy transfers, molecular dynamics or relaxation processes, time-resolved spectroscopy setups involving pulsed light sources are needed.[88–94] Since these processes often occur on extremely short time scales, typically in the range from femtoseconds (10^{-15} s) up to picoseconds (10^{-12} s),[95] the development of ultrashort laser sources in 1991 enabled a whole new research field of time-resolved experiments with sub-100 fs time resolution,[96] only limited by the duration of the ultrashort light pulses.

2.2.1 Transient Absorption Spectroscopy

Transient absorption (TA) spectroscopy is based on the pump-probe principle,[95;97] where the changes in the absorption behavior of a molecular system are measured as a function of time. To observe these changes, the initially relaxed sample has to be excited by a short light pulse ('pump') into a metastable excited state, initiating further photophysical and photochemical reactions before the system relaxes back into its electronic ground state. The dynamics of the excited state molecule and the relaxation process can be monitored by probing the sample with a second short laser pulse ('probe'), which is time-delayed with respect to the excitation pulse (see Figure 2.4a). Typically, a supercontinuum is used as probe pulse due to its broad spectral bandwidth, which allows simultaneous measurement of the absorption changes of the molecular species across a wide wavelength range. Especially in the UV-Vis region, usually broadband white light is used. The theoretical basics as well as the experimental implementation of white light generation can be found in Refs. [98–103]. The spectrally narrow pump pulse is blocked behind the sample, while the transmitted probe pulse is detected by e.g. a CCD camera after it passed a spectrometer, where the pulse is separated into its wavelength components. By varying the time-delay Δt between both pulses, the dynamics of the excited state and the relaxation can be monitored as absorption changes ΔOD over time.[104]

In order to observe photoinduced changes in the absorption behavior of a molecule, also the absorption properties without excitation have to be measured as a reference signal. Finally,

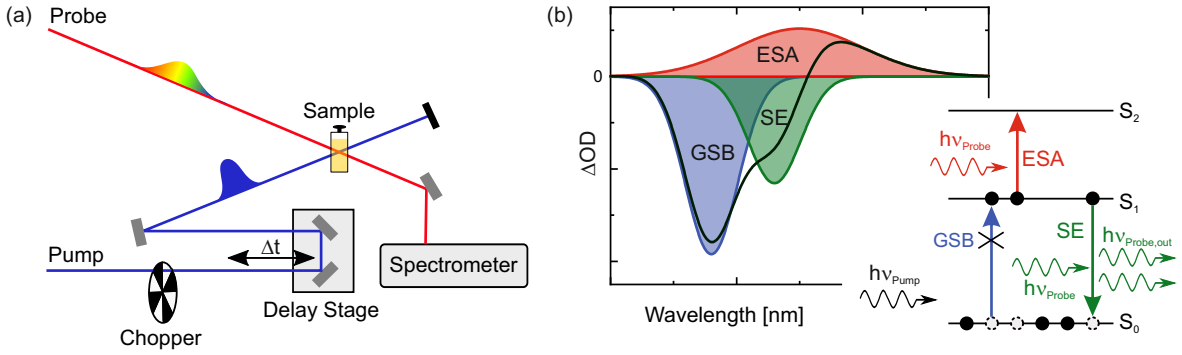

Figure 2.4: Schematic representation of the basic concepts of transient absorption spectroscopy. (a) The sample is excited by the pump pulse (blue), which is blocked afterwards. The sample's spectral changes are monitored by a time-delayed white-light probe pulse (red). The chopper blocks each second probe pulse to ensure the altered detection of the pumped and unpumped sample. (b) The signal contributions occurring in a Transient Absorption experiment after photoexcitation are illustrated in terms of ground-state bleach (GSB; blue), stimulated emission (SE; green) and excited-state absorption (ESA; red). The detected spectrum at a distinct delay time is mostly a superposition of several processes (black curve). Part (a) was adapted from Ref. [105].

those photoinduced changes can be quantified by the differential optical density

$$\Delta OD(\lambda,\Delta t) = OD_{abs}(\lambda,\Delta t) - OD_{ref}(\lambda) = log_{10}\left(\frac{I_{ref}(\lambda)}{I(\lambda,\Delta t)}\right), \tag{2.16}$$

whereas $I(\lambda,\Delta t)$ describes the intensity of the transmitted signal of the previously excited sample, and $I_{ref}(\lambda)$ means the reference signal without excitation.[104] Both intensity profiles follow the Beer-Lambert law. In order to measure alternatingly the absorption properties of the excited and non-excited sample, a chopper is used to block every second pump pulse. The absorption changes are recorded for many well defined delay steps between the pump and probe pulse to monitor the evolution of the excited state dynamics over time. Typically this series of detected absorption spectra is represented in a two-dimensional transient absorption map, combining the temporal and spectral information. The obtained difference signal is usually a superposition of several different processes, as displayed exemplarily on one transient spectrum at a defined delay time $\Delta t > 0$ in Figure 2.4b.
In general, the individual contributions can be differentiated into four main categories with

$\Delta OD < 0$:

- Ground-State Bleach (GSB): Excitation of the sample leads to a partially depopulated

ground state, for which reason the ground-state absorbance is reduced. The calculated difference spectrum consists of a negative signal at the spectral position of the steady-state absorption bands corresponding to the molecules that were excited.

- Stimulated Emission (SE): The interaction of the probe pulse with the previously excited sample leads to a repopulation of the molecular ground state by emitting a photon. The stimulated emission is emitted nearly at the same spectral position as the spontaneous emission and can be observed due to their connection *via* the Einstein coefficients A_{nm} for spontaneous emission and B_{nm} describing induced emission by the relationship $A_{nm}(spon) \sim \frac{B_{nm}(stim)}{\lambda^3}$.[106] These additional photons finally result into a decrease in absorption and thus, a decrease of ΔOD.

$\Delta OD > 0$:

- Excited-State Absorption (ESA): Interaction with the probe pulse leads to further excitation of the already excited sample to a higher-lying state. This excited state has also a characteristic absorbance, resulting in a decreased probe intensity, i.e. a positive signal contribution.

- Product Absorption (PA): If an intermediate or a photoproduct is formed after excitation with the pump pulse, the newly generated molecular species is also characterized by a distinct absorption spectrum. Therefore, interaction with the probe beam causes a higher absorption at the spectral position of the new species, which is detectable as positive difference absorption signal.

Thus, these processes can result in positive or negative transient absorption signals depending on the occupation of higher- or lower-lying states by the excited molecule upon probe pulse interaction. Additionally, the monitored TA data may also exhibit unwanted features like coherent artifacts around $\Delta t = 0$ and a temporal chirp of the probe pulse. Both the spectrally overlapping signal contributions as well as short-time effects require global fitting models and correction techniques for accurate analysis of the excited state dynamics, which are explained in the following in more detail.

Coherent Artifact

In general, the pump-probe spectroscopy can be assigned to third-order nonlinear processes, according to the number of light-matter interactions.[107] This means that the pump pulse inter-

acts twice with the sample, where the first interaction leads to a coherence between the first excited state and the electronic ground state ($+\vec{k}_{pump}$) and the second is responsible for population of the first excited state ($-\vec{k}_{pump}$; note that $+\vec{k}_{pump}$ and $-\vec{k}_{pump}$ can also be assigned *vice versa*). Both interactions proceed simultaneously, followed by one interaction with the probe pulse ($+\vec{k}_{probe}$) resulting in another coherence.[108] Thus, phase-matching is achieved by

$$\vec{k}_{sig} = +\vec{k}_{pump} - \vec{k}_{pump} + \vec{k}_{probe} \,, \tag{2.17}$$

which means that the wave vector of the signal field points in the same direction as the probe beam, for which reason the detector is placed inside the probe beam propagation direction (as shown in Figure 2.4a). Due to the time-delayed probe interaction, the transient absorption signal can be described by a sequential model.[108] However, around time zero when pump and probe pulse are spatially and temporally overlapping, the process becomes non-sequential.[109] In this case, higher-order processes like multiphoton absorption,[110;111] cross-phase modulation (XPM),[111–114] or stimulated Raman scattering[115;116] can arise. All these contributions are summarized under the expression 'coherent artifact' or 'coherent spike', since it appears as dominant, short-lived signal around time zero and is observable over a wide spectral range. In the case of 100 fs laser pulses, the coherent artifact is mainly caused by cross-phase modulation,[110;111;114] where the intensity of one laser pulse has an impact on the phase of another one. Hence, the intense pump pulse, with its temporal envelope $|E(t)|^2$, affects in a time-dependent manner the real part of the refractive index $n(t)$ by

$$n(t) = n_0 + n_2|E(t)|^2 \tag{2.18}$$

of media with higher-order nonlinear susceptibility.[80] Therefore, this effect is also observable in a flow cell with pure solvents. The duration of the coherent artifact is mainly defined by the temporal width of the pump pulse. During the short time of interaction the modulation of refractive index finally leads to changes in the spectral composition of the probe pulse, which is observable as altered absorption. The frequency shift of the probe pulse can be described by

$$\Delta\omega(t) = -2\frac{n_2\omega_0 L}{c}\frac{\delta}{\delta t}|E(t)|^2 \tag{2.19}$$

with the length of medium L and the central probe frequency ω_0, if linearly polarized-light, homogeneous spatial distribution and slowly-varying-envelope approximation are assumed.[111] Ultimately, these varying absorption signals can cover early molecular dynamics of the investigated molecular system. Therefore, it is necessary to employ correction procedures on the

transient data around time zero. Since the origin of the coherent artifact is well understood and it can be modulated very precisely, it is possible to analyze the coherent artifact either mathematically or by subtraction of the data in pure solvents to uncover the fast molecular dynamics.[111;113;114]

Probe Pulse Chirp

In contrast to the previously mentioned cross-phase modulation, where one laser pulse affects another one, self-phase modulation (SPM) is characterized by the phenomenon that the intensity of the pulse modulates its own phase due to the Kerr effect in nonlinear media.[109] The mechanisms and mathematical description of the Kerr effect can be read elsewhere (see Refs. [117–119]). SPM is also a third-order nonlinear process,[103] leading to an intensity-dependent modulation of the refractive index by

$$n(t) = n_0 + n_2 I(t) \, . \tag{2.20}$$

Here, n_0 describes the refractive index of the medium without an incident light field, n_2 is the nonlinear refractive index referred to the third-order nonlinear susceptibility $\chi^{(3)}$, and $I(t)$ means the time-dependent intensity of the laser pulse. Eventually, this intensity-dependent change of the refractive index results in a phase shift Φ of the probe pulse in dependence of the medium's length L,[103] which can be mathematically expressed as

$$\Phi(t) = \frac{\omega}{c} n_2 I(t) L \, . \tag{2.21}$$

Since the intensity of the laser pulse is time-dependent, the nonlinear phase shift is also effected in a time-dependent manner, resulting in a frequency variation of the pulse over time. This entails a spectral broadening of the light pulse with

$$\Delta\omega = \frac{\omega}{c} n_2 \frac{I_0}{\tau} L \, , \tag{2.22}$$

while I_0 and τ describe the peak intensity and the temporal duration of the probe pulse. Therefore, the pulse is no longer bandwidth-limited and the group velocity dispersion (GVD), a phenomenon that the group velocity of light is frequency-dependent in transparent media,[80;82;84] leads to an 'up-chirp' or also called as 'positive chirp', because of the frequency increase with time. Finally in transient absorption maps, this effect is observable by a wavelength-dependent curvature of the data after time zero along the spectral region, because different frequencies of

the probe pulse arrive at the sample at different times. For accurate data analysis of the monitored sample's dynamics, it is necessary to perform a chirp correction of the data set previous to further analysis. For this, a certain number of time delays with maximal pump-probe overlap dependent on the wavelength can be fitted by a third-order polynomial function to model the chirp of the probe beam. Afterwards, every kinetic trace at a specific wavelength can be temporally shifted individually to get an equal time zero position for the whole spectral region.[120]

2.2.2 Fluorescence Upconversion

Fluorescence upconversion is a technique, which is used to investigate ultrafast photoinduced processes in chemistry, biology and physics by detecting the emission behavior of a molecular species with a high temporal resolution, typically on a femtosecond to picosecond time scale. The first picosecond upconversion experiment was implemented 1975 by Mahr and Hirsch.[121] The general working principle of a fluorescence upconversion setup is based on the pump-gate technique,[121–123] as schematically shown in Figure 2.5a. One of the biggest advantages is that the time resolution is only limited by the duration of the two laser pulses. Nowadays, the pump and gate pulses are usually generated by ultrashort laser sources, like Ti:Sa oscillators, providing short pulse duration in the femtosecond region.[124] After photoexcitation of a previously relaxed fluorophore by the pump pulse, the sample quickly returns into the electronic ground state, sometimes by releasing its excess energy in form of emitting photons. Since fluorescence is an incoherent process, which means that it radiates basically in all directions, optical components collect and focus the fluorescence light into a nonlinear crystal. The remaining pump light can be separated from the fluorescence light by e.g. a filter. The fluorescence afterwards interacts with the gate pulse within the nonlinear crystal *via* a sum-frequency generation (SFG) process, leading to a frequency conversion of the fluorescence light to shorter wavelength (blue-shifted). Finally, this upconverted fluorescence light can be detected with a monochromator combined with a photomultiplier tube (PMT).
For recording the full temporal profile of the fluorescence signal, the gate pulse has to be delayed in time compared to the pump pulse by a movable delay stage. This allows to monitor the fluorescence decay step-by-step, as displayed by the scheme in Figure 2.5b. To gain, additionally to the temporal evolution, insights into the spectral profile, it is necessary to record the temporal decay of the fluorescence for each emission wavelength separately. This can be achieved by rotating the crystal, so that the phase-matching condition is best fulfilled for one wavelength at a given angle φ. By measuring the emission decay at several crystal angles, one can get a data set in space and time.

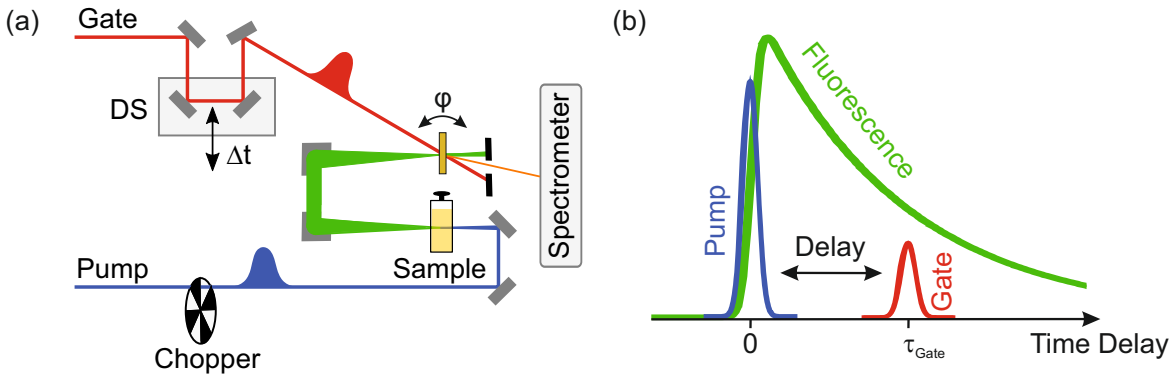

Figure 2.5: Working principle of fluorescence upconversion visualized schematically. (a) The basic setup consists of a pump pulse (blue) and a time-delayed gate pulse (red). Both the sample's emission (green) and the gate pulse are focused into a nonlinear crystal, where the SFG process takes place. By rotation of the crystal, different emission wavelength can be upconverted. (b) After excitation with the pump pulse at $\Delta t = 0$, the emission decay can be monitored by the time-delayed gate pulse. Part (a) was adapted from Ref. [125].

Solvation Effect

The used solvent has a significant impact on the properties of the investigated solute system by several factors like energy transfer efficiency, solvent polarity, viscosity, refractive index, dielectric constant or specific interactions between the solvent and solute molecules. These influences are generally known as 'solvent effects'. However, within this section it should be focused more specifically on the term 'solvation effect', which refers to the impact of solvent molecules on the solute's behavior and properties through the process of solvation.[126] Every dissolved molecule is surrounded by a solvation shell. In the case of a polar solvent, interactions with samples comprising a dipole moment are possible in terms of hydrogen bonding, ion-dipole or dipole-dipole interactions. However for unpolar molecules, this effect is limited to intermolecular Van-der-Waals interactions.[126]

Especially in time-resolved spectroscopy on the fs-time scale, those effects have to be considered and can be observed indirectly by spectral shifts caused by changes in the solute's dipole moment upon irradiation with light. Assuming a fluorophore with a none zero dipole moment dissolved in a polar solvent, often shows a change in dipole moment immediately after excitation. In contrast, the solvent environment remains unchanged directly after excitation, as dictated by the Franck-Condon principle.[127] Usually the fluorophore is excited to higher vibrational levels of the first excited state. This excess vibrational energy can be transferred to the solvent shell in terms of vibrational relaxation (VR). The altered dipole moment of the excited

fluorophore induces a reorientation of the solvation shell's dipole moments, leading to further stabilization associated with an energetic lowering of the first excited state (see Figure 2.6). This process is known as solvation relaxation. By measuring the emission decay in a time-resolved and wavelength dependent manner on ultrashort time scales, the solvation relaxation can be observed by a temporal shift of the intensity maximum towards longer wavelengths, also known as dynamic Stokes shift. The strength of the solvation effect depends on both the specific fluorophore and the chosen solvent.

Additionally to this temporal effect, also spectral shifts in the steady-state emission spectra can occur, which is named solvatochromism. It can be distinguished between positive and negative solvatochromism.[128] The first one is classified as bathochromic shift, which originates from an increased solvent polarity. Upon excitation, the excited state molecular dipole moment is usually larger than in the ground state, for which reason an increased solvent polarity further stabilizes the excited state yielding a reduced energy gap between S_0 and S_1. Consequently, the negative solvatochomic effect is characterized by a hypsochromic shift, which means a blue-shift with increasing solvent polarity. In this case, the ground state is energetically more stabi-

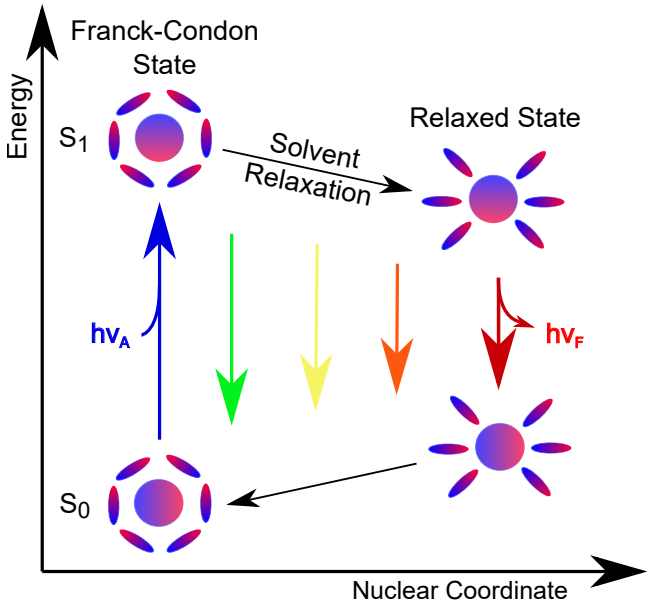

Figure 2.6: Schematic representation of the solvation effect caused by the temporally delayed reorientation of the solvation shell in the excited state. If the dipole-moment of a chromophore (spherical objects) changes during excitation, the solvation shell consisting of polar solute molecules (elliptic objects) responds by a redistribution, finally resulting in an energetically stabilization of the dye and thus, a red-shift of the emission with time. Figure adapted from Ref. [125].

lized than the excited state causing a larger $S_1 - S_0$ energy gap. This phenomenon is observed for molecular species which comprise a larger dipole moment in the ground state. Ultimately, the extent of stabilization depends on the dipole moment's magnitude of the investigated fluorophore, i.e. polar or even charged molecules show a much more pronounced effect than non-polar species.

2.2.3 Time-Correlated Single Photon Counting

Time-Correlated Single Photon Counting (TCSPC) is a widely employed technique for precise measurement of emission events that occur on nanosecond (10^{-9} s) or longer time scales. The general principle of TCSPC is based on detecting the arrival time of single photons emitted or scattered from the sample, in the end constructing a histogram which reflects after many iterations the temporal profile of the emission (see Figure 2.7). Therefore, TCSPC is characterized by many advantages including high time resolution (down to picoseconds), exceptional sensitivity, and the ability to capture individual photon events, which allows the study of excited state dynamics on substances in very small quantities. This principle was first demonstrated in 1961,[129] and later further developed for a broad field of use.[127;130–134]

First, the molecular system has to be excited by a short light pulse, typically generated by a mode-locked picosecond laser, but also other pulsed light sources are possible to use. However, it is important to choose the measurement conditions such that a maximum of one emitted photon per excitation pulse reaches the detector. Otherwise, the histogram discriminates photons with larger arrival times, since only the first incoming photon can be recorded. Only when the photon rate is lower than one event per excitation pulse, the histogram depicts the actual temporal emission decay profile.[127] Indeed usually a detection-*versus*-excitation ratio lower than 10 % is recommended. The reason for this is that the time resolution is achieved by the electronics and currently they are not fast enough to record multiple photons originating from the same excitation pulse, if the emission decay proceeds on the nanosecond time scale. To be more precise, detection of one single photon circumvents the limitation of the time resolution by the electronics.

In order to create a trigger signal, one possibility is to separate a small portion of the short excitation pulse and send it to a fast photodiode. After excitation the sample's emitted light has to be collected and directed with optical components through a monochromator onto a photomultiplier tube (PMT). There each arriving photon creates an electric signal of varying amplitude. Thus, it is not accurate to detect the arrival time of this pulse when a fixed voltage is exceeded, which is known as Leading Edge Triggering (LET). Instead, the arrival time of the pulse is de-

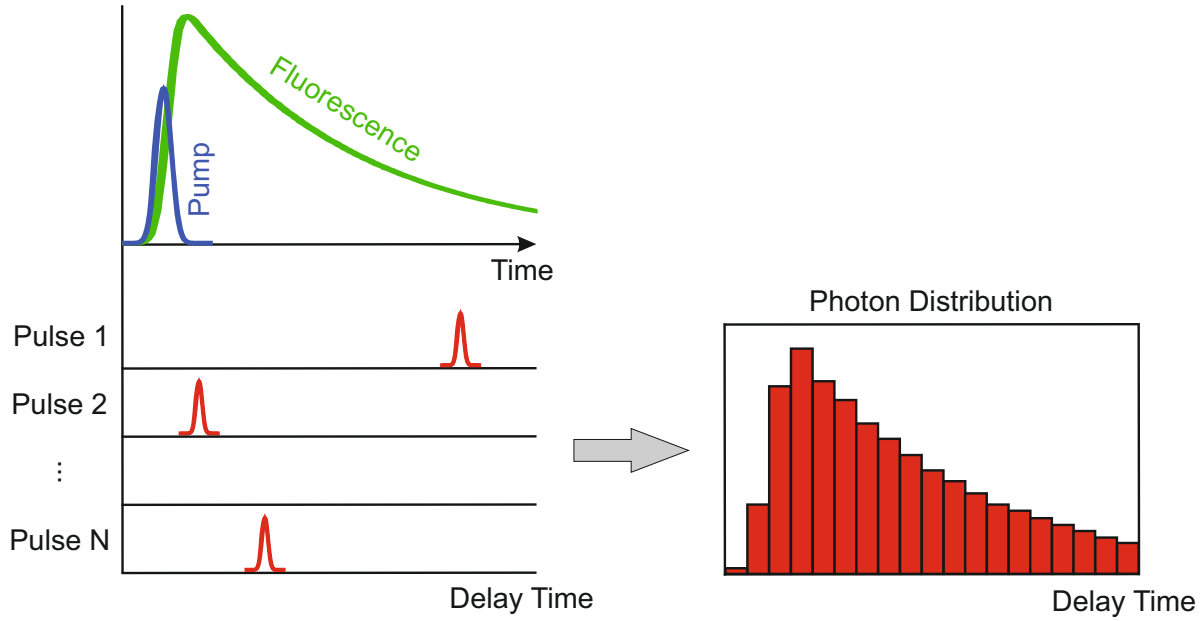

Figure 2.7: Schematic representation of the TCSPC Technique. The time-delay between the excitation pulse and the electronic signal of the TAC creates such a histogram, which depicts the emission decay of the fluorophore.

tected when it has overcome a certain proportion (constant fraction) of its maximum intensity. This minimizes the jitter even if the intensity of the electronic pulses changes from incoming photon to photon. This triggering type is called Constant Fraction Triggering (CFT) and is only possible if the pulses are similar, which means by multiplying a certain factor they can be mathematically converted into each other. However, this assumption is usually satisfied. After passing through the Constant Fraction Discriminator (CFD), where the arrival time is precisely determined, the electronic signal reaches the time-to-amplitude converter (TAC). The first incoming electronic signal functions as 'start' pulse, initiating a voltage ramp in the TAC, where the output voltage increases nearly linear with time, which directly stops when the second electronic signal arrives ('stop' pulse). Now the output voltage of the TAC is proportional to the time difference Δt between the excitation pulse and the first detected emission photon. If the pump pulse is defined as 'start' signal, then the emitted photon acts as 'stop' pulse. As already mentioned previously, due to the well defined measurement conditions, not every excitation pulse results in a photon emitted by the sample. To avoid or reduce false readings, the voltage ramp is limited to a specific range, which means if the 'stop' pulse does not reach the detector within this time range, this event is discarded by a window discriminator (WD). However, the other way around is commonly implemented experimentally, namely using the sample's emitted photon as 'start' signal and the excitation source pulse as 'stop' signal. This attribution is

known as 'reverse mode' and has the advantage that the TAC is only triggered when an emitted photon from the sample reaches the detector. Hence, this procedure results in pronounced reduced measurement times. If necessary, the output voltage at the TAC can be amplified with a programmable gain amplifier (PGA). Afterwards, the (amplified) output voltage is converted into a numerical value by the analog-to-digital converter (ADC). This digital value describes a single event associated with a certain time delay, which gets stored as one index of a storage vector. This index afterwards is evaluated by a Multi Channel Analyzer (MCA) to yield the emission decay as histogram after recording this process for multiple iterations. Since the histogram now consists of channels on the x-axis, a time calibration with a Time Calibrator (TC) is necessary, where the individual indices (channels) of the storage vector are assigned to delay times.[127;130;131]

2.2.4 Streak Camera

A streak camera is a device which can be used as detection unit in the field of time-resolved spectroscopy. It is characterized by a wide wavelength range, a variable time window, and the direct detection of time-resolved processes apart from nonlinear effects. However, the most significant advantage of a streak camera is presumably the ability to detect the temporal and spectral profile simultaneously, resulting in a fast data acquisition.[135] In combination with various equipment possibilities, it can be used in a wide field of applications.[84;95;135–139] During this work, a streak camera was used in both transient absorption and time-resolved emission experiments (Section 3.2.2 and 4.2.2, respectively). In both cases, a spectrograph was positioned in front of the streak camera to get a spatial separation of different wavelengths.
Figure 2.8 displays the general working principle of a streak camera. The incoming signal, represented by optical pulses which are differing in time, wavelength (space) and intensity, is already spatially separated in a horizontal manner according to its wavelength. As mentioned above, this spatial separation can be implemented by a spectrograph (not shown in the diagram). Then the incident light is focused onto a photocathode of the streak tube, where the incoming photons are converted into electrons by the photoelectric effect.[140–142] This means that the number of emitted photoelectrons is proportional to the intensity of the light hitting the photocathode. Afterwards, the emitted electrons are accelerated through the streak tube by an acceleration mesh in order to pass through a parallel-arranged pair of planar sweep electrodes. At this point it is necessary to distinguish between different operation modes. In the Focus Mode, the electrons pass only horizontally separated (spatial separation according to different wavelength) through the electrodes. Here, no further separation of the signal in the vertical

direction takes place. In contrast to the Focus Mode, where no voltage is applied, the Operate Mode is characterized by a time-dependent high voltage at the electrode pair. During that operation mode, the applied voltage is linearly reduced over time, resulting in smaller deflection angles for delayed electrons.[135] In order to ensure that the high voltage will be applied at the right time, namely when the first electron reaches the electrodes, an external trigger signal is used. The practical implementation of the trigger signal in our laboratory can be read in detail in Ref. [143], on the example of a transient absorption experiment on the ns-ms time scale. Whereas the spatial resolution was already displayed on the horizontal axis, the temporal profile is now implemented in the vertical direction. To get the final image, the electrons have to be reconverted into an optical signal. Therefore, the electrons are send through a microchannel plate (MCP),[144;145] which consists of a multitude of thin and parallel-arranged glass capillaries. To multiply the number of electrons several times, the electrons hit the inside of the channels, where secondary electrons with equal characteristics like the primary electrons are emitted. Afterwards, the electrons reach a phosphor screen where the actual conversion into the optical signal, called streak image, takes place.[135] This image can finally be read out by a high-sensitive camera, usually a 2D-CCD camera, resulting in a 2D streak image with spectral and temporal resolution on the x- and y-axis, respectively.

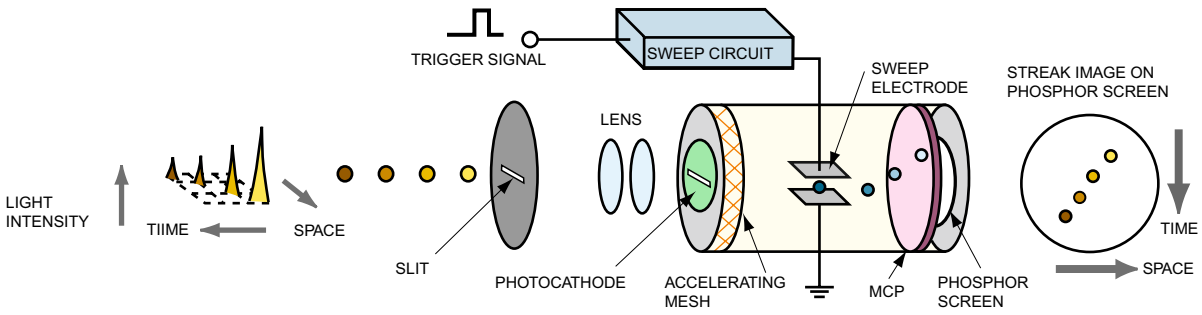

Figure 2.8: Illustration of the operating principle of a streak tube, after the signal is spectrally separated by a spectrograph. Figure taken from Ref. [135].

2.3 Data Analysis

As previously discussed, the different measurement techniques generate varying data formats. While fs-transient absorption and time-resolved experiments with a streak-camera as detection unit result directly in data matrices depending on wavelength and time, in the case of TCSPC, fluorescence upconversion and sub-s TA with an absorption spectrometer each wavelength-

dependent temporal trace is measured individually.
In the simplest case, only one first-order reaction is observed after excitation, which can be described by a monoexponential function

$$I(t) = I_0 \cdot \exp(-t/\tau) \qquad \text{with } \tau = 1/k\,. \tag{2.23}$$

$I(t)$ displays the signal profile of the first-order reaction over time, I_0 is the initial signal after excitation and τ describes the lifetime, which is defined as the mean time that a molecule stays in its excited state. Thus, the lifetime τ describes the time interval in which the intensity drops down to 1/e, i.e. ca. 37%.[127] But, most of the recorded kinetic traces are a superposition of several pathways. A multi-exponential model can be analyzed with the sum of exponential functions[127;146]

$$I(t) = \sum_{i=1}^{N} \alpha_i \cdot \exp(-t/\tau_i)\,. \tag{2.24}$$

In this multi-exponential model, α_i is the pre-exponential factor correlated to the signal intensity of the corresponding process i. Equation 2.23 and Equation 2.24 consider the kinetics at a single wavelength. However, if the number of recorded single traces at different wavelengths is large enough, it is also possible to create a data matrix $\mathbf{S}(\lambda, t)$ in space (wavelength) and time.[147]

2D-Data Matrices

Since the determination of the lifetimes referring to the individual intermediate species is the object of interest, the data matrix has to be analyzed and decomposed into its single components. Therefore, it is important to understand, how the data matrix is constructed. In general, it consists of the sum of different species spectra $\varepsilon_i(\lambda)$ multiplied with their temporal concentration $c_i(t)$, where $i = 1 \ldots N$ symbolizes the number of involved species. The detected data set can be mathematically represented as matrix $\mathbf{S}$ with the structure[148]

$$\mathbf{S} = \begin{pmatrix} S(t_1,\lambda_1) & S(t_1,\lambda_2) & \cdots & S(t_1,\lambda_n) \\ S(t_2,\lambda_1) & S(t_2,\lambda_2) & \cdots & S(t_2,\lambda_n) \\ \vdots & \vdots & \ddots & \vdots \\ S(t_m,\lambda_1) & S(t_m,\lambda_2) & \cdots & S(t_m,\lambda_n) \end{pmatrix}. \tag{2.25}$$

When decomposing **S** into the individual properties of the N contributing species,[148] it leads to

$$\mathbf{S} = \underbrace{\begin{pmatrix} c(t_1,n_1) & \cdots & c(t_1,n_N) \\ \vdots & \ddots & \vdots \\ c(t_m,n_1) & \cdots & c(t_m,n_N) \end{pmatrix}}_{\mathbf{C}} \cdot \underbrace{\begin{pmatrix} \varepsilon(n_1,\lambda_1) & \cdots & \varepsilon(n_1,\lambda_n) \\ \vdots & \ddots & \vdots \\ \varepsilon(n_N,\lambda_1) & \cdots & \varepsilon(n_N,\lambda_n) \end{pmatrix}^T}_{\mathbf{E}^T} \tag{2.26}$$

with overall N molecular species, m data points on the time axis and n individual wavelength positions. This means that each column of matrix **C** describes the concentration profile over time of one component, while every row of matrix $\mathbf{E}^T$ displays the spectrum of the individual species.
Depending on the data acquisition, for example if the time axis is fully linear like in the case of sub-s TA, it is recommended to apply a weighting factor or weighting matrix to the data set prior to fitting in order to achieve suitable analysis of fast dynamics.

Singular Value Decomposition (SVD)

In order to determine, how many processes are involved and thus, to estimate how many fitting functions are needed, a linear algebra method named 'Singular Value Decomposition' (SVD) is initially used. Here, the data matrix **S** with m×n dimensions can be decomposed into

$$\mathbf{S} = \mathbf{U}\Sigma\,\mathbf{V}^T\,, \tag{2.27}$$

where the m×m matrix **U** in dimensions of time contains the left singular vectors and **V** is a n×n matrix, containing the right singular vectors in dimensions of wavelength. The matrix Σ has to contain m×n components, of which the diagonal elements are the singular values σ in the descending order $\sigma_1 \geq \sigma_2 \geq \ldots \geq \sigma_n$ and all other entries are zero. The singular values can be calculated from the square root of the eigenvalues of S^TS. The significance of the singular values to describe the original data matrix decreases with the value order, i.e. larger values are more important for the modeling. In addition, it is also possible to plot the left and right singular vectors, which can be calculated as eigenvectors from SS^T and S^TS, respectively. Thereby, the left singular vectors are related to the time profiles and the right singular vectors represent the spectral contributions of the individual components. If the diagrams of the eigenvectors deviate from noise, this component should be considered for characterization of the measured data

matrix.[149]

Global Analysis

After performing the SVD to estimate the number of considered components, the kinetic constants of each process have to be identified by either global lifetime analysis (GLA) or global target analysis (GTA). The GLA is derived from the sum of several exponential functions to describe the data.[147] In contrast, GTA is based on kinetic schemes and assumes an *a priori* knowledge of the kinetic model.
As already mentioned previously, assuming a first-order or pseudo first-order reaction model, the data can be described by the sum of exponential functions $c_i(t)$ multiplied with the spectral contribution $\varepsilon_i(\lambda)$ of the individual components i with

$$S(\lambda,t) = \sum_{i=1}^{N} c_i(t) \cdot \varepsilon_i(\lambda) \, . \tag{2.28}$$

Furthermore, the time resolution of the individual experiments is not infinitely small, but rather limited by different components, like the pulse duration in fs-TA and fs-fluorescence upconversion, or the response time of the used device as in the case of sub-s TA experiments. Therefore, the recorded signal $S(\lambda,t)$ is a convolution of the molecular signal and the instrument response function (IRF), which can be mathematically described as a convolution of the exponential function with the IRF as

$$S(\lambda,t) = \sum_{i=1}^{N} [\exp(-t/\tau_i) * g(t)] \cdot \varepsilon_i(\lambda) \, , \tag{2.29}$$

where the IRF $g(t)$ determines the maximum achievable time resolution.[150] Within this work, either the IRF was experimentally determined by measuring a sample that only shows light scattering or a normalized Gaussian function of the type

$$g(t) = \frac{1}{\sqrt{2\pi\sigma^2}} \cdot \exp\Big(- \frac{(t-t_0)^2}{2\sigma^2} \Big) \tag{2.30}$$

was used as IRF with the variance σ^2 related to the full width at half maximum (FWHM) by $FWHM = 2\sqrt{2ln2}\sigma \approx 2.3548 \cdot \sigma$. To analyze data matrices generated by experiments with time resolution in the fs region, it is also necessary to get an appropriate model taking into account the coherent artifacts, which can be fitted by the sum of normalized Gaussian function and its

first and second derivatives.[110] By fitting all these exponential and Gaussian functions to the measured data set, the decay associated difference spectra (DADS) for TA processes and decay associated spectra (DAS) for emission signals are created. Those DADS are linear combinations of all individual species spectra with arising signals as negative contributions and decomposing components as positive amplitudes. Each generated DADS corresponds to one kinetic constant k_i. Equivalent to this relation, in the case of emission decays for each decay constant k_i a DAS is generated in the global fitting process. With these DAS it is possible to resolve parallel and spectral overlapping decays. Afterwards, the experimental data matrix $\mathbf{S}(\lambda,t)$ is compared with a reconstructed data matrix $\mathbf{I}_{Fit,i}(\lambda,t)$ of the data by the global fit from the rate constants and the corresponding DADS or DAS. The difference between these two data matrices results in a residual map. The residuals should be minimized in order to reconstruct the experimental data sets appropriate well. This is done in an iterative way by the so-called 'linear least square' method,[151] which compares both data matrices with each other *via*

$$\chi^2 = |\mathbf{I}_{Fit,i}(t) - \mathbf{S}_i(t)|^2 \tag{2.31}$$

in order to optimize the rate constants and the Gaussian function parameters by minimizing the value for χ^2.
Within this work most of the recorded and chirp-corrected data matrices were fitted with the Global Lifetime Analysis routine, written by Roger Kutta.[143]

2.4 Quantum Chemical Calculations – Fundamentals

The goal of computational chemistry is to model and simulate molecular systems and reactions. Nowadays it is a powerful tool to estimate ground-state molecular energies and structures, binding energies, molecular orbitals, electrostatic potentials, vibrational frequencies, spectra like Raman, NMR, CD, UV-Vis, etc., as well as energies and structures of transition states, to name only a few. During this work quantum chemical calculations have been performed to corroborate and complete the interpretation of the experimental results. For this, DFT/TD-DFT as well as MP2/ADC2 methods have been used to optimize the ground-state structure, to calculate the IR frequencies and the vertical excitation energies, and to perform potential energy scans along a defined angle. Therefore, in the following a short description of the principles and approximations on which these methods are based will be discussed.

2.4.1 Hartee-Fock Approximation

In order to get an appropriate understanding of the density-functional theory (DFT) and the Møller–Plesset perturbation theory (MPPT), it is essential to start with a short overview of the Hartree-Fock method.
Hartree-Fock (HF) is an *ab initio* method, which means this theory is derived from theoretical principles and does not include empirical information. This quantum chemical approach uses both the Born-Oppenheimer approximation[152] as well as the single electron approximation within a multi-electron molecular system by neglecting that electrons are correlated particles. Due to this correlation in a many-particle body, it is difficult to solve the Schrödinger equation,[153] even in its time-independent form

$$\hat{H}|\Psi\rangle = E|\Psi\rangle \,. \tag{2.32}$$

Exact solutions are only known for one electron frameworks, like a particle in a box or the hydrogen atom. Instead for bigger molecular systems, some simplifications are needed. Consequently, an approximation to the wave function of the molecular system is provided by treating each electron as moving independently in an average field generated by the other electrons.[154;155] This means that the molecular Hamiltonian can be written as

$$\hat{H} = \hat{T}_e + \hat{T}_n + \hat{V}_{ne} + \hat{V}_{ee} + \hat{V}_{nn} \,, \tag{2.33}$$

of which $\hat{T}_n$ is zero and $\hat{V}_{nn}$ is assumed as constant through the decoupling of electronic and nuclear motion by the Born Oppenheimer approximation. By substituting the kinetic energy operator $\hat{T}_e$ and potential energy operator $\hat{V}_{ne}$ and $\hat{V}_{ee}$ in dependence on one or two electrons, respectively, as terms of single-electron operator $\hat{h}_i$ and the two-electron operator $\hat{w}_{ij}$,[156] leads to the expressions

$$\hat{T}_e + \hat{V}_{ne} = \sum_i^N \hat{h}_i \qquad \text{and} \qquad \hat{V}_{ee} = \frac{1}{2}\sum_i^N \sum_{i\neq j}^N \hat{w}_{ij} \,. \tag{2.34}$$

Thus, the electronic Hamiltonian

$$\hat{H}_e = \sum_i^N \underbrace{\left(-\frac{\Delta(r_i)}{2} - \sum_k^{N_k} \frac{Z_k}{|r_i - R_k|} \right)}_{\hat{h}_i} + \frac{1}{2}\sum_i^N \sum_{i\neq j}^N \underbrace{\frac{1}{|r_i - r_j|}}_{\hat{w}_{ij}} \tag{2.35}$$

in atomic units can be divided into separate Hamiltonians for each individual electron. Even so it should be noted here that these Hamiltonians of the N electrons are still coupled in the

entire Hamiltonian by the Coulomb potential. Furthermore, as additional consequence of the mean-field approach, the molecular wave function of a system with N electrons can be assumed as the product of N single-electron wave functions like

$$\Psi_e(r_1, r_2, ...r_N) \approx \Psi^{HP} = \prod_i^N \psi_i(r_i) = \psi_1(r_1) \cdot \psi_2(r_2) \cdot \ \dots \ \cdot \psi_N(r_N) \ , \tag{2.36}$$

where Ψ_{HP} is known as Hartree product and the eigenfunction ψ_i of the one-particle Hamiltonian characterizes the orbital, with an orbital energy derived from the corresponding eigenvalue. Ultimately, the Schrödinger equation can be simplified to

$$\hat{H}_e \Psi_e(r,R) = E_e \Psi_e(r,R) \tag{2.37}$$

with the eigenvalue E_e reflecting the electronic energy of the molecular system and R representing the nuclei coordinates.
Until now, it has been assumed that the properties of electrons depend only on their coordinates in space. However, electrons are known to possess a spin, which is taken into account by the product of the spatial orbital function $\psi_i(r_i)$ with r_i as coordinates x_i, y_i, z_i of the distinct electrons and the spin function $\sigma_i(s_i)$, resulting in the spin orbital function

$$\chi_i(x_i) = \psi_i(r_i) \cdot \sigma_i(s_i) \ . \tag{2.38}$$

With a spin of $\pm 1/2$, electrons are classified as fermions, for which the Pauli principle[157] determines that the wave function has to be asymmetric under electron exchange. Thus, in the Hartree-Fock method as approximation, the molecular wave function Ψ_e is written as normalized Slater determinant Ψ^{SD} of the one-electron wave functions $\chi_i(x_i)$:[158;159]

$$|\Psi_e\rangle \approx |\Psi^{SD}\rangle = \frac{1}{\sqrt{N!}} \begin{vmatrix} \chi_1(x_1) & \chi_2(x_1) & \dots & \chi_N(x_1) \\ \chi_1(x_2) & \chi_2(x_2) & \dots & \chi_N(x_2) \\ \vdots & \vdots & \ddots & \vdots \\ \chi_1(x_N) & \chi_2(x_N) & \dots & \chi_N(x_N) \end{vmatrix} . \tag{2.39}$$

After the Hartree treatment is achieved, a further basic concept of quantum mechanics has to applied, namely the variational principle according to Rayleigh-Ritz method.[158;160;161] Considering the orthogonality of the single electron wave functions χ_i, the energy can be derived

as

$$\begin{aligned} E^{HF} &= \left\langle \Psi^{SD} | \hat{H} | \Psi^{SD} \right\rangle \\ &= \sum_{i}^{N} \langle \chi_i | \hat{h}_i | \chi_i \rangle + \frac{1}{2} \sum_{i}^{N} \sum_{i \neq j}^{N} \Big(\underbrace{\langle \chi_i \chi_i | \hat{w}_{ij} | \chi_j \chi_j \rangle}_{J_{ij}} - \underbrace{\langle \chi_i \chi_j | \hat{w}_{ij} | \chi_j \chi_i \rangle}_{K_{ij}} \Big) . \end{aligned} \tag{2.40}$$

Here, the first part of Equation 2.40 includes the electronic kinetic energy and the potential energy of the i-th electron or more precisely the Coulomb attraction between nuclei and electron. The latter two terms represent the repulsive Coulomb interactions between the i-th and j-th electron and are called as Coulomb integral J_{ij} and exchange integral K_{ij}, respectively. However, it should be noted that the exchange integral occurs only between two electrons with equivalent spin, due to the orthogonality of the spin functions to each other. Furthermore, the variational principle implies that any valid trial wave function Ψ_{trial}, in this case the Slater determinant Ψ^{SD}, can be understood as upper limit for the real ground-state energy of the electronic system, yielding the relationship

$$E_{trial} = \left\langle \Psi^{SD} | \hat{H} | \Psi^{SD} \right\rangle \geq E_{real} . \tag{2.41}$$

However, the smaller the deviation of the spin orbital function gets compared to the real wave function, the lower the energy will be. Which means the Hartree-Fock method is searching for a wave function χ_i that yields a minimum energy E^{HF}, by altering the orbitals until a set of orbitals is found for which the energy of the molecular system is minimized. This can be achieved by using the Lagrangian multipliers method,[162] which allows to include the condition for orthonormalization of the orbitals, and ultimately ends up with the Hartree-Fock equation

$$\hat{f}_i \chi_i = \varepsilon_i \chi_i , \tag{2.42}$$

where each Lagrangian multiplier ε_i can be interpreted as the orbital energies of the i orbitals. For a detailed derivation of the Hartree-Fock equation see Refs. [154;156;163]. $\hat{f}_i$ is the Fock operator with the formula

$$\begin{aligned} \hat{f}_i &= -\frac{1}{2} \nabla^2(r_i) - \sum_{k}^{N} \frac{Z_k}{|r_i - R_k|} + v^{HF}(i) \\ &= \hat{h}_i + v^{HF}(i) \end{aligned} \tag{2.43}$$

defining the effective one-electron operator. It consists of the one-particle Hamiltonian $\hat{h}_i$ and the Hartree-Fock potential $v^{HF}(i)$, which can be expressed in the term

$$v^{HF}(i) = \sum_{j}^{N} (\hat{J}_j - \hat{K}_j) \tag{2.44}$$

and describes the repulsive potential of a specific electron j, which is affected by the average field of the remaining N-1 electrons ($j \neq i$) in the molecular system. This means, a distinct spin orbital can only be determined, if those of all other occupied orbitals are already known. Therefore, the sets of orbital functions yielding the minimal energy solution is implemented within an iterative process, for which typically the self-consistent field (SCF) procedure is used.[154;156] Finally, during the Hartree-Fock method the Hamilton operator $\hat{H}$ is replaced by the one-particle Fock operator $\hat{f}$, for which reason the electron-electron repulsion that a specific electron experiences is only considered by an average field of all other electrons. Therefore, this method is a mean-field theoretical ansatz and will never result in an exact solution for multi-electron systems, but provides good approximations for many molecules.

2.4.2 Density Functional Theory

Quantum chemical methods that comprise a higher accuracy of the electron correlation due to Coulomb interaction terms have a significant increase in the computational effort in dependence on the size of the chemical system. Therefore, the nowadays most common theoretical method is the density functional theory (DFT), which calculates the molecular properties in terms of the electron density ρ as functional $E[\rho(r)]$, in contrast to the previously described Hartree-Fock ansatz which is based on wave functions Ψ as functional $E[\Psi(r_1, r_2, ...r_N)]$. The fundamental equation of DFT is

$$\rho(r) = N \int dr_2 ... \int dr_N |\Psi(r_1, r_2, ...r_N)|^2 \tag{2.45}$$

to calculate the electron density which is only dependent on the three Cartesian coordinates (and the spin coordinates), instead of the even more complex determination of wave functions with $3N$ coordinates (and the spin coordinates), and defines the probability to find one of the N electrons in the spatial volume dr around r. Thus, the DFT ansatz by Hohenberg and Kohn is less complex compared to HF, where the number of electrons in the system is considered. Furthermore, it is advantageous that integration of the electron density yields the number of involved electrons in the system. Another advantage is that the electron density is an observable itself, unlike the wave function, and can be measured by X-ray diffraction experiments.

Hohenberg-Kohn Theorem

Already in the 1920, the first orbital-free DFT model was derived by Llewellyn Thomas[164] and Enrico Fermi[165]; however, it could not yield satisfactory results due to an inappropriate description of the kinetic energy.[154] It took further decades until Pierre Hohenberg and Walter Kohn revolutionized the density functional theory by developing the famous Hohenberg-Kohn-theorems in 1964,[166;167] which can be summarized as:

1. **Hohenberg-Kohn-Theorem:**
   The ground-state properties, including the total ground-state energy of an electron system, is a distinct functional of the ground-state electronic density and can be written as

$$O[\rho] = \left\langle \Psi_0[\rho] | \hat{O} | \Psi_0[\rho] \right\rangle , \tag{2.46}$$

   whereby the functional is universally usable for each molecular system.

2. **Hohenberg-Kohn-Theorem:**
   The variational principle is valid for electron densities, which means that the energy functional $E_V[\rho]$ of a given potential V only reaches its minimal value, if the electron density ρ is equivalent to the exact ground-state density of the molecular system, meaning

$$E_V[\rho] \geq E_{exact,0} \, . \tag{2.47}$$

To derive an expression of the total ground-state energy as functional of the electron density, the electronic Hamilton-Operator (Equation 2.35) has to be divided into the kinetic energy operator of the electrons $\hat{T}_e$, the electron-electron correlation operator $\hat{V}_{ee}$ and an external potential operator $\hat{V}_{ext}$ comprising the electron-nuclei interaction, like

$$\hat{H}_e = \hat{T}_e + \hat{V}_{ee} + \hat{V}_{ext} \, . \tag{2.48}$$

As already previously done, the Born-Oppenheimer approximation is used, which means that the kinetic energy of the nuclei is neglected and the nuclei-nuclei repulsion is assumed to be

constant. Therefore, the total energy can be written as

$$\begin{aligned} E[\rho] &= \left\langle \Psi_0[\rho] | \hat{T}_e + \hat{V}_{ee} + \hat{V}_{ext} | \Psi[\rho] \right\rangle \\ &= \underbrace{\left\langle \Psi_0[\rho] | \hat{T}_e + \hat{V}_{ee} | \Psi[\rho] \right\rangle}_{F^{HK}[\rho]} + \int \rho(r_i) v_{ext}(r_i) dr_i \,, \end{aligned} \tag{2.49}$$

whereas F^{HK} characterizes the Hohenberg-Kohn functional. This contains the kinetic energy and the electronic repulsion. In analogy to the Fock operator $\hat{f}_i$, one can separate the latter term into a classical Coulomb repulsion integral

$$J[\rho] = \frac{1}{2} \int \int \frac{\rho(r_i)\rho(r_j)}{|r_i - r_j|} dr_i dr_j \tag{2.50}$$

and a non-classical part, describing the exchange-correlation energy $E_{XC}[\rho]$. However, the exact expression of the Hohenberg-Kohn functional, especially the kinetic energy functional and the exchange-correlation functional are still unknown. Nevertheless, it is possible to derive an approximation of the universal functional by different approximations, for which reason DFT describes several molecular systems appropriate well within a relatively low computational effort compared to other more accurate theoretical methods.

Kohn-Sham Theorem

To find a more accurate term of the universal functional, Walter Kohn and Lu Jeu Sham reintroduced orbitals in DFT in 1965.[168] Thus, DFT becomes dependent on the number of electrons in the molecular system, just as the HF ansatz. However, the Kohn-Sham model assumes a model system with N non-interacting electrons being located in a distinct potential, leading to a Hamiltonian of the form

$$\hat{H}_s = \hat{T}_s + \hat{V}_s \,. \tag{2.51}$$

The effective potential v_s includes the external potential v_{ext} and the exchange-correlation potential v_{XC}. According to the first Hohenberg-Kohn theorem, the total ground-state energy of this auxiliary system can be written as

$$E_s[\rho_s] = T_s[\rho_s] + \int \rho_s(r_i) v_s(r_i) dr_i \,, \tag{2.52}$$

while $T_s[\rho_s]$ describes the kinetic energy. Due to the non-interacting character, the Schrödinger equation can be solved exactly by a single Slater determinant, yielding the one-particle eigenvalue equation

$$\hat{f}_i^{KS}\chi_i^{KS} = \varepsilon_i\chi_i^{KS} \tag{2.53}$$

with the Kohn-Sham orbitals χ_i^{KS} and the Kohn-Sham operator

$$\hat{f}_i^{KS} = \left(-\frac{\Delta}{2} + v_s(i)\right) . \tag{2.54}$$

Additionally, Kohn and Sham have shown that the one-particle potential v_s can be chosen such that the electron density ρ_s of the modeled electronic system in Equation 2.52 is equivalent to the ground-state electron density of the target system ρ_0, where interactions between the different particles occur[155] and can be calculated from the Kohn-Sham wave functions by

$$\rho_s = \sum_i^N |\chi_i^{KS}|^2 = \rho_0 . \tag{2.55}$$

To derive a relationship between the non-interacting auxiliary system and the true system, in order to formulate an appropriate expression of the one-particle potential v_s, the ground-state energy term of the target system is rewritten into

$$E[\rho] = T_s[\rho] + J[\rho] + E_{XC}[\rho] + v_{ext}[\rho] . \tag{2.56}$$

Here, T_s still describes the kinetic energy of the non-interacting model system, which can be also obtained from the Kohn-Sham orbitals by

$$T_s = \sum_i^N \langle\chi_i^{KS}| - \frac{\nabla}{2}|\chi_i^{KS}\rangle . \tag{2.57}$$

The other three parts of Equation 2.56 consider the multi-particle interaction *via* the Coulomb repulsion energy $J[\rho]$, the exchange-correlation energy $E_{XC}[\rho]$ and the external potential $v_{ext}[\rho]$. The difference between the assumed kinetic energy term T_s of non-interacting particles and the real kinetic energy as well as the electron correlation and the exchange energies are summarized within the unknown E_{XC} term, which is defined as

$$E_{XC} = \left(T - T_s\right) + \left(V_{ee} - J\right) . \tag{2.58}$$

Further considering both the second Hohenberg-Sham theorem and the equality of the electron densities displayed by Equation 2.55 provides a definition of the one-particle potential v_s:

$$v_s(r_i) = v_{ext}(r_i) + \int \frac{1}{|r_i - r_j|}\rho(r_j)dr_j + v_{XC}[\rho(r_i)] \tag{2.59}$$

with

$$v_{XC} = \frac{\delta E_{XC}[\rho]}{\delta \rho} \,. \tag{2.60}$$

However, v_{XC} itself is still dependent on the density, for which reason the Kohn-Sham equation

$$\Big(-\frac{\Delta}{2} + v_{ext}(r_i) + \int \frac{1}{|r_i - r_j|}\rho(r_j)dr_j + v_{XC}[\rho(r_i)] \Big)\chi_i^{KS} = \varepsilon_i \chi_i^{KS} \,, \tag{2.61}$$

to calculate the ground-state electron density of a target system, has to be solved in an iterative process, equivalent to the Hartree-Fock equations (Equation 2.42). Hence, the same self-consistent field (SCF) procedure can be used by replacing the exchange operator $\hat{K}$ of the Fock operator $\hat{f}_i$ with the exchange-correlation potential v_{XC}.

As already described in detail, it is currently not possible to calculate the exchange correlation functional E_{XC} exactly, for which reason different approximations for this functional are made by using varying functionals. Thereby, these density functionals can be classified into three main categories, while the computational effort increases with the accuracy of the individual functionals. The most simple category is the so-called Local Density Approximation (LDA),[167] which is only based on the local electron density ρ modeled as homogeneous electron gas. Common LDA functionals are for example 'S-VWN' (Slater, Vosko, Wilk, Nusair)[169] and 'PW' (Perdew, Wang).[170] Those functionals provide appropriate results for solid sates like metals, but rather inaccurate properties for molecular systems because of the unprecise consideration of covalent bonding. The Generalized Gradient Approximation (GGA) functionals, like 'B-P86' (Becker, Perdew),[171;172] 'B-LYP' (Becke, Lee, Yang, Parr)[171;173] or 'PBE' (Perdew, Burke, Ernzerhof)[174] yield much better solutions for molecular systems. These functionals incorporate the gradient of the electron density $\Delta\rho$ additionally to the local density ρ. The third type summarizes the hybrid functionals displaying a combination of DFT- and HF-exchange terms. The widely used 'B3-LYP' (Becke, Lee, Yang, Parr)[173;175] functional is one representative of this category. The computational effort of hybrid functionals is comparable to those of HF calculations. However, due to the higher accuracy of hybrid functionals, they usually replace HF-calculations.

The second variable influencing the computational efficiency and the accuracy are basis sets (similar to those used in the HF ansatz), which characterize the spin orbitals and can be roughly

separated into two categories, namely the Gaussian-type orbitals (GTO)[176] and the Slater-type orbitals (STO).[177] STOs are wave functions constructing the atom orbitals by a combination of exponentials and spherical harmonics to describe the exponential decay over longer distances and fulfill Kato's Cusp condition near the nuclei.[155;156;178;179] They provide an exact solution for the Schrödinger equation of the hydrogen atom, but becomes sophisticated for multi-electronic systems. Therefore, in practice usually GTOs, which consist only of Gaussian functions, are used. In contrast to STOs, GTOs can be integrated analytically, but also provide less precise description of the orbital description. For larger distances, the function decays too fast and also the cusp at small distances to the nuclei is missing. Thus, a linear combination of those Gaussian exponentials are used to get a more precise result, which is summarized under the term contracted Gaussian function (CGF).[156;180;181]

So far, there is a huge variety of different basis sets and the library is still growing to develop even more accurate results with high computational efficiency. Mostly, the evolved basis sets in their original form are equipped with additional parameters to consider polarization functions and diffuse functions.

Furthermore, within DFT calculations several additional aspects can be included to reduce the difference between the calculated system and the actual target system. During this work, two extensions were used, namely the dispersion correction scheme by Stefan Grimme's DFT-D approach[182;183] and a continuum solvation model (CSM) to simulate the influence of solvent molecules on the solute.[184;185] The exact definitions of the individual basis sets, the varying functionals, and the distinct extensions are not part of this work, since the focus of this research lies on the time-resolved studies, whose results and the subsequent interpretation was solely supported by quantum chemical calculations.

The previously described DFT method is mainly used to determine ground-state structures, IR-spectra and potential energy surfaces along one coordinate to estimate activation barriers between different isomeric species. In its original form, DFT only allows the calculation in the ground state. To gain knowledge on the excited state of a molecular system, the initial DFT ansatz has to be extended with the Runge-Gross theorem[186] in combination with the linear response theory into a time-domain, known as time-dependent density functional theory (TD-DFT). It can be used for example to calculate electronic excitations of a system to modulate the corresponding UV-Vis absorption spectrum. The mathematical background is described in Refs. [155;187].

2.4.3 Møller–Plesset Perturbation Theory

The Møller–Plesset Perturbation Theory (MPPT or more commonly just MP) is a post-Hartree-Fock *ab initio* method, which corrects the mean-field ansatz of HF. It was proposed 1934 by Christian Møller and Milton Plesset to improve HF by adding higher excitations through a perturbation term.[188] This perturbation theory is based on the many-body perturbation theory (MBPT) to explain electron correlation effects in HF.[189;190] Within the MBPT, the Hamiltonian can be separated into the unperturbed Hamiltonian H_0 and the perturbation term V,[191–193] leading to a weak disturbance of the molecular system, by

$$H = H_0 + \lambda V \; . \tag{2.62}$$

λ characterizes the perturbation parameter, that defines the strength of the disturbance. However, it is assumed that the perturbation is rather small compared to H_0, for which reason the energy E and the perturbed wave function Ψ can be written as a Taylor expansion in powers of λ in the form

$$E = E^{(0)} + \lambda E^{(1)} + \lambda^2 E^{(2)} + ... \; \lambda^n E^{(n)} \tag{2.63}$$

$$\Psi = \Psi^{(0)} + \lambda \Psi^{(1)} + \lambda^2 \Psi^{(2)} + ... \; \lambda^n \Psi^{(n)} \; . \tag{2.64}$$

Thus, these equations can be differentiated into different parts, since all parameters with the suffix 0 describe the zero-order correction term, all parameters with the coefficient 1 stand for first-order corrections and so on. Ultimately, the perturbed Schrödinger equation can be derived to

$$\begin{aligned} &\Big(H_0 + \lambda V\Big)\Big(\Psi^{(0)} + \lambda \Psi^{(1)} + \lambda^2 \Psi^{(2)} + ... \; \lambda^n \Psi^{(n)}\Big) = \\ &\qquad \Big(E^{(0)} + \lambda E^{(1)} + \lambda^2 E^{(2)} + ... \; \lambda^n E^{(n)}\Big)\Big(\Psi^{(0)} + \lambda \Psi^{(1)} + \lambda^2 \Psi^{(2)} + ... \; \lambda^n \Psi^{(n)}\Big) \end{aligned} \tag{2.65}$$

and from this, the order-by-order specific corrections can be calculated representing higher order of perturbation. This can be done by expanding the products and sort the individual terms on both sides of the equation by orders of λ. Then, one can equate the terms of same order on the left and right hand side.

By further rearrangement, the following set of equations are generated:

$$\begin{aligned}
\lambda^0 &: \left(H_0 - E^{(0)}\right)\Psi^{(0)} = 0 \\
\lambda^1 &: \left(H_0 - E^{(0)}\right)\Psi^{(1)} = \left(E^{(1)} - V\right)\Psi^{(0)} \\
\lambda^2 &: \left(H_0 - E^{(0)}\right)\Psi^{(2)} = \left(E^{(1)} - V\right)\Psi^{(1)} + E^{(2)}\Psi^{(0)} \\
&\vdots \\
\lambda^n &: \left(H_0 - E^{(0)}\right)\Psi^{(n)} = \left(E^{(1)} - V\right)\Psi^{(n-1)} + E^{(2)}\Psi^{(n-2)} + \ldots E^{(n)}\Psi^{(0)} \,.
\end{aligned} \tag{2.66}$$

The Møller-Plesset perturbation theory is actually a special case of the MBPT, where the Hamiltonian H_0 is defined as the sum of one-electron Fock operators: [189;190]

$$H_0 = \sum_i^N f_i \,. \tag{2.67}$$

In combination with the zero-order perturbation term (λ_0 in Equation2.66), $E^{(0)}$ has to be the sum of orbital energies:

$$\begin{aligned}
&\left\langle \Psi^{(0)} | H_0 - E^{(0)} | \Psi^{(0)} \right\rangle = 0 \\
\Leftrightarrow \quad & E^{(0)} = \left\langle \Psi^{(0)} | H_o | \Psi^{(0)} \right\rangle = \sum_i \varepsilon_i \,.
\end{aligned} \tag{2.68}$$

Furthermore, from the first-order perturbation term in Equation2.66 it follows that

$$\begin{aligned}
&\left\langle \Psi^{(0)} | H_0 - E^{(0)} | \Psi^{(1)} \right\rangle = \left\langle \Psi^{(0)} | E^{(1)} - V | \Psi^{(0)} \right\rangle \\
\Leftrightarrow \quad & \underbrace{\left\langle \Psi^{(0)} | H_0 | \Psi^{(1)} \right\rangle - E^{(0)} \left\langle \Psi^{(0)} | \Psi^{(1)} \right\rangle}_{=0} = E^{(1)} \left\langle \Psi^{(0)} | \Psi^{(0)} \right\rangle - \left\langle \Psi^{(0)} | V | \Psi^{(0)} \right\rangle
\end{aligned} \tag{2.69}$$

of which the terms on the left hand side cancel each other, due to the validity of the ground-state Schrödinger equation $H_0\Psi_0 = E_0\Psi_0$ and the Hermitian character of the Hamiltonian, where $\left\langle \Psi | \hat{H}\Psi \right\rangle = \left\langle \Psi | \hat{H}\Psi \right\rangle^* = \left\langle \hat{H}\Psi | \Psi \right\rangle$. Thus, the first-order perturbation energy can be derived to

$$E^{(1)} = \left\langle \Psi^{(0)} | V | \Psi^{(0)} \right\rangle \,. \tag{2.70}$$

However, the sum of the unperturbed energy and the first-order perturbation yields just the

Hartree-Fock energy, since

$$\begin{aligned} E^{(0)} + E^{(1)} &= \left\langle \Psi^{(0)} | H_0 | \Psi^{(0)} \right\rangle + \left\langle \Psi^{(0)} | V | \Psi^{(0)} \right\rangle \\ &= \left\langle \Psi^{(0)} | \underbrace{H_0 + V}_{=H} | \Psi^{(0)} \right\rangle \\ &= E^{HF} \,, \end{aligned} \tag{2.71}$$

which is not an improvement of the HF ansatz. Therefore, at least a perturbation of second-order has to be considered to improve the initial theory. Finally, this correction can be expressed as

$$E^{(2)} = \sum_{s>0} \frac{|\left\langle \Psi_s | V | \Psi^{(0)} \right\rangle|^2}{E^{(0)} - E_s} \,, \tag{2.72}$$

where Ψ_s are the substitution functions spanning the virtual orbital space and E_S are the corresponding virtual orbital energies.[154;194] The virtual space is created by single, double, triple, etc. excitations of electrons from occupied to virtual orbitals and can be classified by the excitation level,[154;195] which describes the number of virtual spin orbitals which contributes to the unperturbed wave function $\Psi^{(0)}$, i.e. a single excitation means an excitation level of one, double excitation is taken into account by an excitation level of two, and so on. In general, it is only reasonable to consider a doubly excited state, since single excitations do not contribute in accordance to Brillouin's condition, and the terms for triple or higher excitations also vanish due to the Condon-Slater rules.[196–198] A detailed derivation of the second-order perturbation energy as well as higher-order Møller-Plesset perturbation theories, like MP3, can be found in Refs. [154;194;195;199;200].

In analogy to DFT, MP2 is only suitable for ground-state calculations, like S_0-geometry optimizations. For excited state calculations, e.g. to estimate the UV-Vis absorption spectrum, correlated excited state methods of the ADC*n* (*n*-th order Algebraic Diagrammatic Construction) family are used.[201] Within this work, ADC2 was applied to calculate the vertical excitation energies to get the absorption spectra of the distinct molecular systems. This method is also based on perturbation theory and represents the excited state equivalent to MP2 for ground-state calculations.

CHAPTER 3

1,3,5-Triphenylformazan

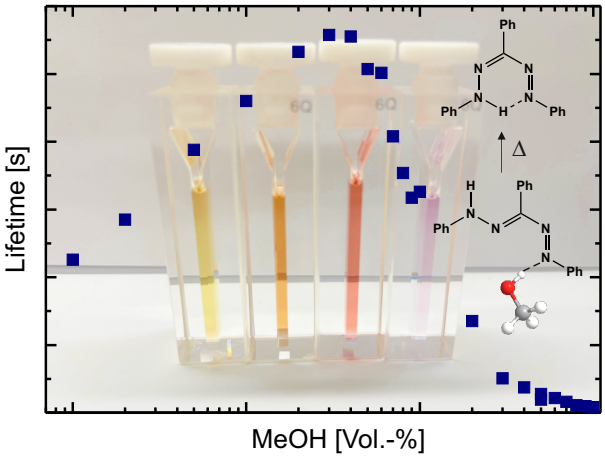

3.1 Introduction **42**

3.2 Experimental and Theoretical Approaches **45**

3.3 Results and Discussion **49**

3.4 Conclusion and Outlook **75**

This chapter is based on publications [1] and [2]. SW with support in setting up experiments by RJK performed the main part of experiments and all calculations. SS carried out several measurements in toluene solution. PN conceived and supervised the project. All authors analyzed and discussed the data and participated in writing the manuscript. The permissions for reproducing the original articles can be found on pp. XCIII.

3.1 Introduction

Formazans have the general formula $R^1-NH-N=CR^2-N=N-R^3$, bearing both a hydrazone (–C=N–N–) and an azo group (–N=N–). They have synthetic applications, such as in the production of open-shell verdazyl compounds[202–206] or as versatile formazanate ligands in organometallic complexes.[206–213] In general, formazans can be obtained by the reductive reaction of the corresponding, usually colorless, tetrazolium salt. One of the most prominent representative of these chromogenic molecular pairs, which was first synthesized as early as 1894,[214] is 2,3,5-triphenyltetrazolium chloride (TTC) and its formazan analogue 1,3,5-triphenylformazan (TPF). A solution of colorless TTC (for studies on its photochemistry, see Refs. [214–223]) will turn red upon the formation of TPF.[224] This chromogenic reaction has numerous applications, for example, using the enzymatic reduction of tetrazolium salts to formazans in biological assays to indicate cellular respiration and cell growth,[227–229] in agriculture to examine the germinability of seeds,[230;231] in chromatographic sugar determination,[232] and in medicine, especially in cancer research,[233–235] but also in areas like dosimetry,[223] chemical synthesis,[206;218] as chelating agents in organometallic chemistry,[206;236] or most recently the oxidation of amino acids by excited tetrazolium salts.[237;238]

Due to possible isomerization in both the azo and the hydrazone group upon excitation with visible light, TPF can be present in various isomeric forms. Thus, TPF exhibits a unique photochromism which depends on the excitation conditions and the solvent environment. Despite several studies, which focus on luminescence,[204;239] solvatochromism,[1;240–243] quantum yield determination,[244] electrochemistry,[239;245;246] laser flash photolysis,[226;247;248] quantum chemical calculations,[240;245;249–252] Raman and IR spectroscopy,[240;253–255;255;256;256–259;259;260] temperature variation,[225;226;261;262] and the impact of high pressure[262] to name a few, the interplay of light-induced processes which set in on an ultrafast time scale and extend to minutes has not been comprehensively studied for TPF. With regard to the involved intermediate species of TPF, several photoisomerization mechanisms of TPF are discussed in literature which differ in the thermal and photochemical reaction pathways between TPF isomers. The initial assignment was made by Kuhn and Weitz,[225] later modified by Langbein,[261] and concretized in a follow-up study by Grummt and Langbein;[226] further discussions of these schemes can be found in the literature.[256;263]

Although they all have in common the involvement of four isomeric forms of TPF, as shown in Figure 3.1; note that the orientation of the single bonds adjacent to the double bonds are sometimes drawn differently[256;263] and lead to further stable isomers, which will be discussed later in more detail (see Section 3.3.2). The energetically most-stable isomer is the trans-syn

form (also called 'red I', Figure 3.1), which is stabilized by an intramolecular hydrogen bond, forming a quasi-aromatic heterocycle. Illumination with visible light leads to an isomerization around the N=N double bond, yielding a cis-syn isomer ('red II', Figure 3.1). For this species, an intramolecular hydrogen bonding can occur as well. Afterwards, thermal isomerization around both N=N and C=N leads to the trans-anti analogue ('yellow I', Figure 3.1), which is accompanied by a color change of the solution from red to yellow. Spectroscopically, a hypsochromic shift from around 490 nm to 405 nm is observable in toluene solutions.[1;225;226;248;261] Under dark conditions, the trans-anti isomer thermally relaxes back into the energetically-favored trans-syn form *via* an anti-syn isomerization around the C=N double bond. This thermal isomerization was shown to proceed most remarkably in toluene,

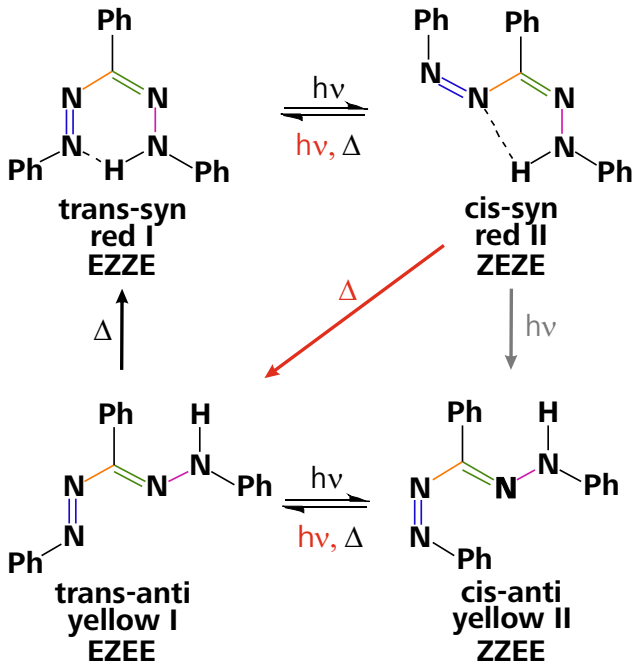

Figure 3.1: The two most prominent photoisomerization schemes of TPF after excitation, as introduced by Kuhn and Weitz[225] and by Grummt and Langbein.[226] Black arrows and symbols indicate pathways present in both models, while gray elements are only found in the Kuhn-Weitz scheme and red elements only in the Grummt-Langbein scheme, respectively. In literature, different nomenclatures are used describing principally the same species or group of molecular structures. The first nomenclature 'trans/cis' and 'syn/anti' corresponds to the N=N double bond (blue) and the C=N double bond (green), respectively. Depending on their spectral characteristics, the second nomenclature sorts them into 'red' and 'yellow'. In both nomenclatures the orientation of the adjacent C–N (orange) and N–N (magenta) single bonds is not clearly defined, but will be discussed in Section 3.3.2, which necessitates a third designation of all four bonds by 'E/Z'.

with a strong temperature dependence, rather small activation barriers (i.e., 4.6 kcal/mol,[225] 5.2 kcal/mol,[261] or 8.8 kcal/mol[262]), and astonishing values for the half-life of yellow I (138.9 h at 5 °C,[225] 13.2 h at 21 °C,[261] or 44.5 h at 25 °C,[262] respectively). However, it was already remarked early on that these numbers might be rather inaccurate[225;261;264] because the slightest impurities in the toluene already catalyze the thermal back-reaction to red I. However, when absorbing visible light, a photostationary state can be realized. Thus, the trans-anti isomer may follow another pathway, yielding a second yellow species, the cis-anti analogue ('yellow II', Figure 3.1). Both yellow forms can be characterized by absorption spectra with different extinction coefficients[224;226;261] and a broader absorption band for yellow II.

In order to unveil the full relaxation pathway after photoexcitation, we investigated different aspects of the light-induced reactions of TPF with various techniques. Initially, all relevant time scales are monitored from the primary steps, occurring in sub-ps, to the slowest thermal equilibrations, occurring within minutes (see Section 3.3.1). Several different pump-probe setups were used to monitor this extended time window, which is fs to ns transient absorption (TA) based on femtosecond lasers, ns to ms TA with ns excitation pulses, and ms up to minutes with pulsed light-emitting diodes (LEDs) as pump source. Additionally to the experimental data, DFT and TD-DFT calculations were performed to reassess the assignment of the involved isomers, before the interconnection between these different isomeric species partially proceeding *via* proton transfer is discussed (Section 3.3.2). Furthermore, due to the previously mentioned extraordinary sensitivity of the thermal relaxation from yellow I to red I, this relaxation behavior is investigated under the impact of cosolvents added to toluene (Section 3.3.3). These studies corroborate that hydrogen bonding between TPF and a cosolvent molecule plays a decisive role. Moreover, it is important whether this cosolvent molecule is part of a hydrogen-bonded network with other cosolvent molecules.

3.2 Experimental and Theoretical Approaches

The theoretical basics to understand the working principle of the used setups are previously explained in Chapter 2. The following section focuses on the practical implementation in the laboratory. Furthermore, the applied quantum chemical methods with the used parameters are described in more detail, while the underlying mathematical and physical fundamentals are also partly declared in Section 2.4.

3.2.1 fs-ns Transient Absorption Spectroscopy

For fs to ns transient absorption spectroscopy, a Ti:Sa amplifier system (Libra, Coherent) generated laser pulses with an energy of 1.2 mJ at a repetition rate of 1 kHz and a wavelength centered at 800 nm. Around 0.8 mJ of those were used to pump an optical parametric amplifier (TOPAS-C, Light Conversion), yielding pulses at 530 nm or (after a further nonlinear process) 330 nm. After passing a prism compressor, consisting of a quartz prism pair, these pulses were focused into the sample for excitation with a pulse energy of around 300 nJ and a diameter of 100 µm. For the probe beam, the remaining part of the 800 nm pulses were used to pump a home-built, two-stage noncollinear optical parametric amplifier (NOPA)[265] adjusted to ca. 500 nm, generating probe pulses with an energy of around 20 µJ. Similar to the pump beam, they were also compressed by a quartz prism pair, before focusing into a moving 1 mm calcium fluoride (CaF_2) plate to generate a white-light (WL) supercontinuum.[266] Then, this was split into a reference beam, bypassing the sample, and a probe beam, traversing the sample. These two beams were independently imaged onto two home-built grating spectrographs, and their spectra were recorded with photodiode arrays (S3901-512Q, Hamamatsu, 512 pixels) at 1.5 nm resolution. The polarizations of pump and probe beams were set to the magic angle (54.7°)[120;267] before reaching the 100 µm flow cuvette (quartz glass, Starna) to exclude possible polarization and anisotropy effects. The temporal resolution was around 100 fs, and the temporal delay was introduced by a cornercube retroreflector on a delay stage (M-531.2S, Physik Instrumente) placed in the pump beam. The sample solution was set to an optical density between 0.2 and 0.3 at 480 nm over an pathlength of 100 µm.

3.2.2 ns-ms Transient Absorption Spectroscopy

For ns to ms TA, a Nd:YAG ($Nd:Y_3Al_5O_{12}$) laser with a repetition rate of 10 Hz and pulse duration around 8 ns (Surelite II, Continuum) was used as excitation source. The Nd:YAG laser produces light pulses with either 532 nm (second harmonic) or 355 nm (third harmonic), while the latter one can also act as pump beam for an optical parametric oscillator (OPO; Surelite OPO Plus, Continuum) generating tuneable pulses in a spectral range between 410 nm - 680 nm with pulse energies up to 55 mJ. Within this work, 355 nm, 410 nm and 532 nm pulses each with an energy of 10 mJ were utilized to excite the sample. First, an optical telescope compensates the divergence of the pump beam, which is caused by the OPO, before it is directed *via* a prism pair onto a high-energy shutter (LS055, nmLaser; shutter 2 in Figure 3.2), which allows single

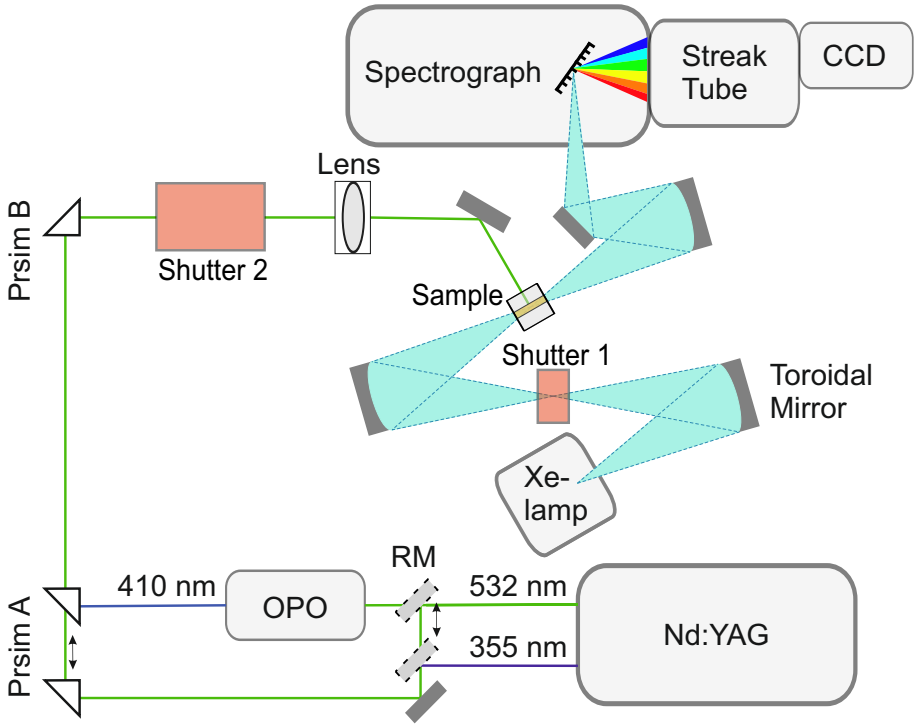

Figure 3.2: Schematic representation of the ns-ms transient absorption. The pump beam of either 355 nm, 410 nm or 532 nm light is generated by a Nd:YAG laser, potentially combined with an OPO. The arrangement of the removable mirror (RM) and prism A depends on the excitation wavelength. In the case of 410 nm excitation, the OPO is pumped by the second-harmonic (532 nm) of the Nd:YAG laser. The pathway of the 355 nm and 410 nm pump beam is equivalent to the crayoned 532 nm one (green line) behind prism B until they reach the sample. A cylindrical lens ensure the homogeneous excitation of the sample volume over the full 10 mm path length of the probe beam, which is generated by a Xe-flash lamp and reaches the detection unit until traversing through the sample. The pump pulses are blocked behind the sample.

pulse selection. Behind the shutter, a plano-convex cylindrical lens ensures excitation of the sample over the whole width of the cuvette in horizontal direction. The probe light is generated by a pulsed 150 W Xe-flash lamp (MSP-05, Müller Elektronik-Optik), originating white light pulses from 250 µs up to 10 ms. A toroidal mirror focuses the pump beam onto an electronic shutter (LS6ZM, Uniblitz; shutter 1 in Figure 3.2) to block the continuous background light of the Xe-flash lamp. It ensures a gently approach with the sample, which becomes important for molecules with high conversion rates, and enables a major number of measuring scans without changing the sample volume. Afterwards, the probe beam is focused into the sample perpendicular to the pump beam, before the transmitted part of the probe beam is collected by a third toric mirror, which finally focuses the probe pulses onto the entrance slit of the spectrograph (Bruker 200is). The spectrograph contains a grid (100 lines/mm), which defines the spectral resolution. Lastly, a streak camera (C7700, Hamamatsu Photonics), comprising a streak tube and a CCD camera (ORCA-CR, Hamamatsu Photonics), ensures the temporal resolution of the probe beam. In general, the used streak camera contains 512×512 pixel with which a spectral region from 350 nm to 750 nm can be covered, whereas the time window can be varied between 500 ns up to 10 ms. For a detailed explanation of the streak camera's working principle see Section 2.2.4; for further information on the experimental implementation see Refs. [139;268]. The experimental setup is schematically shown in Figure 3.2.
For the experiments displayed in this work, a 2 mm (excitation path) × 10 mm (probe path) quartz glass cuvette (Starna) was used. The sample was circulated through the flow cuvette from an external sample reservoir of 4 ml. The optical density of the sample was set to 0.5 OD at 355 nm or 0.4 OD at 500 nm depending on the excitation wavelength over an optical path length of 10 mm.

3.2.3 ms-min Transient Absorption Spectroscopy

In order to record ms to min TA data, a UV-Vis absorption spectrophotometer (Cary60, Agilent) was combined with a LED as excitation source in a perpendicular arrangement. The wavelength-dependent temporal evolution of the absorption signal could be monitored with a time increment of 12.5 ms by the kinetic mode of the spectrometer. For some of the performed experiments, a different spectrophotometer (UV 1800, Shimadzu) was used; however, with a time increment of 480 ms. The LED's temporal rectangular pulse width was also set to 12.5 ms or 480 ms, respectively. The sample ($V \leq 250$ µl) was inside a rectangular quartz cuvette (Starna, 10 mm × 2 mm). There, the absorption was monitored over the 10 mm optical path length, while the LED was pointed onto the 2 mm path length to ensure homogeneous il-

lumination of the entire sample volume. Ultimately, each wavelength-specific kinetic trace was measured at least three-times and then averaged to get a better signal-to-noise ratio. The TA data were monitored in 10 nm steps.
Furthermore, the same data acquisition method was used in combination with a home-build cryostat to get more information about the temperature-dependent behavior, e.g. to calculate the activation barrier in different solvent environments. The utilization of the cryostat required a different UV-Vis absorption spectrophotometer (Perkin Elmer, Lambda 9 UV/VIS/NIR Spectrophotometer) with a temporal resolution of 0.1 s. The temperature was varied from -5 °C up to 30 °C in 5 °C steps. During these measurements, the sample was stored in a (10×10) mm quatz cuvette.
The sample's concentration was set around 0.5 OD at 480 nm over an optical path length of 10 mm for all ms-min TA experiments.

3.2.4 Quantum Chemical Calculations

Quantum mechanical calculations on all stable TPF conformers were performed using the Orca package.[269;270] All ground-state structures were optimized on the level of restricted closed-shell density-functional theory (RHF-DFT) using the B3LYP functional[173;175] and the def2-TZVP basis set[271;272] with D4 dispersion correction.[182;183] The ground-state affiliation of each optimized geometry was verified by vibrational frequency calculations. Afterwards, the first 20 vertical excitation energies were calculated by TD-DFT level of theory and enveloped by Gaussian functions to get an estimation of the corresponding UV-Vis spectrum of each optimized ground-state structure. Furthermore, potential barriers connecting the individual conformers were roughly estimated (as DFT is not able to correctly describe the bond rotation around double bonds, due to the consideration of only one Slater determinant) from the crossing points for the relaxed potential energy surfaces (PES) along the rotational motion around a corresponding bond starting from each stable conformer using B3LYP/def2-TZVP level of theory.

3.3 Results and Discussion

3.3.1 Photochemistry of TPF

The steady-state UV-Vis absorption spectra of TPF detected in methanol and acetonitrile solution are nearly identical, with two main absorption bands peaking around 300 nm and 480 nm, of which the latter comprises a weak shoulder on its red edge (see solid curves in Figure 3.3). In unsubstituted formazan, the lowest electronic transition is of $n-\pi^*$ character.[249] The same is found for TPF, albeit with a negligible oscillator strength, so that the major absorption band in the visible is dominated by a $\pi-\pi^*$ transition[242;273] to the second excited state S_2 (see also in the Appendix Figure A.17 with corresponding DFT calculations). For the TPF absorption spectrum in toluene solution (blue curve in Figure 3.3), a small spectral shift of the low-frequency $\pi-\pi^*$ transition band by ~10 nm is observed. However, even daylight changes the photochemical equilibrium among the isomers, as the absorption bands of the red isomeric TPF species decrease, while especially around 400 nm the absorption increases (dashed curves in Figure 3.3). This behavior was already reported in literature, where the formation of the yellow isomeric species was observed in acetonitrile[274] as well as in toluene/benzene solutions[225;226;248;261] by an increased absorption around 400 nm under irradiation with visible light. Constantly illumi-

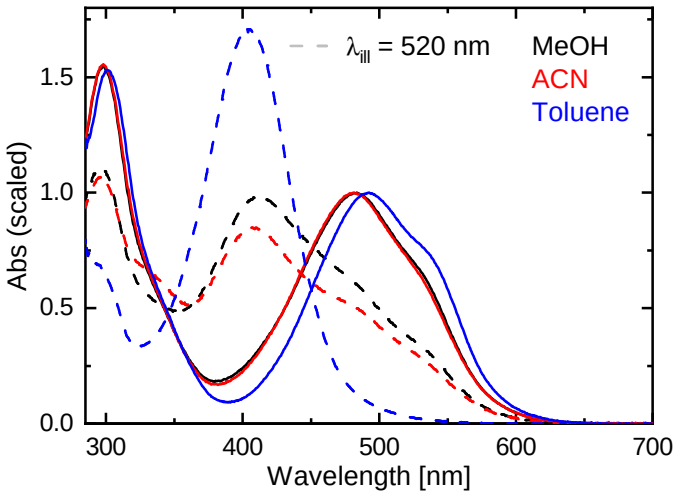

Figure 3.3: Steady-state absorption spectra of TPF dissolved in methanol (black), acetonitrile (red), and toluene (blue). The solid curves display the ground-state absorption spectra (normalized to the maximum around 500 nm), while the dashed spectra correspond to the photostationary state under illumination with 520 nm light.

nating TPF in methanol solution with 520 nm light also leads to the formation of the yellow species (see Figure 3.3). In comparison to toluene, where the equilibrium is nearly fully shifted under these conditions, in acetonitrile and methanol a distinct amount of TPF molecules remains in its initial conformation, indicated by both the lower absorption around 400 nm and the remaining contribution at 500 nm (compare black/red dashed curves in Figure 3.3 with the blue dashed curve).

Since the formation of the yellow isomeric TPF species is most favorable in toluene solution, further isomerization experiments in dependency on varying illumination wavelengths were performed in this solvent. To shift the equilibrium between the isomers, the TPF solution, which had fully relaxed in dark conditions, was illuminated for a certain time with different wavelengths at 405 nm, 455 nm and 520 nm. Afterward, the LED was switched off, and one UV-Vis absorption spectrum was measured (which takes about 27 s with the given spectrometer). This procedure was repeated for different illumination intervals, as shown in Figure 3.4a-c. A photostationary state had already been reached after 10 min of illumination, and the color of the solution changed to yellow. However, the absorption spectrum measured directly after stopping the illumination (red curve) slightly deviates from the actual absorption spectrum of the photostationary state (added as a green curve, measured with the illumination still on). This difference has been observed before,[225;226;261] and the latter one is indicative of yellow II, which can be produced photochemically from yellow I but relaxes back to yellow I within 1.1 s (*vide infra*) and thus does not contribute to the curves of Figure 3.4 except for the green curve. Furthermore, it is not surprisingly that the equilibration strongly depends on the illumination wavelength. In comparison to irradiation with 520 nm light, which shifts the equilibrium in toluene nearly fully to the yellow isomeric species, in the case of 405 nm light a bigger part of the isomers remains in the red isomeric form indicated by the higher absorption intensity around 500 nm. Additionally, also the amount of yellow II molecules is strongly dependent on the excitation wavelength. For the back-relaxation, the illumination of the yellow solution in the photostationary state was stopped, and the measurement of the absorption spectrum was initiated after a defined time interval (Figure 3.4d-e). Those data show that the isomerization processes are fully reversible, as indicated by two isosbestic points at around 345 nm and 450 nm.

As already mentioned previously, the thermal back-relaxation from yellow II to yellow I proceeds within several hundreds of ms, for which reason this relaxation process could be monitored over time with an absorption spectrometer. The temporal evolution was detected at an observation wavelength of 400 nm for different illumination wavelength (see Figure 3.5). Thereby, the black part shows the initial absorbance before illumination. After some time the LEDs were switched on until a photostationary state was reached, marked by the green region and after-

wards switched off to observe the thermal reorientation of yellow II species, which is indicated by the red curve. In dependence on the illumination wavelength, different equilibration ratios between the red and yellow species are generated. Thus, the initial intensity increase after

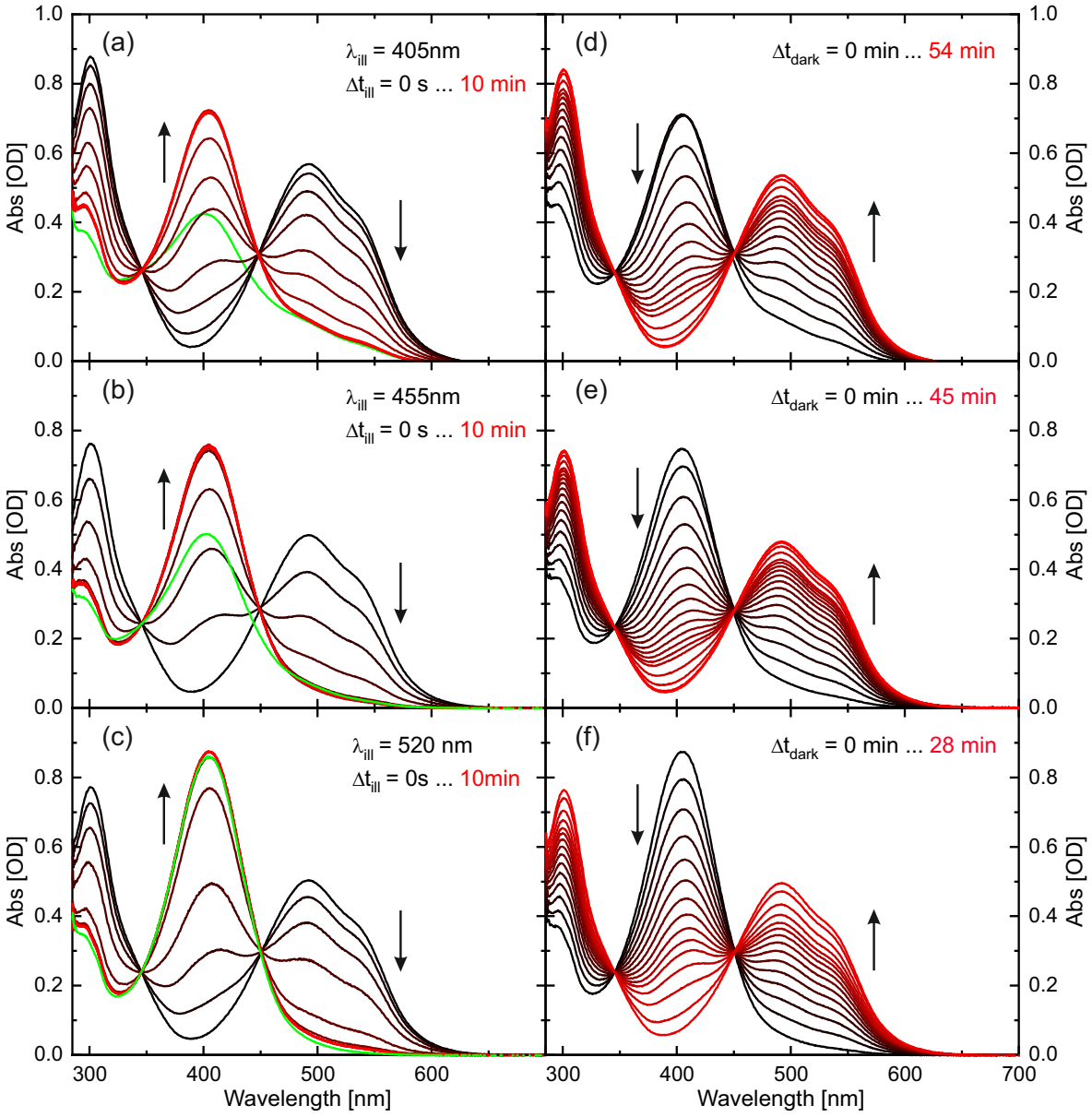

Figure 3.4: Illumination series in toluene with different LEDs emitting at 405 nm (a), 455 nm (b) and 520 nm (c) to study the influence of the irradiation wavelength. All three series were recorded in the same way, namely illuminated for the indicated time intervals (always doubled between 0.5 s - 10 min), then the LED was turned off and the absorption spectrum was measured. The green spectrum was taken for the photostationary state (i.e., with the LED still on). (d-f) Spectra taken at indicated time intervals after stopping the illumination. The back-relaxation was fully reversible within minutes in all cases.

stopping irradiation with 405 nm light (see Figure 3.5a) hints to a thermal back-relaxation from yellow II to yellow I, which is caused by the higher molar extinction coefficient of yellow I compared to yellow II. Afterwards, yellow I also starts to relax back into the initially excited red isomeric species (note that the temporal course of the final back-relaxation reaching the starting absorbance before excitation is not fully shown here). In contrast, in the case of 565 nm illumination the final back-relaxation directly starts without any intermediate step after switching off the LED. Thus, with 565 nm irradiation yellow II cannot be accumulated, since yellow I does not absorb at this illumination wavelength, which assists the previously drawn assumption that yellow II is only formed from yellow I. Furthermore, it becomes evident that the green curve in Figure 3.4 constitutes also a mixture of the yellow species with predominantly yellow I molecules at higher illumination wavelengths, which explains the increased absorption intensity as well as the red-shift with increasing irradiation wavelength.

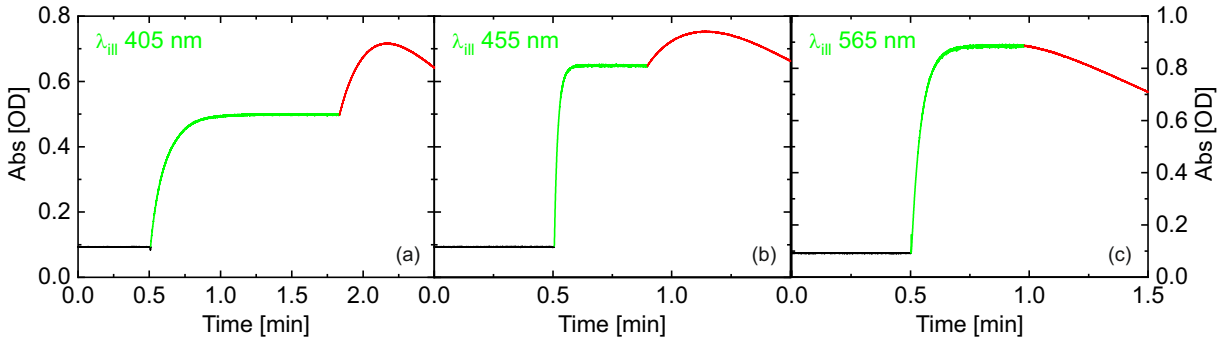

Figure 3.5: Equilibration between the different isomeric species of TPF in dependence on the illumination wavelength in toluene. The temporal evolution was detected with a UV-Vis absorption spectrometer at an observation wavelength of 400 nm. The black region describes the initial absorbance without illumination. The green part shows the absorption changes over time under constant irradiation with a (a) 405 nm, (b) 455 nm and (c) 565 nm LED, while the red curve displays the thermally driven absorption changes after illumination. Note that the latter one is only shown for the first few seconds and does not represent the full relaxation process.

In the literature, a debate about the exact isomerization mechanism, especially about the conversion step from the red isomers to the yellow species derived from observed absorption changes and laser flash photolysis studies, can be found.[225;226;261;263] To verify both the isomerization pathway to the yellow forms and the back-relaxation into red I, broadband transient absorption experiments have been performed on various time scales, which is described in the following. The addition of other substituents to the formazan may allow a light-induced reaction from yellow I to red I,[247] but for TPF it only proceeds thermally.[225;261]

After elucidation of the various isomerization processes in neat solutions, the final back-relaxation from the yellow isomeric species into the initial red TPF form was also studied in dependence

on solvent variations, on which Section 3.3.3 focuses.

fs-ns Transient Absorption of 1,3,5-Triphenylformazan

The initial photodynamics of TPF were followed by recording the TA on a fs to ns time scale after excitation either at 530 nm or 330 nm. Transient absorption spectra of TPF are shown in Figures 3.6a,c for methanol solution. In both cases, two regions of increased absorption around 400 nm and 600 nm are observed, together with the ground-state bleach (GSB) in the spectral region around 500 nm. Whereas the overall signal intensity decreases with time, a contribution persists beyond the experimental time window of 2 ns.[221] The decay-associated difference spectra (DADS), resulting from a global multiexponential fit to the data matrices with four time constants, are displayed in Figures 3.6b,d, respectively [contributions for modelling the coherent artifact[120] are not shown for clarity].
The fastest process, with decay time τ_1 being 0.3 ps and 0.2 ps, respectively, for the two excitation wavelengths, may be assigned to isomerization dynamics connected to the azo group. For trans-azobenzene, the excited-state dynamics directly towards a conical intersection exhibit a decay time around 0.3 ps,[24;25;275–279] with similar values reported for related compounds.[280–282] However, there is also a further excited-state motion in trans-azobenzene on a time scale of 1 ps–3 ps, assigned to diffusion-type motion[24] or the passage of a barrier in the excited state.[278] Along these lines, the positive signals around 400 nm and 600 nm (red DADS in Figure 3.6b,d) may indicate absorption features of molecules still in an excited state that depopulates with decay time τ_2 mainly into the ground-state configuration that was present prior to excitation, as can be seen by the negative contribution in the red DADS. We link the more pronounced excited state absorption (ESA) for excitation at 330 nm compared to 530 nm to the excess energy introduced by the higher photon energy. The DADS with τ_3 (green DADS) may reflect relaxation dynamics accompanied by vibrational cooling of molecules either in the excited state or already in the ground state all ending in the most stable conformer that was initially excited. Although the dominant fraction of excited molecules returns to the initial ground state configuration, a GSB at 480 nm and a product absorption around 330 nm remains on a time scale >2 ns (see also blue DADS) substantiating the formation of another stable photoisomer. Note that TPF is in an equilibrium of two ground state conformers with predominantly red I but also a few red II conformers, so that the TA data observed after excitation at 330 nm resemble the superposed dynamics of both isomers which explains the small differences in the absorption strength and dynamics compared to the situation when exciting at 530 nm. This aspect will become more evident on a longer time scale (*vide infra*).

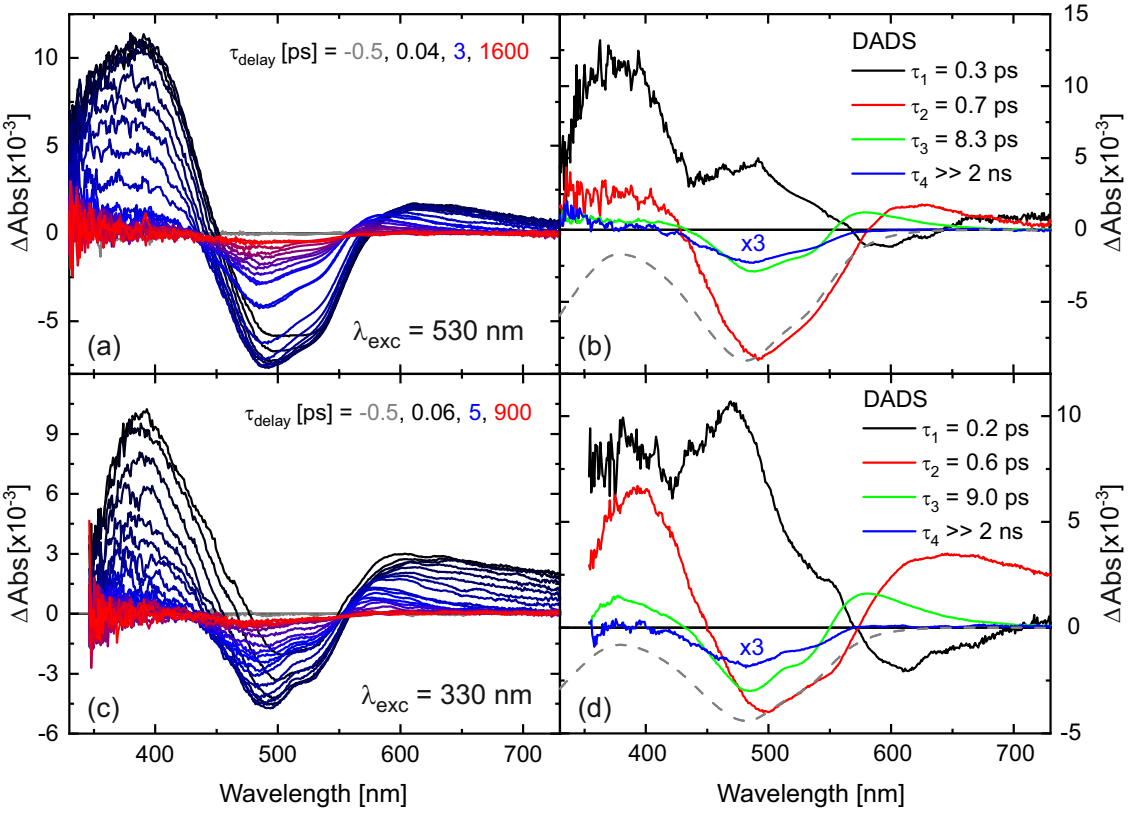

Figure 3.6: Transient absorption of TPF in methanol after excitation at 530 nm (a) and 330 nm (c) after defined delay times on a fs-ns time scale. The corresponding DADS from a global exponential fit to the data are given in (b,d). The scaled and inverted absorption spectrum of the initial sample is given by a gray-dashed line for comparison.

The TA data in the fs-ns time range of TPF in the solvent acetonitrile are very similar and can be analyzed and interpreted accordingly (see Figure A.3). Only time constant τ_3 assigned to vibrational cooling is by a factor of two larger compared to the situation in methanol. The more rapid vibrational cooling in methanol compared to acetonitrile was reported for other systems and is related to intermolecular hydrogen-bonding in protic environments aggravating energy transfer from the solute to the solvent.[283;284]

There is an alternative rationale for the dynamics on the ps time scale. From resonance Raman studies it was concluded that the initial photoinduced process is an excited-state intramolecular proton transfer (ESIPT).[256] Since the isomer red I that predominates in solution is a hydrogen-bonded quasi-aromatic heterocycle, there is a striking congruence with intramolecularly H-bonded β-diketones which have been studied with laser flash photolysis[285;286] and ultrafast spectroscopy approaches.[93;287–290] The latter revealed that ESIPT occurs within less than 0.1 ps,

followed by relaxation to the lowest excited state in a few ps, and subsequent depopulation of the excited state on a time scale of 10 ps both by relaxation to the hydrogen-bonded ground-state isomer and the formation of other isomers by rotation around a single or double bond. Given the similarity of the molecular system and of the detected time scales, an analogous assignment of processes to the observed dynamics is plausible as well.
A quantitative analysis of our data assuming a fully branched model, in which each transient species is partially converting into each other and partially converting back into the ground-state species, gave a value of 7 % for the quantum yield of product formation [see Kutta *et al.*[139], also containing detailed discussion on the general analysis of global fit data]. This is significantly lower than both isomer formation after ESIPT in β-ketones [e.g., 36 % for acetylacetone in acetonitrile][289] and N=N isomerization in trans-azobenzene [31 % for n$-\pi^*$ and 15 % for $\pi-\pi^*$ excitation in acetonitrile, slightly different yields in other solvents],[278] so that an identification of the initial reaction step is not unambiguous from the TA data but will be further analyzed in Section 3.3.2. The rather low quantum yield could be related to the significant $\pi-\pi^*$ character (delocalized over the entire molecular framework) of the initially excited S_2 in TPF (see Appendix Figure A.17), but might also originate from the intramolecular hydrogen bond stabilizing the planar configuration of the six-membered chelated ring, thereby disfavoring an out-of-plane motion required for photoisomerization. Nonetheless, our TA data corroborates that although the vast majority of excited red I molecules returns to the red I configuration, the decision along which reaction pathway the system evolves involving several thermal isomerizations (see Section 3.3.3) is already made within the first few ps.

ns-ms Transient Absorption of 1,3,5-Triphenylformazan

In order to follow the reaction dynamics further on a ns to ms time scale, the TA of TPF after exciting at 532 nm or 355 nm was recorded with a pump-flashlamp-probe spectrometer using a streak camera as detection unit (see Section 3.2.2). The TA data recorded for TPF in methanol after excitation at 532 nm consist of one absorption band around 340 nm and the GSB at 480 nm. Both features rise faster than the temporal resolution of the used setup, which agrees with the formation of these two TA features within a few ps as determined in the previous part by fs-ns TA, and persist beyond the time window of 1 ms. Hence, a global monoexponential model yielding one DADS (magenta curve in Figure 3.7a) is sufficient to fully describe the data, and this DADS matches the one for τ_4 of the fs-ns TA measurements (blue-dotted curve in Figure 3.7a). When exciting at 355 nm, the same absorption band at 340 nm is observed as after

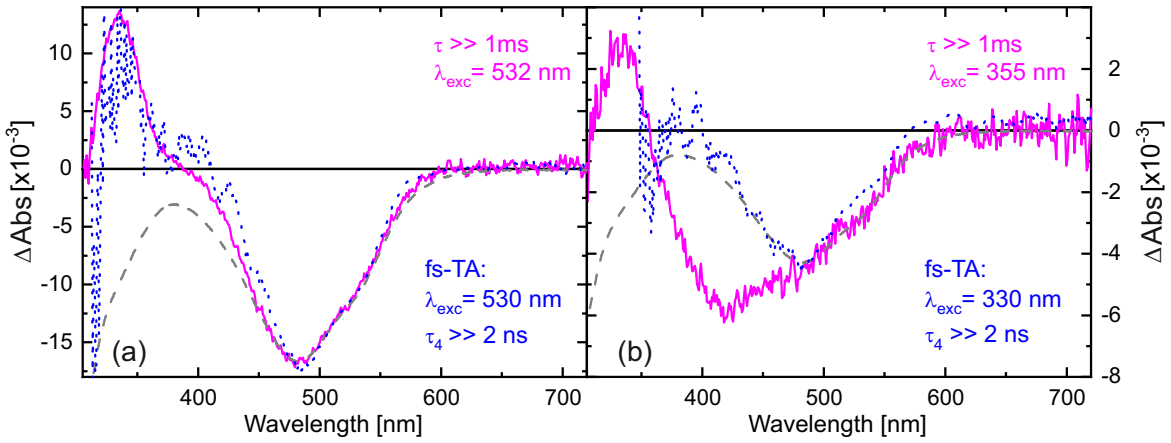

Figure 3.7: DADS of TPF in methanol after excitation at 532 nm (a) and 355 nm (b). The magenta DADS result from a global monoexponential fit to the data on a 1 ms time window. The blue dashed curves are the DADS corresponding to τ_4 of the fs-ns TA experiments (blue curves in Figure 3.6b,d) scaled to match the negative contribution at around 500 nm. The inverted absorption spectrum of the initial sample also scaled to the negative contribution at around 500 nm is given by a gray-dashed line for comparison.

532 nm excitation. However, the GSB is broader in this case, ranging from 350 nm up to 600 nm. Comparing the DADS with the absorption spectrum of TPF under 520 nm illumination (black-dashed line in Figure 3.3) reveals the origin for this behavior. The intense Xe-flashlamp of ms duration used as probe source in the ns-ms TA experiment is sufficient to prepare a mixture of red I and yellow I isomers prior to the excitation of the system by the intense pump pulse so that exciting at 532 nm leaves the yellow isomers unaffected, whereas exciting at 355 nm allows the excitation of both isomers, causing a GSB signal comprising the spectral signature of both. To note, in the fs-ns TA experiment (blue dashed line in Figure 3.7b) no accumulation of a probe-light induced photostationary equilibrium between forms red I and yellow I is observed due to significantly shorter and less intense probe pulses. Again, the ns-ms TA data obtained for TPF in acetonitrile (Figure A.6) and toluene (see Figure 3.9) are very similar to the ones recorded in methanol.

ms-min Transient Absorption of 1,3,5-Triphenylformazan

The preceding two TA measurement series have shown that the species absorbing around 340 nm is formed on an ultrafast time scale and persists well beyond 1 ms. Hence, ms to min TA mea-

surements were performed exciting TPF either at 390 nm, 405 nm, 455 nm, or 530 nm. The maximal time window of all four measurements was set to 1 min, sufficient for detecting the full recovering process to the initial ground state situation of TPF in methanol. All data matrices were analyzed by a global biexponential fit, yielding the DADS shown in Figure 3.8. Comparison to the DADS from the ns-ms TA measurements (pink curve in Figures3.8a,d) confirms that the same dynamics that were monitored up to 1 ms can now be followed completely. The cyan DADS corresponding to τ_4 exhibits a positive absorption peaking around 340 nm for all excitation wavelengths.This absorption band is not due to the yellow isomers that absorb around 405 nm but rather originates from red II. Its absorption in the visible spectral range, which is related to the hydrazone group, may be similar to that of red I, but its UV absorption band is red-shifted compared to that of red I. The two isomers differ by isomerization in the azo group and hence we note that trans-azobenzene also has a more intense and higher-energy absorption compared to cis-azobenzene.[291;292] Thus, we conclude that excitation of red I leads

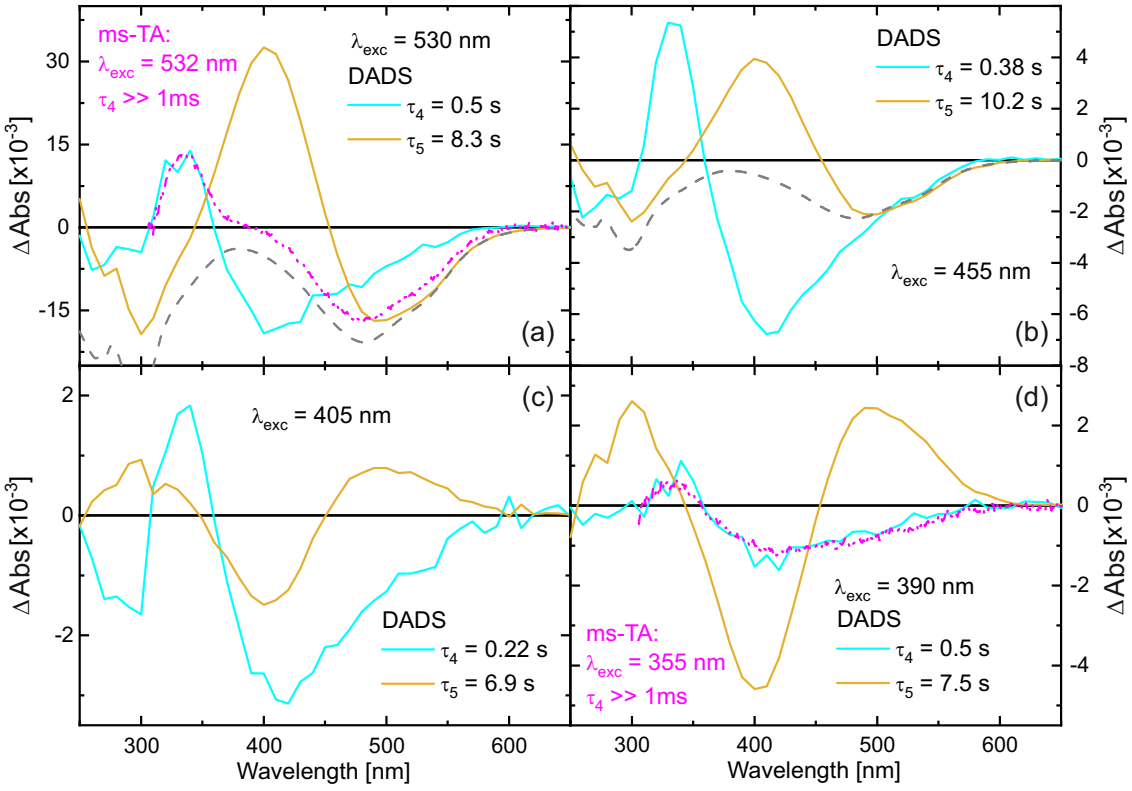

Figure 3.8: DADS of TPF dissolved in methanol, obtained by a global biexponential fit to the data matrices detected after excitation at 530 nm (a), 455 nm (b), 405 nm (c) and 390 nm (d). The gray-dashed line represents the absorption spectrum of the solution, while the pink DADS are taken from Figure 3.7 for comparison.

to the formation of red II in accordance with the isomerization scheme of Figure 3.1 derived from previous models.[225;226] The DADS furthermore comprises negative contributions around 500 nm and around 405 nm. These negative amplitudes resemble spectral features of red I and yellow I, respectively, and thus give evidence that photochemically formed red II thermally relaxes back to red I and to yellow I with a decay time of a few hundred milliseconds. The typical absorption feature of formed yellow I is seen at 405 nm in the orange DADS corresponding to τ_5. Thus, the slowest dynamics observed after 530 nm excitation are described by the orange DADS, which shows the spectral features of red I as a negative amplitude (compare the gray-dashed inverted ground-state absorption spectrum) and the absorption feature of yellow I as a positive amplitude, demonstrating the thermally activated back relaxation to red I on a time scale of 10 s (Figure 3.8a).

Figure 3.8b shows a similar experiment, but with 455 nm excitation. As red I and red II both absorb at 455 nm, here contributions of both isomers show up in the data. The observed dynamics can nonetheless be interpreted on the lines of the 530 nm excitation experiment in Figure 3.8a, as the additional contribution of excited red II are rather low.

The situation changes when exciting TPF at 400 nm (Figure 3.8c). Now, only a small amount of red I is excited, again giving rise to the dynamics described by the cyan DADS that is very similar to the two situations with 530 nm or 455 nm excitation, respectively. However, since in the dark also yellow I contributes to a small amount to the ground state equilibrium (see Figure 3.1) it is excited by 405 nm light giving rise to yellow II formation. This is substantiated by the second DADS (orange) that shows a positive absorption feature of yellow II at around 500 nm that decays with a lifetime of ca. 7 s (Figure 3.8c) back into yellow I identified by the characteristic negative amplitude at 405 nm.

The data recorded with 390 nm excitation (Figure 3.8d) agrees with this interpretation, because at this wavelength, red I can be excited even worse, whereas yellow I still has a high extinction coefficient, so that the cyan DADS (mostly representing relaxation after generation of red II from red I) becomes smaller whereas the orange DADS (comprising yellow II photogenerated from yellow I) gains in relative intensity.

In comparison to the kinetics in methanol, the ground-state processes of TPF on a ms to min time scale are slower in acetonitrile (see Figure A.11), but still much faster than in toluene solution (see Figure A.12), where the thermal back-relaxation takes several minutes. Finally, this long-range connectivity between the different isomers is also in accordance with the revised model by Grummt and Langbein.[226] It is also noted that the here determined decay times in toluene are orders of magnitude lower than the values of many hours, reported for studies with excessively purified toluene. This is not surprising because during this work although

anhydrous toluene was used, but without further purification. Repeating the measurements on different days regularly led to slightly deviating lifetimes mainly in toluene solutions, which were related to small temperature differences, varying humidity levels, and possibly traces of impurities in the cuvettes.
By these experiments it was possible to determine the lifetime of TPF's red II and yellow I conformers in dependence on varying solvent environments. Also some absorption characteristics of yellow II, like the small spectral blue-shift or the reduced extinction coefficient compared to yellow I, could be specified. However, the lifetime of yellow II could not be estimated by a single excitation of a red TPF solution. Therefore, the following section is focused onto the specification of yellow II.

Characterization of Yellow II

After spectroscopic verification that yellow II is not directly formed after excitation of red I, but instead from further illumination of yellow I, time-resolved absorption experiments of a yellow solution were carried out. TA experiments on a time window of 1 ms and an excitation at 532 nm were performed. Since the thermal relaxations are slowest in unpolar solvents, TPF was dissolved in toluene to generate this yellow solution.

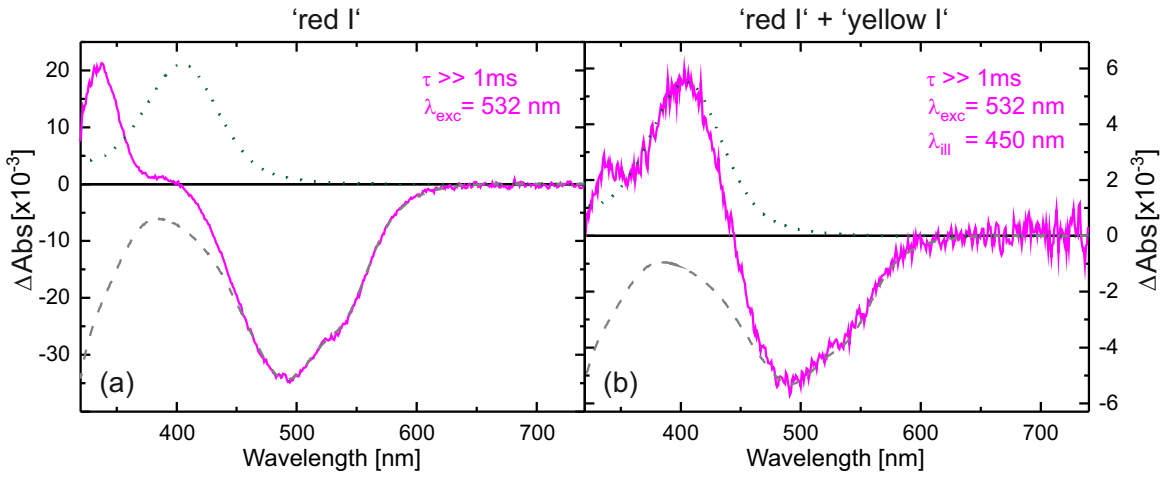

Figure 3.9: Transient absorption during the first millisecond after excitation with a 532 nm pulse from a Nd:YAG pump laser. DADS when exciting a toluene solution of TPF (a) that was in the dark before and (b) when the reservoir was constantly illuminated with 450 nm light (LED2, cw). The discontinuous lines are scaled spectra of a solution in the dark (gray dashed lines, inverted) and spectrum of the photostationary state (green dotted lines).

We illuminated a reservoir of the TPF solution constantly with an intense 450 nm LED to create a majority of yellow species. This solution was circulated and needed about 4 s from the reservoir to the cuvette, which means that both red I and the yellow isomeric species were present in this solution. Since yellow II is characterized by a broader absorption band compared to that of the yellow I isomer (*vide infra*), the nanosecond laser pulse at 532 nm can excite both the red I and yellow II isomers.

When this applied to the yellow TPF solution, absorption signals within the experimental time resolution arise that do not change within the monitored time interval of 1 ms, i.e., they are associated with a decay time widely exceeding 1 ms equivalent to those corresponding to a TPF solution previously kept in the dark. The corresponding decay-associated difference spectra (DADS) of both toluene solutions (one kept in the dark and one constantly illuminated with 450 nm light) are displayed in Figure 3.9 for comparison reasons; together with the inverted ground-state absorption spectrum (dashed) and the absorption spectrum of the photostationary state (dotted) from Figure 3.4b. The negative signal clearly corresponds to the ground-state bleach (GSB) of the red I isomers and the formation of red II from red I is evident from the peak at 330 nm in both experiments. However, only in the case of the yellow solution, a few yellow II isomers previously generated in the reservoir can reach the cuvette and will be excited. They photoisomerize to yellow I, as can be seen by the new absorption signal at 405 nm in Figure 3.9b. Thus, we conclude that a photochemical isomerization in the azo group of yellow II is possible within the nanosecond time resolution of the experiment. This is not in line with the model by Kuhn and Weitz,[225] where yellow II can only be formed thermally from red II. Therefore, our studies support the model later inferred by Grummt and Langbein[226] in which yellow II can only be generated photochemically from yellow I.

Moreover, we performed an experiment under the same conditions except for the laser pulse wavelength, which was shifted to 410 nm. In this way, yellow isomers generated in the reservoir can be efficiently excited, whereas the red isomers have a very low absorptivity. Again, TA signals appear within the time resolution and do not show a decay on a millisecond time scale. The corresponding DADS is displayed in Figure 3.10a. The negative signal can now be identified as the GSB of yellow I that turns into yellow II, whose absorption is lower at 405 nm[225] but broader than that of yellow I (not visible in Figure 3.4b due to superposition with red I) so that positive wings are visible at the low- and high-energy sides of the GSB.

However, to determine the lifetime of yellow II molecules in toluene, we applied TA with a UV-Vis spectrometer on a time scale of seconds to a solution that was constantly illuminated with a 450 nm LED during measurement so that both yellow isomeric forms were mainly present. An LED at 405 nm excites yellow I, which can isomerize to yellow II; then, thermal back-

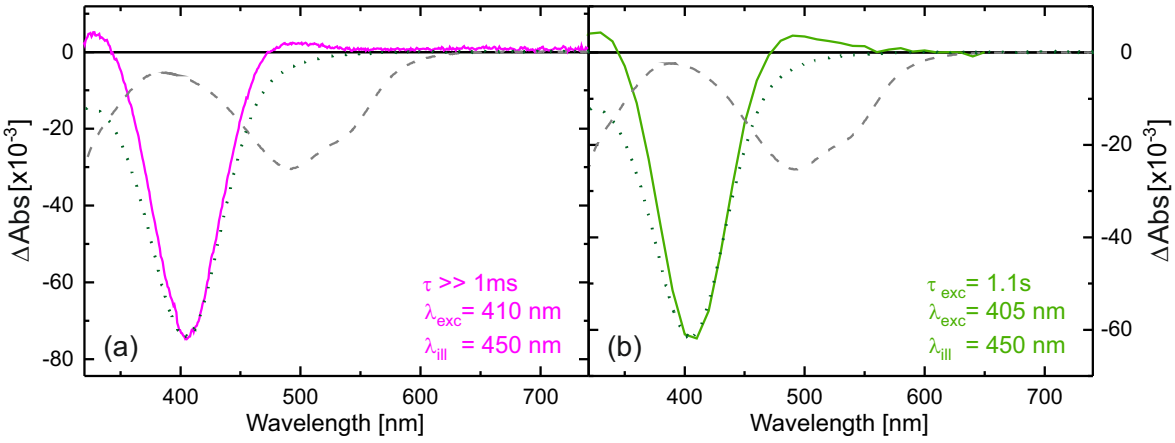

Figure 3.10: Transient absorption of TPF dissolved in toluene. (a) DADS of the signal observed during the first millisecond after excitation with a nanosecond laser pulse at 410 nm (Nd:YAG combined with OPO, pump). During this experiment, an external reservoir filled with the TPF solution was illuminated with 450 nm light (LED2, cw). (b) DADS (decay time 1.1s) of the signal after excitation with a 405 nm pump (LED1, pulsed for 100 ms) while the solution was constantly illuminated with 450 nm light (LED2, cw), generating the photostationary state. The discontinuous lines are the scaled absorption spectra of a solution in the dark (gray dashed lines, inverted) and the spectrum of the photostationary state (green dotted line, inverted).

isomerization occurs. The corresponding TA signals disappear with a single decay time of 1.1 s, as represented by the DADS in Figure 3.10b (note at this point that the exact value is dependent on the amount of water impurities in the solution, due to the high sensitivity of TPF regarding external influences like humidity and solvent environment; compare Section 3.3.3). Thus, Figure 3.10 substantiates that the photoexcitation of yellow I only leads to yellow II (presumably in an ultrafast trans-cis isomerization process such as that observed for azobenzene and related azo compounds),[24;282;293–300] which then relaxes back. No photochemical pathway from yellow I or yellow II to a red form was found, which is in accordance with inferences found in the literature.[225;226;261]

3.3.2 Analysis of Reaction Pathways

Simulation of Ground-State Conformers

Most of the previous experimental studies on the photochemical processes of TPF do not differentiate possible rotamers beyond the four isomers obtained from the cis-trans isomerizations

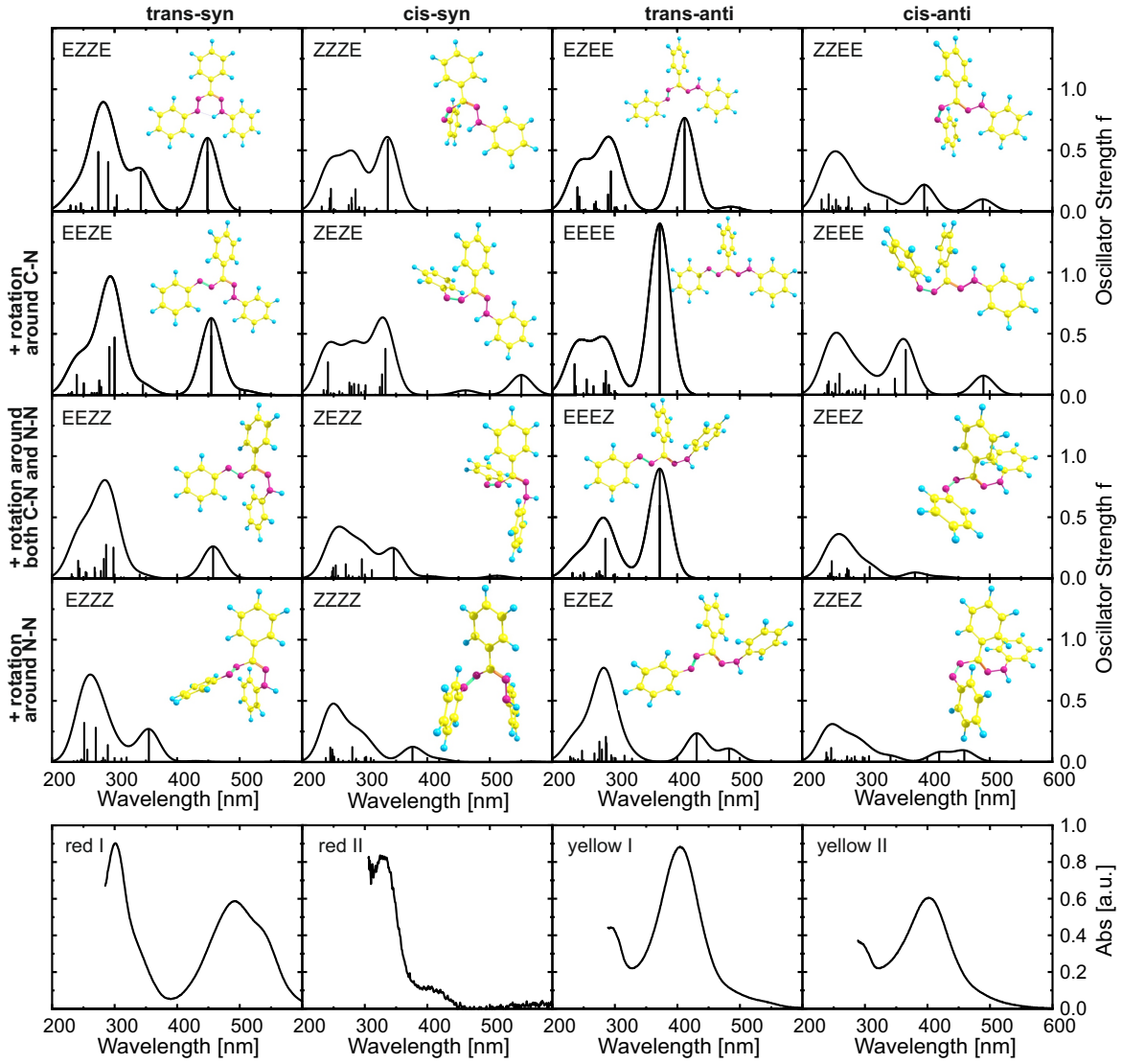

Figure 3.11: Top 16 panels: Results from DFT calculations for the 16 isomers considered in this study. The optimized ground-state geometries are displayed together with the calculated absorption spectra (the oscillator strengths at the corresponding transition energies are given as stick spectrum convoluted each with a Gaussian of a 40 nm width at half maximum). The orientations with respect to the N=N and C=N double bonds are identical within each column, whereas the ones with respect to the C–N and N–N single bond are the same for each row. Bottom 4 panels: Experimentally determined spectra of the four isomers corresponding to the double-bond orientations given at the top of each column. The red I spectrum is the ground-state absorption spectrum of a toluene solution, yellow I was measured directly after illumination with 455 nm of a toluene solution, yellow II corresponds to the photostationary state in toluene induced by 455 nm light, and red II is estimated by subtracting the GSB from the pink DADS in Figure 3.7a.

around the N=N and the C=N double bond, resulting in the trans-syn nomenclature also displayed in Figure 3.1. Theoretical studies [e.g., Buemi *et al.*][249;251] have addressed further rotamers, as we will also do in the following. For our discussion of the reaction pathways, we further take into account the rotations around the two adjacent single bonds, so that each of the four isomers labeled in Figure 3.1 may lead to four distinguishable conformers. Our calculations at the B3LYP/def2-TZVP/D4 level of theory indeed result in 16 corresponding ground-state minima, i.e., 16 potentially stable conformers, which however strongly differ in energy and the height of the barriers connecting them.

The optimized structures of the 16 conformers are plotted in Figure 3.11, together with the absorption spectra obtained from the calculations. For a systematic description, we use the E/Z nomenclature and start from the N=N double bond. Thus, the most stable isomer (red I, trans-syn) with the intramolecular hydrogen bond is the EZZE conformer, reflecting the E (trans) configuration with regard to the N=N double bond, Z with regard to N–C, Z (syn) for C=N, and E for the N–N single bond, respectively. Each row of panels in Figure 3.11 represents a variation of a single bond, as indicated on the left, whereas each column represents an isomerization of a double bond.

The absorption spectra, even within one column and hence only due to rotation around single bonds, vary substantially (for a comparison with calculations using the CAM-B3LYP functional and including a conductor-like polarizable continuum model, see Appendix Figures A.15 and Figure A.16). To allow a comparison to experiment, the lowest row of panels in Figure 3.11 gives experimental absorption spectra, where always one isomeric species is dominating. Starting on the left with the absorption spectrum of the solution in the dark (corresponding to red I), followed by the spectrum of red II derived from spectra of intermediates in time-resolved experiments, additionally to the spectrum of yellow I measured directly after illumination and the spectrum of yellow II obtained in the photostationary state. In the visible spectral range, the simulated spectra of EZZE and EEZE are very similar and match best with the experimental spectrum corresponding to red I, although the experimental data is red-shifted and exhibits a shoulder at longer wavelengths not reproduced in the simulations. Both aspects might be related to a significant stabilization effect caused by the intramolecular hydrogen bond, which the calculations might underestimate. The spectrum of the intermediate red II matches best with ZZZE or ZEZE, substantiating that the initial process after photoexcitation involves a trans-cis isomerization around the N=N double bond. Comparing the experimental and theoretical spectra, also the assignment of EZEE as the yellow I species is confirmed. Furthermore, a comparison of the experimental spectrum of yellow II with the calculated spectra in the right-hand column yields the best agreement for the ZZEE conformer, whose absorption peaks around

400 nm and 490 nm might not be identifiable as separate peaks in the experimental spectrum. While the juxtaposition of the theoretical with the experimental spectra from time-resolved measurements confirms the involvement of the four species initially included in the Kuhn-Weitz and Grummt-Langbein reaction schemes (see Figure 3.1), the actual sequence of transformations cannot be deduced. Especially, the thermal process from red II (ZEZE) to yellow I (EZEE) in the Grummt-Langbein scheme (diagonal arrow in Figure 3.1) formally necessitates isomerization around both the N=N and the C=N double bond. Experiments indicated that this might be a bimolecular process and that two TPF molecules are required.[226] In the following section, we provide an analysis for identifying which conformers are involved.

Interconnection among Isomers

For merocyanine systems in which eight cis/trans isomers can occur, it is illustrative to represent them as the corners of a cube, so that each edge of the cube corresponds to a change of one orientation from cis to trans or *vice versa*.[36] For an analogous treatment of TPF and the 16 structures shown in Figure 3.11, a four-dimensional hypercube, often called tesseract, would be required, which has 16 corners (i.e., isomers) and 32 edges (i.e., reaction pathways involving one rotation). In order to plot it in two dimensions, the tesseract can be represented for instance by its Schlegel diagram (a perspective 3D view, with the fourth dimension pointing inwards, Figure 3.12a) or by an orthogonal projection,[301] from which the hypercube graph Q4 is obtained.[302;303] Transferred to the TPF isomer manifold (Figure 3.12b), each of the 16 isomers is thus connected to four other isomers by a line. As follows from the properties of hypercube graphs,[303] the lines can be separated into 4 groups, which correspond to the 4 possible rotational degrees of freedom in TPF as indicated by the color in Figure 3.12b. Note that each isomer is connected to one line of each color (as there are four possible rotations), and lines of identical color are parallel in this representation.
We have further calculated the energy of the 16 isomers (given in the circles together with the abbreviation of the isomer) as well as the 32 barriers (values given above the lines representing the rotation) to go from one isomer to another. In this way, one can visualize nicely how the reaction might proceed. The EZZE (red I) isomer is the energetically most favorable one, and all four possible rotations to reach another isomer are energetically uphill, exhibit a significant barrier, or both. As inferred from the experiments, EZZE performs a trans/cis isomerization around the N=N bond (i.e., it follows the blue line in Figure 3.12b) upon photoexcitation, reaching ZZZE. Looking at the possible pathways of ZZZE, one can deduce that an almost

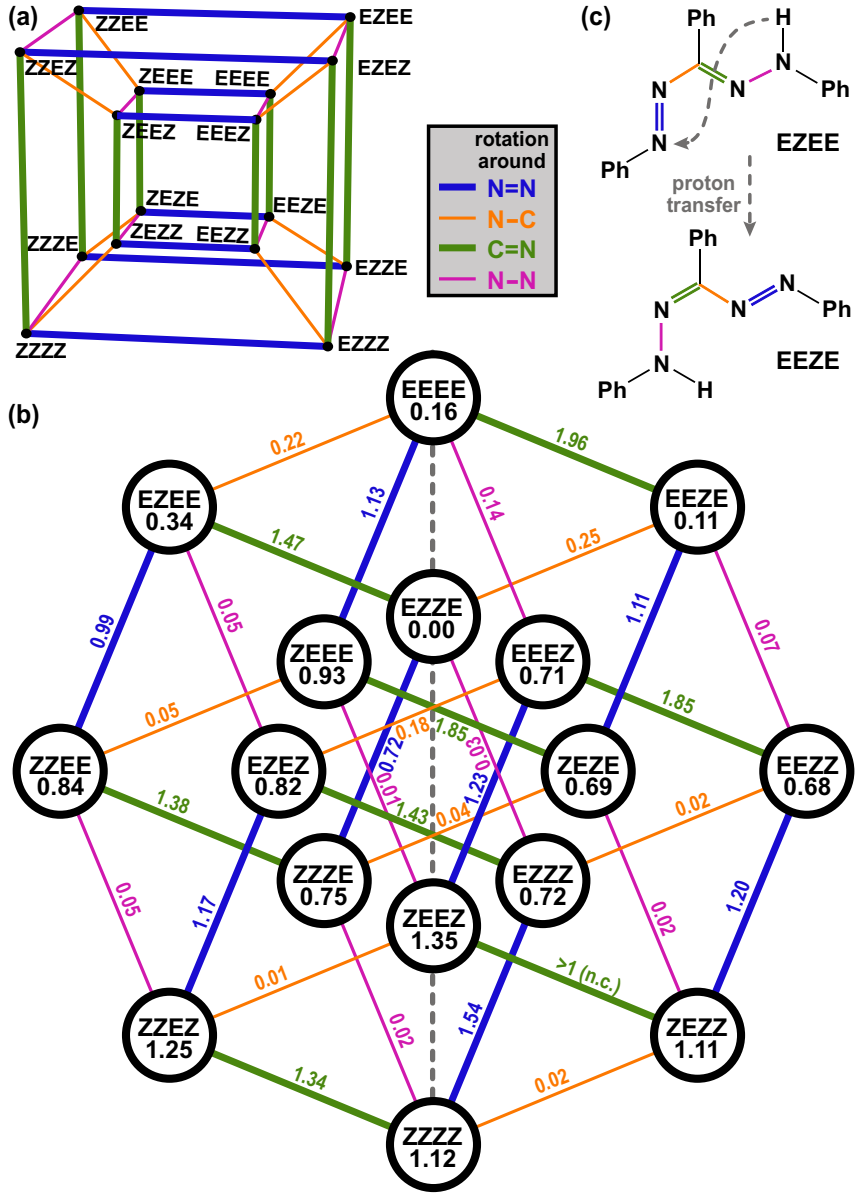

Figure 3.12: Reaction pathways illustrated as Schlegel diagram (a) or hypercube graph (b). The isomers' calculated energies, referenced to the energetically most stable geometry EZZE, are written in the circles, barrier heights are shown above the reaction pathway; all values are in eV. The final single point energies of the individual isomers were optimized by DFT calculations on the B3LYP/def2-TZVP level of theory. The energy barriers between two adjacent isomeric species of TPF are roughly estimated by relaxed surface scans along a fixed torsional angle. The stated values along the possible pathways always describe the amount of energy to overcome the energy barrier from the energetically higher lying isomer to the energetically more favored species. The performed calculations are summarized in the Appendix Figure A.19. Note that in case of one barrier height the calculation did not converge (n.c.). (c) Exemplarily displays that a proton transfer from the phenylhydrazone to the azo group is associated with the formation of an isomer with reversed nomenclature.

barrierless and slightly downhill pathway is possible by rotation around the N–C bond (orange line), yielding ZEZE (isomer red II). From there, no further rotation is plausible, because of too high barriers and energetically disfavored isomers.

So how is it possible that a thermal process leads from ZEZE (red II) to EZEE (yellow I) without any detectable intermediates? In chelated formazan isomers exhibiting an intramolecular hydrogen bond, intramolecular proton transfer was reported to occur in the ground state,[247;304–306] and also IR spectra in solution and in the solid state point towards this pathway.[254;255] A combined IR and resonance Raman study, also of unsymmetrical derivates of TPF, found evidence for this tautomerism even in the photochemical generation of non-chelated isomers and interpreted the transfer step to occur in the excited state.[256] Owing to the symmetry of the TPF molecule, transferring a proton from the phenylhydrazone to the azo group reverts the order of single and double bonds. Thus, the nomenclature is reverted, as exemplarily shown in Figure 3.12c. In the hypercube graph of Figure 3.12b, this means that such a proton transfer eventually is equivalent to a reflection on the central vertical line (dashed in gray).

Hence, for chelated isomer ZEZE (red II), the next step might be a proton transfer, resulting in the formation of EZEZ, which will immediately relax to the energetically lower-lying EZEE (yellow I). Therefore, we infer that for the thermal process from red II to yellow I in Figure 3.1, it is not necessary to isomerize around both double bonds, but only to transfer a proton. The same rationale can also explain how the reaction proceeds further. From EZEE (yellow I), a return to the most stable isomer EZZE (red I) formally necessitates a thermal rotation around the C=N double bond with a rather high activation barrier. However, if the proton is transferred, EEZE is obtained, from where it is much easier to reach EZZE because only a rotation around the N–C single bond is required, which has a distinct smaller activation barrier of around 0.25 eV [E_A value roughly estimated from the PES calculations in the gas phase]. By temperature-dependent sub-s TA experiments (see in the Appendix Figure A.13), an activation barrier for the thermal relaxation from yellow I to red I of $\sim$0.35 eV could be calculated in methanol solution; a rather small value for a cis/trans isomerization around a double bond. However, this barrier is very similar to the calculated activation barrier for rotation around the C−N single bond from conformer EEZE to reach species EZZE. The difference between those two values might be explained by solvent-dependent stabilization effects in methanol solution, underestimated in the quantum chemical calculations. Thus, finally also supports the hypothesis of a proton-transfer involved relaxation pathway.

While for chelated isomers, the proton transfer may proceed directly, for other isomers the distance between the donating and the accepting nitrogen atom is too far. In principle, also an intermediate [as is of relevance in formazan synthesis][251;307;308] with two azo groups and the

H atom at the interjacent C atom is conceivable, but much less stable than the formazan tautomers[249] (see also Appendix Figure A.18). However, the transfer might occur *via* a proton wire mechanism, i.e., in a Grotthuss-type fashion[309–311] as was found in water but also identified in other protic solvents.[312–314] Hence, the isomerization involving proton transfer should only be possible in protic solvents or in aprotic solvents containing at least traces of protic cosolvents. Indeed, the thermal isomerization from EZEE (yellow I) to EZZE (red I) occurs extremely slow in thoroughly dried toluene, and values up to 138.9 h[225] are reported for the half-life of EZEE. Addition of slight amounts of protic solvents drastically accelerate the reaction,[225;262] and in case of alcohols as a cosolvent, a correlation with the H-bonding donating ability of the alcohol was found during this work and is discussed in detail in the following section. Hence, while hydrogen bonding to nitrogen atoms being part of a double bond may also facilitate a ground-state isomerization, in the case of TPF an actual proton transfer might contribute to a significant extent.

3.3.3 Isomerization Kinetics in Solvent Admixtures

Impact of Solvent Parameters

The addition of cosolvents can already have a huge impact on the isomer distribution and spectral signatures even in the absence of any light. Therefore, we recorded absorption spectra in neat solvents first. The absorption spectra are shown in Figure 3.13. For a $\pi - \pi^*$ transition, the molecule's dipole moment usually increases upon excitation and hence one would expect a bathochromic shift as the solvent polarity increases. However, hydrogen bonding to the solvent may have an opposite effect.[315] The empiric Kamlet-Taft parameter α is an indicator for the hydrogen-bond donor (HBD) ability of the solvent, while β describes the hydrogen-bond acceptor ability, and π^* is associated with polarizability/dipolarity.[315;316] The HBD ability is most pronounced for fluorinated alcohols, so we also investigated trifluoroethanol (TFE), hexafluoroisopropanol (HFIP), and perfluoro-tert-butanol (PFTB).
Table 3.1 summarizes the Kamlet-Taft parameters as well as pK_a values of the solvents. A correlation of the absorption maximum in the visible spectral regime with the parameter α is displayed in Figure 3.14. While the effect for solvents with small α values is moderate, an increased HBD ability leads to a pronounced hypsochromic shift. We conjecture that strong hydrogen bonds toward the basic nitrogen atoms are formed in the ground state of TPF.

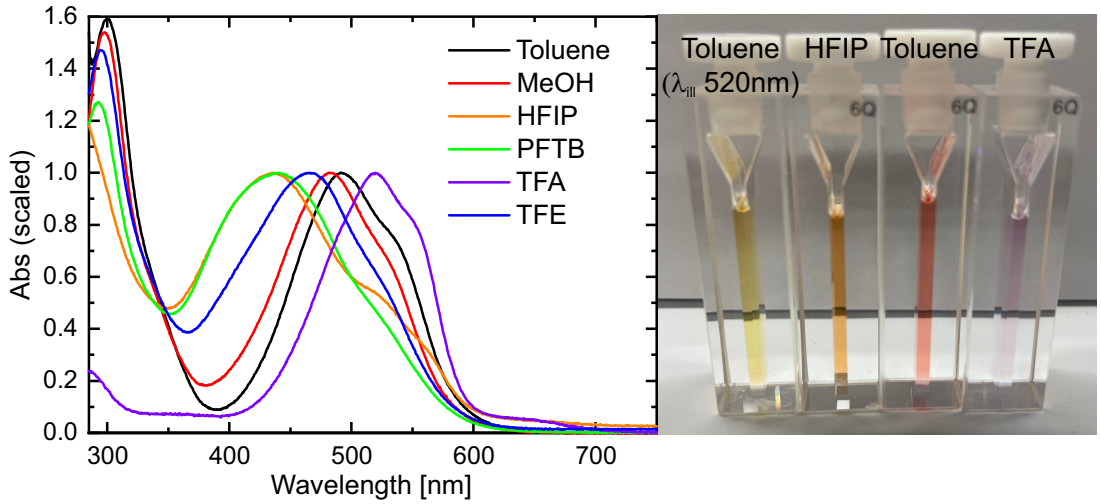

Figure 3.13: Normalized UV-Vis absorption spectra of TPF dissolved in several solvents. The inset shows the color change of TPF dissolved in different solvents from left to right as follows: toluene solution after illumination with a 520 nm LED (yellow), HFIP (orange), toluene (red), and TFA (purple).

Table 3.1: Kamlet-Taft parameters[316] and the pK_a values of the used solvents

Solvent	α	β	π^*	pK_a
Toluene	0.00	0.11	0.49	40[317]
Cyclohexane	0.00	0.00	0.00	45[318]
ACN	0.19	0.40	0.66	25[319]
$CHCl_3$	0.20	0.10	0.69	15.5[320]
MeOH	0.98	0.66	0.60	15.5[321]
i-PrOH	0.76	00.84	0.48	17.1[322]
DMSO	0.00	0.76	1.00	35[323]
DMF	0.00	0.69	0.88	
TFE	1.51	0.00	0.73	12.4[321]
HFIP	1.96	0.00	0.65	9.3[324]
PFTB	>2[325]			5.4[326]
TFA			0.50	0.23[322;327]

Solvatochromism in Binary Mixtures

The solvent may also have an influence on the ground-state equilibrium of the different isomers. To explore this, we look at binary mixtures of toluene with other solvents. For methanol,

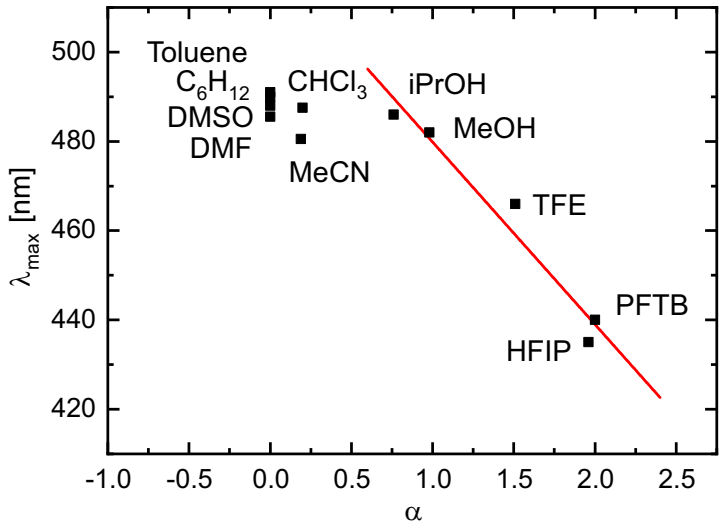

Figure 3.14: Spectral position of the absorption maximum in the visible spectral range of TPF in various solvents as a function of the Kamlet-Taft parameter α. The red line is a guide to the eye for the five studied alcohols.

besides the hypsochromic shift of the low-frequency absorption band, increased absorption around 400 nm with higher methanol content was observed, which hinted toward a changed ground-state equilibrium (see Figure 3.15, red curves). In a neat toluene solution under constant illumination with our 520 nm LED, it was possible to establish a photostationary state in which the equilibrium was strongly shifted to the yellow isomers. For identical illumination conditions, the addition of MeOH causes a decrease of the corresponding 405 nm absorption

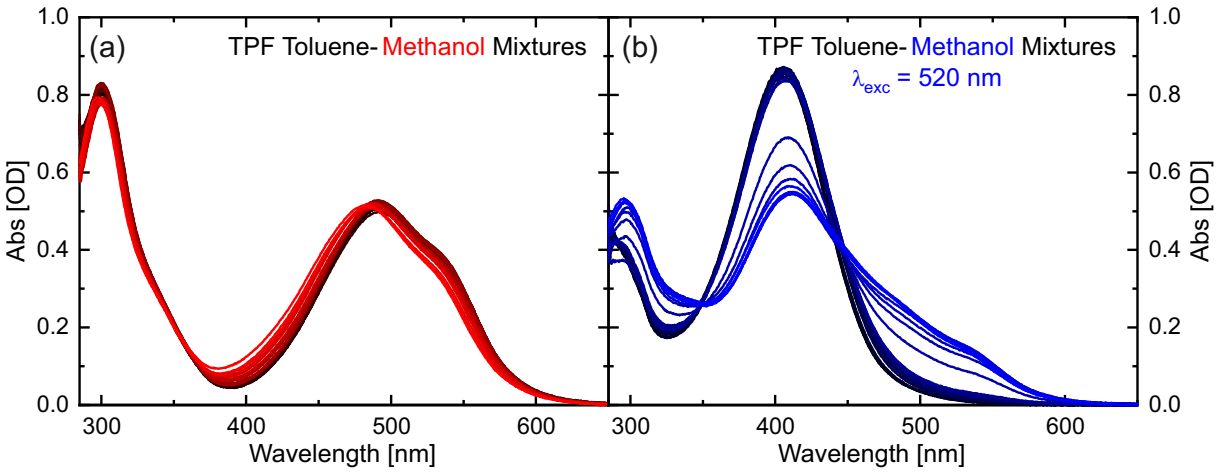

Figure 3.15: UV-Vis absorption spectra of TPF kept in the dark (black to red curves) in (a), dissolved in neat toluene (black curve) with an increasing amount of methanol up to pure methanol (red curve), and under constant illumination with 520 nm light (black to blue curves) in (b).

peak and a higher contribution in the region around 500 nm for the photostationary state. This already suggests that the thermal relaxation from yellow I to red I is accelerated in the presence of alcohol (blue curves in Figure 3.15).

The effect should be even more pronounced in alcohols with a higher polarity and HBD ability. The corresponding absorption spectra for HFIP as a cosolvent are shown in Figure 3.16a, starting with neat toluene (black spectrum) and increasing the HFIP amount until reaching a 1:1 volume ratio of both solvents (red spectrum). The increased absorption around 400 nm and the decreased intensity around 490 nm, which was accompanied by a spectral blue-shift, point again toward a ground-state equilibrium possibly comprising more yellow isomers as the HFIP fraction increases. With regard to isomerization kinetics, it can be deduced from Figure 3.16b that it is basically no longer possible to accumulate the yellow isomers under our illumination conditions with a significant amount of HFIP, since the relaxation back to red I is too fast.

In order to substantiate that hydrogen-bond interactions rather than actual protonation are relevant in the fluorinated alcohols, we also used trifluoroacetic acid (TFA) as a cosolvent. With 0.1 V-% TFA, it is already no longer possible to shift the equilibrium toward the yellow TPF isomer with the 520 nm LED. In contrast to all other tested cosolvents, increasing the TFA fraction leads to a spectral red-shift (Figure 3.13) and a higher absorptivity. Furthermore, the intensity of the UV absorption band related to the azo group is strongly reduced (Figure 3.13) since the basic nitrogen atoms get protonated. Thus, those changes can be attributed to the protonation of TPF by the TFA, an effect that was ruled out as a major contribution for the other cosolvents

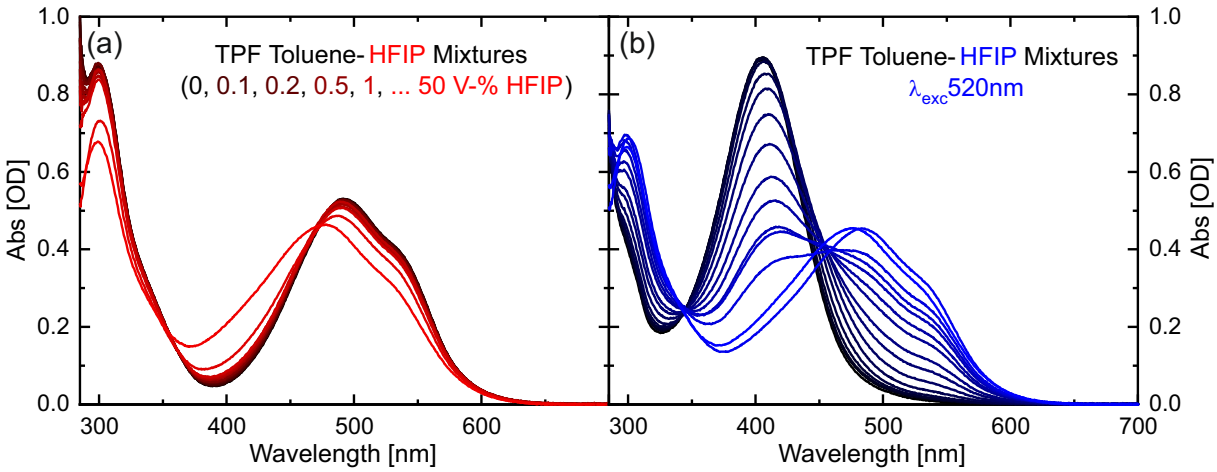

Figure 3.16: UV-Vis absorption spectra of TPF dissolved in toluene (black) with an increasing volume amount of HFIP up to a 1:1 mixture (red/blue). While (a) the black and red curves display the spectra of solutions kept in the dark, (b) the black and blue spectra were measured during constant illumination with 520 nm light.

(see Table 3.1 for a comparison of the pK_a values). Nonetheless, we note that small TFA admixtures might be beneficial for future studies on ion-pair formation involving formazan species.

Relaxation Behavior with Cosolvents

Besides the spectral properties, cosolvents will also impact the temporal characteristics of isomerization processes. In order to investigate this, TA experiments for the thermal relaxation of the 405 nm band, i.e. yellow I to red I, after excitation were conducted for several binary solvent mixtures with increasing volume amounts of methanol. Each kinetic was analyzed by a biexponential fit in analogy to Figure A.12 in the Appendix. The data and corresponding fits for TPF in toluene solutions with added methanol (0-3 V-%) are displayed in Figure 3.17a. The decay time τ_5 is plotted as a function of the methanol fraction in Figure 3.17b, while the analogous plot for τ_4 can be found in the Appendix Figure A.14. The slowest decay constant τ_5 becomes longer until it reaches a maximum value at a volume fraction of 3 % methanol. With still larger methanol admixtures, the opposite trend is visible until the thermal isomerization from yellow I to red I proceeds within a few seconds in neat methanol.
The acceleration with increasing alcohol concentrations is expected because the solvent environment gets more and more polar. Sueishi and Nishimura[262] have shown that the thermal

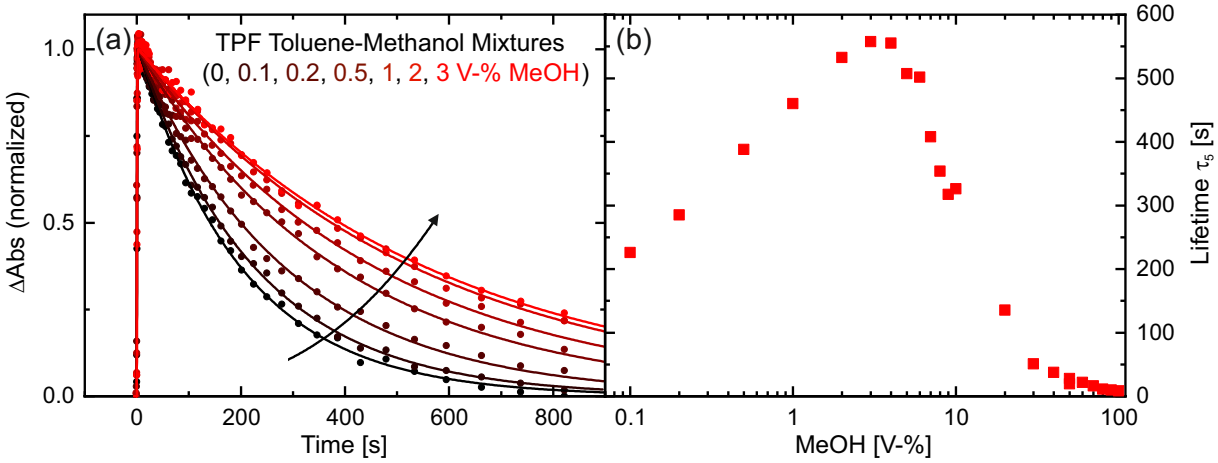

Figure 3.17: Kinetic traces and time constants τ_2 determined for the thermal isomerization from yellow I to red I after excitation with 520 nm light for 12.5 ms. (a) The kinetic profiles are represented by the measured time traces at 400 nm (dots) and the corresponding fits (lines). (b) The data were plotted with a logarithmic abscissa, showing the dependence of τ_2 on the increasing volume amount of methanol in the toluene solution.

isomerization in the hydrazone group is not a pure rotation around the double bond but rather an inversion mechanism is active, yet the transition state is still polar and therefore the reaction is accelerated in more polar environments. The polarity of toluene/methanol mixtures, determined with the normalized Dimroth-Reichardt $E_T(30)$ scale,[315] rapidly increases with the MeOH content and thus indicates preferential solvation; however, it is an overall monotonically growing function.[328] Thus, a maximum such as that observed in Figure 3.17b can not be explained solely by polarity effects.

In studies using binary solvent mixtures, synergistic effects are sometimes encountered such that a certain effect is more pronounced in the mixture than in the neat solvents. For instance, this has been observed for the ring-closure of a merocyanine[329] or for excited-state lifetimes and quenching in various systems.[330–337] Saini and Das[331–333] have studied curcumin in toluene/methanol mixtures and observed that the nonradiative rates associated with an intramolecular hydrogen bond in curcumin are modulated by the presence of protic cosolvents. In our study, TPF in its red I form is also stabilized by an intramolecular hydrogen bond that is not present in the yellow I isomer. The latter can form a hydrogen bond with a protic cosolvent, which in turn might hinder the relaxation toward the quasi-aromatic heterocycle of red I. Thus, the lifetime τ_5 initially increases for small admixtures of methanol. Once these get larger, at least two effects play an important role. On the one hand, the polarity of the solvent environment increases. On the other hand, the hydrogen-bonded methanol molecule might be part of a hydrogen-bonded network with other methanol molecules, giving rise to a competition with regard to where to bind to. In the case of nascent carbenes in binary solvent mixtures, it was shown that small amounts of protic cosolvents lead to a different reaction pathway because the hydrogen bond is very strong yet cannot lead to proton transfer without the participation of a further protic molecule.[338;339] For a coumarin dye, Barman and Sahu[335] observed that with binary mixtures of an aprotic solvent and phenol, the fluorescence was most efficiently quenched with little amounts of phenol, and further addition of phenol led to the formation of phenol clusters that hydrogen-bond less strongly to the dye. We interpret our data along the same lines. At small methanol fractions, individual methanol molecules possibly form strong hydrogen bonds with yellow I and thus efficiently slow the relaxation. If there are many MeOH molecules in the vicinity of a TPF molecule, this effect is weakened due to competing hydrogen bonds among the methanol molecules and the increase in polarity. With a higher methanol proportion, τ_5 approaches the value of bulk methanol.

The fluorinated alcohol HFIP has several unique properties that make it highly attractive for various synthetic applications.[324;327;340–345] It is very polar and has a high HBD ability, which further increases upon dimer and trimer formation[342] in contrast to other alcohols. Thus, with

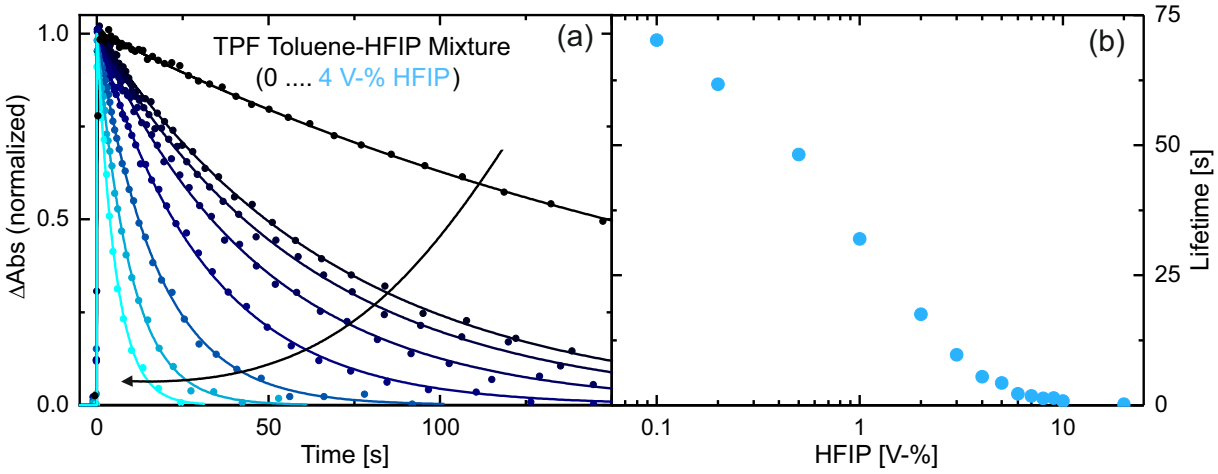

Figure 3.18: Kinetic traces and time constants τ_2 determined for the thermal isomerization from yellow I to red I after excitation with 520 nm light for 12.5 ms. (a) The kinetic profiles are represented by the measured traces at 400 nm (dots) and the corresponding fits (lines). (b)The data were plotted with a logarithmic abscissa, showing the dependence of τ_2 on the increasing volume amount of HFIP in the toluene solution.

HFIP as a cosolvent, we expect τ_5 to decrease even more rapidly and reach a maximum for tiny admixtures if at all. However, no maximum was found for τ_5, which changed so drastically that yellow I was hardly observable above 10 V-% of HFIP (Figure 3.18b), in agreement with the observations made in Figure 3.16b. HFIP usually contains traces of HF[341] that could accelerate

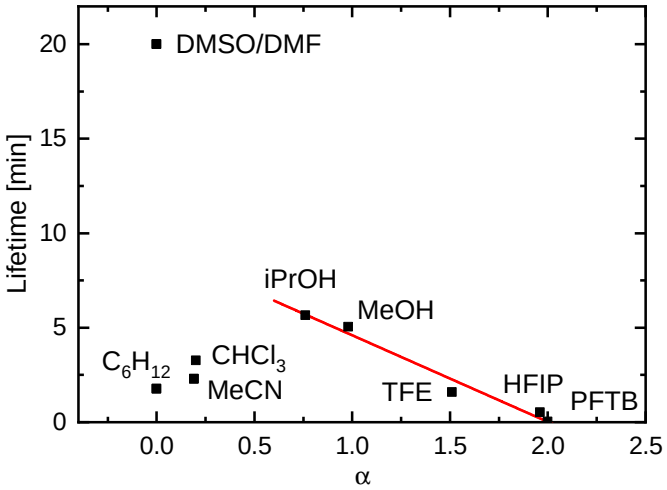

Figure 3.19: Time constant τ_5 determined for the thermal isomerization from yellow I to red I in binary solvent mixtures of toluene and 1 V-% of the cosolvents as a function of the Kamlet-Taft parameter α of the cosolvents.

the reaction *via* acid catalysis, a contribution that might further add to the rather short relaxation times of yellow I in toluene with HFIP admixtures.

Just like the solvatochromic shifts, we also compared the relaxation time τ_5 for the different solvents. For this, the value of τ_5 was plotted when 1 V-% of a cosolvent was added to the toluene. As can be seen from Figure 3.19, the alcohols exhibit a τ_5 value almost linearly dependent on α. We note that the data of Figure 3.19 were measured on a different day with a slightly different temperature and humidity than the other measurements, so the absolute value for the 1 V-% methanol admixture is not identical to the value in Figure 3.17. However, the trend is evident when measured on the same day, as indicated by the red line. Among the aprotic cosolvents, 1 V-% of DMF and 1 V-% of DMSO led to a remarkable increase in τ_5. The reason for this behavior is in the high hydrogen-bond accepting ability of DMSO (see $\beta = 0.76$ in Table 3.1). Thus, DMSO acts as a hydrogen-bond breaker[346;347] and will strongly bind to the NH part of the hydrazone group, thereby hindering the isomerization around the C=N bond.[348] Accordingly, the reason for the prolonged τ_5 value is complementary to the explanation for the maximum in Figure 3.17b: the cosolvent molecule hinders the formation of the quasi-aromatic heterocycle of red I, now by accepting a hydrogen bond from the TPF.

3.4 Conclusion and Outlook

Within this work, a possible reaction pathway of the isomerization processes of TPF after photoexcitation could be derived from transient absorption spectroscopy over a broad time range from femtoseconds up to minutes (Section 3.3.1). The experimental data were interpreted in combination with the quantum chemical calculations, in order to draw a plausible isomerization scheme proceeding over several isomeric species of TPF (Section 3.3.2).

The primary reaction step when exciting TPF with light is an isomerization around the N=N double bond through which the electronic ground state is reached on an ultrafast time scale. Our combined experimental and theoretical study unveiled that the initially excited conformer EZZE (red I) thus turns into ZZZE and from there directly to ZEZE. The low barrier found for the latter step might even imply that the excited-state isomerization and rotation around the N–C single bond might proceed in a concerted fashion. Following spectroscopically the evolution of the newly formed ZEZE (red II), it was shown that the next reaction step occurs on a time scale of hundreds of milliseconds, yielding EZEE (yellow I). For this reaction step, we propose that an intramolecular proton transfer significantly contributes, so that no isomerization around a double bond is necessary. Along these lines, the reaction step from EZEE (yellow I) back to EZZE (red I) might also include a proton transfer and proceed *via* EEZE, so that again no rotation around a double bond is required. However, additional excitation of EZEE (yellow I) leads to another yellow isomeric species of TPF, namely ZZEE (yellow II), characterized by a spectrally broader absorption band and a lower molar extinction coefficient compared to yellow I. However, this yellow II conformer cannot be generated directly by excitation of the red TPF species, but only from further illumination of yellow I, to which it also thermally relax back within seconds.

Finally, the above described conclusions are verified by observations in different solvents, and interpreted in the context of a Grotthuss-type mechanism, also explaining the remarkably high decay times reported for the last relaxation step (τ_5) of the TPF photocycle in dried aprotic solvents. Furthermore, an extraordinary sensitivity of this slowest relaxation step from yellow I back into red I in dependency on the solvent environment was observed, for which reason TPF was investigated in various solvents and binary solvent mixtures consisting of toluene and either a protic or aprotic cosolvent (Section 3.3.3). It was possible to show that cosolvents drastically influence the lifetime of yellow I. Generally, the reaction is accelerated by the addition of polar cosolvents, but with only small amounts of cosolvents it can also be slowed because the formation of the quasi-aromatic heterocycle is hindered by a hydrogen bond with a cosolvent molecule. The mechanism works with the latter being either a strong hydrogen-bond donor or

a hydrogen-bond acceptor. Therefore, these studies contribute to the emerging field of steering photochemical reactions using rational solvent variations. In synthetic applications where photoisomers of formazans are either favorable or undesired, a purposeful adaptation of the solvent environment might prove beneficial for the reaction outcome.
Finally, it might be worthwhile to investigate whether also in molecules with a larger separation between the azo and the hydrazone group compared to that in TPF, a similar acceleration of the ground-state equilibration is found in protic solvent environments. These aspects could also be of interest in the field of organocatalysis, where hydrazone compounds find increased attention.[349–356]

CHAPTER 4

Tropylium Salts

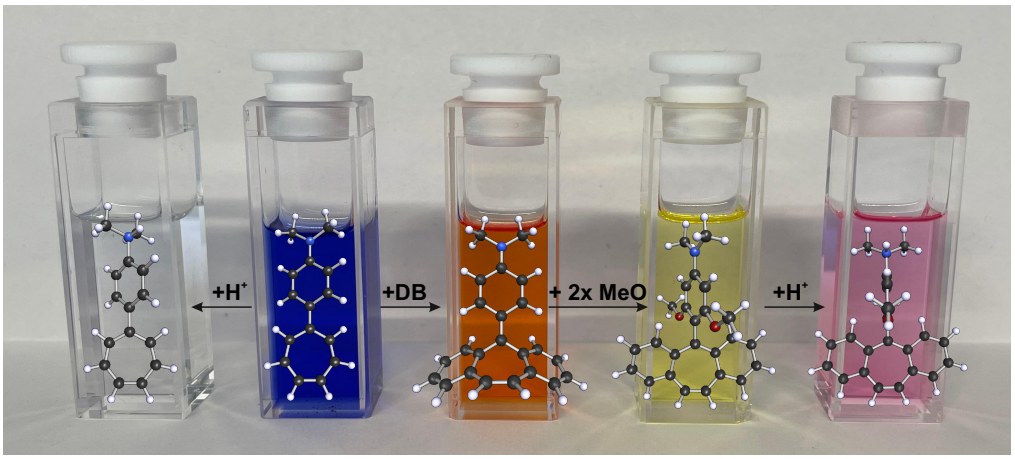

4.1 Introduction **78**

4.2 Experimental and Theoretical Approaches **80**

4.3 Results and Discussion **88**

4.4 Conclusion and Outlook **112**

This chapter forms the basis for publication [3] and [4]. RDC, DJML and TVN synthesized all tropylium dyes. FB and ER carried out all of the fs-TA experiments. BG supported SW with the fs-ns and ps-ns emission experiments. RJK performed one of the PES scans and helped SW by performing the µs-ms TA. JP carried out the measurements with a co-salt. SW performed the main part of experiments and all calculations. PN conceived and supervised the project. SW, RJK and PN analyzed and discussed the data and participated in writing the present manuscript.

4.1 Introduction

The tropylium cation ($C_7H_7^+$)[357;358] has remarkable properties with an unusual stability despite its positively charged nature, and its characteristics can be influenced systematically by various substituents.[359–368] The unique combination of reactivity and stability separates this class of molecules from many other cationic species. Many studies addressed the chemical behavior, e.g. charge-transfer and reduction characteristics,[367;369–377] the impact of heterocycles fused to tropylium,[378;379] or the properties of dibenzotropylium.[55;360;368;380] With regard to physicochemical properties, spectroscopic and theoretical work relying on Hückel MO theory[361;362;381–383] started in the 1960s, and more recently in particular Abraham and colleagues[56;384–397] systematically investigated the photogeneration of diverse aryltropylium derivatives, electrochemical properties, photochemical pathways, or the behavior in constraining environments for aryltropylium compounds by applying various spectroscopic techniques as well as quantum chemical methods. Other groups also explored the photochemical reactivity[398–401] and the emission characteristics[402;403] of diverse tropylium systems. Numerous applications were reported, for instance as red-emissive fluorophores,[402;403] as robust guests in zeolites[55;401] and cage-like arene systems,[56;394;396;404;405] as softer organic alternatives for metal-based reagents, and in particular as flexible catalysts.[54;61;66;406–420] One intriguing example of substitution is the combination of the electron-poor tropylium moiety with an electron-rich aromatic system, yielding so called 'push-pull' or donor-acceptor organic dyes. These tropylium adducts exhibit special photochemical properties,[54] such as absorption and fluores-

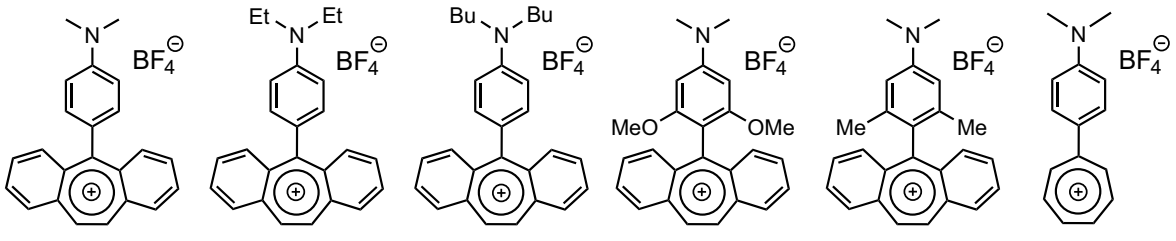

Figure 4.1: The six studied molecular systems, sketched here as dibenzotropylium (DBTrop) or tropylium (Trop, in the case of $\mathbf{6}^+$) compounds together with their tetrafluoroborate counter ions. The dialkylaniline scaffold is either unsubstituted, i.e. for dimethylaniline (DBTrop-DMA, $\mathbf{1}^+$ and Trop-DMA, $\mathbf{6}^+$), diethylaniline (DBTrop-DEA, $\mathbf{2}^+$), and dibutylaniline (DBTrop-DBA, $\mathbf{3}^+$), or substituted in 3- and 5-position with methoxy (DBTrop-2MeO-DMA, $\mathbf{4}^+$) or methyl groups (DBTrop-2Me-DMA, $\mathbf{5}^+$), respectively.

cence in the visible range, pronounced solvatochromism, and aggregation-induced emission (AIE)[421–423] effects, where the formation of aggregates induces or enhances the emission of light . A main application area of these organic dyes lies in opto-electronics an inherent part of everyday life, as for instance optical data storage, data carriers, computer screens, and organic light-emitting diodes (OLEDs).[57;58;63] Recent studies focused on the synthesis of those 'push-pull' organic dyes, consisting of two distinct molecular parts that possess a donor and an acceptor functionality.[54]

Here, we systematically investigate the photodynamics of six cationic compounds that are formally comprised of a tropylidene moiety linked directly to an electron-rich aniline scaffold, for simplicity plotted as tropylium systems in Figure 4.1 together with tetrafluoroborate (BF_4^-) as weakly coordinating counterion. We will show that the positive charge for compounds **1**$^+$, **2**$^+$, and **3**$^+$ is at the nitrogen rather than at the seven-membered ring, whereas for **4**$^+$, **5**$^+$ and **6**$^+$, the ground state is a tropylium compound. In addition, the effect of protonation and the ability to form dicationic species in the electronic ground- and excited-state is explored. The emission dynamics were studied by employing three time-resolved fluorescence techniques in order to capture both ultrafast and nanosecond dynamics, and additionally two setups were used to monitor transient absorption changes on timescales from fs to ms. The rationale to compare different substituents and protonation states serves two purposes: on the one hand, to disclose the charge localization which dictates the photochemical properties, and on the other hand, to demonstrate the versatility of the compounds for which the fluorescence lifetime may vary by more than two orders of magnitude and which may act as a photobase.

4.2 Experimental and Theoretical Approaches

The investigated tropylium salts and their derivatives were synthesized by the group of Prof. Dr. Than V. Nguyen at the University of New South Wales in Sydney (Australia). The solvent dichloromethane (DCM; Acros Orcanics, 99.5 % for spectroscopy, stabilized with amylene; and Merck, Uvasol for spectroscopy), the trifluoroacetic acid (TFA; Riedel-de Haën) and the tetra-n-butylammonium tetrafluoroborate (TBAB; Alfa Aesar, 99 %) were used without further purification.
The basic concepts of the here shown experimental setups are already explained in Chapter 2. It should be noted that all time-resolved emission experiments of tropylium salts on the fs-ns region by fluorescence upconversion as well as most of the ps-ns time-resolved emission experiments using a combination of spectrograph and streak camera as detection unit were performed during my time for obtaining my master's degree at the Ruhr-University in Bochum. However, the conclusions derived in Section 4.4 are also based on some of these results. In order to ensure completeness of the content, the data which are fundamental for understanding are also listed in this chapter.
Additionally, it should be mentioned that the measurement of the fs-ns transient absorption data was carried out by Ferdinand Bergmeier in the group of Prof. Dr. Eberhard Riedle at the Ludwig Maximilian University in Munich. The subsequent correction procedure, the fitting process, and data analysis reported within this work was done in our group.
Finally, in the end of this section, the used quantum chemical methods including the chosen parameters are mentioned.

4.2.1 fs-ns Emission Experiments using Fluorescence Upconversion

Ti:Sa-Oscillator – Principle of Operation

The Ti:Sa oscillator (Mira Model 900-B, Coherent) is pumped by a frequency-doubled solid-state neodymium-doped yttrium orthovanadate (Nd:YVO_4) laser (Verdi V10, Coherent) that provides a vertically polarized 532 nm output beam. The pump beam is focused into the titanium-doped sapphire (Ti:Al_2O_3) crystal, which acts as gain medium, after the polarization is changed by 90° *via* a polarization-rotating periscope already included in the Mira design. The oscillator has a tuning range from 710 nm up to 910 nm at a repetition rate of 76 MHz with pulse durations down to 100 fs. However, for all experiments shown in this chapter, laser pulses with a

central wavelength of 800 nm were used to operate the upconversion setup. The temporal width (FWHM) of the generated pulses was verified with a home-build SHG-FROG[103] (see in the Appendix Figure B.13). The general working principle of the Mira oscillator is schematically shown in Figure 4.2.

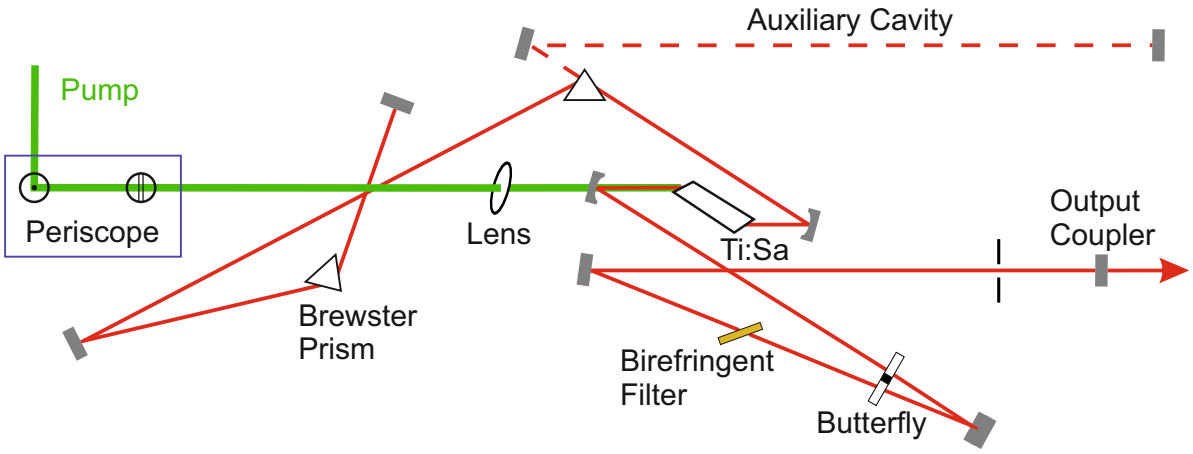

Figure 4.2: Setup of the used Ti:Sa-Oscillator 'Mira'. An Nd:YAG laser generates the pump beam, whose polarization is rotated by a periscope before focusing it into the Ti:Sa crystal. The auxiliary cavity is only used for alignment. Figure drawn according to Ref. [424].

The ultrashort laser pulses are generated *via* so-called 'Kerr Lens Modelocking' (KLM) within the Ti:Sa crystal.[82;96] In the resonator cavity of length L, several modes with slightly different frequencies, according to the relation $nL = \lambda/2$, are produced. However, those multiple oscillating modes are without a fixed phase relation to each other, which is known as 'continuous wave' (CW) operation. To initiate a modelocked operation, a butterfly ('starter') made of silica starts to oscillate, which causes a small and rapid change of the cavity length. If now several modes are interfering constructively due to this random phase relation change, they form a short laser pulse. As described in Section 2.1, the refractive index becomes intensity-dependent for high electric fields, resulting in self-focusing by the optical Kerr effect in the crystal. Thus, the diameter of the modelocked beam is smaller than that of the continuous wave, for which reason an aperture is placed in front of the output coupler to block the cw-beam. The group velocity dispersion (GVD) is compensated by a pair of Brewster prisms in the cavity and a smooth tunability of the output wavelength during operation is achieved by a birefringent filter (see Figure 4.2).

Fluorescence Upconversion Setup

The fluorescence upconversion (FLUP) system used in this work was initially purchased as commercially available product (FluoMax-SC, IBPhotonics), but significantly modified in our group. A schematic representation of the FLUP setup is shown in Figure 4.3.
First, the initially horizontally-polarized laser pulses are directed towards a half-wave plate (HWP) to change their polarization direction. Then, the laser beam is focused onto a BBO crystal, where a SHG process takes place generating 400 nm pulses for sample excitation. The second-harmonic beam is separated from the fundamental by a dichroic mirror (DM), being reflective for 400 nm and transmissive for 800 nm light. Afterwards, the pump beam passes

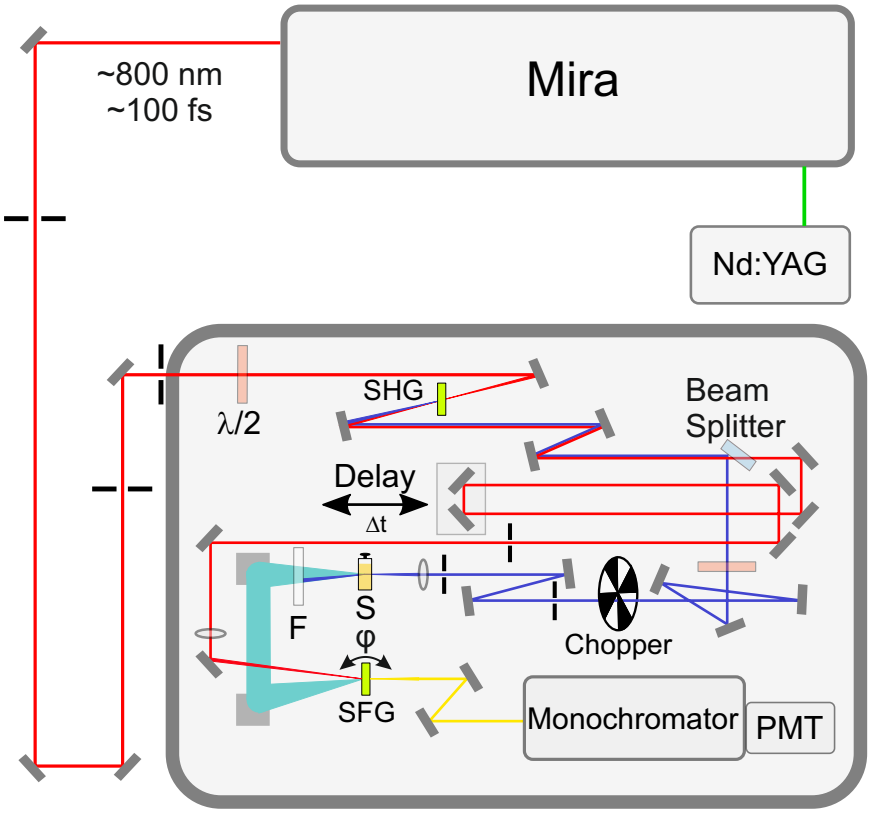

Figure 4.3: Schematic representation of the used fluorescence upconversion setup. After second-harmonic generation (blue line) from the fundamental 800 nm pulses (red line) within the SHG crystal, the 400 nm pump pulse is separated from the 800 nm gate pulse by a dichroic mirror (Beam Splitter). The temporal delayed gate pulse upconverts the fluorescence of the sample *via* an SFG process before detection. The remaining excitation light is absorbed by a filter (F) behind the sample (S). Figure adapted from Ref. [125].

through a second half-wave plate to achieve magic angle (54.7°)[120;267] operation, before it is focused onto a cuvette to excite the sample. The excitation light is blocked behind the sample by a filter, while the sample's fluorescence is collected and focused by a pair of parabolic mirrors onto a SFG crystal (also a BBO crystal). The fundamental is used as gate pulse and can be delayed in time by a movable delay-stage, before being focused onto the same SFG crystal to upconvert the sample's emission. As already described in Section 2.1.3, the phase-matching conditions are only fulfilled for one frequency at a given crystal position. By a stepwise rotation of the SFG crystal and by varying delay times between the pump and gate pulse, it is possible to monitor the emission in space and time. Usually, a photomultiplier tube (PMT) in combination with a monochromator is suitable for detection, since the generated SFG signal is commonly located in the UV or visible spectral region. Additionally, a chopper is placed within the excitation pathway to ensure the altered measurement of the pumped and unpumped sample. With the here described setup a maximal time window of 2 ns can be scanned. The IRF was determined to around 250 fs by measuring the Raman band of H_2O (see Appendix Figure B.14). All experiments were performed in a flow cell with a 1 mm optical path length (Starna) and a sample's optical density of 0.1 at 400 nm over the 1 mm cuvette length.

4.2.2 ps-ns Emission Experiments using a Combination of Spectrograph and Streak Camera

The schematic representation of the used setup to perform time-resolved emission measurements on a ps to ns time scale using a combination of spectrograph and streak camera as detection unit can be found in Figure 4.4. For excitation of the sample three pulsed laser diodes with wavelengths of 266 nm (PicoQuant LDH-P-FA-266), 375 nm (PicoQuant LDH-P-C-375), and 405 nm (PicoQuant LDH-P-C-405B) at a repetition rate of 20 MHz were available. The generated pulses are characterized by pulse widths (FWHM) of around 80 ps, 40 ps, and 50 ps, respectively (see Appendix Figure B.6). However, during this work only the 266 nm and 405 nm pulsed laser diodes were used. The excitation pulses were focused into the sample, located in a (2×10) mm quartz cuvette (Starna), and blocked after passing the 2 mm sample path length by a reflective (for 266 nm pulses, Newport 20CGA-280) or colored (for 405 nm pulses, ThorLabs NWG430) long-pass filter. The sample's emission is collected and focused onto a glass fiber by a combination of two lenses. The glass fiber is connected to a monochromator (Princeton Instruments SP2150i), where the spectral separation takes place before the emitted photons reach the streak tube (Hamamatsu C10627-11) combined with a 2D-CCD camera (Hamamatsu

C9300-508). In order to ensure the operation at magic angle (54.7°)[120;267] to record pure population changes, a polarizer was placed between the two collecting lenses (see Figure 4.4).
During the measurements, a sweep voltage running at 20 MHz was applied to the streak tube. The time window could be varied between 1 ns and 50 ns, and the sensitive spectral region of the camera extended from 200 nm up to 850 nm, enabling the time-resolved detection of many emission decays. The sample's concentration was set to 0.1 OD over a 2 mm path length at the excitation wavelength.

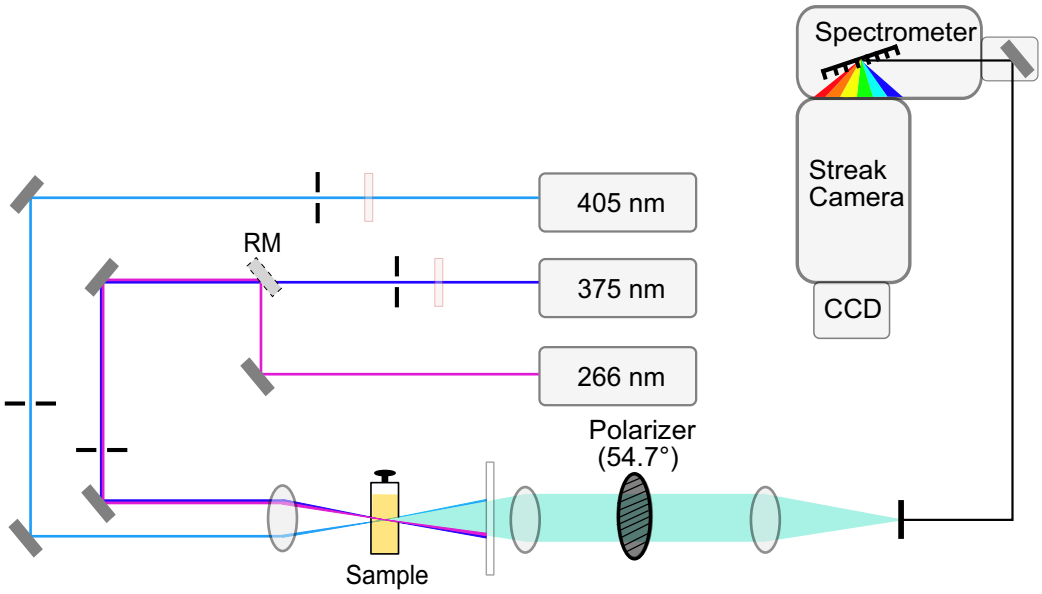

Figure 4.4: Illustration of the time-resolved fluorescence experiment on the ns-time range with a streak camera as detection unit. Three pulsed laser diodes were available for excitation at 405 nm (blue), 375 nm (purple), and 266 nm (pink), while the latter two have the same pathway behind the removable mirror (RM). The sample's emission is displayed in turquoise, passing through a polarizer, which was adjusted to magic angle (54.7°) with respect to the polarization of the excitation pulse.

4.2.3 ns Emission Experiments using TCSPC

For excitation of the sample, a pulsed LED at a repetition rate of 500 kHz was used. In general, three different LEDs were available with central excitation wavelengths of 280 nm, 370 nm, and 445 nm (NanoLED, Horiba JOBIN YVON) with pulse durations around 1 ns (FWHM). The spectral and temporal characteristics of the LEDs are summarized in the Appendix in Figure B.8. However, during this work only the 370 nm LED was used as excitation source.
The excitation pulses were focused into the sample by a toric mirror and blocked behind the

sample. The emitted photons were collected perpendicular to the incident beam by a second toric mirror, which also focuses them onto a monochromator combined with a PMT (R928). In the case of just photophysical processes, the total decay rate is generally given by the sum of the radiative and non-radiatve rate, where typically non-radiative processes include internal conversion and intersystem crossing. In order to get a better signal-to-noise ratio by reducing the dark current, which is caused by the thermal emission of electrons from the photocathode and the dynodes, the PMT is cooled down to -25°C. Furthermore, a band pass filter after the excitation LED may be used for a more selective excitation and a cut off filter may be used for blocking scattered excitation light. A more detailed description of the used TCSPC experiment including the data acquisition is already reported in Ref. [143].
During this work, a time window of 40 ns was used. The concentration of the sample was set to 0.3 OD at the excitation wavelength over a 10 mm optical path length.

4.2.4 Quantum Yield Determination using an Ulbricht Sphere

The emission quantum yield Φ is a characteristic quantity for luminescent samples, that is defined as the ration between the number of emitted photons and the number of absorbed photons,[127] i.e.

$$\Phi = \frac{k_r}{k_a} = \frac{k_r}{k_r + k_{nr}} \,. \tag{4.1}$$

In the case of just photophysical processes, the total decay rate is generally given by the sum of the radiative and non-radiatve rate, where typically non-radiative processes include internal conversion and intersystem crossing.[127]
The quantum yield can be easily determined by an Ulbricht Sphere. It is a hollow sphere, whose inner surface is covered with a diffuse, totally reflecting material, most commonly barium sulfate ($BaSO_4$). In general, there are two different working principles of an Ulbricht Sphere with a 2π and 4π arrangement, but only the latter one is used for the determination of quantum yields. The setup and the common working principle of an Ulbricht Sphere are shown in Figure 4.5. In the 4π arrangement, the sample is placed in the center of the Ulbricht sphere, so that the fluorescence of the sample can be emitted in all directions.
Within this work, the quantum yields were determined with the commercially available Ulbricht Sphere setup (CC9920-02, Hamamatsu), using a 150 W Xenon lamp as excitation source, which in combination with a monchromator allows excitation between 250 nm and 800 nm. The emis-

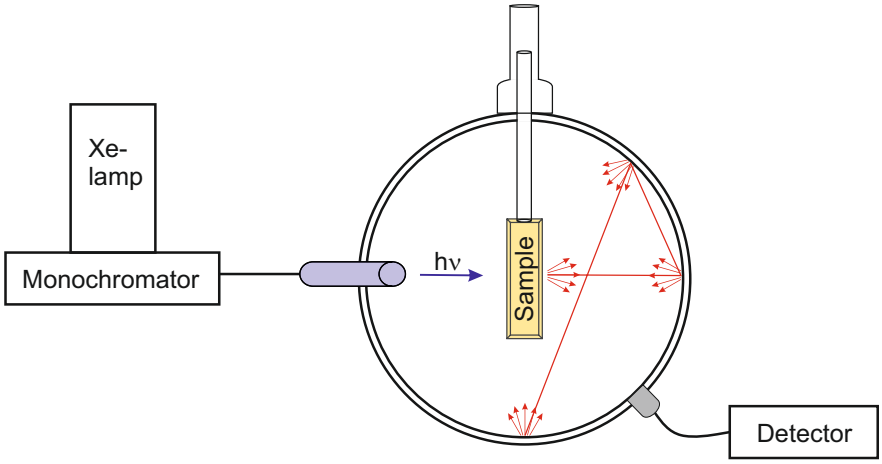

Figure 4.5: Working principle of an Ulbricht Sphere schematically represented. After excitation of the sample (blue arrow), the emitted photons are diffusely reflected at the inner wall of the sphere (red arrows), which is coated with a diffuse, totally reflecting material, like $BaSO_4$. Liquid samples are placed in the center of the sphere, and the aperture at the cuvette's shaft is covered to avoid scattering light from the outside.

sion of the sample is detected by a CCD-spectrometer with a range from 300 nm up to 950 nm. The samples were located in a (10×10) mm cuvette with an optical density of 0.1 at the excitation wavelength.

4.2.5 Transient Absorption

For studying the excited state absorption behavior of the tropylium salts, two different TA setups were used; one on a fs to ns time scale and the other one with a ns to ms time range.
Since the fs-ns TA experiment was performed by our collaboration partners, here only the most important parameters are mentioned. For excitation, an Yb-based 250 fs industrial grade pump laser was combined with a newly designed NOPA system to generate pulses with a central wavelength of 550 nm and a pulse length of 10-20 fs. For detection, CaF_2-based ultrabroad probe pulses were used.
The ns-ms TA experiment is explained in detail in Section 3.2.2. The Nd:YAG laser was combined with the OPO to generated 450 nm excitation pulses. The time window was varied between 500 ns and 10 ms in dependence on the distinct tropylium dyes and the used solvent. The sample's optical density was set to 0.1 - 0.3 at the excitation wavelength over a 10 mm path length.

4.2.6 Quantum Chemical Calculations

Quantum chemical calculations on all six tropylium cations were carried out with the Turbomole package[425;426] for *ab initio* electronic structure calculations *via* the graphical user interface TmoleX. Ground-state geometry optimizations were performed on the level of density-functional theory (DFT) using the B3LYP functional[173;175] and the def2-TZVP basis set.[271;272] To verify that the found geometries correspond to the ground-state structures, vibrational excitation energies were calculated for all stable conformers. Furthermore, the first 20 vertical excitation energies were determined by ADC2 level of theory using aug-cc-pVDZ as basis set,[427–429] and afterwards convoluted with a Gaussian function to account for spectral broadening present in the experimental spectra recorded in solution. To gain insights into the photodynamics of the individual tropylium dyes, relaxed potential energy surfaces (PES) were calculated by the cc-pVDZ basis set[427] within MP2/ADC2 level of theory.

4.3 Results and Discussion

4.3.1 DBTrop with Unsubstituted Dialkylanilines (1^+ - 3^+)

Steady-State Spectra

The compounds $\mathbf{1}^+$, $\mathbf{2}^+$, and $\mathbf{3}^+$ exhibit absorption (solid lines in Figure 4.6) and fluorescence (dashed lines) in the visible range and show a very similar characteristics. The absorption spectra comprise three individual bands around 500 nm, 400 nm, and 270 nm. The latter is accompanied by a weak shoulder towards longer wavelengths. Exciting either the band at 400 nm or at 500 nm results in almost identical emission spectra, consisting of one structureless emission feature at around 635 nm (Figure 4.6a and in Appendix Figure B.1), indicating that the radiative deactivation originates from the lowest-lying excited state, as expected from Kasha's rule. When exciting at 266 nm, a further emission around 500 nm occurs in addition to the main emission peak at around 635 nm (Figure 4.6b). The excitation spectra associated with the main emission agree in both spectral position and relative intensities with the corresponding absorption spectra. By contrast, the 500 nm emission band is only present after excitation in the deep-UV part of the absorption spectra, as also becomes evident from the excitation spectrum (brown, long-dashed curve in Figure 4.6c).

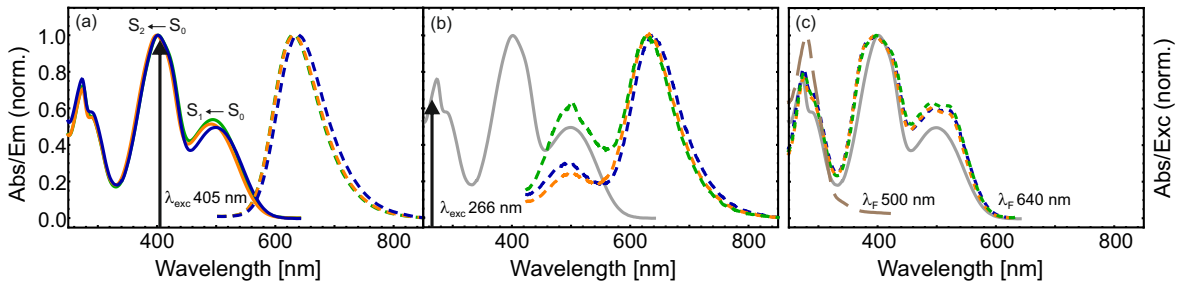

Figure 4.6: Absorption (solid lines), fluorescence (dashed in (a) and (b)) and excitation spectra (dashed in (c)) of $\mathbf{1}^+$ (blue), $\mathbf{2}^+$ (orange), and $\mathbf{3}^+$ (green) in DCM. The excitation wavelength is 405 nm in (a) and 266 nm in (b), whereas the emission wavelength for the excitation spectra in (c) is 640 nm (dashed) and 500 nm (long dashed). The gray line in (b) and (c) displays the absorption spectrum of $\mathbf{1}^+$, as a reference for the very similar absorption spectra of all three dyes, as well as the excitation spectrum in (c) referring to the 500 nm emission of $\mathbf{1}^+$.

Time-Resolved Fluorescence

Following excitation at 405 nm (see Appendix Figure B.3 for the TRE-maps) all dyes show a monoexponential emission decay (Figure 4.7a). Furthermore, the fluorescence lifetime slightly decreases with larger alkyl substituents at the amino group. The corresponding decay times obtained by the global fit are summarized in Table 4.1.

Since there is a second emission band when exciting in the deep-UV (Figure 4.6b), further experiments with excitation at 266 nm were performed. The higher-energy excitation has virtually no effect on the lifetimes obtained for the main emission band around 640 nm, as similar results for the τ_1 decay are found for both 405 nm and 266 nm excitation (see Table 4.1), corroborating that dynamics along the same deactivation pathway are monitored. Unfortunately, the emission signal around 500 nm, which is also present after 266 nm excitation, was too weak for an emission lifetime determination in pure DCM by the used setups. Femtosecond fluorescence upconversion[133;297;430–434] experiments with pump pulses centered at 400 nm further disclose a rapid spectral red-shift within the first few ps. A wavelength-dependent biexponential fitting model as visualized exemplarily for $\mathbf{1}^+$ in Figure 4.7b (data for $\mathbf{2}^+$ and $\mathbf{3}^+$ are juxtaposed in the Appendix Figures B.9 and B.10) yields values of 1.2 ps to 1.3 ps for the time constant τ_0 which can be attributed to solvent reorientation[123;126] after excitation, in good agreement with values reported for DCM.[123] This assignment is substantiated by the observation that τ_0 is a decay time for the high-energy edge of the fluorescence, but its relative amplitude (right panel in Figure 4.7b) decreases with respect to the main emission decaying with τ_1, and eventually τ_0

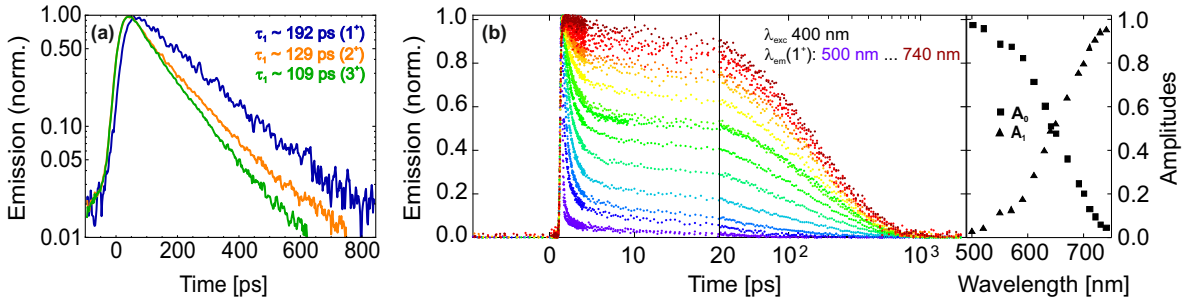

Figure 4.7: (a) Fluorescence decay of $\mathbf{1}^+$ (blue), $\mathbf{2}^+$ (yellow), and $\mathbf{3}^+$ (green) at an emission wavelength of 640 nm after excitation at 405 nm in DCM, observed with a streak camera. (b) Ultrafast fluorescence upconversion at different wavelengths after 400 nm excitation of $\mathbf{1}^+$ in DCM. Note that the abscissa is plotted on a linear scale up to ~20 ps and logarithmically afterwards. A biexponential fit emphasizes an increased amplitude of τ_1 with higher wavelengths (right panel), while the proportion of the faster contribution associated with τ_0 decreases, as indicative for solvent dynamics.

might turn into a rise time at emission signals above 740 nm which could not be recorded for technical reasons. The results obtained with both time-resolved emission techniques agree and a decreasing τ_1 in the order of $\mathbf{1}^+ > \mathbf{2}^+ > \mathbf{3}^+$ is observed (see Table 4.1).

Table 4.1: Fluorescence decay constants and emission quantum yields of the investigated systems dissolved in DCM or DCM-TFA solution. Gray-shaded boxes indicate that the corresponding measurement was not performed. The errors regarding the quantum yields were calculated by the standard deviation.

Sample in DCM		**1^+**	**2^+**	**3^+**	**4^+**	**$4H^{2+}$ (4^++TFA)**	**$5H^{2+}$ (fresh)**	**$5H^{2+}$ (5^++TFA)**
Streak Camera	τ_1 [ps]	192	129	109	70	482		
(λ_{exc}=405 nm)	[ns]						26	
TCSPC	τ_1 [ns]							4.7
(λ_{exc}=370 nm)	τ_2 [ns]							25
Streak Camera	τ_1 [ps]	192	125	110				
(λ_{exc}=266 nm)								
Upconversion	τ_0 [ps]	1.2	1.2	1.3	6.2			
(λ_{exc}=400 nm)	τ_1 [ps]	193	124	103	43			
	τ_2 [ps]	–	–	–	192			
Quantum Yield	[%]	0.68	0.52	0.46	0.10	0.42	8.16	10.96
(λ_{exc}=400 nm)	±	0.04	0.04	0.04	0.01	0.04	0.02	0.3

Time-Resolved Absorption

The photodynamics of $\mathbf{1}^+$ were further investigated by monitoring transient absorption (TA) on a fs to ns time scale. The corresponding TA map (Figure 4.8a) exhibits oscillatory signals due to impulsive vibrational excitation of the solvent at early delay times. A global multiexponential fit which comprises four exponential functions and also models the coherent artifact[120] yielded decay-associated difference spectra (DADS) as shown in Figure 4.8b [note that the functions which model the coherent artifact are not shown here for clarity]. The DADS associated with $\tau_0 = 0.6$ ps unveils a stimulated emission spanning from 500 nm to longer wavelengths, which in combination with the positive contribution above 700 nm is indicative of the solvation-related Stokes shift that was also observed in the fluorescence upconversion data of Figure 4.7b. The lifetime τ_{tw} with 24 ps might be assigned to a relaxation in the excited state accompanied by a

structural reorientation, which would be in line with the quantum chemical calculations (compare Figure 4.11). The blue DADS with $\tau_1 = 181$ ps discloses the decay of an excited-state absorption (ESA) as well as of the stimulated emission, thus reflecting the same process associated with the 192 ps decay found in the time-resolved emission experiments (see Table 4.1). Noteworthy, the spectral position of the negative signal is red-shifted with regard to the stationary emission, because it further describes a rise component of a positive absorption around 750 nm that relaxes with a time constant τ_2 of 405 ps (green DADS) and fully refills the ground-state. This new absorption might either represent an ESA signal from a non-emissive excited-state geometry that relaxes to the ground state with 405 ps, or the absorption of a ground-state conformer that has to overcome a barrier to return to the initial geometry.

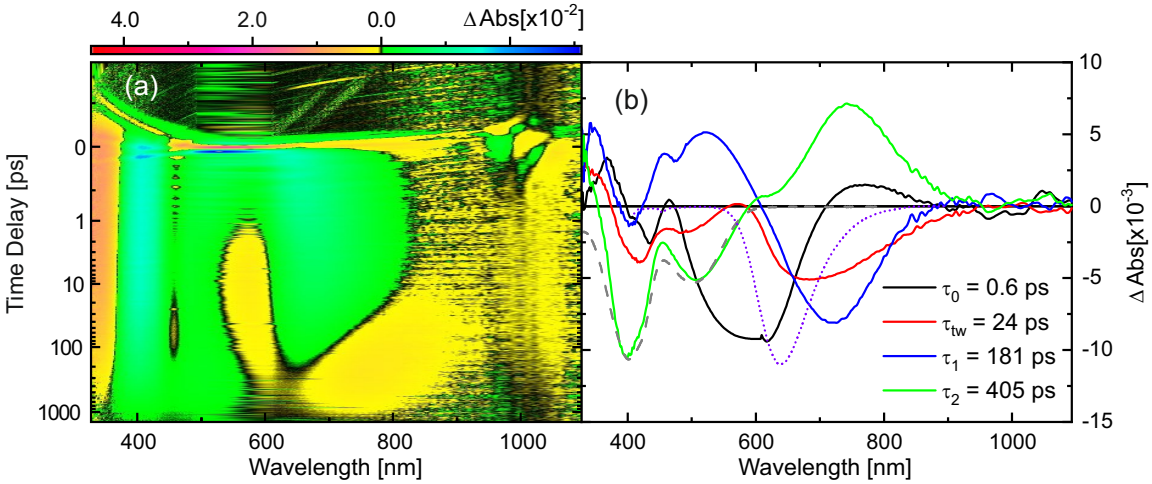

Figure 4.8: (a) Transient absorption data of $\mathbf{1}^+$ in DCM after 550 nm excitation. (b) DADS obtained by global fit with four exponential functions. The scaled and inverted absorption and emission spectra are included as gray-dashed and purple-dotted lines, respectively.

Computational Studies

To further elucidate this aspect as well as the faster excited-state processes, computational studies were performed. A blue-shifted emission band associated with a distinctly different UV excitation spectrum (Figure 4.6) has not been reported for tropylium compounds before, but it is reminiscent of the situation in Thioflavin T (ThT), a dye where also a dimethylaniline unit is connected to a cationic moiety, namely a benzothiazolium. In ThT, two emission bands with corresponding excitation spectra are reported.[435–437] The first one originates from conformers close to the S_0 minimum in which the two moieties are twisted by about 37° with respect to

each other. The π-electron system extends over both moieties, and these conformers give rise to the main absorption and emission band. Upon excitation, the moieties start to rotate and reach the S_1 minimum, described as a twisted intramolecular charge transfer (TICT) state[438] that is non-fluorescent and where the twist angle is 90°. The second emission band of ThT is blue shifted, as is the excitation spectrum, and is due to conformers that are close to a 90° angle already in S_0. Exciting them, no charge is transferred and no rotational motion in S_1 sets in, and the two moieties behave like independent chromophores.[435;437] For various aryltropylium compounds, Kharlanov, Abraham, and Rettig[393] computationally found conditions similar to the first situation in ThT, i.e. minima at around 30° for S_0, and 90° and a shift of the positive charge away from the tropylium in the S_1 state. The second situation, that is starting from S_0 conformers with almost perpendicular geometry, was not considered, but the determined energy barriers in S_0 were found to be low so that a similar behavior is not unlikely.

In view of these reports, we performed quantum chemical calculations to first explore the structures in the S_0 state. For $\mathbf{1}^+$, $\mathbf{2}^+$, and $\mathbf{3}^+$, two stable ground-state structures **A** and **B** were found (Figures 4.9 and Appendix Figure B.16), whereby conformer **A** is energetically more favored by 0.24 eV, 0.29 eV, and 0.40 eV, respectively. In both structures, the DBTrop unit is not planar but bent. In $\mathbf{1}^+_\mathbf{A}$, the DMA unit is tilted slightly upwards, whereas in $\mathbf{1}^+_\mathbf{B}$, it is twisted by ∼55°. Thus, in conformers **A** the π-system extends over both moieties, whereas in **B** the interaction is less distinct, so that the two units are closer to two independent chromophores.

Consequently, the vertical excitation energies (calculated at ADC2/aug-cc-pVDZ level of the-

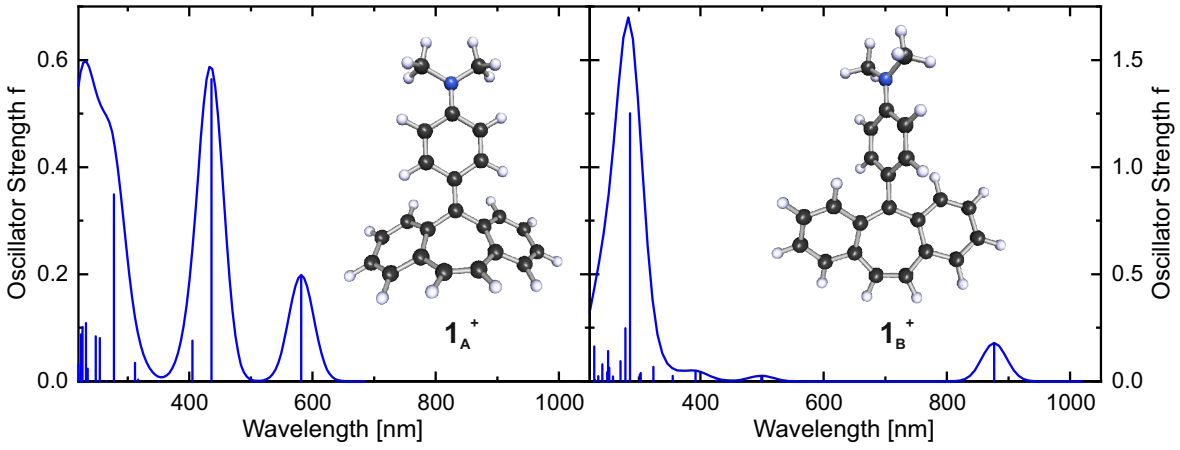

Figure 4.9: Stable ground-state structures **A** and **B** computationally found for $\mathbf{1}^+$ by DFT calculations on the B3LYP/def2-TZVP level of theory. For both optimized geometries, vertical excitation transitions without solvent environment were calculated (ADC2/aug-cc-pVDZ). Convolution of each oscillator strength at a distinct transition energy with a Gaussian of a 20 nm width at half maximum results in the displayed UV-Vis spectra.

ory with Turbomole 4.4) and determined absorption spectra (Figure 4.9) nicely reflect this behavior and show similarities to the experimentally determined absorption spectrum. Hence, we conclude that the two low-energy absorption bands are associated with conformer **A** and contain charge-transfer character (compare Appendix Table B.2). When the sample is excited with 266 nm, it might be possible that both conformer **A** and those few molecules present as conformer **B** can be excited. In this case, the excitation spectrum monitored at a fluorescence wavelength of 500 nm (Figure 4.6c) is solely caused by **B** which mainly absorbs well below 400 nm. However, it can also not be excluded that small impurities in the sample are responsible for the weak 500 nm emission and the corresponding excitation spectrum in the UV region. The two conformers differ not only in geometry, but most remarkably in the localization of the positive charge. The electrostatic potential, represented as density isosurface, of $\mathbf{1}_{\mathbf{A}}^{+}$ and $\mathbf{1}_{\mathbf{B}}^{+}$ is visualized in Figure 4.10. Due to the cationic nature of $\mathbf{1}^{+}$, the whole isosurface map consists of positive values. Some regions can be distinguished by a more pronounced positive potential against others. In the case of $\mathbf{1}_{\mathbf{A}}^{+}$, the most positive part is localized at the DMA unit, whereas the DBTrop ring system comprises the smallest positive potential. Therefore, conformer **A** can be understood as a chinoidal structure. In contrast, conformer **B** is characterized by a highly positive tropylium ring, which explaines the planar aromatic geometry. Thus, the most stable conformer in case of $\mathbf{1}^{+}$, $\mathbf{2}^{+}$, and $\mathbf{3}^{+}$ is not a dibenzotropylium-dialkylaniline but rather can be understood as a dibenzotropylidene-dialkylanilinium cation, in stark contrast to aryltropylium systems like discussed in Section 4.3.3 in the case of $\mathbf{6}^{+}$.

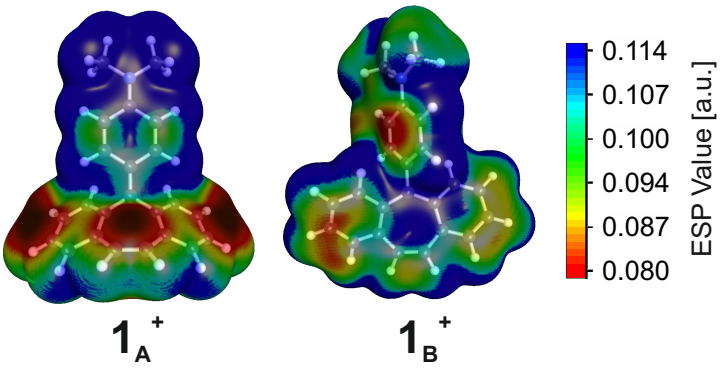

Figure 4.10: Electrostatic potential surface (isovalue 0.001) of structures $\mathbf{1}_{\mathbf{A}}^{+}$ and $\mathbf{1}_{\mathbf{B}}^{+}$, plotted from DFT/B3LYP/def2-TZVP calculations.

For insight into the photodynamics, relaxed potential energy surface (PES) scans were performed for $\mathbf{1}^{+}$ in the ground state S_0 and the first excited state S_1 along the torsional angle φ (spanned by $C_1 - C_7 - C_8 - C_9$; for atom numbering see explanation according to Table 4.2), which defines the tilting between the DBTrop framework and the DMA moiety (Figure 4.11).

Structure **A** is energetically more stable in S_0 than **B**, but in S_1 the situation switches. In S_1, conformer **B** is the energetically most stable structure, with a 90° twist between DBTrop and DMA moieties, which means that the π-systems of both parts are completely independent of each other. Furthermore, a third structure has to be considered in the first excited singlet state, namely $(\mathbf{1}_\mathbf{A}^+)^*_\mathbf{twisted}$, which is characterized by an additional twist within the DMA between the benzene ring and the dimethylamine group (see Figure 4.11). The PES according to the T_1 state was also calculated. Since they are nearly identical to those of S_1, except of the slight lowering in energy in the case of conformer **A**, it is only displayed in the Appendix Figure B.17.

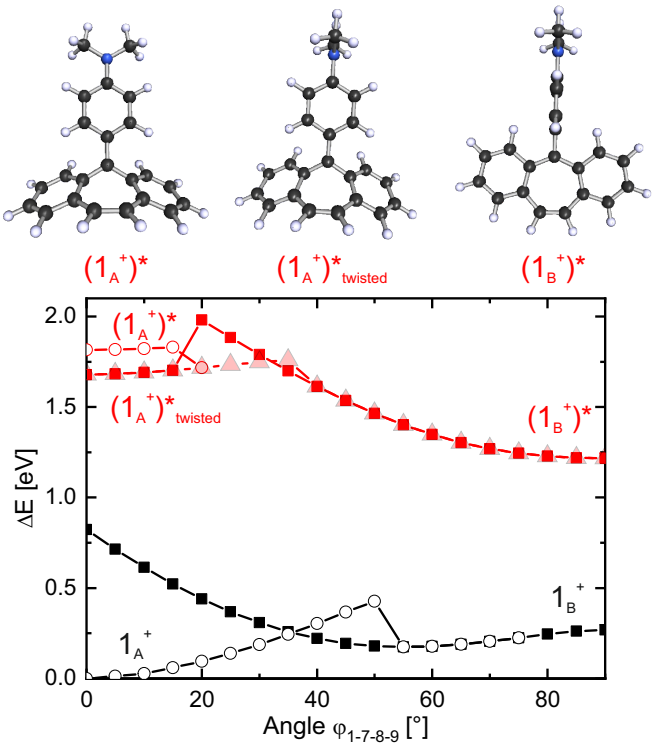

Figure 4.11: Relaxed PES scans along the dihedral angle $C_1 - C_7 - C_8 - C_9$, defining the twist between the DBTrop and DMA moieties of $\mathbf{1}^+$, in S_0 (black) and S_1 (red). The scans were calculated by starting from both conformers **A** (circles) and **B** (rectangles). In the excited state, an additional conformer $(\mathbf{1}_\mathbf{A}^+)^*_\mathbf{twisted}$ has to be considered (triangles).

The calculated PES can be used to rationalize the fs-TA data (Section 4.3.1). Within the first 24 ps, the structural reorientation in the excited state from $(\mathbf{1}_\mathbf{A}^+)^*$ to $(\mathbf{1}_\mathbf{A}^+)^*_\mathbf{twisted}$ could be observed, before the **A** emission ceases with a rate constant of τ_1^{-1} to which besides the radiative rate, reorientation to $(\mathbf{1}_\mathbf{B}^+)^*$ *via* a slight barrier contributes. The longest lifetime τ_2 then describes the

decay of the absorption of ground-state $\mathbf{1}_\mathbf{B}^+$ and reverse charge transfer to restore $\mathbf{1}_\mathbf{A}^+$. However, due to the PES according to $\mathbf{1}_\mathbf{B}^+$, which only increases in energy along the rotational motion down to $\varphi = 0°$ and does not show any reorientation into conformer **A**, there possibly might be a different relaxation pathway. An alternative explanation could be that conformer **A** performs an ISC into the T_1 state, instead of the reorientation to $(\mathbf{1}_\mathbf{B}^+)^*$. Then τ_2 can be assigned

Table 4.2: Twist angle φ (red), tilt angle θ (green), bending angle α (blue), and arching angle β (orange). Due to the arched geometry of the DBTrop unit, φ is calculated from the two dihedral angles $\varphi_{6-7-8-13}$ and $\varphi_{1-7-8-9}$ (listed in the Appendix Table B.1) *via* $\frac{1}{2}(\varphi_{6-7-8-13} + \varphi_{1-7-8-9})$. The tilt angle θ is defined by the dashed green arrows: one connecting atoms 7 and 8, and the other one going through the center of atoms 1, 2, 5, and 6 and the middle of the bond between atoms 3 and 4. The angle α describes the bending of the aniline, given by the blue dashed arrows connecting atoms 7 and 8 as well as 11 and 14. The angle β quantifies the arching of the DBTrop unit and is calculated from the normals to the orange planes, defined by atoms 5, 22 and 24 or 2, 18 and 20 for the two benzene units. Full planarity of the DBTrop unit would correspond to $\beta = 180°$.

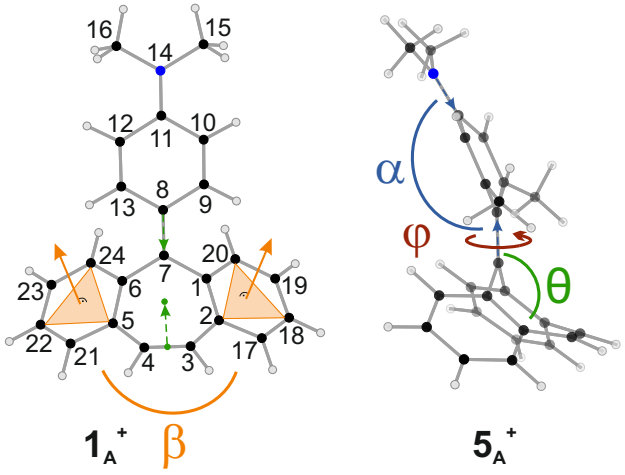

Compound	Conformer A				Conformer B			
	φ	θ	α	β	φ	θ	α	β
$\mathbf{1}^+$	4.49	119.79	179.50	132.28	55.86	179.57	179.84	152.26
$\mathbf{2}^+$	4.24	119.18	179.34	132.06	54.28	179.87	179.95	151.51
$\mathbf{3}^+$	4.19	118.89	179.15	131.86	54.19	179.86	178.31	151.46
$\mathbf{4}^+$	1.59	110.54	157.39	120.74	68.02	179.97	179.85	159.22
$\mathbf{5}^+$	2.57	113.46	150.24	121.06	73.95	179.90	179.96	161.81

to the radiationless transition from the triplet back into the ground state, regaining $\mathbf{1}_{\mathbf{A}}^{+}$.
Moreover, the compounds $\mathbf{1}^{+}$, $\mathbf{2}^{+}$, and $\mathbf{3}^{+}$ only differ by the length of the alkyl chains at the tertiary amine, raising the question for the origin of the faster relaxation with larger alkyl groups (Figure 4.7a). For aryltropylium systems, it was reported that the electron donor strength (EDS) of the aryl substituent has an influence on the twist angle.[385;393] The higher the EDS, the more planar is the S_0 minimum conformer, and the better the deactivation by twisting in the S_1 state. The EDS of N-N-dialkylaniline units increases with alkyl chain length, but steric effects need to be considered as well.[439] Hence, we calculated by how much the compounds deviate from planarity (Table 4.2). For the S_0 minimum structure, all calculated angles φ, θ, α, and β slightly decrease with alkyl chain length, resulting in a more strongly bent and twisted geometry in the order $\mathbf{1}^{+} < \mathbf{2}^{+} < \mathbf{3}^{+}$. Thus, the charge-shift character of the excitation increases and the S_1 dynamics may occur more rapidly, in full accordance with the observed fluorescence decay times.
The tilt angle θ is found to be close to 180° for conformers **B** of $\mathbf{1}^{+}$, $\mathbf{2}^{+}$, and $\mathbf{3}^{+}$, as expected for an aromatic tropylium moiety, and the aniline substituent is twisted by about $\varphi = 54°$. By contrast, there is basically no twist of the aniline substituent ($\varphi \approx 4°$) for conformers **A**, and the aniline part together with atom C7 are tilted strongly upwards by $\theta \approx 120°$, thus impugning an aromatic tropylium and rather indicating a chinoidal structure again.

Crystal structures from XRD experiments[440] for $\mathbf{1}^{+}$, $\mathbf{2}^{+}$, and $\mathbf{3}^{+}$ very much resemble the geometries found for conformer **A** in the quantum chemical calculations presented in this work. Thus,

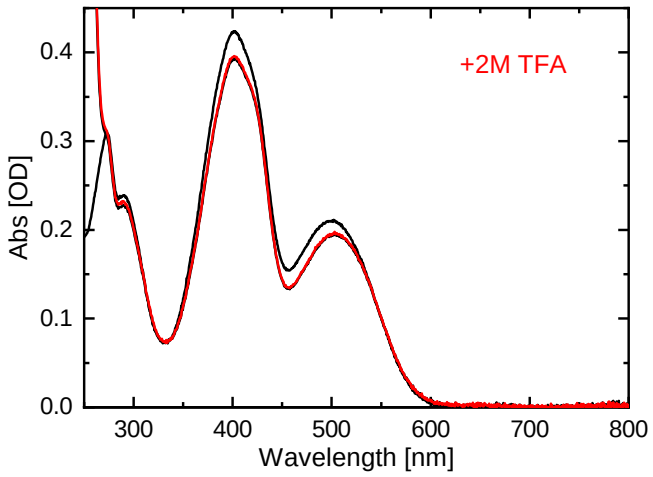

Figure 4.12: UV-Vis absorption spectrum of $\mathbf{1}^{+}$ measured in pure DCM (black) and after adding 2 M TFA (red).

both in the solid state and in solution, conformation **A** prevails, and hence the positive charge is not located at the seven-membered ring. As a consequence, the nitrogen atom does not exhibit a lone pair and hence should not be protonatable. This is experimentally confirmed by addition of TFA to a DCM solution of $\mathbf{1}^+$. Even with a large TFA excess, the absorption spectrum (Figure 4.12) of $\mathbf{1}^+$ is only less affected. As previously mentioned, also a few molecules of **B** are present in the solution and can be protonated by TFA, which is responsible for the observed differences. However, the major part of $\mathbf{1}^+$ molecules remains unaltered. Only in the transient absorption monitored after photoexcitation of $\mathbf{1}^+$ in a DCM-TFA solution, the characteristic double-band structure of the protonated cations are observable, as later discussed in the end of Section 4.3.2.

4.3.2 DBTrop with Substituted Dimethylanilines ($\mathbf{4}^+$ and $\mathbf{5}^+$)

Spectral Characteristics

The previous studies have shown that for the compounds $\mathbf{1}^+$, $\mathbf{2}^+$, and $\mathbf{3}^+$ the chinoidal conformer **A** is energetically more favorable than **B** with the twisted aniline moiety. By introducing methyl or methoxy groups to the latter, compounds $\mathbf{4}^+$ and $\mathbf{5}^+$ are obtained, for which geometry optimizations (DFT/B3LYP/def2-TZVP) again unveil two stable ground-state structures **A** and **B**. The side groups lead to steric hindrances, which can be counteracted in conformer **B** by an increased twist angle φ (see Table 4.2). As the π-systems of the aniline and the DBTrop moiety are then also less coupled, the DBTrop unit gets closer to planarity with the arching angle β changing by $\sim 10°$. For conformer **A**, the side groups do not cause a rotation but strong distortions (see calculated structure of $\mathbf{5}_\mathbf{A}^+$ in the explanation of Table 4.2): the dialkylaniline moiety is tilted even further (θ decreases by 10°) and intrinsically bent (α decreases by more than 20°), the DBTrop unit now is arched more strongly ($\beta \approx 120°$). As a consequence, for $\mathbf{4}^+$ and $\mathbf{5}^+$, conformer **B** is energetically more favored by 0.02 eV and 0.22 eV, respectively. The trend in energy difference can be rationalized since two methyl substituents in $\mathbf{5}^+$ possess a more pronounced steric hindrance (1.7 kcal·mol^{-1}) than the less rigid methoxy groups in $\mathbf{4}^+$ (0.6 kcal·mol^{-1}), according to their A-values.[441] This steric hindrance of the substituents is also reflected in the φ values of 68° for $\mathbf{4}_\mathbf{B}^+$ and 74° for $\mathbf{5}_\mathbf{B}^+$.

In DCM solution, the absorption spectrum of $\mathbf{4}^+$ (Figure 4.13a) is dominated by a band around 360 nm accompanied by a shoulder on the low-frequency side. The virtual absence of bathochromic charge-transfer bands indicates that the S_0 minimum structure is twisted. The distinctly

different shape of the absorption spectra of $\mathbf{4}^+$ and $\mathbf{5}^+$ (Figure 4.13a and b) compared to the ones of $\mathbf{1}^+$ to $\mathbf{3}^+$ (Figure 4.6) further confirms the predominance of conformer **B** for $\mathbf{4}^+$ and $\mathbf{5}^+$ in solution, and so does a juxtaposition to the respective spectra derived by calculations for both conformers (Figure 4.13d and e).

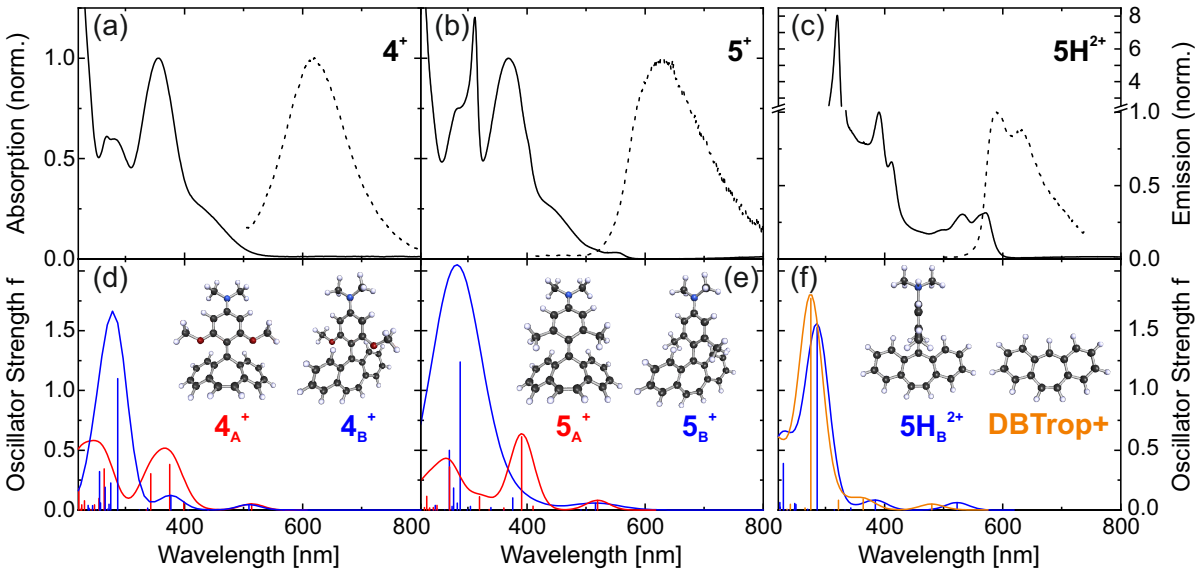

Figure 4.13: Comparison of the normalized absorption (solid) and fluorescence spectra (dashed) of (a) $\mathbf{4}^+$, (b) $\mathbf{5}^+$, and (c) $\mathbf{5H}^{2+}$ dissolved in DCM. (d-f) DFT calculations on the B3LYP/def2-TZVP level of theory for compounds (d) $\mathbf{4}_\mathbf{A}^+$ and $\mathbf{4}_\mathbf{B}^+$, (e) $\mathbf{5}_\mathbf{A}^+$ and $\mathbf{5}_\mathbf{B}^+$, (f) $\mathbf{5H}_\mathbf{B}^{2+}$ and DBTrop+. For each optimization, the vertical excitation transitions without solvent environment were calculated (ADC2/aug-cc-pVDZ) and each oscillator strength corresponding to a certain transition energy was convoluted with a Gaussian of 20 nm width at half maximum, resulting in the displayed UV-Vis spectra.

Protonation of the Substituted Dimethylanilines

With conformers $\mathbf{4}_\mathbf{B}^+$ and $\mathbf{5}_\mathbf{B}^+$, for which the positive charge is delocalized over the DBTrop moiety as shown by the electrostatic potential surface maps (see in the Appendix Figure B.18), prevailing in DCM solution, it should be possible to protonate the nitrogen atom. By a stepwise addition of TFA to a solution of $\mathbf{4}^+$ (Figure 4.14) the characteristic absorption band at 360 nm decreases, while two double-peaked bands around 400 nm and 550 nm as well as a sharp peak at ~310 nm appear. The spectrum shown in red corresponds to the protonated species $\mathbf{4H}^{2+}$. The same behavior is found for the formation of $\mathbf{5H}^{2+}$, which we could also independently obtain from the divalent salt (Figure 4.13c). Spectra of the protonated compounds exhibit double-peak

structures, both for the absorption bands around 400 nm and 550 nm, and for the fluorescence (see Appendix Figure B.2), which has been reported to be characteristic for unsubstituted DBTrop.[442] One can thus deduce that only the DBTrop moiety gives rise to these spectral features, and this is confirmed by calculations which show that the twist angle φ is close to 90° and hence the π-systems of the moieties are decoupled in the dications (Figure 4.13f).

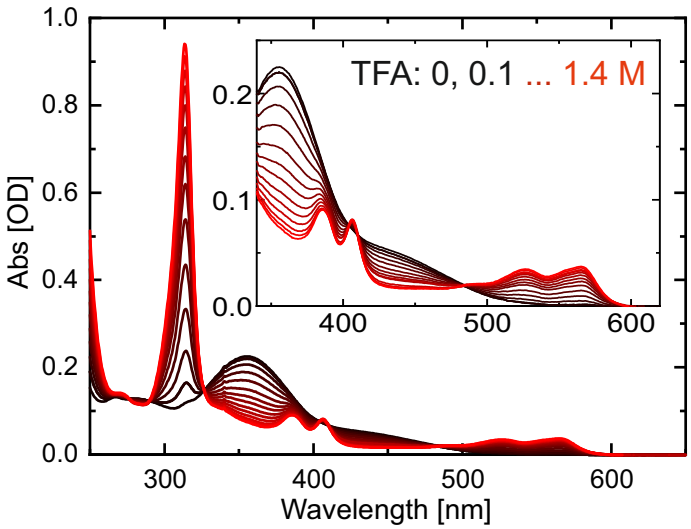

Figure 4.14: Absorption spectra of $\mathbf{4}^{+}$ in DCM with stepwise addition (+0.1M) of TFA, yielding $\mathbf{4H}^{2+}$.

Fluorescence Lifetimes of Monocationic Species

The measured time-resolved emission decays of $\mathbf{4}^{+}$ in DCM, recorded with the streak camera after excitation with 405 nm, yield a decay lifetime of ca. 70 ps (Table 4.1, and in Appendix Figure B.3). Since the fluorescence lifetime of $\mathbf{4}^{+}$ is in close approximation to the IRF of the streak-camera setup, the photodynamics were additionally investigated in fluorescence upconversion studies (Appendix Figure B.11). The photodynamics of $\mathbf{4}^{+}$ are distinctly different from those observed for $\mathbf{1}^{+}$, $\mathbf{2}^{+}$, and $\mathbf{3}^{+}$, yielding time constants of 6.2 ps (τ_0) and 43 ps (τ_1) and 192 ps (τ_2) at 630 nm. The shortest lifetime τ_0 possibly describes a combination of solvent dynamics, which is supported by its decreasing amplitudes with higher wavelengths (see Appendix Figure B.12), and the TICT from the tropylium to the aniline moiety. Then, τ_1 represents the deactivation process of the excited fluorophore $\mathbf{4}^{+}$. The third component has a very small amplitude and its τ_2 value of 192 ps is equivalent to the one of $\mathbf{1}^{+}$, indicating that a minor amount of the sample was not substituted with methoxy groups.

Thus, introducing methoxy groups at the benzene ring leads to a more rapid excited-state deactivation than for $\mathbf{1}^+$, despite the additional sterical hindrance. The reason for it is the opposite direction of the charge transfer in the excited state. As evidenced by the absorption spectra and the calculations (Figure 4.13), mainly conformer **B** is present in solution for compound $\mathbf{4}^+$ and $\mathbf{5}^+$, resulting in an already remarkably pre-twisted geometry in the ground state (see angle φ for conformer **B** in Table 4.2). In this regard, it is noteworthy that in the neutral TICT dye anthracene-dimethylaniline (with anthracene being sterically not too different from DBTrop), the formation rate of the charge-transfer state after excitation is accelerated if two methyl groups are attached to DMA in analogy to $\mathbf{5}^+$, and the conclusion is drawn that this rate is generally lower for excitation of a more planar conformer than for a more twisted one.[443]

Fluorescence Lifetimes of Dicationic Species

In DCM, the fluorescence decay of $\mathbf{5H}^{2+}$, freshly prepared from the dicationic salt, was monitored after excitation with 405 nm light (see Appendix Figure B.5) and fitted by a global monoexponential model, yielding an emission lifetime of 26 ns. In a further measurement of $\mathbf{5}^+$ dissolved in DCM with additional TFA to stabilize the protonated species, the recorded decay trace at 590 nm after excitation at 370 nm shows approximately the same emission lifetime of 25 ns (see Appendix Figure B.7).
Analysis of the time-resolved emission of $\mathbf{4H}^{2+}$ in a DCM-TFA solution, measured with the streak camera under 405 nm excitation, yielded a monoexponential decay with 482 ps and thus a significantly prolonged emission in comparison to its deprotonated analogue $\mathbf{4}^+$ ($\tau = 43$ ps). The variation in the decay times for methyl ($\mathbf{5H}^{2+}$) and methoxy ($\mathbf{4H}^{2+}$) substitution at the dimethylaniline can be explained again by the different rigidity as quantified by the A-values, which are a quantity to describe the bulkiness of substituents, in addition, the equilibrium ground-state structures of both salts are dissimilar (compare Table 4.2).

Time-Resolved Absorption of $\mathbf{4}^+$

At an excitation wavelength of 430 nm, fs-ns TA was performed for $\mathbf{4}^+$ (Figure 4.15a). Global lifetime analysis with three exponential functions yielded DADS as displayed in Figure 4.15b [again: contributions according to the coherent artifact[120] are not shown for simplicity]. The shortest contribution with 1.2 ps can be assigned to the solvent reorientation and the formation of the TICT state. An excited-state absorption (ESA) around 500 nm disappears on the same

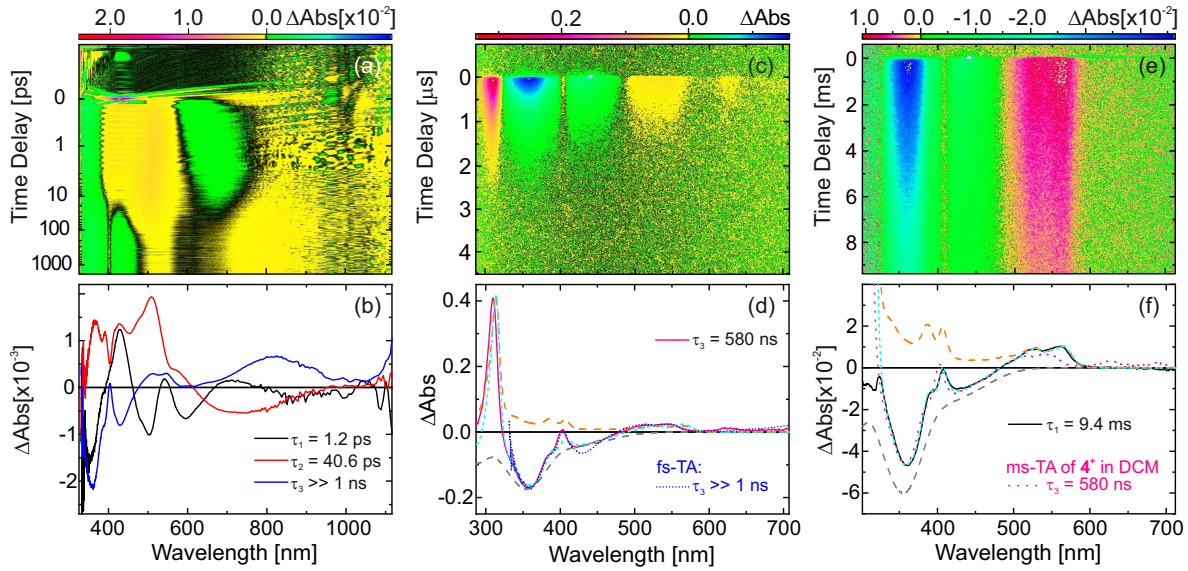

Figure 4.15: Transient absorption maps of $\mathbf{4}^{+}$ in DCM, monitored after 430 nm excitation on a fs-ns time scale (a) and after 450 nm excitation on a µs time scale (c), compared to the transient absorption of $\mathbf{4H}^{2+}$ in DCM-TFA detected after 450 nm excitation on a 10 ms time window (e). (b,d,f) The corresponding DADS results from global lifetime analysis based on the exponential ansatz. For comparison, the inverted absorption spectrum of $\mathbf{4}^{+}$ in DCM (gray dashed curve) and the absorption spectrum of $\mathbf{4H}^{2+}$ in DCM-TFA solution (orange dashed curve) are included. Furthermore, a superposition of both steady-state spectra is also displayed (cyan dashed line), which matches the DADS in (d) and (f) relatively well.

time scale as the stimulated emission at 700 nm, thus describing the decay of the TICT state with 40 ps, in good accordance with the determined emission lifetime of 43 ps (Table 4.1). Remarkably, there is an additional long-lived signal exceeding the experimental time window of 1 ns.

Ultimately, this signal decays monoexponentially on a µs time scale with a lifetime of 580 ns (Figure 4.15c-d). The DADS consists of a relatively sharp product absorption (PA) at 310 nm in addition to a very weak PA around 550 nm and a ground-state bleach with maximum at 360 nm. The DADS is simply a linear combination (cyan dashed in Figure 4.15d) of the steady-state absorption spectra of $\mathbf{4}^{+}$ in DCM (gray dashed in Figure 4.15d) and of $\mathbf{4H}^{2+}$ in DCM-TFA mixtures (orange dashed in Figure 4.15d). Thus, it can be concluded that upon excitation, the pKa value changes, so that protonation of $\mathbf{4}^{+}$ towards $\mathbf{4H}^{2+}$ becomes possible. The proton is most likely abstracted from water impurities in DCM, and release of the proton once the molecule is back in the ground state takes 580 ns owing to a lack of potential acceptors.

If this interpretation of $\mathbf{4}^{+}$ acting as a photobase were applicable, addition of TFA should enhance the lifetime of the formed $\mathbf{4H}^{2+}$ because TFA even further reduces the amount of potential

acceptors.[444] The corresponding TA (Figure 4.15e) up to 10 ms exhibits a dispersed emission signal around 600 nm which basically follows the IRF, and a monoexponentially decaying signal with a lifetime of ∼9.4 ms. Again, comparison of the DADS to a linear combination of the spectra of $\mathbf{4}^{+}$ and $\mathbf{4H}^{2+}$ gives almost perfect agreement (Figure 4.15f), and so does the comparison of the DADS in Figure 4.15f to the one in Figure 4.15d. Thus, the same process is monitored, but with the remarkable difference that the presence of TFA increases the lifetime of $\mathbf{4H}^{2+}$ by four orders of magnitude.

The transient increase of dicationic species is even conceivable if the formation of dicationic species is remarkably smaller in the ground state, as found for compounds $\mathbf{1}^{+}$, $\mathbf{2}^{+}$, and $\mathbf{3}^{+}$. Therefore, the photodynamics of $\mathbf{1}^{+}$ in a DCM-TFA mixture after excitation with 450 nm pulses were also monitored up to 100 µs (Figure 4.16a). Indeed, also a long-lived signal is observed here, with a DADS corresponding to 31 µs. By comparison to the inverted absorption spectrum of $\mathbf{1}^{+}$ (dashed gray in Figure 4.16b), it is evident that the DADS is comprised of the ground-state bleach of $\mathbf{1}^{+}$ and a transient product with an intense peak around 320 nm and a minor one at roughly 420 nm, as it is characteristic for the dicationic species (compare Figure 4.14 or Appendix Figure B.2 for the spectra of $\mathbf{4H}^{2+}$ and $\mathbf{5H}^{2+}$). Thus, even though $\mathbf{1}^{+}$ cannot efficiently be protonated in the ground state, it can be well protonated in the excited state, allowing the transient observation of $\mathbf{1H}^{2+}$. This is only possible because the positive charge migrates from the aniline moiety where it is located in the ground state to the seven-membered ring, thus

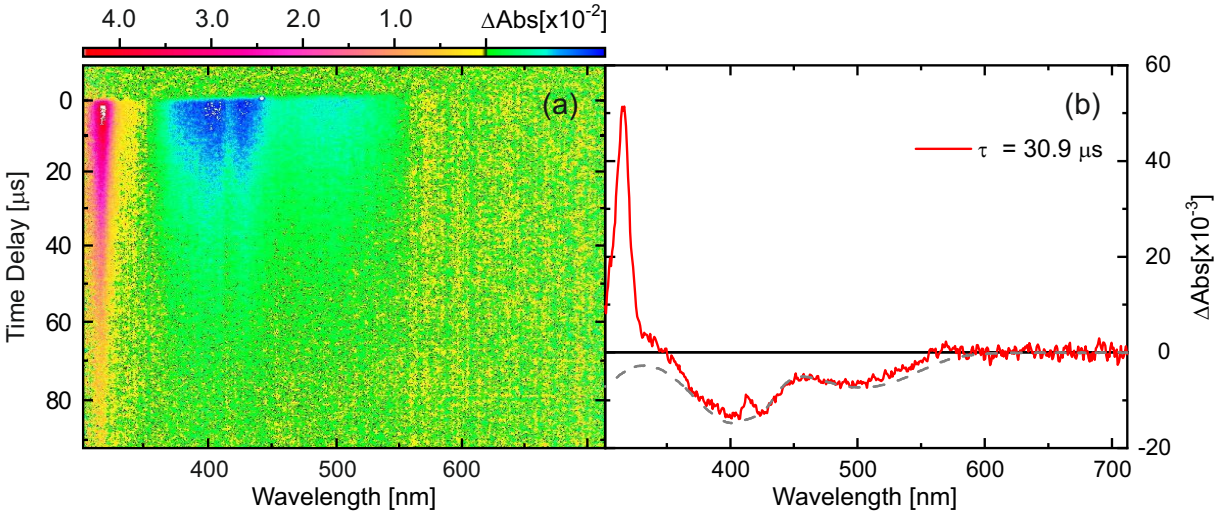

Figure 4.16: µs-TA experiments of $\mathbf{1H}^{2+}$, dissolved in DCM-TFA. (a) The TA map was recorded after 450 nm excitation with a time window of 100 µs. The results of a global lifetime analysis using a mono-exponential function is displayed as DADS in (b). The inverted steady-state absorption spectrum is added as gray-dashed line.

enabling the subsequent protonation of the nitrogen atom. The rather long lifetime of 31 µs is explicable by the need for a proton acceptor in the vicinity before the initial conformer $\mathbf{1}_{\mathbf{A}}^{+}$ can be restored again. These molecules thus combine the properties of a TICT compound and a photobase.

4.3.3 Unsubstituted Trop-DMA without the DB-Ring-System (6^+)

The previously discussed tropylium compounds $\mathbf{1}^+$ to $\mathbf{5}^+$ have in common the possibility of two stable ground-state structures **A** and **B**. However, if the DBTrop part is reduced by the two benzene rings, than only the seven-membered tropylium ring is linked to the aniline scaffold, yielding compound $\mathbf{6}^+$. Within geometry optimizations (DFT/B3LYP/def2-TZVP) only one stable ground-state structure is found, which is characterized by a twist angle φ of around 24° (see Figure 4.17). Furthermore, the density isosurface map of $\mathbf{6}^+$ comprises the most positive potential within the tropylium ring, supporting the aromaticity of this structure. Therefore, in comparison to the other studied dyes the geometry of $\mathbf{6}^+$ resembles conformer **B** rather than **A**. The measured UV-Vis absorption spectrum of $\mathbf{6}^+$ in DCM looks completely different compared to those of the previously discussed compounds $\mathbf{1}^+$ to $\mathbf{5}^+$, and is shown in Figure 4.17. It con-

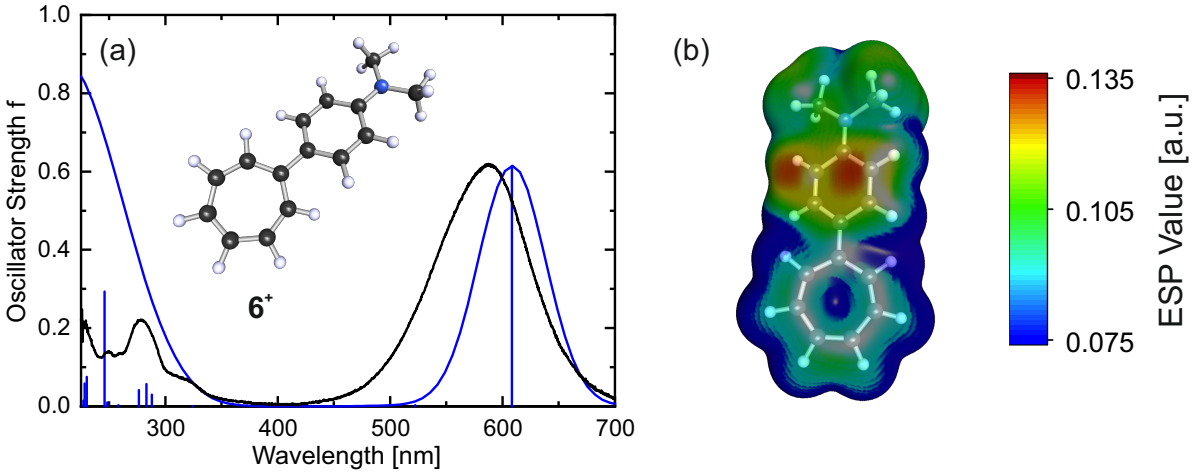

Figure 4.17: (a) Absorption spectrum of $\mathbf{6}^+$ in DCM (black) compared to the quantum chemically calculated spectrum (blue) in the gas phase on the ADC2 level of theory using the aug-cc-pVDZ basis set. Each calculated oscillator strength corresponding to a transition energy was convoluted with a Gaussian of a 20 nm width at half maximum. The corresponding ground-state geometry is included on the left-hand side. (b) The electrostatic potential surface (isovalue 0.001) of $\mathbf{6}^+$ plotted from the DFT/B3LYP/def2-TZVP calculation.

sists of one major absorption band peaking at 590 nm and a second much weaker band around 270 nm. The calculated vertical excitation energies match the experimental resonances of the electronic transitions with an absorption band around 600 nm, and further contributions in the UV region (also included in Figure 4.17). Due to the much smaller conjugated π-system of the tropylium moiety compared to that of compounds $\mathbf{1}^+$ to $\mathbf{5}^+$, a hypsochromic shift of the $\pi - \pi^*$ transition band could be expected; however, a bathochromic shift is observed, which at least results from a significantly more planar geometry and a much smaller twisting angle φ than that of the dibenzotropylium samples enhancing the π-system over the alkyl chain.
By exciting into the absorption maximum with 590 nm light, a very weak emission band peaking around 670 nm was observable (see Figure 4.18b). The corresponding excitation spectrum shows a small spectral blue-shift in comparison to the absorption maximum, and has its maximal intensity in the UV-region. However, excitation in the UV-Vis range below 450 nm results in a second, very intense emission band around 500 nm, corresponding to excitation bands which are not responsible for the main absorption contributions (see Figure 4.18a).

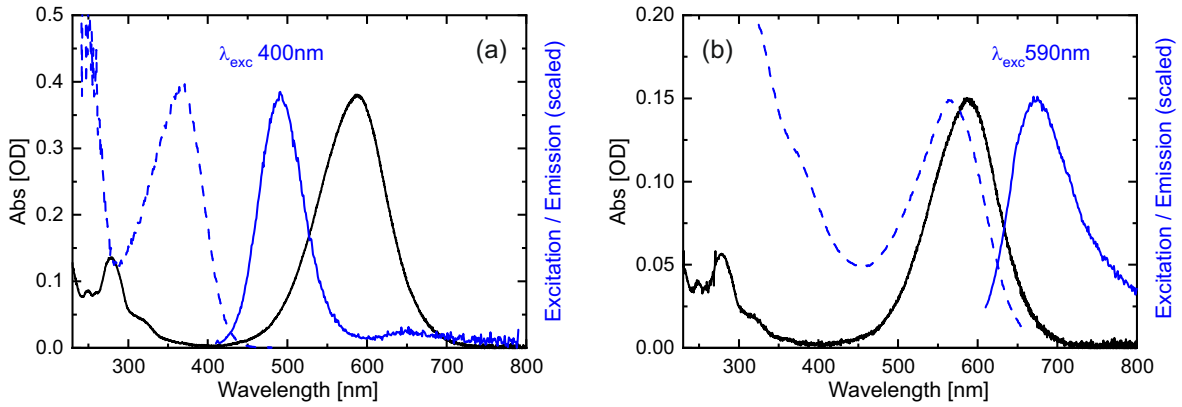

Figure 4.18: Absorption spectra of $\mathbf{6}^+$ in DCM (black), compared to the scaled emission spectra after 400 nm (a) and 590 nm excitation (b) and the corresponding excitation spectra (blue solid and dashed curves, respectively).

Thus, it can be concluded that there is a second species in solution, which either has a small extinction coefficient or is present in minor amounts, but comprises a strong emission. In literature, the photochemistry of aryl-substituted cycloheptatrienes is well discussed, reporting a boat-like shape of the seven-membered ring which results in absorption bands below 370 nm.[391;445] Therefore, it might be possible that slight impurities in the solution, e.g. water, are coordinating to the positively charged tropylium ring. Due to such a coordination, the tropylium would lose its aromaticity, which could be responsible for the unusual emission at 500 nm. For further confirmation of this hypothesis, the vertical excitation energies of $\mathbf{6}^+$ substituted with

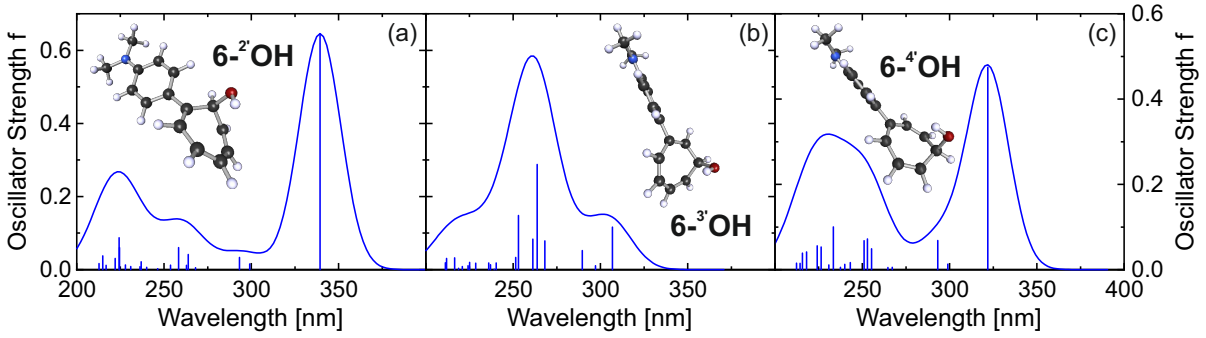

Figure 4.19: Stable ground-state structures computationally found for **6-$^{2'}$OH**, **6-$^{3'}$OH** and **6-$^{4'}$OH** by DFT calculations on the B3LYP/def2-TZVP level of theory. For both compounds, vertical excitation transitions without solvent environment were calculated (ADC2/aug-cc-pVDZ) and convoluted with Gaussians of a 20 nm width at half maximum, resulting in the displayed UV-Vis spectra.

a hydroxyl group in 2-, 3-, and 4-position of the tropylium ring, yielding the neutral compounds **6-$^{2'}$OH**, **6-$^{3'}$OH**, and **6-$^{4'}$OH**, respectively, were calculated. Due to its expected absorption spectrum, **6-$^{3'}$OH** may be excluded as origin (see Figure 4.19b). Nevertheless, both calculated spectra of **6-$^{2'}$OH** and **6-$^{4'}$OH** (Figure 4.19a and c) show some similarities to the measured excitation spectrum, supporting the previously drawn hypothesis. However, the observed 500 nm emission might also originate from completely different, minor impurities in the sample. Since those could not be excluded, the exact reason for the 500 nm emission band is still unknown. In order to shed more light on the origin of the strong 500 nm emission, further investigations like mass spectrometry experiments are planned. Therefore, to determine the decay time of the 670 nm emission band without rate constants of the still obscure, but dominant fluorescence at 500 nm, it is necessary to excite the sample with light above 500 nm. Thus, ms-TCSPC was performed after excitation at 532 nm, but unfortunately the emission signal was either to short or to weak for detection.

Then the transient absorption of **6$^+$** in DCM was monitored on a fs to ns time scale, unveiling relatively fast excited state dynamics. Already after a few picoseconds, the molecular system is fully relaxed back into the initial ground state. The TA detected after 550 nm excitation is shown in Figure 4.20, together with the DADS resulting from a global biexponential fit. The DADS corresponding to τ_1 consists of an excited state absorption peaking below 400 nm. However, the majority of excited molecules repopulates the initial ground-state during the first 1.4 ps (τ_1), which is indicated by the GSB at 590 nm. The inverted and scaled absorption spectrum of **6$^+$** in DCM is also included for comparison in Figure 4.20 as gray, dashed line. Although the position of the peak maxima of the GSB and the inverted absorption spectrum are equivalent, they differ

in their spectral width. Around 500 nm, this difference can be attributed to the overlap with the ESA, whereas the broader GSB at the red-edge might be possibly attributed to an overlap with a weak stimulated emission signal peaking around 650 nm. If the spectral broadening of the GSB is caused by an overlapping SE, this would explain, why no emitted photons could be detected within the ms-TCSPC experiment mentioned above. The second DADS associated to τ_2 with 5.3 ps consists also of a positive and a negative region, but looks more like the first derivative of an absorption band, which usually indicates vibrational cooling. Thus, τ_2 can be attributed to the vibrational cooling of a hot ground state.

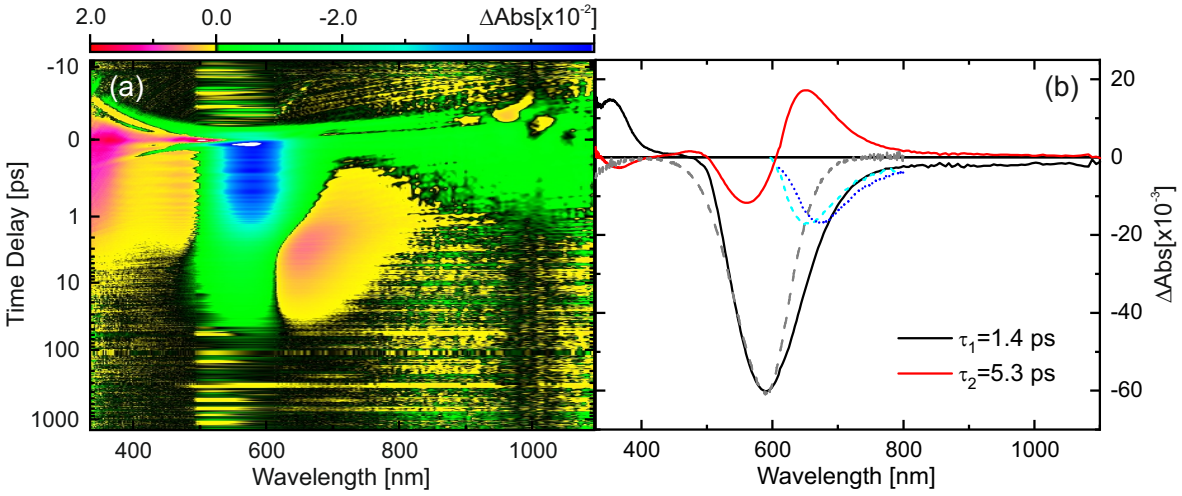

Figure 4.20: (a) Transient absorption map of $\mathbf{6}^+$ in DCM monitored after 550 nm excitation. (b) DADS obtained by global lifetime analysis with two exponential functions. The scaled and inverted absorption and emission spectra are included as gray-dashed and blue-dotted lines, respectively. The cyan-dashed curve describes the difference between the GSB (negative black) and the inverted absorption spectrum (gray dashed) between 600 nm and 800 nm.

Furthermore, relaxed PES calculations along both possible rotational angles, namely the C−C and C−N single bond, were performed on ROHF-DFT/B3LYP/aug-cc-pVDZ level of theory for the S_0 optimization and RHF-TD-DFT/B3LYP/aug-cc-pVDZ level of theory for the transition energies, as shown in the Appendix Figure B.19. Since the rotation around the C−N single bond has a negligible small influence on the PES, only the rotation around the C−C single bond is considered in Figure 4.21, similar to those previously shown for the compound $\mathbf{1}^+$, calculated on the MP2/ADC2 level of theory with cc-pVDZ basis set. As mentioned previously, the energetically most stable structure in the ground state is characterized by a small tilting between the tropylium and the aniline part. However, in the first excited state S_1 the situation changes, since the geometry becomes energetically most stable for a 90° twist between both molecular parts, as already discussed in the case of conformer $\mathbf{1}_\mathbf{B}^+$ in Section 4.3.1.

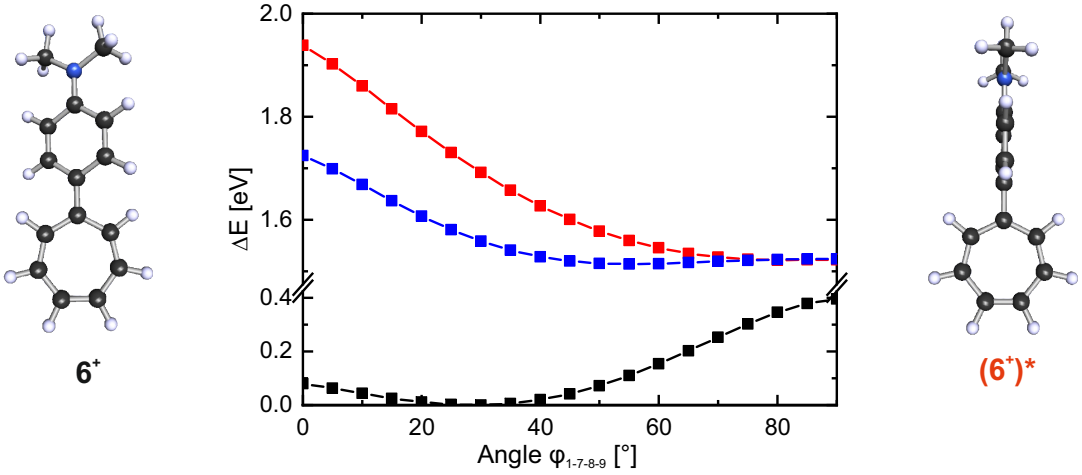

Figure 4.21: Relaxed PESs calculated on the MP2(for S_0) and ADC2(for S_1 and T_1) level of theory using the aug-cc-pVDZ basis set, scanned along the dihedral angle $C_1 - C_7 - C_8 - C_9$, which defines the twist between the Trop and DMA moieties of $\mathbf{6^+}$ in S_0 (black), S_1 (red) and T_1 (blue).

In literature, already calculations on various aryltropylium compounds are published, including compound $\mathbf{6^+}$, for which in the ground state a twist angle φ of 29° and a charge transfer from the alkyl part to the tropylium ring among photoexcitation was found, agreeing with the here discussed results.[393] Furthermore, PES scans on the model of an aniline-substituted tropylium cation (TRAM) were reported.[393] Those indicated a much smaller energy increase for a planarization than for further twisting up to 90° in the ground state. After vertical excitation in the Franck-Condon region, the system planarizes. It was expected that the relaxation process proceeds from this Franck-Condon region. However, from the absence of emission, they inferred that instead a twisted biradicaloid geometry is reached after vibrational cooling into the first relaxed excited state. In addition, their calculations revealed a small $S_1 - T_1$ energy gap, for which reason Abraham and co-workers assumed that ISC leads to efficient emission quenching by a fast non-radiative deactivation.[393]

Finally, our results reveal some new aspects, from which another pathway can be derived. First, the fs-ns TA spectroscopy does not show any signal contribution which can be attributed to a triplet state. Since the ground-state bleach is fully recovered within a few picoseconds, which would also be unusual fast for a triplet state lifetime, it is not likely that the T_1 signal was just too weak for detection within this experiment, and second, we observed a very weak emission signal after excitation into the main absorption band, which also does not agree with the hypothesis of a non-radiative deactivation. From our results, it can be concluded that after excitation,

a TICT state $(\mathbf{6}^+)^*$ might be reached, which performs a fast deactivation into the ground-state within 1.4 ps accompanied by a weak emission. Then the longer lifetime τ_2 with 5.3 ps describes the vibrational cooling of a hot ground state by rotation around the C−C single bond along the PES to yield the initially thermalized ground-state structure.

Protonation of the Trop-DMA

In analogy to conformers $\mathbf{4}_\mathbf{B}^+$ and $\mathbf{5}_\mathbf{B}^+$, the positive charge is delocalized over the tropylium ring for compound $\mathbf{6}^+$, as verified by the potential surface map (in Figure 4.17). Therefore, it should be possible to protonate the nitrogen atom of the dimethylaniline moiety. Thus, a stepwise addition of TFA to a DCM solution of $\mathbf{6}^+$ yielded a decrease of the main absorption band at 590 nm, and an increased absorption intensity around 350 nm (see Figure 4.22).

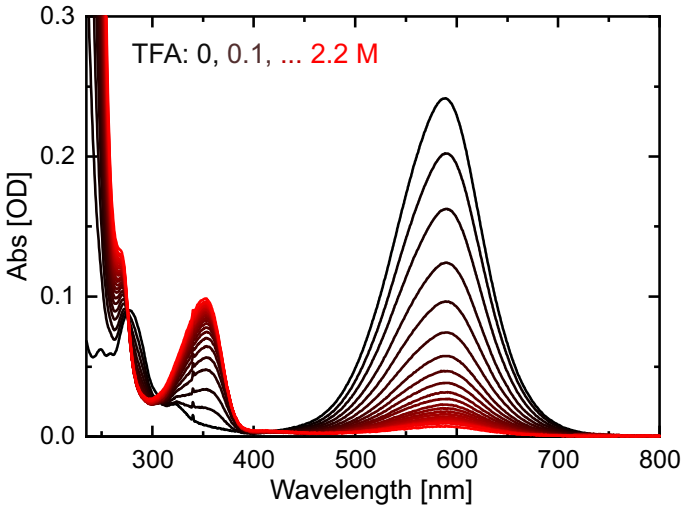

Figure 4.22: Absorption spectra of $\mathbf{6}^+$ in DCM with stepwise addition (+0.1 M) of TFA, yielding $\mathbf{6H}^{2+}$.

After excitation into this new absorption band, emission peaking at 410 nm could be detected, as represented in Figure 4.23a. The corresponding excitation spectrum fits the absorption spectrum very well. Furthermore, geometry optimizations indicated a twist angle φ of 44°, being larger than that of unprotonated $\mathbf{6}^+$, but much smaller than in the case of protonated compounds $\mathbf{4H}^{2+}$ and $\mathbf{5H}^{2+}$. The calculated vertical excitation energies of $\mathbf{6H}^{2+}$ consist of similar contributions like the experimentally observed spectrum (compare Figure 4.23), confirming the generation of $\mathbf{6H}^{2+}$ in DCM-TFA solution.

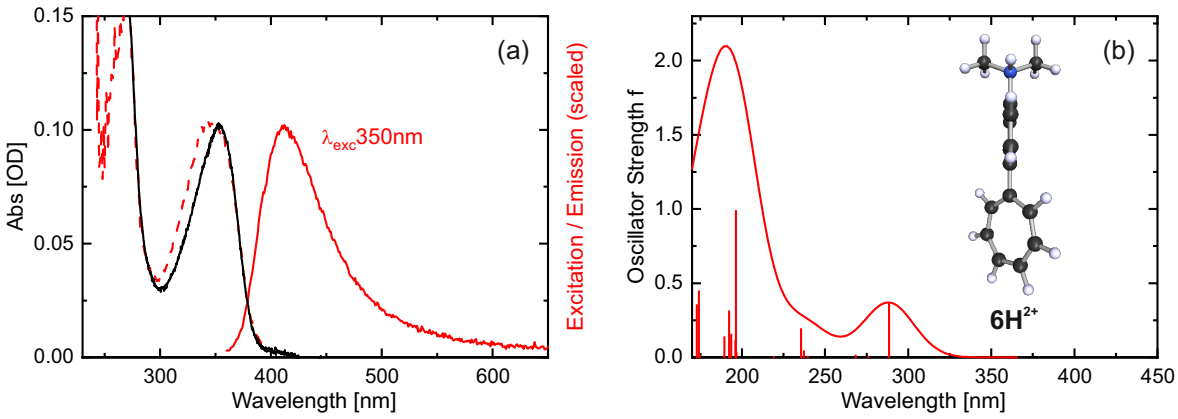

Figure 4.23: (a) Absorption spectrum of $\mathbf{6H^{2+}}$ in DCM-TFA solution (black) compared to the scaled emission spectrum recorded after 350 nm excitation (red-solid) and the corresponding excitation spectrum (red-dashed). (b) Computationally optimized ground-state geometry of $\mathbf{6H^{2+}}$ found by DFT/B3LYP/def2-TZVP level of theory, together with the vertical excitation transitions (ADC2/aug-cc-pVDZ) enveloped with a Gaussian function of 20 nm width at half maximum, yielding the UV-Vis spectrum.

Excitation with 350 nm light results in an emission band with a maximum at 410 nm. Similar to the results of $\mathbf{4H^{2+}}$, a prolonged decay time of this emission is expected. Therefore, ns-TCSPC traces after excitation with 370 nm light were recorded (see Appendix Figure B.15b). A global lifetime analysis yielded two time constants. The shorter one τ_1 falls below the IRF of $\sim$1 ns, but could be assigned to the emission of $\mathbf{6H^{2+}}$ in accordance with the corresponding DAS, while τ_2 of 3.8 ns could be attributed to the still unknown species emitting at 500 nm (compare Appendix Figure B.15c). The latter assignment was additionally confirmed by a time-resolved emission study on $\mathbf{6^+}$ in DCM after excitation at 405 nm , revealing a decay time of $\sim$3 ns for the 500 nm emission band (see Appendix Figure B.15a).

Ion-Pair Formation Favored by Addition of a Co-Salt

Furthermore, the influence of a co-salt regarding the spectral properties of $\mathbf{6^+}$ was investigated. The normalized absorption spectra detected after stepwise addition of tetra-n-butylammonium tetrafluoroborate (TBAB) to a solution of $\mathbf{6^+}$ in DCM show a small spectral blue shift (see Figure 4.24a). Since these changes are relatively small, the wavelength-shift of the absorption maximum of the $\pi - \pi^*$ band is plotted against the added TBAB concentration in Figure 4.24c, unveiling the same spectral behavior as already reported for similar aryl-tropylium ions.[387] Abraham *et al.* attributed the observed spectral changes of the intramolecular charge transfer

band to an increased ion-pair formation. They proposed that the electron acceptor strength of the tropylium part is decreased, due to the formed ion pair between the positively charged tropylium ring and the added counterions, which results in a blue shift of the charge transfer band. In contrast, they did not observe any spectral shift of the absorption bands below 350 nm by an increased TBAB concentration, since these bands correspond to transitions localized in the tropylium ring.

In the next step, we also recorded the emission spectra of $\mathbf{6}^+$ after excitation at 590 nm in dependence on the TBAB concentration, as shown in Figure 4.24b. By adding small salt con-

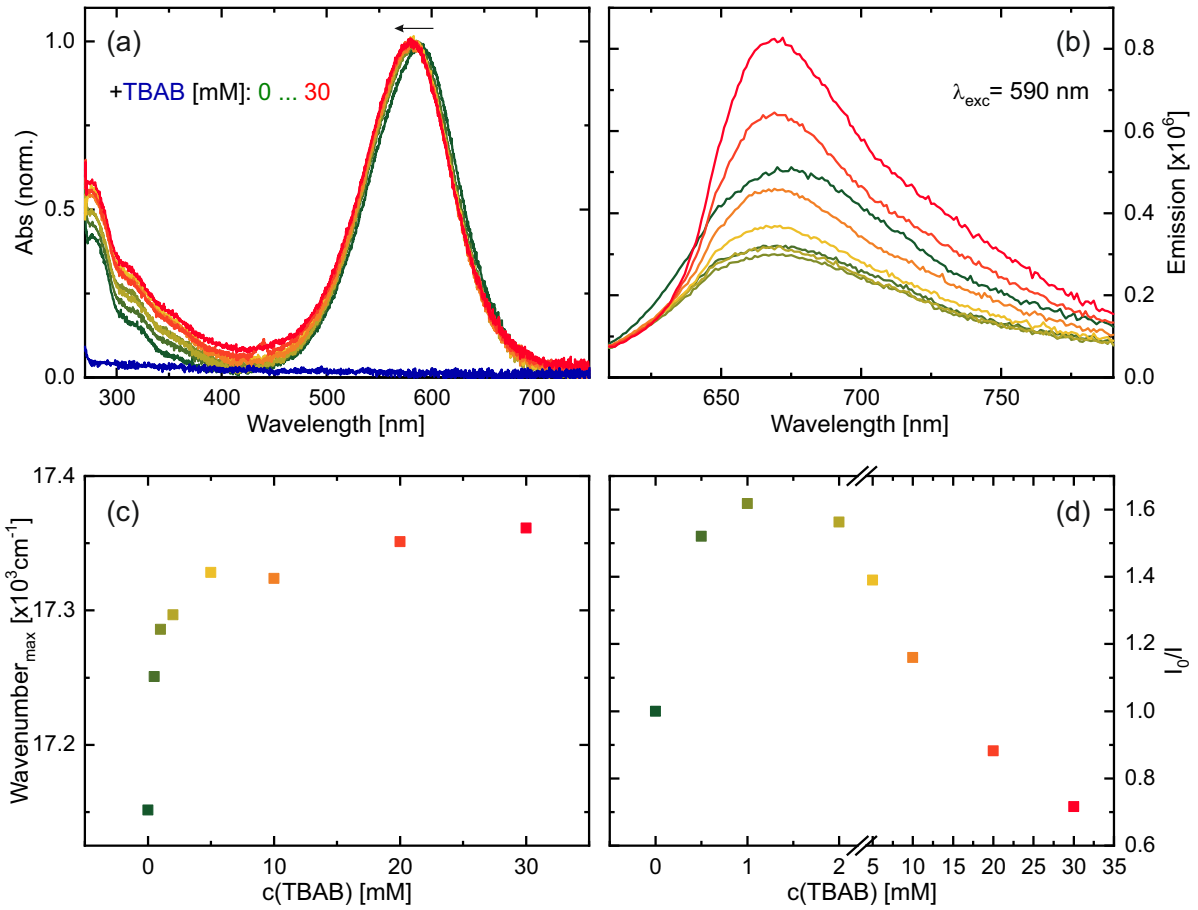

Figure 4.24: Influence of TBAB as co-salt on the spectral characteristics of $\mathbf{6}^+$ in DCM. (a) Normalized absorption spectra and (b) emission spectra detected after 590 nm excitation of $\mathbf{6}^+$ dissolved in DCM (20 µM) with additional TBAB amounts ranging from 0 mM up to 30 mM. The absorption spectrum of the neat TBAB dissolved in DCM is included in (a) as blue curve. (c) Wavelength of the absorption maximum corresponding to the $\pi - \pi^*$ band plotted in dependence on the TBAB concentration. (d) The quantum yield of $\mathbf{6}^+$, calculated on basis of the 670 nm emission band detected after 590 nm excitation, is plotted in dependence on the TBAB concentration, yielding a so-called Stern-Volmer plot.

centrations up to 1 mM, the emission intensity decreases, while the oppositely directed effect was observed for higher TBAB concentrations. The corresponding Stern-Volmer plot shows an emission quenching until a 1 mM TBAB concentration is reached (see Figure 4.24d). Due to the increased ion-pair formation between the tropylium cation and the TBAB anion, the amount of free $\mathbf{6}^{+}$ ions is reduced leading to a quenched emission, which agrees with the observations already reported for similar aryl-tropylium cations.[387] At even higher TBAB concentrations, it might be possible that the ions start to aggregate,[446;447] resulting in a reduced ion-pair affinity. If such an ion aggregated structure is formed in DCM solution, the deactivation of $\mathbf{6}^{+}$ *via* rotation around the single bond connecting both molecular parts might be restricted by this ion aggregated network. However, this hypothesis should be further verified by additional investigations, e.g. with diffusion ordered spectroscopy (DOSY) experiments to detect a possible complex formation or aggregation.

4.4 Conclusion and Outlook

This chapter focused on the photochemical investigation of differently substituted aryl tropylium cations. It could be shown on the compounds $\mathbf{1}^+$ to $\mathbf{3}^+$ (Section 4.3.1) that the alkyl chain length in the aniline moiety has a marginal effect on the photodynamics, although the excited state lifetime decreases in the order $\mathbf{1}^+ > \mathbf{2}^+ > \mathbf{3}^+$, which we attributed to the slightly different tilting and bending angles of the distinct tropylium cations. Furthermore, two stable ground-state conformers **A** and **B** were found by DFT calculations. Conformer **A** is characterized by a boat-shaped DBTrop-system and an out-of-plane tilted DMA unit, whereas the DBTrop in conformer **B** is more planar but slightly wavelike-shaped and consists of a pronounced twist between the DBTrop and the aniline part. Calculation of the electrostatic potential unveiled a different charge distribution within both geometries. In the case of **A**, the most positive region is localized at the DMA unit, resulting in a chinoidal structure. In contrast conformer **B** comprises the most positive part at the tropylium ring, which assists the aromaticity of the π-system. However, in the case of compounds $\mathbf{1}^+$ to $\mathbf{3}^+$, geometry **A** is energetically more favored in both crystal structures[440] and DCM solution. By fs-ns transient absorption spectroscopy combined with PES scans, it was possible to derive a potential relaxation pathway, which includes an excited state structure characterized by an additional 90°-twist within the DMA unit between the benzene ring and the dimethylamine substituent. A longer lifetime additionally indicated a further structural reorientation either yielding conformer **B** in the ground state or reaching a triplet state, before relaxing back into the initial ground-state.
For compounds $\mathbf{4}^+$ and $\mathbf{5}^+$ the situation changes (Section 4.3.2). Due to the sterical hindrance of the side groups, structure **B** is indeed characterized by a stronger tilting between both molecular parts in comparison to those of $\mathbf{1}^+$ to $\mathbf{3}^+$, but simultaneously becomes energetically more stable than **A**. As a consequence, the photochemical characteristics change distinctly, which is not only observable by the steady-state spectra, but rather by transient absorption and further protonation. Since in the case of structure **B**, the positive charge is delocalized over the tropylium ring system, the nitrogen within the DMA moiety can be (in contrast to compounds $\mathbf{1}^+$ to $\mathbf{3}^+$) protonated by addition of TFA to a DCM solution, yielding a characteristic double-band structure in both the absorption and emission spectra. Furthermore, fs-ns TA on $\mathbf{4}^+$ in DCM yielded a shorter time constant describing the decay of the TICT state, and long dynamics, whose lifetime exceeded the time window. Therefore, µs-TA was performed and indicated that the pKa value changes upon excitation, resulting in a protonation of $\mathbf{4}^+$ to $\mathbf{4H}^{2+}$ even within the excited state. Despite the absence of effective protonation of $\mathbf{1}^+$ by TFA in the ground state, the same excited-state dynamics of $\mathbf{1H}^{2+}$ in DCM-TFA solution could be observed by µs-TA. Excitation leads to

a charge transfer from the aniline moiety to the tropylium ring system making the protonation of the nitrogen possible. Therefore, we could show that those molecular species comprise both the properties of a TICT compound and a photobase.
Reduction of the tropylium ring system, as shown on compound $\mathbf{6}^{+}$ (Section 4.3.3), even results in varying photochemical properties. For $\mathbf{6}^{+}$ only one stable ground-state structure exists, with a much smaller tilting angle between both molecular parts. Thus, the π-system is enhanced over the DMA unit leading to red-shifted absorption and emission signals. Fs-ns TA showed very fast excited-state dynamics, where the TICT state is depopulated in 1.4 ps. Furthermore, effective protonation of $\mathbf{6}^{+}$ is also possible, due to the delocalization of the positive charge over the tropylium ring. In addition, we could show on the example of $\mathbf{6}^{+}$ that an increased ion-pair formation can be induced by a co-salt, resulting in emission quenching. However, if a distinct concentration of the co-salt is reached, an oppositely directed effect was observed, which might be caused by aggregation effects. In order to verify these observations, further investigations like DOSY experiments are planned.
Finally, within this thesis it was shown that small changes in the molecular constitution as well as the addition of different co-substrates in solution, like acids or further salts, have a high impact on the photochemistry. We found out that this effect mainly originates from different spatial configurations in dependence on the bulkiness of the substituents leading to the formation of individual conformers with varying photochemical properties. Thus, these mechanistic studies might contribute to improve already established applications or to develop new utilizations, like in synthesis where only a distinct conformeric species is required, by a selective substitution of the tropylium dyes to form only one specific conformation.

CHAPTER 5

Chiral Phosphoric Acid-Imine Complexes

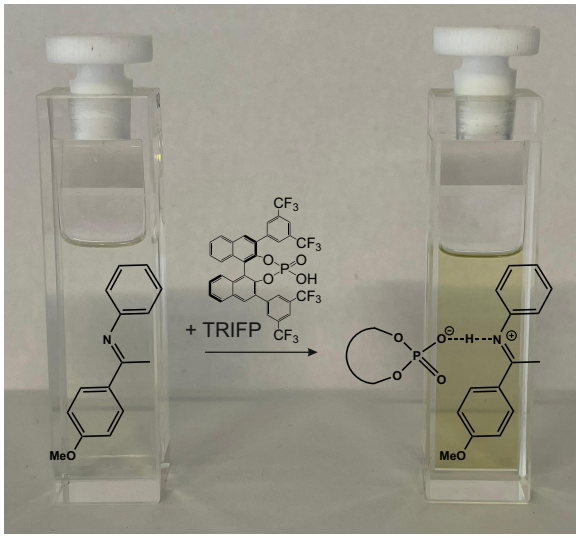

5.1 Introduction **116**

5.2 Experimental and Theoretical Approaches **119**

5.3 Results and Discussion **124**

5.4 Conclusion and Outlook **140**

Christian Scholtes synthesized all imine substrates. Sylvia Schlöglmann helped SW with absorption experiments performed at cryogenic temperatures, while Roger Kutta supported SW by fs-ns TA experiments.

5.1 Introduction

BINOL (1,1'-Bi-2-naphthol) derived chiral phosphoric acids (CPA) are known as efficient, asymmetric Brønsted acid catalysts in several enantioselective reactions.[72;73;448–450] The underlying principle involves the protonation *via* hydrogen-bonding of a substrate by the Brønsted acid, which results in an energetically lowering of the LUMO (Lowest Unoccupied Molecular Orbital) and thus, promoting the reaction with a nucleophile.[76] Furthermore, the versatility of Brønsted acid catalysis can be even more enhanced by additional binding sides within the catalyst, e.g. by introducing a Brønsted basic group, leading to supplementary substrate activation and orientation.[451]

Since the first report of Brønsted acid calaysts by Akiyama[75] and Terada,[452] differently 3,3'-substituted CPAs are developed and used in a huge variety of distinct organic syntheses like Mannich-type reactions,[453–455] Strecker-type reactions,[73;456], enantioselective additions,[457;458]

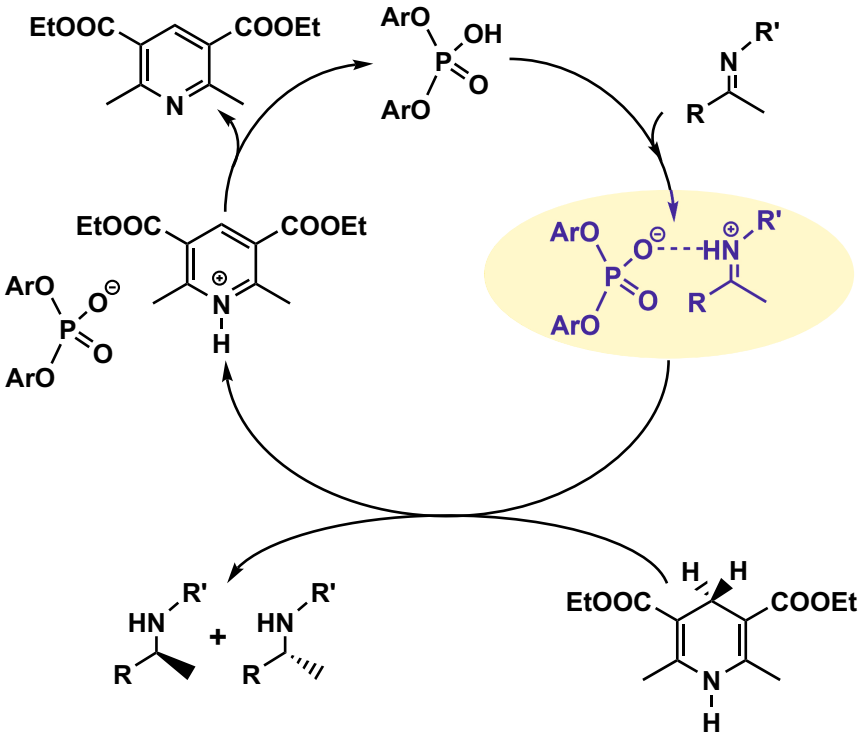

Figure 5.1: Catalytic cycle of the asymmetric transfer hydrogenation of imine substrates using a chiral phosphoric acid as catalyst and a Hantzsch ester as hydrogen source. The highlighted region displays the ion-paired CPA/imine complex, which was spectroscopically studied during this work.

hetero-Diels-Alder reactions,[459] Friedel-Crafts alkylations,[460–464], Pictet-Spengler reactions,[465] transfer hydrogenations[72;449;466] and reductive aminations.[448;467;468] The most common 3,3'-substituents are 2,4,6-triisopropylphenyl groups yielding the Brønsted acid catalyst 'TRIP', 3,5-bis(trifluoromethylphenyl) groups resulting in 'TRIFP', and triphenylsilyl groups leading to 'TiPSY'.[72;76;449] Those diverse substituents significantly impact both the reactivity and the stereoselectivity of the previously mentioned reactions,[72;448;449;466;469] just like the reaction environment.[72;74;77] Thus, several theoretical studies[470–476] were performed to unveil the involved intermediates and interactions which are responsible for the reactivity and enantioselectivity by correlating them to structural parameters, like the size and angle of the substrate binding pocket of the different CPAs or the rotational barrier of the 3,3'-substituents.[471]

So far, experimentally gained information about the hydrogen-bonded CPA/substrate complex are rather low. However, the most mechanistic studies are based on the transfer hydrogenation of imines[450;466;468;477] as model system, like shown in Figure 5.1. Thereby, a Hantzsch Ester (HE, 1,4-dihydropyridine ester) acts as hydrogen source, since it is known as mild reducing agent.[72;449;478] During this reaction, a binary complex by the imine and CPA is proposed (marked by the yellow area in Figure 5.1), acting as precatalytic intermediate, and is followed by a ternary complex formation after Hantzsch ester addition.[72]

The first experimental structural analysis of the CPA/imine complex was performed by X-ray crystallography[448;479] and later further improved by various NMR spectroscopy methods.[77;78;480–487] It could be shown that both types of complexes are coexisting in the reaction mixture, namely ion-paired and hydrogen-bonded CPA/imine complexes,[480] whereas the ion-paired one is the dominating species,[78] which was found to be the key part of the transfer hydrogenation.[77] Moreover, those investigations unveil four different binding situations in the binary

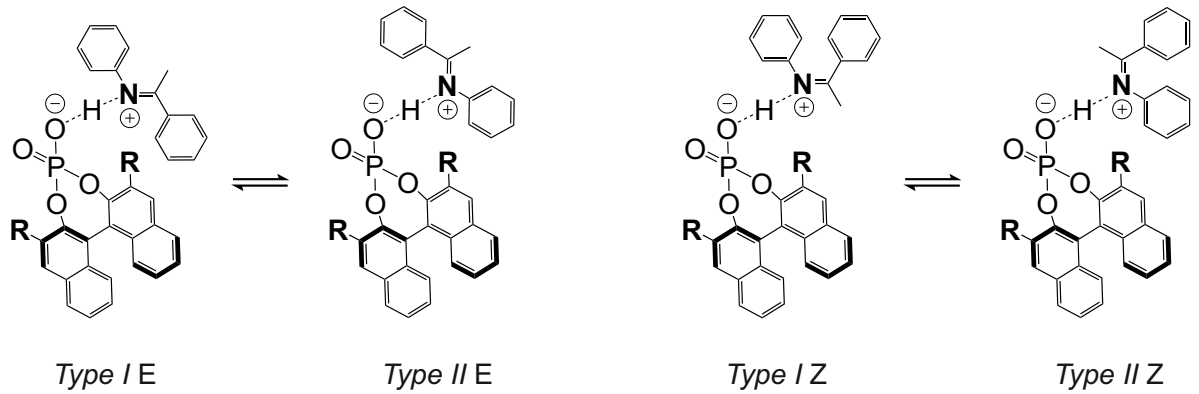

Figure 5.2: Structures of the four distinguishable binary CPA/imine complexes. Both E- and Z-type imines are characterized by a high mobility within the complex, resulting in reorientation between *Type I* and *Type II*. Figure drawn according to Ref. [483].

ion-pair complex,[78;482] which was already predicted by quantum chemical calculations for the ternary CPA/imine/nucleophile complex.[488] The four core structures of the binary CPA/imine complex assigned to '*Type I* E', '*Type II* E', '*Type I* Z' and '*Type II* Z' are shown in Figure 5.2. While the E-imine complex is the energetically favorable one,[448] the Z-imine complex was assumed to be the more reactive type.[453;488] Furthermore, all four binary complex structures contain a strong and highly covalent hydrogen-bond character.[78] In addition, both imine types show a high mobility within the ion-paired complex. Even at 180 K, the imine can change its orientation inside the complex.[482] While in the E-type complex the imine reorientates *via* tilting, the Z-imine has a reduced steric hindrance in the complex, so that a rotation of the imine is possible additionally to tilting, which finally results in the loss of asymmetry.

For the ternary CPA/imine/nucleophile complex, which is formed after Hantzsch ester addition, a 'three-point interaction model' is predicted by theoretical investigations.[488–490] If the CPA comprises both an acidic and a basic group, it can act as hydrogen-bond donor regarding the imine and simultaneously as hydrogen-bond acceptor for the nucleophilic Hantzsch ester, resulting in two hydrogen bonds between the catalyst and the substrates. Additionally, a third interaction between the imine and the Hantzsch ester is assumed, due to steric effects. Thus, a rigid preorganized structure of the ternary CPA/imine/HE complex is expected, yielding to a concerted reaction mechanism, which might be responsible for the experimentally observed high enantioselectivity. Such a binding situation should be possible for both E- and Z-imine, resulting in the formation of different amine enantiomers.[470;488–491]

The goal of this work was to investigate the isomerization process of the imine in the reaction mixture with time-resolved absorption spectroscopy. Despite the theoretical calculations and NMR studies regarding structural properties and hydrogen-bond behavior within the binary and ternary complexes, the reaction mechanism is so far not fully understood. Especially the research regarding the imine isomerization in presence of the phosphoric acid or both CPA and Hantzsch ester is still underrepresented. Therefore, sub-s to min TA at cryogenic temperature (Section 5.3.1 and 5.3.2) and fs-ns TA at room temperature (Section 5.3.3 and 5.3.4) were performed. The E/Z isomerization for three differently substituted imines could be observed at cryogenic temperatures. Furthermore, the photochemical behavior of the pure substrates TRIFP (CPA) and tBu-HE were studied, before the binary reaction mixture of imine and phosphoric acid forming the ion-paired complex were investigated (Section 5.3.2). To evaluate the experimental data, additionally some quantum chemical calculations were carried out on the experimentally used reactants and later also for further imine substrates, which were predicted as suitable imine species for further experimental investigations.

5.2 Experimental and Theoretical Approaches

The underlying working principle of the used setups are previously explained in Chapter 2. In this section, the practical implementation in the laboratory is described (Section 5.2.1 and 5.2.2). Especially the difficulties to work at cryogenic temperatures under inert conditions and with high sample concentrations are discussed, which necessitated the enhancement of the subs to min TA setup including the cuvette design several times (see Section 5.2.2). Ultimately, this section ends with the description of the used theoretical methods and parameters (see Section 5.2.3).
The differently substituted imine samples were synthesized and characterized by Christian Scholtes and co-workers of the working group of Prof. Dr. Ruth Gschwind at the University of Regensburg. The phosphoric acid (R)-3,3'-Bis-[3,5-bis-(trifluormethyl)-phenyl]-1,1'-binaphthyl-2,2'-diyl-hydrogenphosphat (TRIFP; Sigma Aldrich, 95 % purity), the Hantzsch ester di-tert-butyl 2,6-dimethyl-1,4-dihydropyridine-3,5-dicarboxylate (HE; Sigma Aldrich, 97 % purity), the solvent dichlormethan (DCM; Sigma Aldrich, anhydrous, $\geq$99.8 %, containing 40-150 ppm amylene as stabilizer) and the acids trifluoro acetic acid (TFA, Riedel-de Haën), formic acid (Sigma Aldrich), and acetic acid (Sigma Aldrich) were used without further purification.

5.2.1 fs-ns Transient Absorption Spectroscopy

For studying the excited-state absorption behavior of the imines and the TRIFP/imine mixtures, the same fs-ns TA setup which is already explained in Section 3.2.1 was used, but with some modifications. The here used setup does no longer comprise prism compressors and the delay stage generating a temporal delay up to 4 ns was replaced by another one (Zaber, X-LRT1000AL-AE53C), with which a time delay up to 6 ns can be detected. Furthermore, 305 nm pulses were used for excitation of the sample, whose concentration was set between 0.2 and 0.3 OD at 305 nm. The sample was pumped from an external reservoir through a 500 µm cuvette (Starna).

5.2.2 ms-min Transient Absorption Spectroscopy at Cryogenic Temperatures

For monitoring both the steady-state absorption and time-resolved TA at cryogenic temperature, a UV-Vis absorption spectrometer (Cary 60, Agilent) was combined with a cryostat (UNISOKU Co., CoolSpek USP-203) and in the case of TA additionally equipped with a 365 nm-LED (ThorLabs, M365D1 at 0.7 A and M365LP1 at 1 A) as excitation source. However, firstly the construction of this setup to generate reproducible measurement conditions and secondly the design of the cuvette, which had to fulfill several criteria due to the sample's characteristics, were rather challenging.
In order to generate an ion-paired complex within the binary TRIFP/imine mixture in adequate amounts, a concentration of 50 mM of each component has to be used. Therefore, a cuvette with an optical path length of 10 µm was used to reach an appropriate optical density of the sample. To the best of our knowledge, a cuvette with an even smaller optical path is not commercially available. The first measurements were performed with a 10 µm cuvette (Starna) consisting of two quartz glass plates with a hollow sphere in one plate, and ultimately both glass plates are pushed together by a metal bracket (compare model **A** in Figure 5.3 without the metal bracket). However, this cuvette design was not tight enough, for which reason the strongly volatile solvent DCM could evaporate, resulting in a crystallization of the substrates, as shown on the example of **A** in Figure 5.3. Especially the N_2-flow within the cryostat accelerated the solvent evaporation.

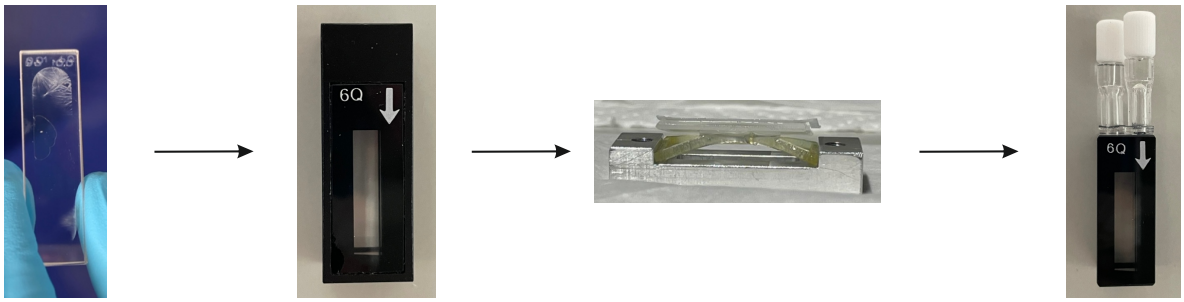

Figure 5.3: Development of a suitable cuvette design, which fulfills all requirements given by the sample's characteristics.

Additionally to this solvent evaporation, further sample specific requirements had to be fulfilled. The imine substrates can react with water impurities, which are mainly caused by the hygroscopic phosphoric acid, to an unwanted side product (*vide infra*, Section 5.3.2), for which

reason water-free conditions had to be achievable. Furthermore, the Hantzsch ester is sensitive to molecular oxygen performing an unwanted photoreaction (*vide infra*, Section 5.3.1), which additionally requires O_2-free conditions. Therefore, it is necessary to create a closed system within the cuvette.

Thus, for further experiments a 10 µm flow cuvette (Starna) was tested. It consists of one quartz cuvette covered by a metal frame (model **B** in Figure 5.3), which acts as connection for the tube system to the external reservoir. During this work, this cuvette was used in a stationary way without sample exchange, for which reason the openings on top were sealed with two setscrews. However, those types of cuvette, which are made of different materials are not convenient for low temperature experiments. Their expansion behavior due to temperature changes is a material-specific value and thus, rather different for quartz glass and metal materials. Therefore, the low temperature within the cryostat caused some tensions between the cuvette and the metal frame, which ultimately resulted in a cracked and partially broken cuvette core making it useless for further experiments.

Afterwards, we designed a cuvette model on our own (see model **C** in Figure 5.3; note that only one half of the cuvette is shown here). It comprises a metal frame which can be tightened by two screws. Two rubber spacer between the metal frame and the quartz plates avoids some tensions of the different materials due to temperature changes. The optical path length of the cuvette can be varied by a teflon spacer between the glass plates. The appropriate working of the cuvette was tested with different solvents, like methanol, acetonitrile and DCM. With the first two solvents a smooth functioning of the cuvette could be achieved even at low temperatures. Only DCM caused strong deformation of the rubber during the preparation, making the constitution of both cuvette parts impossible (compare model **C** in Figure 5.3).

Finally, a fourth 10 µm cuvette was designed by a combination of the quartz glass core of model **B** with two glass tubes attached at the openings to enable the filling of the cuvette with the sample (compare model **D** in Figure 5.3). Furthermore, the additional glass tubes can be covered by screw caps, which ensures a closed system to work under O_2-/H_2O-free conditions after a sample preparation in the glove box. The smaller outer dimensions of the cuvette due to omission of the metal frame are compensated by a PTFE bracket, which can be placed around the cuvette and ensures a precise placement within the cryostat (not shown in Figure 5.3).

Furthermore, it was not possible to use the same perpendicular arrangement of the LED compared to the absorption spectrometer's detection pathway as already described in Section 3.2.3, due to the very small optical path of the cuvette. Therefore, the direction of the illumination light had to be arranged parallel in regard to the detection pathway of the spectrometer. The free space between the cryostat and the spectrometer was too small to place one of the available

fibers in this gap. Thus, a construction comprising a D-mirror was installed at the outside of the cryostat so that the emitted light of the perpendicularly arranged LED can reach the sample (see Figure 5.4). It had to be ensured that the installed mirror does not block the detection pathway, which can be achieved by a small angle within the illumination pathway resulting in a deviation of the parallel arrangement of both pathways to each other. The angle should be as small as possible for which reason a D-mirror was used, in order to ensure that the sample volume is still illuminated as constantly as possible. Within this arrangement the illumination light or its scattering light just reaches the detector, which would cause a destruction of the detection unit. Therefore, the entrance slit of the detector was covered during illumination.
So far, only the challenges regarding the here investigated substrates are explained. However, there are also some difficulties using the cryostat, that are independent of the studied molecular system. Thus, we observed a constantly growing baseline offset over longer measuring periods, which could be attributed to sublimating H_2O below 0° and additionally CO_2 below -79°C. In order to prevent such sublimations at the cuvette windows, a relatively strong N_2 gas flow is recommended. Moreover, the difference in altitude between the cryostat itself and the liquid

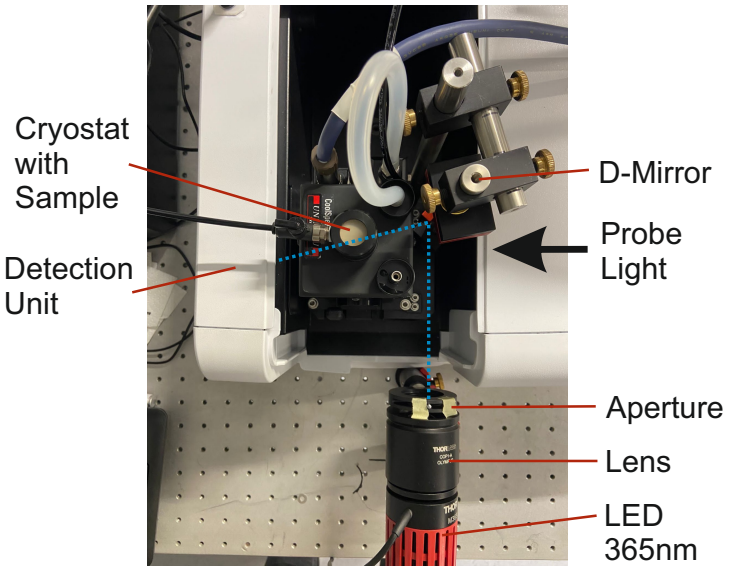

Figure 5.4: Picture from the UV-Vis absorption spectroscopy setup implemented in the laboratory using a cryostat to generate cryogenic temperatures. The 365 nm-LED is placed outside the absorption spectrometer within a perpendicular arrangement to the probe light path of the spectrometer. The illumination light is directed onto the sample within the cryostat *via* a D-shaped mirror. During illumination the 365 nm light has to be blocked behind the cryostat to avoid damages at the detector. Note that this blocker as well as the additional components of the cryostat, like the temperature controller and the liquid N_2-reservoir are not included in this representation.

N_2-reservoir has to be big enough in order to ensure a constant delivery of the liquid nitrogen at the cryostat. Additionally, the liquid N_2-reservoir should always be kept as full as possible, in order to ensure constant cooling at a distinct temperature. Otherwise the flow path within the cryostat is somewhere freezing up inhibiting a sufficient flow of the liquid nitrogen, which finally results in drastic temperature changes during the measurement.

5.2.3 Quantum Chemical Calculations

Theoretical calculations on the imine substrates were done using the Turbomole package[425;426] *via* the graphical user interface TmoleX. For ground-state geometry optimizations density-functional theory (DFT) with the functional B3LYP[173;175] and the basis set def2-TZVP[271;272] were used. Furthermore, vibrational frequency calculations were performed for all optimized structures to verify the ground-state affiliation, before the first 20 vertical excitation energies were determined by TD-DFT/CAM-B3LYP/aug-cc-pVDZ level of theory.[427–429;492] By combining them with Gaussian functions, the UV-Vis absorption spectra corresponding to the different imine isomers were obtained. In the case of para-methoxy-imine, additionally relaxed potential energy surface (PES) scans for the ground and first excited state were modeled using MP2/ADC2 with the cc-pVDZ basis set,[427] respectively.

5.3 Results and Discussion

5.3.1 Ground-State Dynamics of the Pure Substrates

Photochemistry of Imines at Cryogenic Temperatures

In the beginning, all necessary substrates were characterized by steady-state absorption spectroscopy under illumination, before the investigation of the substrate mixtures was started. For that, overall three differently substituted imine reactants were studied, namely the (E)-1-(naphthalene-2-yl)-N-phenylethan-1-imine (para-naphthalene-imine, **1**), the (E)-1-(4-methoxyphenyl)-N-phenylethan-1-imine (para-OMe-imine, **2**) and the (E)-1-(4-nitrophenyl)-N-phenylethan-1-imine (para-NO_2-imine, **3**).
The absorption spectrum of para-naphthalene-imine (**1**) dissolved in DCM consists of two double-band structures peaking around 280 nm and 340 nm (see black curve in Figure 5.5a). Additionally, a third absorption band at 250 nm could be observed, but the sample's concentration was too high to resolve this band completely. In order to observe the isomerization process from E to Z, the sample was illuminated with 365 nm light for a certain time (red curve in Figure 5.5a). Since the back-relaxation of the Z-imine was expected to proceed on a ps-time scale, the solution was cooled down to -80°C during the whole experiment to slow down the kinetics. This enabled detection of the isomerization-induced spectral changes with an UV-Vis absorption spectrometer, which requires about 27 s to monitor the full spectral range from 190 nm up to 1100 nm. Thus, we could find out that the Z-conformer of substrate **1** shows a higher extinction coefficient below 230 nm compared to its E-analogue. However, above 230 nm the absorption intensity slightly decreased under illumination. These spectral changes were fully reversible under dark conditions even at -80°C, as indicated by an isosbestic point at 235 nm in Figure 5.5b. The absorption spectra corresponding to the E- and Z-conformer of imine **1** were also estimated by TD-DFT calculations. The vertical excitation energies enveloped by Gaussian functions are included in Figure 5.5c in blue and orange for **E-1** and **Z-1**, respectively. Both spectra are relatively similar. They mainly differ by a blue-shift of the Z-imine compared to the E-type imine. The experimentally gained UV-Vis spectrum is also included as blue-dashed curve for comparison reasons. The main absorption band at 250 nm can be attributed to the $\pi - \pi^*$ transition, whereas the branch around 340 nm corresponds to the $n-\pi^*$ transition. The double-peak band around 280 nm could not be modeled by these calculations, but is presumably caused by naphthalene. It is already reported in literature that the UV-Vis absorption spectrum of naphthalene consists of a vibrational fine structure,[493–497] which perfectly matches the structured absorption

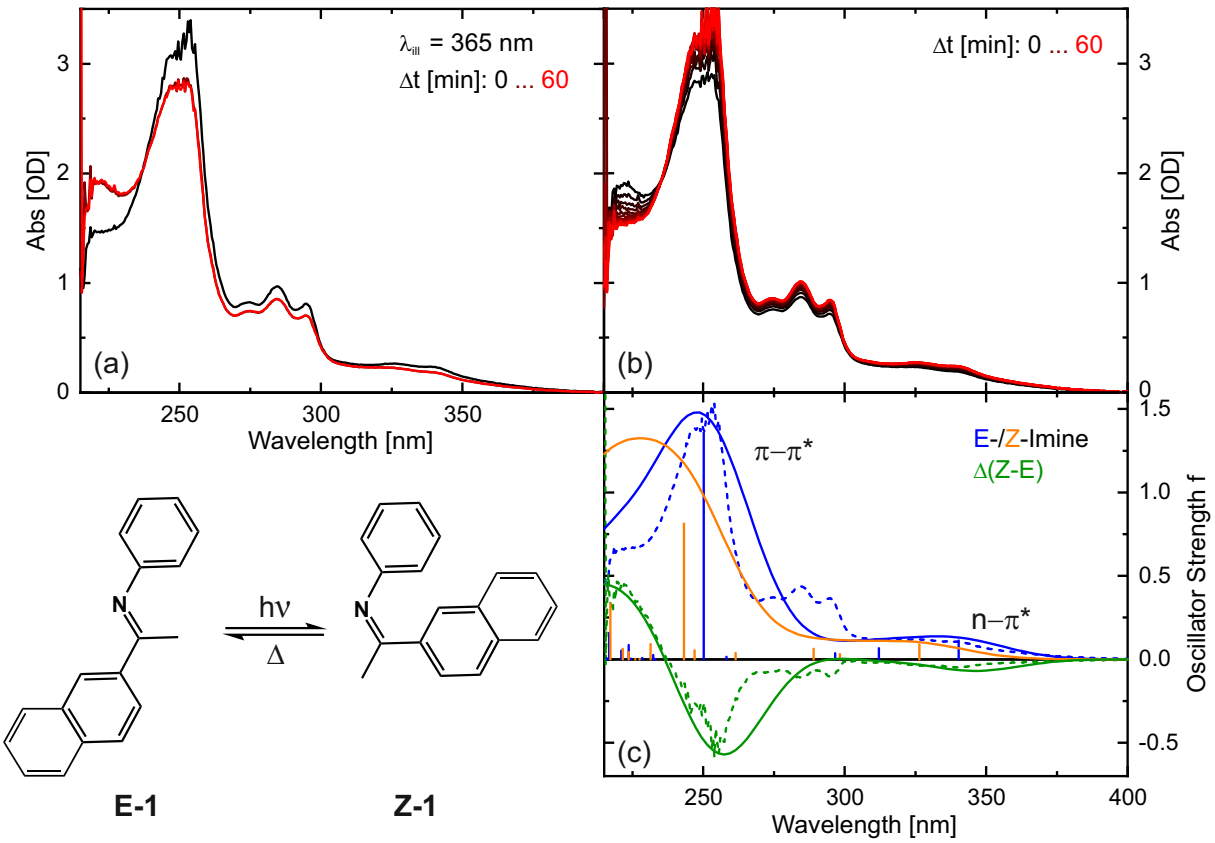

Figure 5.5: Absorption characteristics of the E- and Z-conformer of naphthalene-imine **1**. (a) The steady-state UV-Vis absorption spectrum of **1** in DCM at -80°C is shown in black. Illumination with 365 nm light causes spectral changes due to isomerization from E to Z as displayed by the red curve. (b) Back-relaxation in the dark at -80°C until the initial spectrum is reached as shown by the red curve. (c) The calculated absorption spectra of both optimized ground-state structures (TD-DFT/CAM-B3LYP/aug-cc-pVDZ; blue: **E-1**, orange: **Z-1**) are compared to the experimentally detected and scaled absorption spectrum of **1** in DCM, corresponding to the E-conformer (blue-dashed curve; identical to the black spectrum in (a)). The calculated oscillator strengths at the corresponding transition energies are given as stick spectrum convoluted each with a Gaussian of a 15 nm width at half maximum. Both calculated spectra are blue-shifted compared to the experimental spectra, for which reason an empirical correction of 0.25 eV was applied to the calculations. Furthermore, the difference between the blue and orange spectra was calculated and included as green-solid curve, in order to compare it with the difference (green-dashed) drawn from the black and red spectra shown in (a).

and around 280 nm in Figure 5.5a and b.

Since the steady-state absorption spectrum of the Z-type naphthalene-imine was not directly observable from the experimental data, because e.g. the red curve in Figure 5.5a is mainly due to E-imines and a small amount of Z-conformers, the difference between the spectra before illumination and after reaching the photostationary equilibrium after constant illumination is

calculated and shown as green-dashed curve in Figure 5.5c. Additionally, the difference between the calculated spectra of the E- and Z-imine was drawn for comparison reasons (solid green curve in Figure 5.5c). Both difference spectra contain similar contributions, namely two negative areas around 250 nm and 320 nm and a positive feature in the UV region. Only the double-band structure at 280 nm does not match the calculations as already discussed previously. Thus, it can be concluded, that the experimentally observed changes are caused by the isomerization from **E-1** to **Z-1**.

The absorption spectrum of para-methoxy-imine (**2**) in DCM comprises a band at 270 nm with a branch at the lower-frequency edge (black curve in Figure 5.6a). After 10 min of illumination at 365 nm, a photostationary state was reached, indicating an increased absorption around 240 nm due to Z-imine formation. Equivalent to substrate **1**, the intensity above 250 nm decreases (red curve in Figure 5.6a). Without constant illumination, the isomerization was again fully reversible at -80°C, as shown on the back-relaxation providing three isosbestic points at 215 nm, 225 nm and 260 nm in Figure 5.6b. However, the spectral changes of the E/Z-isomerization is rather small below 225 nm.

The TD-DFT calculations, yielding the absorption spectra of **E-2** and **Z-2** (blue and orange in Figure 5.6c, respectively) are compared to the measured one corresponding to the E-type imine in DCM. Both experimental and calculated spectra are nearly identical, comprising the n$-\pi^*$ branch at the red edge of the main $\pi - \pi^*$ excitation band. Furthermore, the difference spectrum of the theoretically obtained E-/Z-imine absorptions are compared to the one calculated from the absorption spectra before and after constant illumination (black curve subtracted from red curve which were represented in Figure 5.6a). Both difference curves (included as solid and dashed green lines in Figure 5.6c) comprise equivalent contributions and thus, indicates the isomerization from **E-2** to **Z-2**.

The absorption behavior of para-nitro-imine (**3**) is very similar to those of imine **2**, but shows a slight red-shift of the whole spectrum. Thus, the main absorption band is peaking at 280 nm and the shoulder at the red edge shows a weak absorption beyond 400 nm (see black curve in Figure 5.7a) in contrast to sample **1** and **2**, which do not absorb above 400 nm. Under constant illumination with 365 nm light the same spectral changes are observed as previously described, namely a decrease in absorption above 265 nm and a small increase around 245 nm. However, additionally to the absorption intensity change, a small spectrally blue-shift especially of the main absorption bands above 265 nm was observable (see red curve in Figure 5.7a). Furthermore, it should be noted that the photostationary equilibrium was reached already after 10 s of illumination, which however can be attributed to a significantly increased light intensity (used LED: M365LP1) compared to this used for the observation of the isomerization of imine **1** and

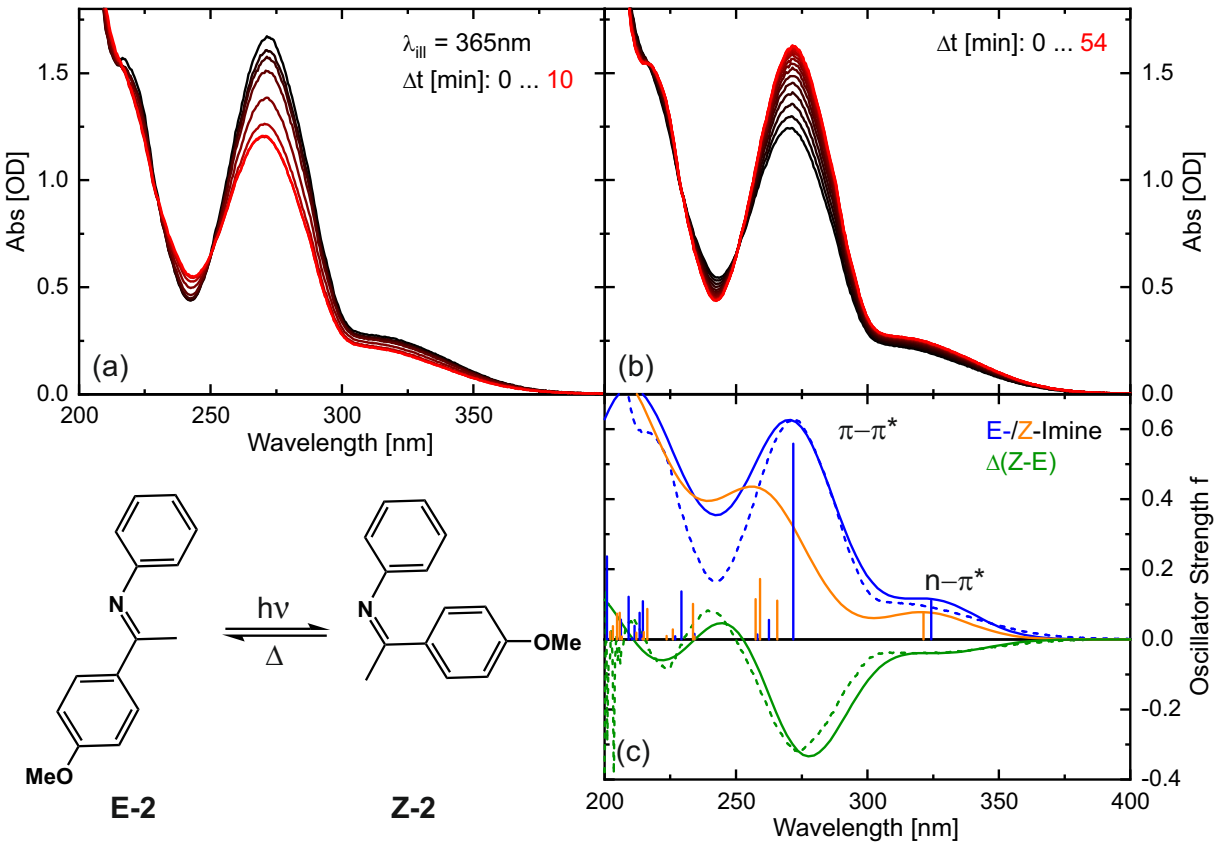

Figure 5.6: Absorption characteristics of the E- and Z-conformer of para-methoxy-imine **2**. (a) The steady-state UV-Vis absorption spectrum of **2** in DCM at -80°C is shown in black. Illumination with 365 nm light causes spectral changes due to isomerization from E to Z as displayed by the red curve. (b) Back-relaxation in the dark at -80°C until the initial spectrum is reached as shown by the red curve. (c) The calculated absorption spectra of both optimized ground-state structures (TD-DFT/CAM-B3LYP/aug-cc-pVDZ; blue: **E-2**, orange: **Z-2**) are compared to the experimentally detected and scaled absorption spectrum of **1** in DCM, corresponding to the E-conformer (blue-dashed curve; identical to the black spectrum in (a)). The calculated oscillator strengths at the corresponding transition energies are given as stick spectrum convoluted each with a Gaussian of a 15 nm width at half maximum. Both calculated spectra are blue-shifted compared to the experimental spectra, for which reason an empirical correction of 0.25 eV was applied to the calculations. Furthermore, the difference between the blue and orange spectra was calculated and included as green-solid curve, in order to compare it with the difference (green-dashed) drawn from the black and red spectra shown in (a).

2 (used LED: M365D1).

Again the back-relaxation was monitored at -80°C without illumination, resulting in three isosbestic points at 220 nm, 235 nm and 265 nm, and therefore, representing a fully reversible isomerization process (Figure 5.7b). The calculated UV-Vis spectrum of **E-3** also models the experimentally detected one very well (solid and dashed blue curves in Figure 5.7c, respectively).

Furthermore, the same difference spectra were calculated as done two times before for imines **1** and **2** (included as green curves). Both difference curves are nearly identical, which indicates the isomerization between **E-3** and **Z-3**.

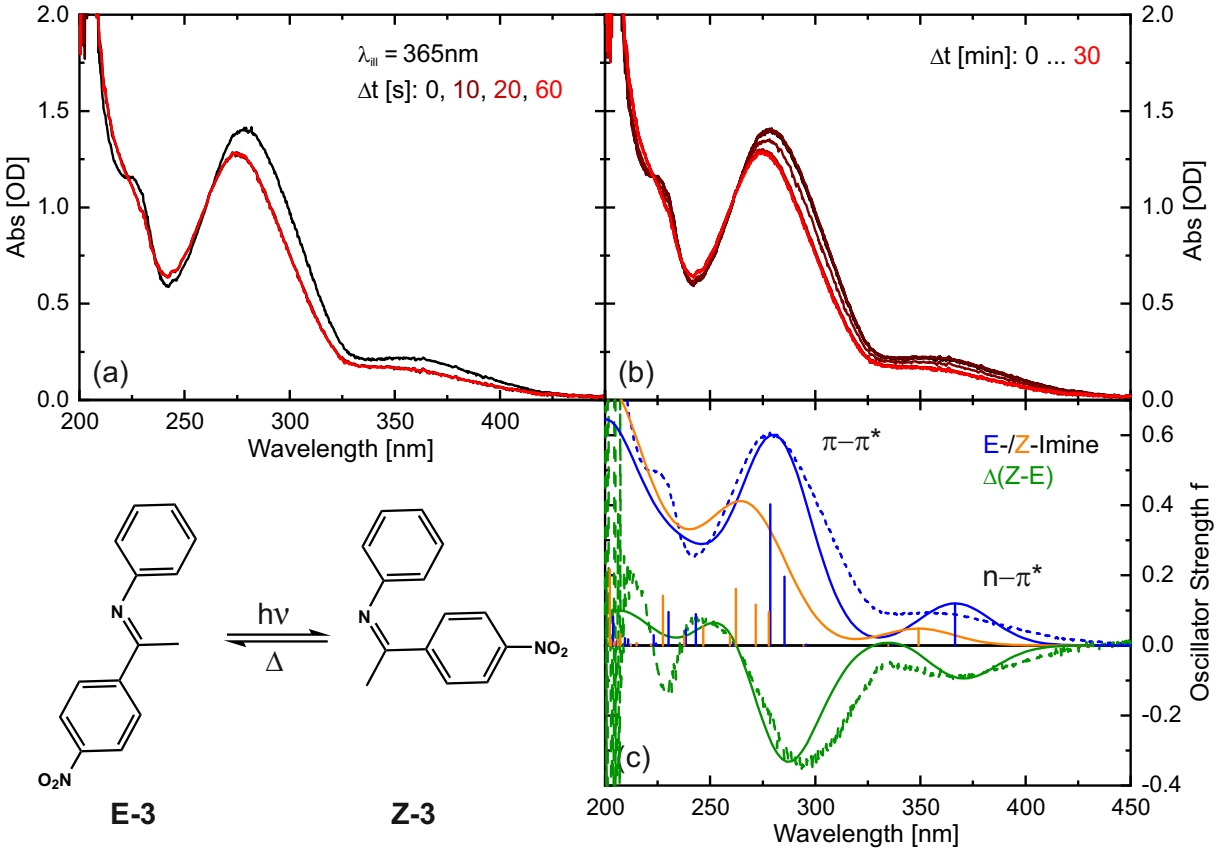

Figure 5.7: Absorption characteristics of the E- and Z-conformer of para-nitro-imine **3**. (a) The steady-state UV-Vis absorption spectrum of **3** in DCM at -80°C is shown in black. Illumination with 365 nm light causes spectral changes due to isomerization from E to Z as displayed by the red curve. (b) Back-relaxation in the dark at -80°C until the initial spectrum is reached as shown by the red curve. (c) The calculated absorption spectra of both optimized ground-state structures (TD-DFT/CAM-B3LYP/aug-cc-pVDZ; blue: **E-3**, orange: **Z-3**) are compared to the experimentally detected and scaled absorption spectrum of **1** in DCM, corresponding to the E-conformer (blue-dashed curve; identical to the black spectrum in (a)). The calculated oscillator strengths at the corresponding transition energies are given as stick spectrum convoluted each with a Gaussian of a 15 nm width at half maximum. Both calculated spectra are blue-shifted compared to the experimental spectra, for which reason an empirical correction of 0.25 eV was applied to the calculations. Furthermore, the difference between the blue and orange spectra was calculated and included as green-solid curve, in order to compare it with the difference (green-dashed) drawn from the black and red spectra shown in (a).

Photochemistry of the Chiral Phosphoric Acid TRIFP at Cryogenic Temperatures

The photochemical behavior of the pure chiral phosphoric acid TRIFP (**4**) was also investigated before studying the mixture. Its absorption spectrum in DCM solution is shown in Figure 5.8, consisting of two main absorption bands at 220 nm and 255 nm accompanied by a structured branch at the red edge absorbing below 350 nm. Since the CPA/imine mixture was excited at 365 nm and the used LED has a certain spectral width, it was investigated if the blue branch of the LED has also an influence on the pure catalyst TRIFP. However, as evident from Figure 5.8, the phosphoric acid is photostable under irradiation with 365 nm light at the given time resolution, meaning that there might be some excited-state dynamics which are not detectable by the used spectrometer. The small intensity decrease over time can be attributed to a decomposition of the catalyst due to irradiation with light. Finally, it was concluded that the spectral properties of the pure TRIFP in DCM can be assumed as constant under these measurement conditions.

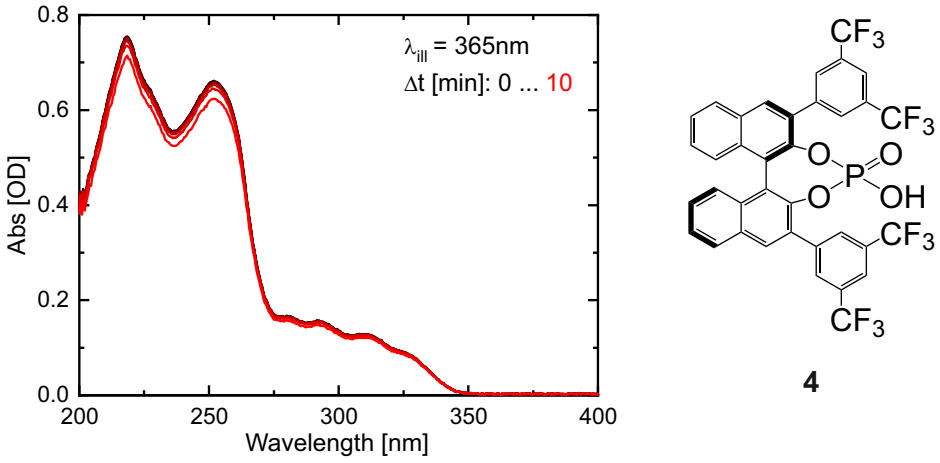

Figure 5.8: Steady-state absorption spectra of TRIFP (**4**) in DCM at -80°C. Illumination with 365 nm light does not induce any spectral changes, except of a slight intensity decrease due to decomposition of the sample.

Photochemistry of the Hantzsch Ester at Cryogenic Temperatures

Ultimately, also the photochemical behavior of the pure Hantzsch ester **5** dissolved in DCM was studied. The steady-state absorption spectrum before illumination consists of a relatively broad absorption band at 360 nm and two peaks around 230 nm and 250 nm (see black curve in Figure 5.9). Illumination with 365 nm ligth results in the formation of a stable photoproduct mainly absorbing around 280 nm (red curve). Already after 5 min of irradiation a big amount

of the initial substrate is converted.

This light induced reaction can be attributed to the photooxidation of the Hantzsch ester in presence of oxygen (O_2).[498–502] Thus, to ensure that the Hantzsch ester can act as reduction agent within the catalytic cycle, this unwanted oxidation of the Hantzsch ester needs to be avoided, for which reason oxygen-free conditions must be achievable for the investigations of the ternary CPA/imine/HE complex.

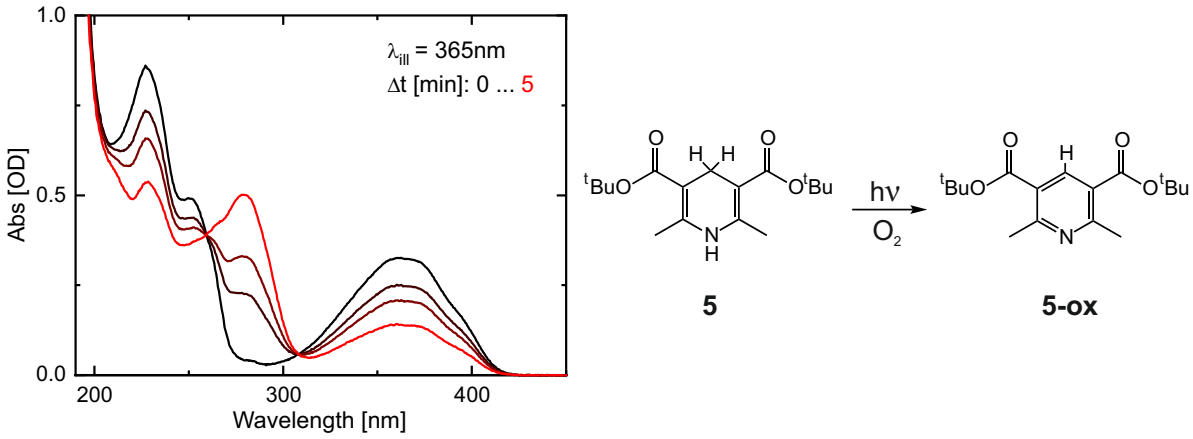

Figure 5.9: UV-Vis absorption spectra of the tert-butyl-Hantzsch ester (**5**) dissolved in DCM and measured at -80°C. Illumination at 365 nm result in significant spectral changes, due to a photooxidation by molecular oxygen (O_2).

5.3.2 Ground-State Dynamics of Binary Mixtures

After investigating the pure substrates, we studied the photochemistry of the binary mixtures consisting of TRIFP and the imine **1** or **2** in a 1:1 concentration ratio. First of all, the sample solution of the imine dissolved in DCM turns from colorless or light yellow (depending on the used imine reactant) into an intensive yellow color after addition of the phosphoric acid, which indicates the complex formation. The measured absorption spectra of TRIFP/**1** and TRIFP/**2** in DCM are represented in Figure 5.10. For comparison, the pure substrate spectra are also included, since each absorption spectrum of the mixture results from an equilibrium between the single molecular species and those forming the binary complex. In order to visualize which contributions are specifically caused by the ion-paired complex, the difference between the spectrum of the mixture and the single component spectra was drawn for both solutions and included as dashed-green curve in Figure 5.10. Both complex spectra have in common absorption features in the visible range with maxima around 340 nm. While the absorption of

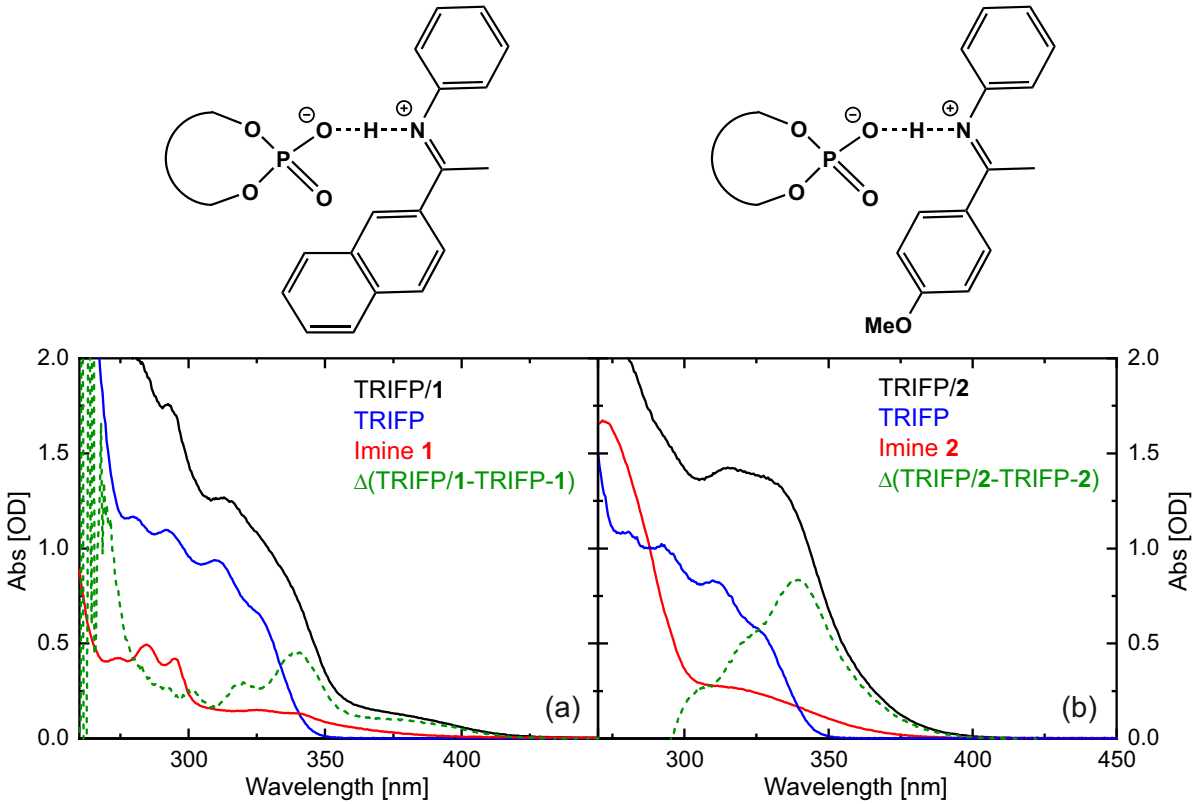

Figure 5.10: Steady-state absorption spectra of the binary TRIFP/imine mixture (black), the pure phosphoric acid TRIFP (blue) and the pure imine (red), dissolved in DCM and detected at -80°C. For both imine substrates **1** (a) and **2** (b) the spectral differences between the mixture and the sum of the single components were calculated (green-dashed) *via* subtraction of the TRIFP and imine spectra (blue and red, respectively) from the TRIFP/imine spectrum (black).

TRIFP/**1** is just ranging above 400 nm, that of TRIFP/**2** expires at 400 nm. Furthermore, the difference spectrum in the case of imine **2** comprises also a negative region (which is not shown in Figure 5.10b, but included in Figure 5.12), which means that the extinction coefficient of the complex is lower in this spectral range compared to that referring to the single substrates' sum. For the TD-DFT calculations of the binary mixture, a strongly simplified model was used, due to the molecular size of the full complex system. It was assumed that the imine forms a covalent bond to the hydrogen atom, instead of binding *via* hydrogen bonding and Coulomb interactions. In order to verify if this simplification can be used, further acid/imine mixtures were spectroscopically analyzed exemplarily on substrate **1**. Therefore, trifluoroacetic acid (TFA), formic acid and acetic acid with decreasing acidity as indicated by the pK_a values of 0.23,[322;327] 3.75,[503;504] and 4.76,[504;505], respectively, were added to a solution of imine **1** in DCM (note that TRIFP has a pK_a value of 2.63).[506] In the case of adding TFA or formic acid, a distinct change

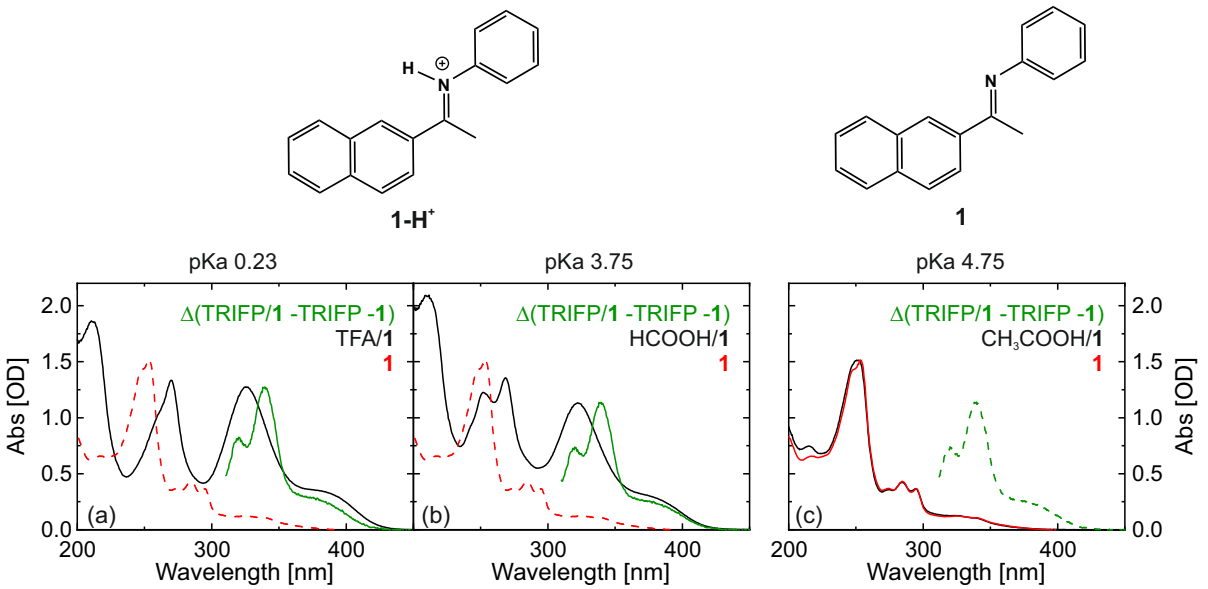

Figure 5.11: UV-Vis absorption spectra of imine **1** in DCM (red) and after adding 5 V-% of either (a) TFA, (b) formic acid or (c) acetic acid (black) at room temperature. For comparison also the absorption characteristics assigned to the binary TRIFP/**1** complex from Figure 5.10a measured at -80°C are included (green).

of the absorption spectrum was observed, as displayed in Figure 5.11a and b, while the absorption behavior by adding acetic acid stays nearly unaltered (see Figure 5.11c). Thus, it was concluded that the acidity of formic acid is still high enough to protonate the imine's nitrogen atom, whereas acetic acid is too weak for such a protonation. Since TRIFP is according to its pK_a value a stronger acid than formic acid, and the experimentally observed spectral changes of an imine solution by adding either TFA, TRIFP or formic acid are very similar to each other, as obvious by comparing the green and black curves in Figure 5.11a and b, the iminium cation was assumed to be a sufficient model for the binary TRIFP/imine complex within the theoretical calculations performed during this work, despite the strong simplification.

The calculated spectra of the E-type iminium cations $\mathbf{1H^+}$ and $\mathbf{2H^+}$ (magenta curves in Figure 5.12) are characterized by a pronounced red shift compared to those of their imine analogues **1** and **2**. In order to compare the experimental data of the binary complex with the TD-DFT calculations, the difference between the calculated spectra of the E-iminium-ions $\mathbf{1H^+}$ and $\mathbf{2H^+}$ (magenta curves) and the corresponding E-type imine spectra of **1** and **2** (blue curves) were drawn as solid green lines in Figure 5.12. The calculated difference spectra of the experimental data shown in Figure 5.10 are also included as dashed green curve for comparison. In both cases the difference spectra are relatively similar to each other and comprise equal contributions. Finally both the color change of the solution resulting from spectral changes in the absorption

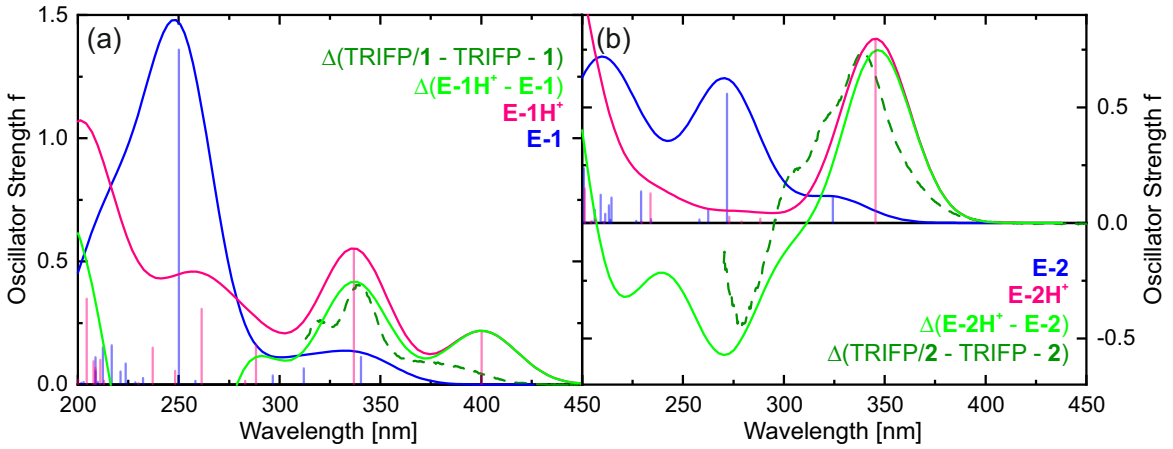

Figure 5.12: Comparison of the calculated absorption spectra of (a) imine **E-1** (blue) and its protonated analogue **E-1H$^+$** (magenta) and (b) of imine **E-2** (blue) and its iminium cation **E-2H$^+$** (magenta). The calculated oscillator strengths at the corresponding transition energies (TD-DFT/CAM-B3LYP/aug-cc-pVDZ) are given as stick spectrum convoluted each with a Gaussian of a 15 nm width at half maximum. All calculated spectra are red-shifted by applying an empirical correction of 0.25 eV, so that the calculated imine spectra (blue) are equivalent to those shown in Figure 5.5c and 5.6c. Furthermore, the difference between the blue and magenta spectra were calculated (solid green) and compared to the difference spectra gained from the experiments (dashed green; adapted from Figure 5.10).

behavior of the mixture as well as the experimentally observed spectral similarities to the theoretically gained spectra of the iminium cation used as model system indicate the complex formation in DCM solution.

After verification of the binary TRIFP/imine complex formation in solution, its photochemical behavior was investigated. However, instead of a reversible isomerization process we observed the same irreversible reaction both with and without illumination and also independent on the temperature (see Figure 5.13a-c). In all three cases, the substrates were used without previous drying and under normal atmosphere. Therefore, the imine was presumably reacting with some water impurities in the solution, preventing the complexation with the phosphoric acid. Thus, the experiment was repeated but with previously dried substrates, water-free solvent and under Ar-atmosphere (Figure 5.13d). However, no spectral changes indicating an isomerization could be observed. The slight intensity decrease can be attributed to a decomposition of the sample. Even so this experiment should be repeated with a higher sample concentration. As obvious from comparison with the other spectra in Figure 5.13a-c, the absorption intensity and thus, the sample's concentration displayed in Figure 5.13d still deviates from the previous measurements, resulting in a reduced amount of complex formation.

Although we could so far not observe any spectral changes experimentally at -80°C indicating

an isomerization in the binary substrate mixture, the expected absorption changes were theoretically obtained by TD-DFT calculations (see Figure 5.14). The difference spectra, gained by subtracting the spectra according to the E-iminium cations $\mathbf{1H^+}$ and $\mathbf{2H^+}$ from those of their Z-analogous, mainly point to an absorption decrease and a slight spectrally red-shift of the $\pi - \pi^*$ band during isomerization from the E-iminium cation to the Z-type analog.
However, in both cases the expected spectral changes during isomerization in the complex are rather small. Therefore, UV-Vis absorption spectra of further imines comprising varying molecular structures and substituents were calculated (see in Appendix Figures C.1-C.4) to find a

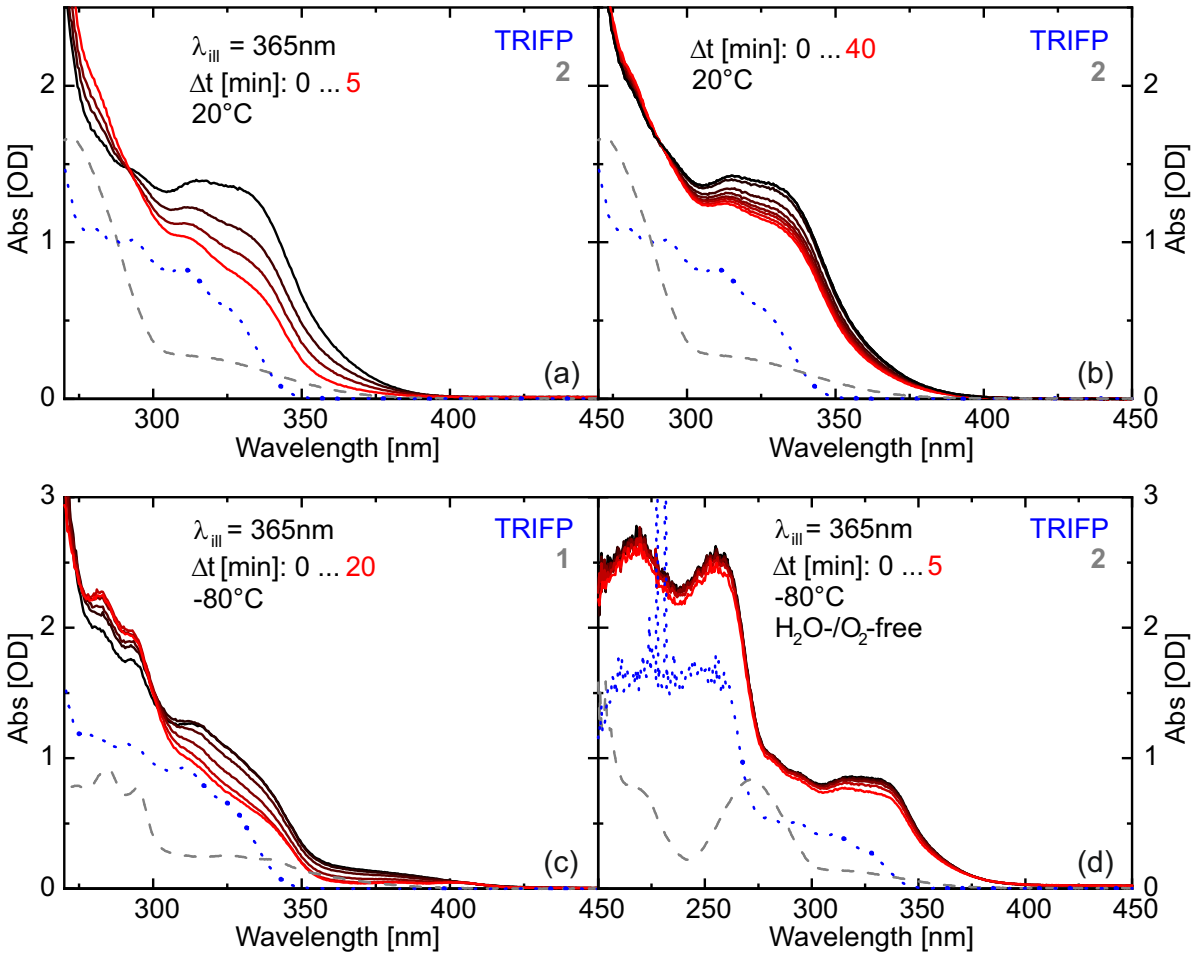

Figure 5.13: Spectrally observed changes of the binary TRIFP/imine mixture dissolved in DCM (a) with illumination at 365 nm at room temperature, (b) without illumination at room temperature, (c) with illumination at 365 nm at -80°C and (d) with illumination at 365 nm at -80°C under Ar-atmosphere. In (c) a sample solution of imine **1** was used, while otherwise imine **2** was studied. For comparison also the absorption spectra of the phosphoric acid TRIFP and the pure imine substrates are included (blue-dotted and gray-dashed curves, respectively).

system bearing bigger spectral changes during isomerization, which would facilitate the experimental observation of this process.

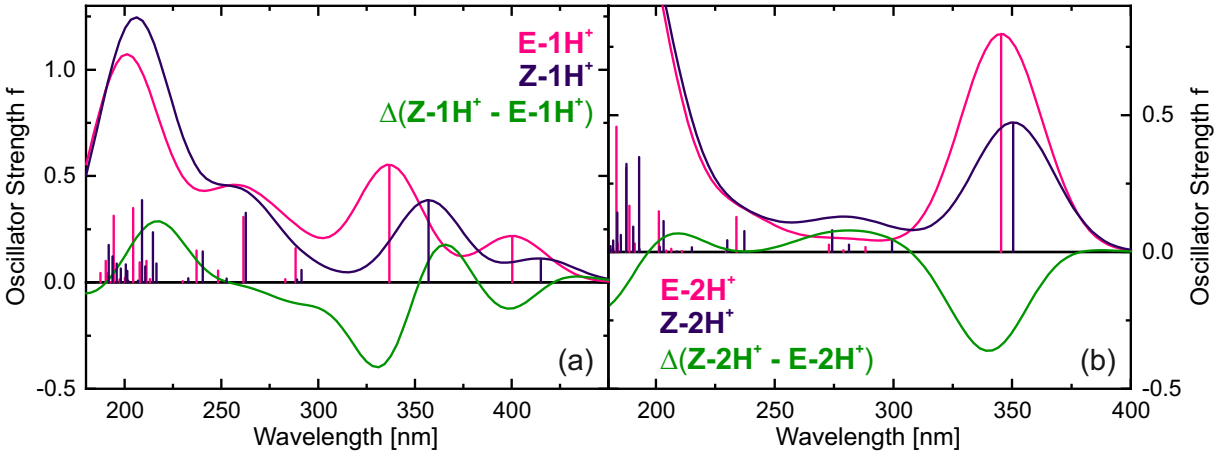

Figure 5.14: Comparison of the calculated absorption spectra of (a) iminium ion **E-1H$^+$** (magenta) and the corresponding Z-conformer **Z-1H$^+$** (purple) and (b) of the protonated species **E-2H$^+$** (magenta) and its Z-type iminium cation **Z-2H$^+$** (purple). The calculated oscillator strengths at the corresponding transition energies (TD-DFT/CAM-B3LYP/aug-cc-pVDZ) are given as stick spectrum convoluted each with a Gaussian of a 15 nm width at half maximum. All calculated spectra are red-shifted by applying an empirical correction of 0.25 eV, so that the shown E-iminium spectra (magenta) are equivalent to those previously represented in Figure 5.12. Additionally, the difference between the magenta and purple spectra were calculated (green) in order to estimate the expected spectral changes due to isomerization.

5.3.3 Excited-State Dynamics of the Pure Imine

The excited-state dynamics of imine **1** were also investigated by detecting its transient absorption on a fs to ns time scale after 305 nm excitation at room temperature. A global fit with three exponential functions yielded the decay-associated difference spectra shown in Figure 5.15. The DADS according to $\tau_1 = 1$ ps consists of an ESA at 400 nm and a GSB at 350 nm. The same spectral contributions are also found in the red DADS corresponding to τ_2 with 69 ps, but with smaller amplitudes and a slight spectral blue-shift of the ESA to 370 nm. Those fast dynamics can be attributed to a rapid deactivation from the excited state back into the initial ground state. For miraxanthin V which comprises both a C=C and a C=N double bond, transient absorption spectroscopy unveiled similar excited-state lifetimes of 2.2 ps and 20.8 ps in water.[507] Each of these decay times was assigned to one stereoisomeric species of miraxanthin V formed after photoexcitation by a cis/trans-isomerization around the C=N double bond. While the shorter

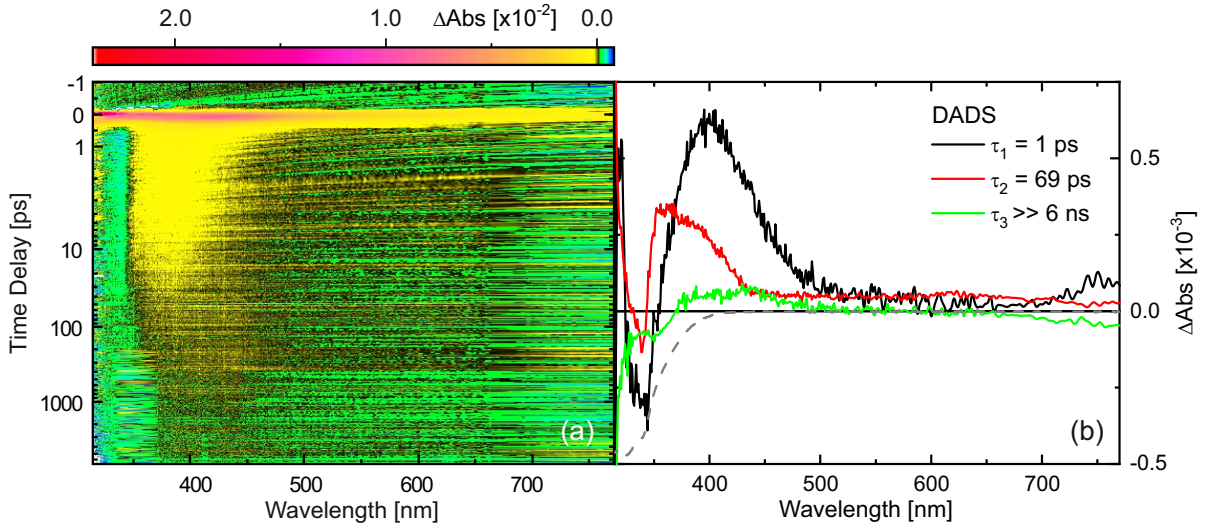

Figure 5.15: (a) Transient absorption map of imine **1** in DCM after 305 nm excitation at room temperature. (b) DADS obtained by global lifetime analysis with three exponential functions. The scaled and inverted absorption spectrum is included as gray-dashed line.

time constant was associated with the Z-isomer with respect to the C=N double bond, the longer lifetime was assumed to correspond to the E-type compound also with respect to the C=N double bond.[507] Additionally, there is also a third lifetime τ_3 in our experiments that exceeds the detectable time window of 6 ns and contains a weak PA between 380 nm and 460 nm additionally to a GSB below 370 nm. Those contributions might be assigned either to an intermediate species, like a photoisomer or more likely to the formation of a side product, e.g. generated by a reaction with water impurities in the solution.

For a better understanding of the observed rapid deactivation, the PES along the torsional angle $\varphi_{\mathrm{Ph-C=N-Ph}}$ from 0° to 360° were calculated for the ground state S_0 and the first excited state S_1 (be aware that the geometries at 0° and 360° are equivalent to each other). However, due to the bigger molecular size of imine **1** compared to imine **2** and thus, the enhanced computational afford in the case of **1**, these calculations were performed for imine **2** which comprises a smaller substituent group. The ground-state PES unveils two potential wells at 0° and 180° which can be attributed to the Z- and E-conformers, respectively, while the latter one is energetically slightly more favored by 0.06 eV. The PES according to the first excited state also comprises two potential wells but with minima at 90° and 270°, where the energy barrier between the two isomers in the ground state reaches its maximal values. However, the calculated PES in the ground state showed for the energy barrier maxima a plateau with nearly identical energy values between 70° and 110° as well as between 250° and 290°, which means that TD-DFT is not a suitable method to describe the dynamics of this molecular species in the regions around 90° and 270°.

However, this might indicate a conical intersection (CI), which would explain the fast deactivation of imine **1** due to a barrierless pathway. In order to describe a possibly conical intersection usually the CAS-SCF method is used.

In comparison, for miraxanthin V also a fast excited-state deactivation *via* a low lying $S_1 - S_0$ conical intersection is assumed.[507] By a combination of experimental and theoretical data, furthermore the deactivation pathway is expected to be initiated by an excited-state rotation about the C=N double bond. Such a rotational pathway was already found for other photoswitching molecules like 7-hydroxyquinoline,[508] N-(3-pyridinyl)-2-pyridinecarboxamide,[509] and salicylidene methylamine.[510;511] It becomes possible by a weakening and thus, an elongation of the C=N double bond upon excitation, which finally results in a decreased barrier.[507] Comparison of the calculated ground- and excited-state geometries of imine **2** indeed shows an elongated C=N bond length in the S_1 state, while the C−C and C−N single bond lengths are shortened simultaneously. In order to further explore, if the fast deactivation of the imine occurs over ro-

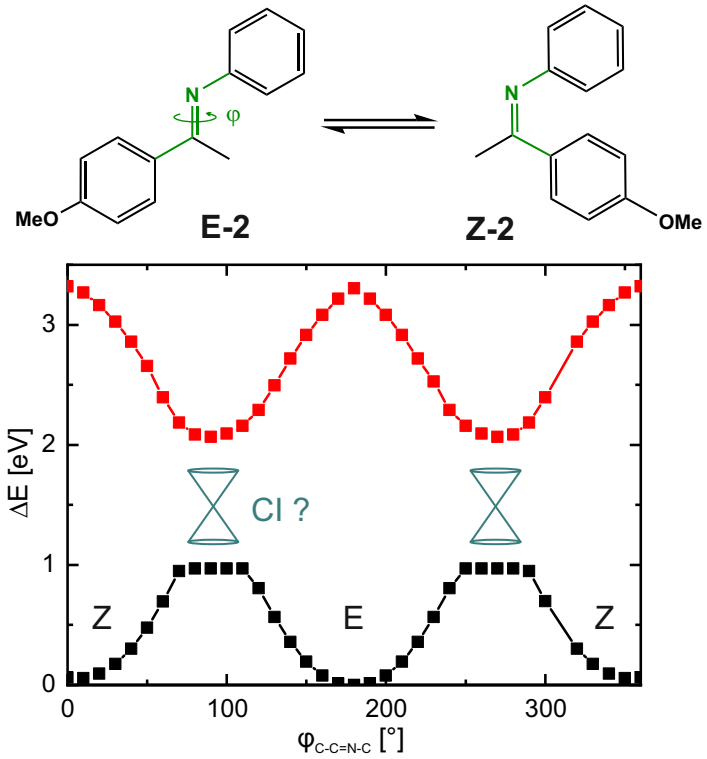

Figure 5.16: Relaxed PES scans performed on imine **2** along the dihedral angle φ spanned by $(Ph)C_1 - C_7 = N_8 - (Ph)C_9$, defining the conformational type (E or Z), in S_0 (black) and S_1 (red). The scans were calculated on the MP2 (for S_0) and ADC2 (for S_1) level of theory using the aug-cc-pVDZ basis set by starting from the Z-imine with 0°. The geometry at 310° did not converge for which reason the corresponding energy is not shown.

tation about the C=N double bond, future experiments should address further variations of the environment, e.g. to determine the excited-state lifetimes in dependence on the solvent viscosity, which should cause a prolonged lifetime with increasing viscosity in the case of a rotational deactivation pathway.

5.3.4 Excited-State Dynamics of the Binary Mixture

For insights into the excited-state dynamics of the ion-paired complex, a binary TRIFP/**1** mixture was studied by fs-ns TA after excitation at 305 nm. The data matrix was analyzed by a global fit with four exponential functions. The fitted lifetimes are shown in Figure 5.17 with the corresponding DADS. Both shorter contributions with 3.3 ps (τ_1) and 85 ps (τ_2) are comparable to the excited-state dynamics of the pure imine **1** (see Section 5.3.3). The corresponding DADS consists of a GSB at 350 nm and an ESA around 400 nm. However, both DADS show also further spectrally broad ESA bands exceeding the detectable spectral region up to 770 nm, which might be caused by either the TRIFP/**1** complex or the pure TRIFP. Since excitation at 305 nm does not specifically result in an excitation of the ion-paired complex, instead also the single substrates TRIFP and imine **1** are excited, too, the exact assignment of the observed contributions becomes more complicated. Unfortunately, the excited state dynamics of pure TRIFP are

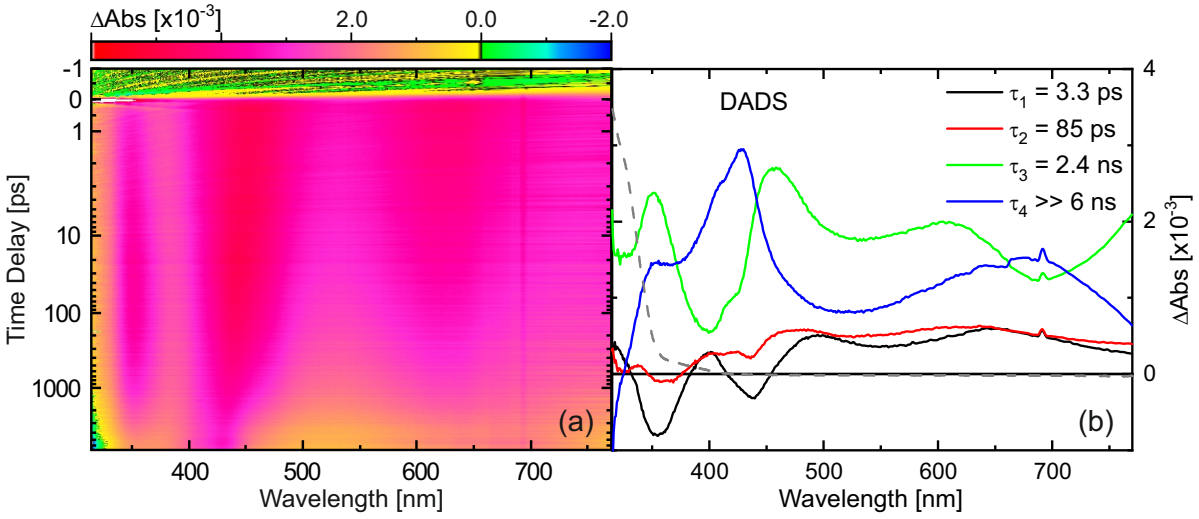

Figure 5.17: (a) Transient absorption map of the binary TRIFP/imine **1** mixture in DCM after 305 nm excitation at room temperature. (b) DADS obtained by global lifetime analysis with four exponential functions. The scaled absorption spectrum is also included as gray-dashed line.

also unknown. Therefore, a precise attribution of the longer lifetimes τ_3 with 2.4 ns and τ_4 with a decay constant exceeding the time window of 6 ns was not possible during this work. So, in general the here shown TA data of the mixture unveil only some slower dynamics proceeding on the ns-time scale compared to the pure imine **1**, which is fully relaxed within 69 ps. Therefore, it is assumed, that the fast deactivation pathways, which were observed for imine **1** are inhibited for the iminium-ions formed in the complex.

5.4 Conclusion and Outlook

During this work, we achieved to build a setup with which light-induced spectral changes in the ground state with rapid back-relaxations, like isomerizations, are detectable on a sub-s to min time scale by slowing down the kinetics *via* sample cooling. Furthermore, it was possible to design a new cuvette allowing the spectroscopic investigation of substrates with either very high extinction coefficients or high sample concentrations, which are additionally sensitive to oxygen or water and need to be handled under inert conditions (see Section 5.2.2).
The enhancement of the setup and the new cuvette design were necessary to investigate the ion-paired TRIFP/imine complex spectroscopically. During the transfer hydrogenation of imines catalyst by Brønsted acids, the formation of such a binary complex is proposed. However, experimental insights regarding the reaction mechanism and its intermediates are underrepresented. Thus, we investigated the photochemical behavior of such an ion-paired TRIFP/imine complex formed within a 1:1 substrate ratio; each with a concentration of 50 mM. However, before studying the complex, all relevant substrates were investigated individually. Thus, the photochemistry of three differently substituted imines, namely naphthalene-imine **1**, para-methoxy-imine **2** and para-nitro-imine **3** dissolved in DCM were examined. The light-induced isomerization from the energetically favored E-type imine to its Z-analogue could be spectroscopically observed for all three substrates at cryogenic temperature. The subsequent back-relaxation was also detectable in the dark within several minutes even at -80°C. The used phosphoric acid TRIFP was stable under 365 nm illumination. However, it is necessary to dry the TRIFP catalyst before adding it to an imine solution, owing to its hydrophilicity to prevent an unwanted side reaction with water, presumably reducing the imine to its amine analogue.
Although generating dried conditions, so far the imine isomerization within the mixture could not be observed. The expected spectral changes along isomerization were gained by theoretical calculations on a strongly simplified model system using an iminium cation instead of the full hydrogen-bonded complex. Ultimately, these predicted absorption spectra unveiled only slight spectral differences and shifts. Thus, it might be possible that the absorption behavior within the complex is too similar for observation with the used setup or more likely, the sample's concentration was too low during this experiment, resulting in a rather low complex concentration making it unable to detect those small changes. Therefore, these experiments created the basis for further investigations, like illuminating the binary TRIFP/imine mixture under Ar-atmosphere with a higher substrate concentration.
Furthermore, the substituents at the imine reactant can be changed to molecular groups, which result in more differentiating absorption spectra of the corresponding E- and Z-type imine. In

order to find such imine samples, further theoretical calculations can be performed. The most distinct changes of the so far calculated imine spectra are observed for an imine where the methyl group is exchanged with a hydrogen atom. In future, the investigations regarding the isomerization process within the mixture will therefore be carried out with this imine reactant.
Since the assignment of the excited-state dynamics monitored after excitation of the binary mixture to a distinct photochemical or photophysical process was challenging, the behavior of the catalyst TRIFP in the excited state should also be detected. Furthermore, the fs-ns TA of the binary mixture should be investigated after excitation at a wavelength where specifically the ion-paired complex can absorb, e.g. in the case of a TRIFP/**1** complex excitation around 400 nm should be preferred to reduce excited-state absorptions caused by the single components.
Ultimately, also the photochemical behavior of the ternary TRIFP/imine/HE complex formed in a 1:1:1 concentration ratio should be investigated to gain spectroscopic insights regarding the proposed mechanism of the asymmetric transfer hydrogenation of imine substrates.

CHAPTER 6

Summary

The utilization of molecular switches is an ever-growing field. Not only in nature a lot of processes are based on isomerizations. Also many industrial methods take advantage of molecular switches proceeding *via* such an isomerization process. Thus, isomerizations are already established in a variety of processes in different sectors, like the food chemistry, agriculture, large-scale technical syntheses and the development of novel technical devices. In order to improve the current functionalities or to extend the application possibilities to e.g. alternative sustainable technologies, it is necessary to investigate and understand the underlying mechanism and the physical, chemical and biological properties of the individual molecular isomers. More detailed insights lead to a better controllability and also a higher tunability of the processes and thus, providing a higher potential for the development of even more complex applications.

Therefore, this thesis focuses on the mechanistic study of light-induced molecular reorientations of three different classes of molecules using time-resolved spectroscopy. By combining the transient absorption of 1,3,5-triphenyl formazan (TPF), which was monitored on time scales ranging from femtoseconds up to minutes, we were able to follow the whole isomerization process. Since isomerization is possible around two double-bonds, elucidation of the relaxation pathway of TPF became more complicated. Hence, the analysis of the experimental data was supported by quantum chemical calculations. We concluded that photoexcitation leads to an excited-state isomerization accompanied by additional rotation of a single bond. The subsequent relaxation process proceeds *via* several isomeric species of TPF, until the initially excited isomeric form is fully repopulated. The isomerization mechanism was studied in different solvents to elucidate the influence of polar protic, polar aprotic and unpolar environments as well as the effect of binary solvent mixtures onto TPF, generated by adding either a protic or an aprotic cosolvent to an unpolar sample solution. According to the extraordinary sensitivity to

its environment indicated by strongly effected lifetimes of the intermediate isomers, we assume that some relaxation steps rather favor an intramolecular proton transfer than an isomerization around the double bond. A potential relaxation pathway partially assisted by a proton transfer is a completely new aspect within the elucidation of the isomerization mechanism of TPF. Furthermore, especially the remarkably sensitivity of the individual isomeric species regarding the solvent environment might be advantageous in some applications, like syntheses where the photoisomerization of formazans can act beneficially or would disturb the reaction. Finally, it can be concluded that the strongly affected photochemical behavior of TPF by external influences classifies such molecules as potential reactant in the emerging field of steering photochemical reactions.

A high impact on the photochemical properties was also found by varying functional groups within tropylium cations. In a systematic study regarding the absorption and emission characteristics of overall six differently substituted tropylium salts consisting of an electron-poor tropylium moiety connected directly to an aniline scaffold, it was shown that in dependency on the steric effect of the substituents different conformeric species are favored in solution. While changing the chain length of the alkyl groups attachd to the nitrogen atom has a rather marginal effect, a structural reorientation is found by introducing functional groups in 3- and 5-position of the benzylic aniline ring. Both conformeric geometries are spectroscopically characterized by distinguishable absorption behaviors. Quantum chemical calculations also unveiled a deviating localization of the positive charge. The unsubstituted tropylium cations show a quinoidal-like structure with the positive charge delocalized over the aniline scaffold. In contrast, the sterical hindrance of the additional substituents lead to a distinct twist between both molecular parts of which the dibenzotropylium framework comprises the most positive region as typically expected for tropylium cations. Therefore, it was possible to additionally protonate those substrates at the nitrogen atom, yielding a two-times positively charged species with completely changed absorption and emission characteristics. For one tropylium derivative, the emission lifetime was enhanced due to protonation by five orders of magnitude in time. Furthermore, we could show, that the substituted samples act as photobase in DCM and DCM-TFA solutions. Even for the unsubstituted tropylium compounds a photobasic behavior could be observed in DCM-TFA solution during this work, which means these molecules comprise the properties of both a TICT compound and a photobase simultaneously.

Furthermore, reducing the aromatic π-system of the tropylium moiety also results in distinct changes regarding the spectral properties. Its $\pi - \pi^*$ absorption band is red-shifted, while emission followed by excitation of this band is strongly quenched. Additionally, only one conformational geometry comprising a positively charged tropylium ring was found by theoretical

calculations. As a consequence of the absence of bulky substituents, a fast deactivation *via* rotation around the single bond connecting both molecular parts was observed by fs-transient absorption spectroscopy. Moreover, by addition of a second salt to the tropylium solution, we found indications for the ability to form ion pairs, whose photochemistry might also be interesting for future applications and should thus be analyzed further.

Ultimately, the discovery of various possible conformeric species in solution is probably the most relevant aspect for future applications. Exemplary in the synthesis, it might be advantageous if only one specific conformer is present during a reaction in order to control the resulting product or its yield, which can be easily achieved by selective functionalization of the tropylium dyes with different substituents.

A further omnipresent topic in chemistry is the formation of ion pairs in solution, since a broad variety of organic and inorganic reactions and syntheses comprise an ion-paired intermediate species within their mechanisms. The possibility to form ion pairs was not only found for the previously discussed tropylium salts, but rather during the here investigated asymmetric transfer hydrogenation on the example of the enantioselective imine reduction. In order to investigate the isomerization process within the binary ion-paired complex between the chiral phosphoric acid and the imine spectroscopically at cryogenic temperatures, the design of a suitable cuvette and a setup for constant illumination was necessary. Within this thesis the requirements, like a very short optical path length, a water- and oxygen-free atmosphere or constant cooling over long periods, are discussed and the consequent challenges by the implementation in the laboratory are described. Finally, it was possible to develop a suitable experiment providing the potential for future studies regarding the isomerization behavior of the imine substrates first within the binary mixtures of CPA and imine and later after further addition of the Hantzsch ester forming the ternary CPA/imine/HE complex.

This work about time-resolved spectroscopy on overall three different molecular systems unveiled new insights regarding their photochemistry and photophysics. Understanding the effect of varying substituents, different solvent environments, and added co-substrates or co-solvents on the spectral characteristics and mechanistic pathways of each class of molecules might be beneficial for improving current functionalities and developing future application possibilities.

APPENDIX A

1,3,5-Triphenylformazan

Transient Absorption

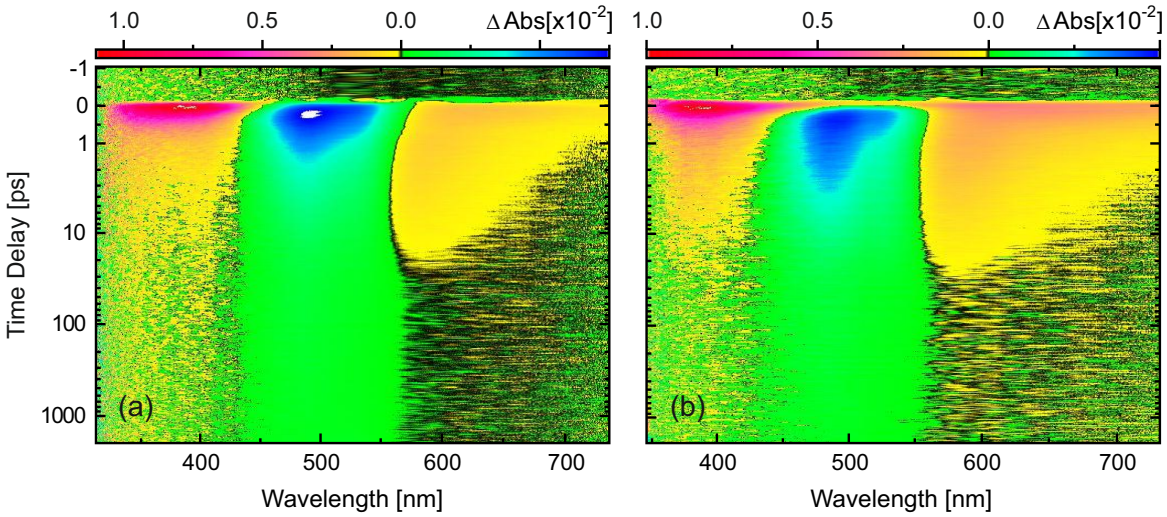

Figure A.1: Monitored transient absorption of TPF in methanol after excitation at 530 nm (a) and 330 nm (b) on a fs-ns time scale. The corresponding analysis is represented in Figure 3.6.

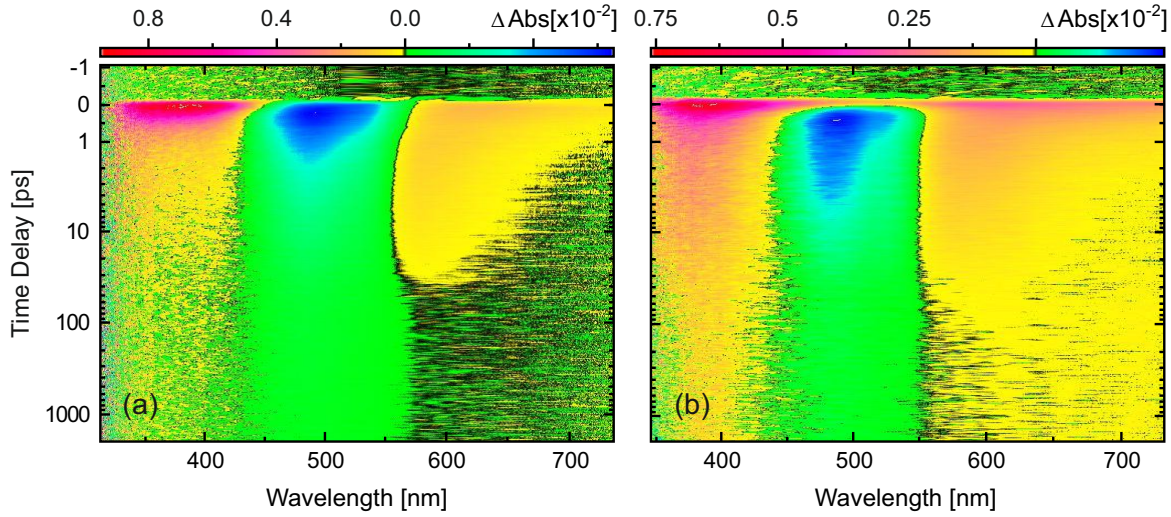

Figure A.2: Monitored transient absorption of TPF in acetonitrile after excitation at 530 nm (a) and 330 nm (b) on a fs-ns time scale. The corresponding analysis is represented in Figure A.3.

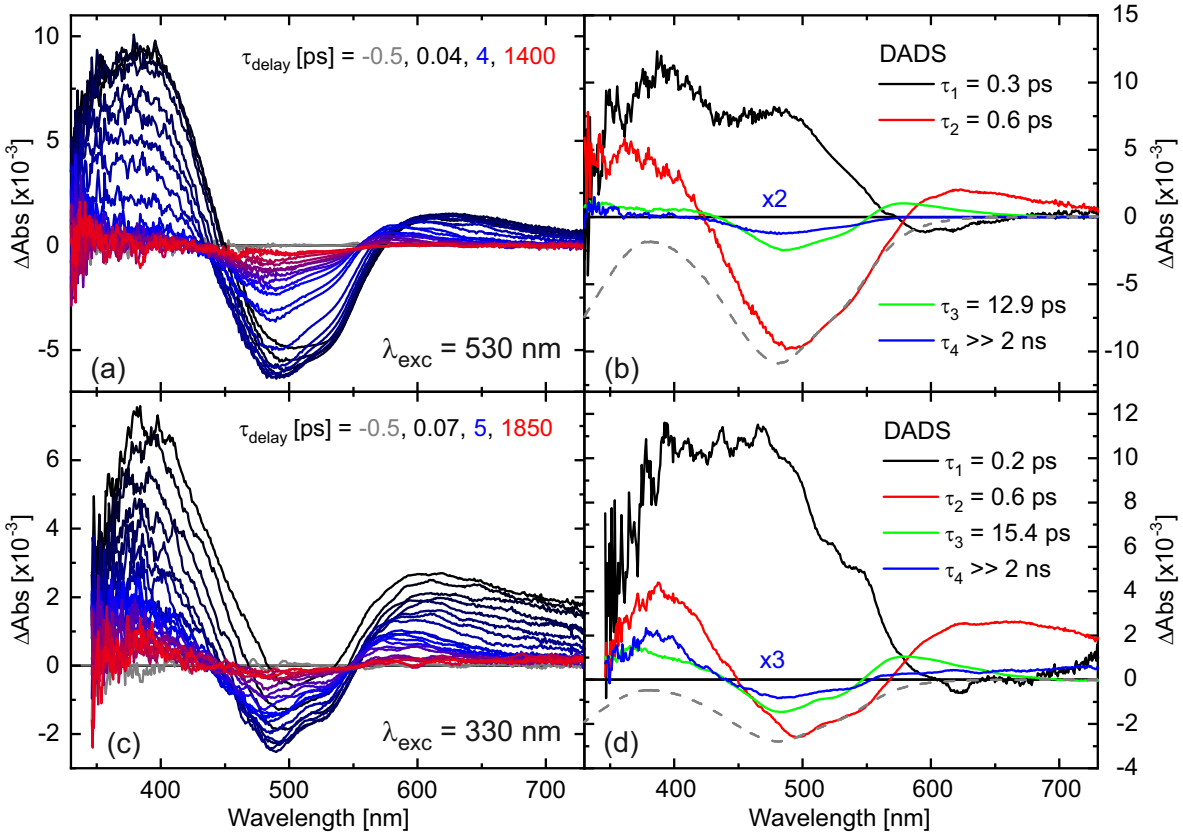

Figure A.3: Transient absorption of TPF in acetonitrile after excitation at 530 nm (a) and 330 nm (c) after defined delay times on a fs-ns time scale. The corresponding DADS from a global exponential fit to the data are given in b and d. The scaled and inverted absorption spectrum of the initial sample is given by a gray dashed line for comparison.

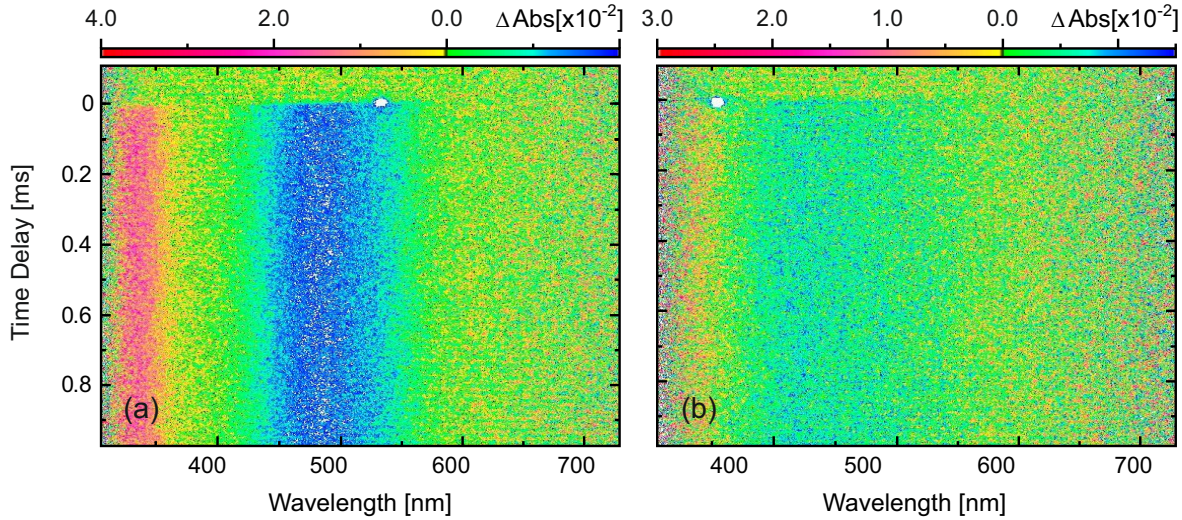

Figure A.4: Monitored transient absorption of TPF in methanol after excitation at 532 nm (a) and 355 nm (b). The corresponding analysis is represented in Figure 3.7.

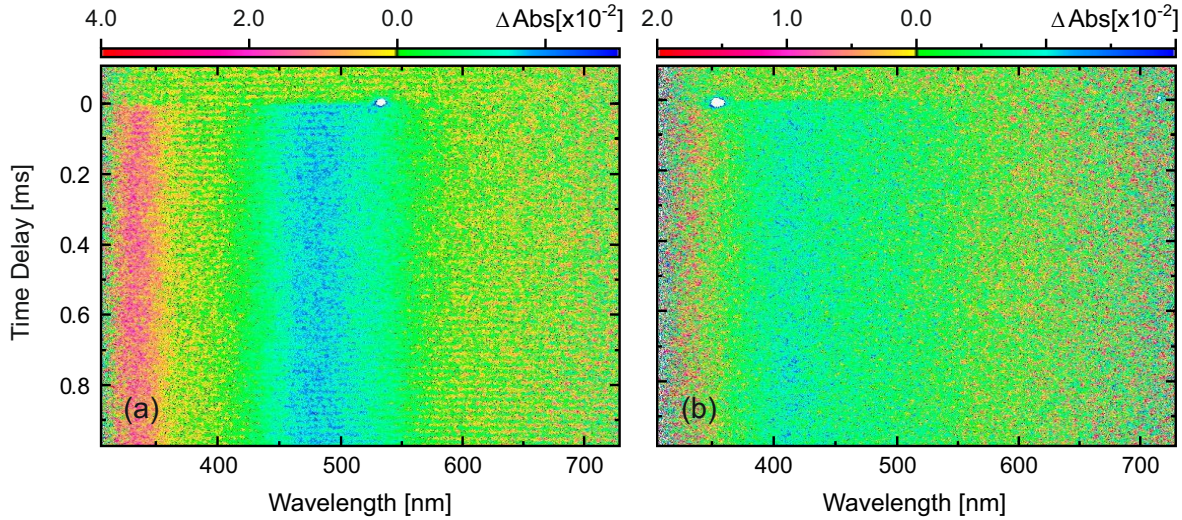

Figure A.5: Monitored transient absorption of TPF in acetonitrile after excitation at 532 nm (a) and 355 nm (b). The corresponding analysis is represented in Figure A.6.

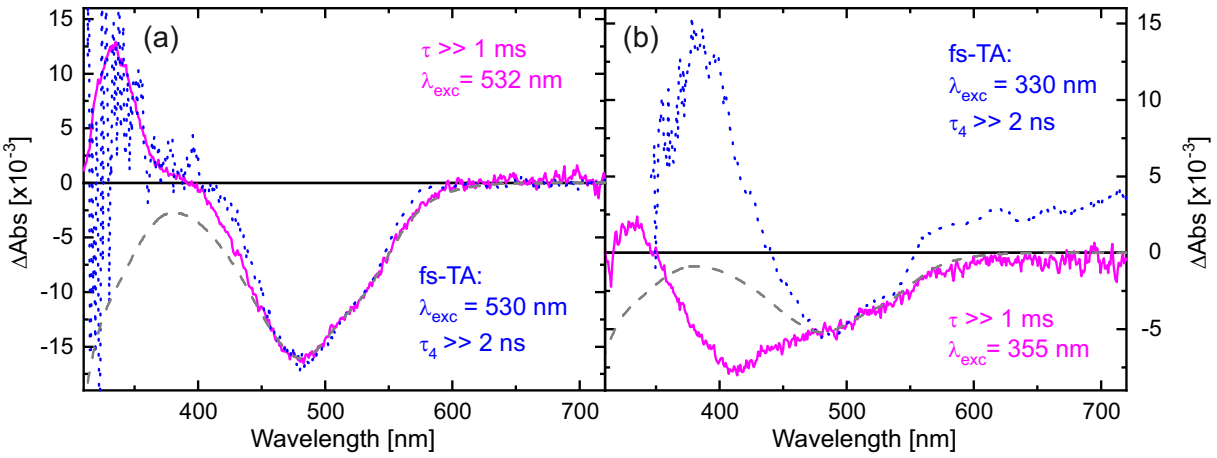

Figure A.6: DADS of TPF in acetonitirle after excitation at 532 nm (a) and 355 nm (b). The magenta DADS result from a global monoexponential fit to the data on a 1 ms time window. The blue dashed curves are the DADS corresponding to τ_4 of the fs-ns TA experiments (blue curves in Fig. A.3b,d) scaled to match the negative contribution at around 500 nm. The inverted absorption spectrum of the initial sample also scaled to the negative contribution at around 500 nm is given by a gray-dashed line for comparison.

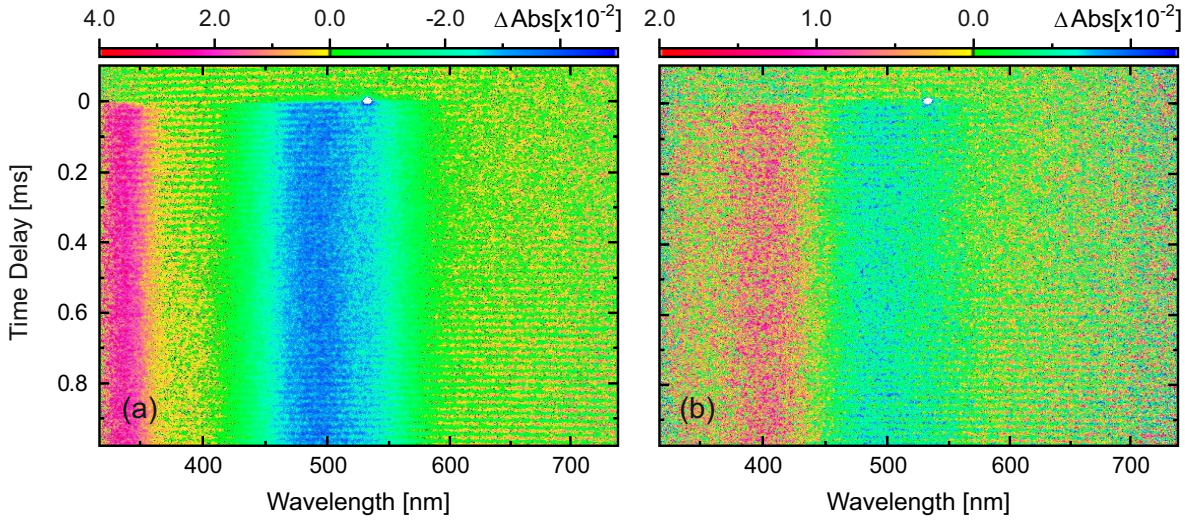

Figure A.7: Monitored transient absorption of TPF in toluene, which was previously kept in the dark (a) and which was constantly illuminated with 450 nm light before pumping through the sample's cuvette (b). Each TA was measured on a 1 ms time window after excitation at 532 nm. The corresponding data analysis is represented in Figure 3.9.

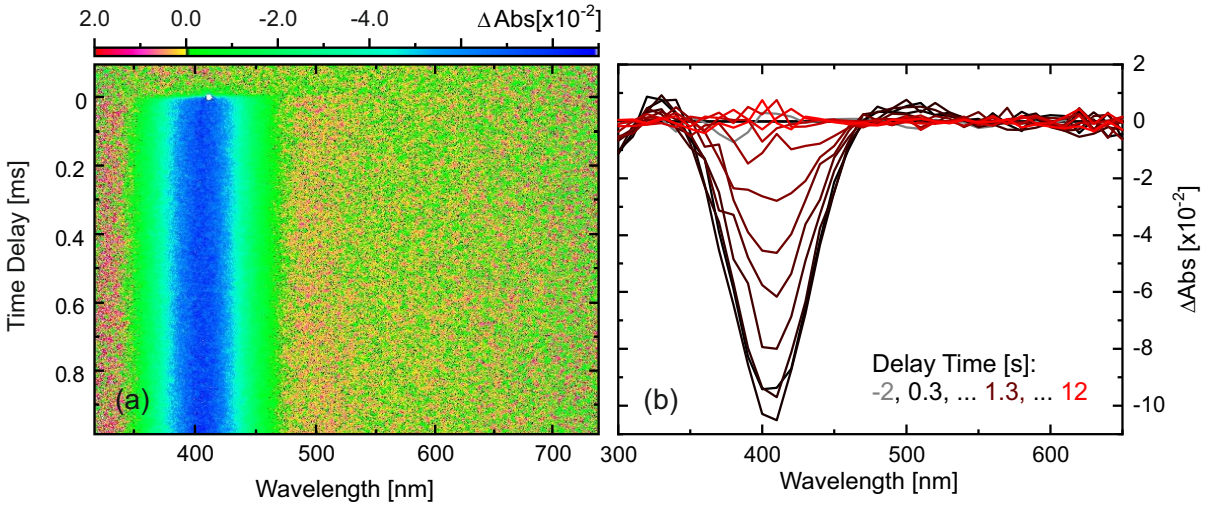

Figure A.8: (a) Monitored transient absorption of TPF in toluene, which was constantly illuminated with 450 nm light before pumping through the sample's cuvette. (a) The TA was measured on a 1 ms time window after excitation at 410 nm. (b) Transient absorption at defined delay times after excitation at 405 nm on a sub-s time scale. The corresponding data analysis is represented in Figure 3.10.

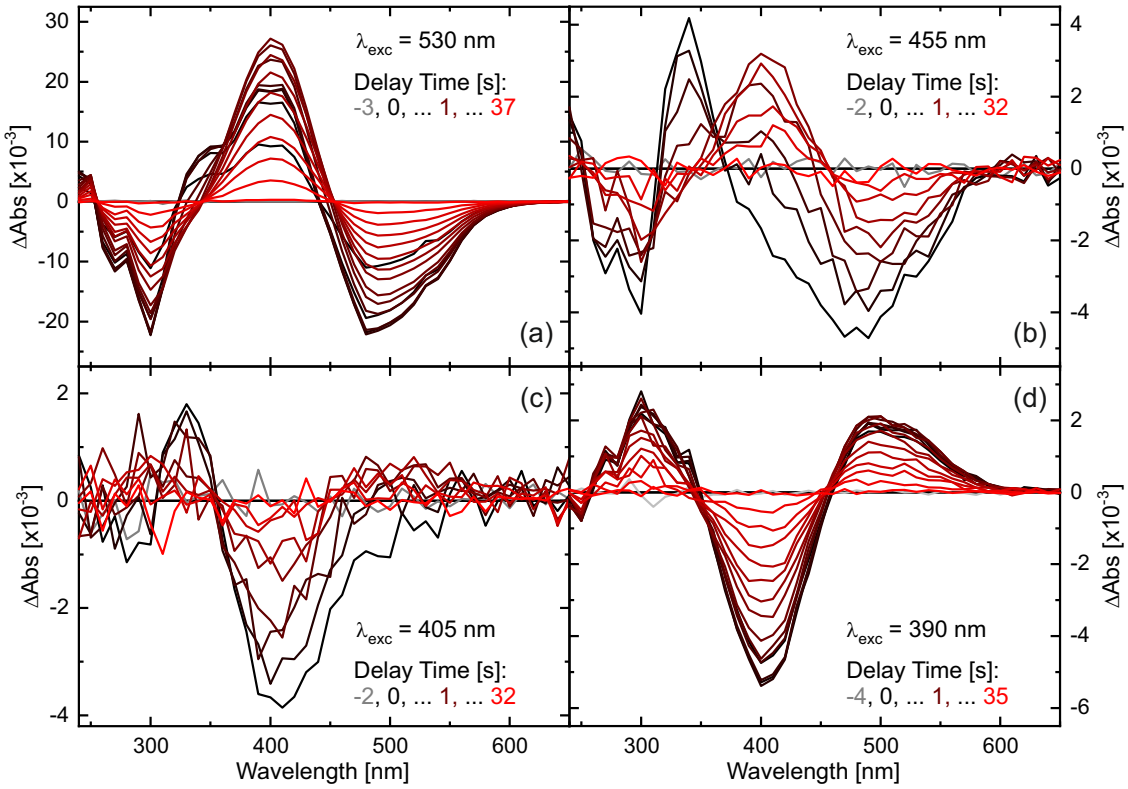

Figure A.9: Transient absorption of TPF dissolved in methanol after excitation at 530 nm (a), 455 nm (b), 405 nm (c), and 390 nm (d) after defined delay times on a sub-s time scale. The corresponding analysis is shown in Figure 3.8. Note that the TA data in (a) and (d) were smoothed due to the different data acquisition compared to (b) and (d).

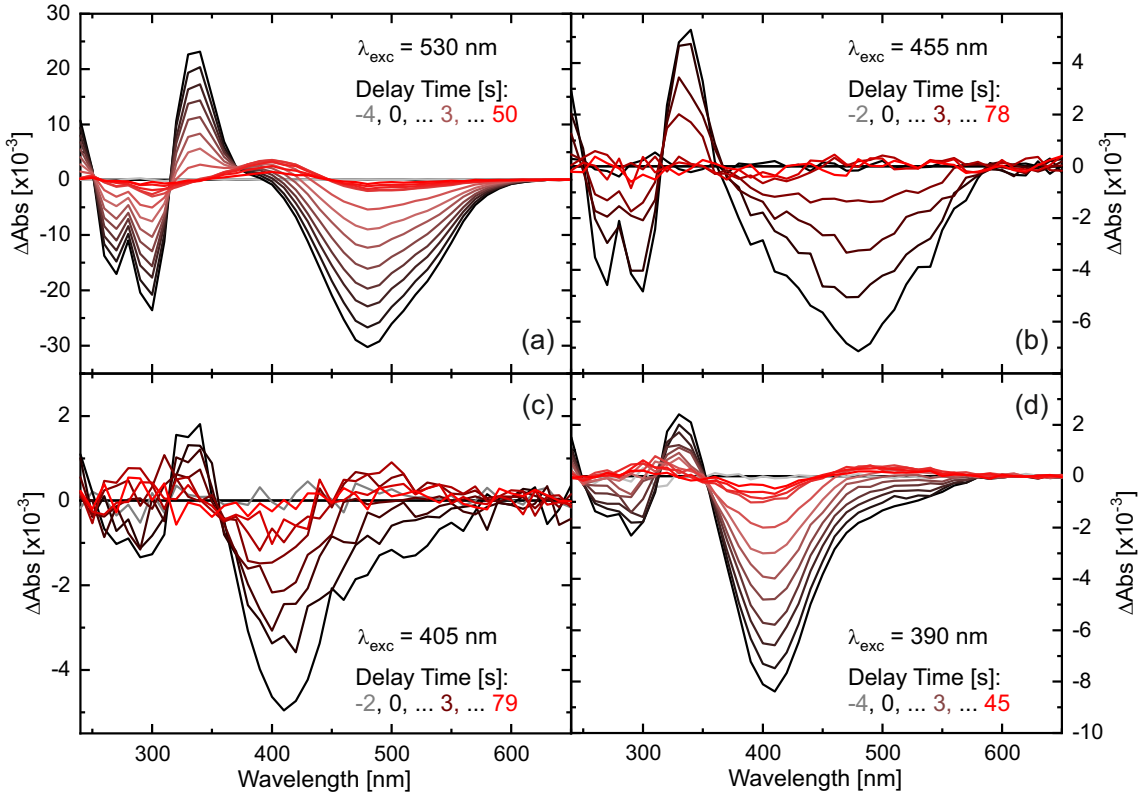

Figure A.10: Transient absorption of TPF dissolved in acetonitrile after excitation at 530 nm (a), 455 nm (b), 405 nm (c), and 390 nm (d) after defined delay times on a sub-s time scale. The corresponding analysis is shown in Figure A.11. Note that the TA data in (a) and (d) were smoothed due to the different data acquisition compared to (b) and (d).

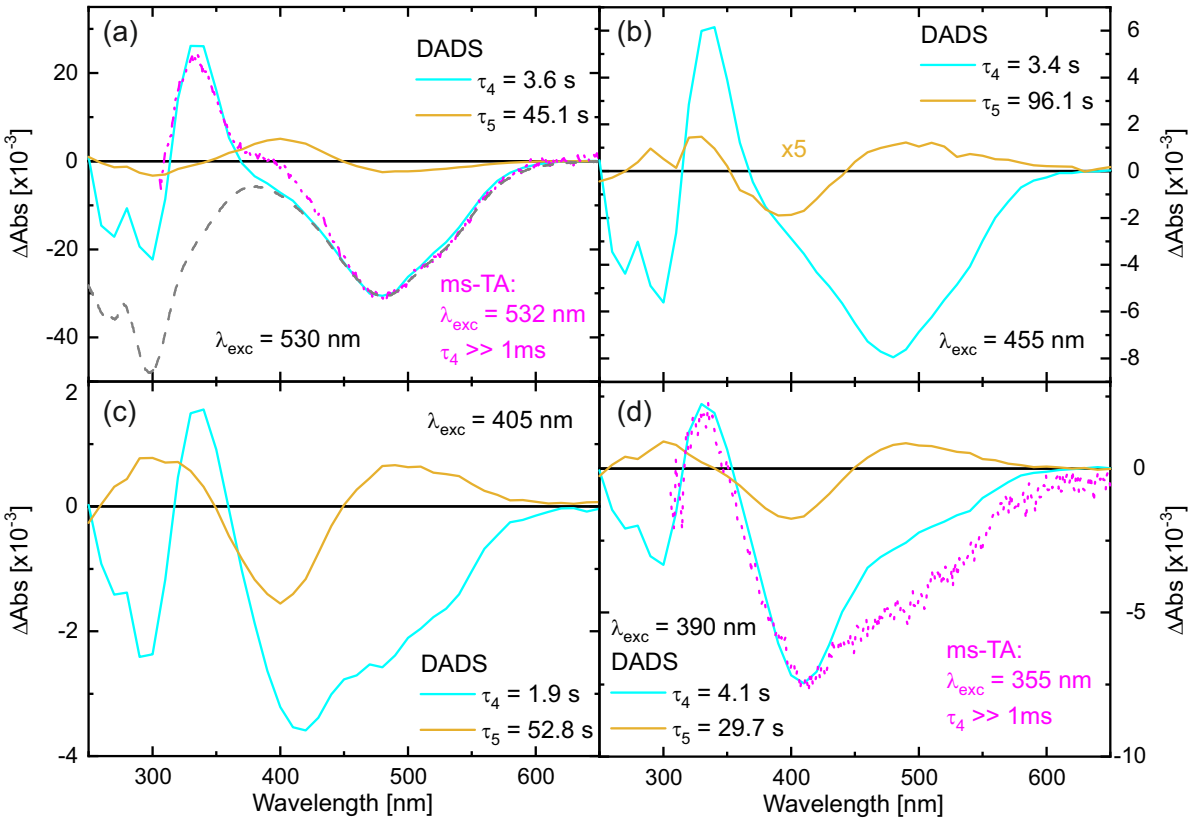

Figure A.11: DADS of TPF dissolved in acetonitrile obtained by a global biexponential fit to the data matrices detected after excitation at 530 nm (a), 455 nm (b), 405 nm (c) and 390 nm (d). The gray dashed line represents the inverse absorption spectrum of the initial solution, while the pink DADS are taken from Figure A.6 for comparison.

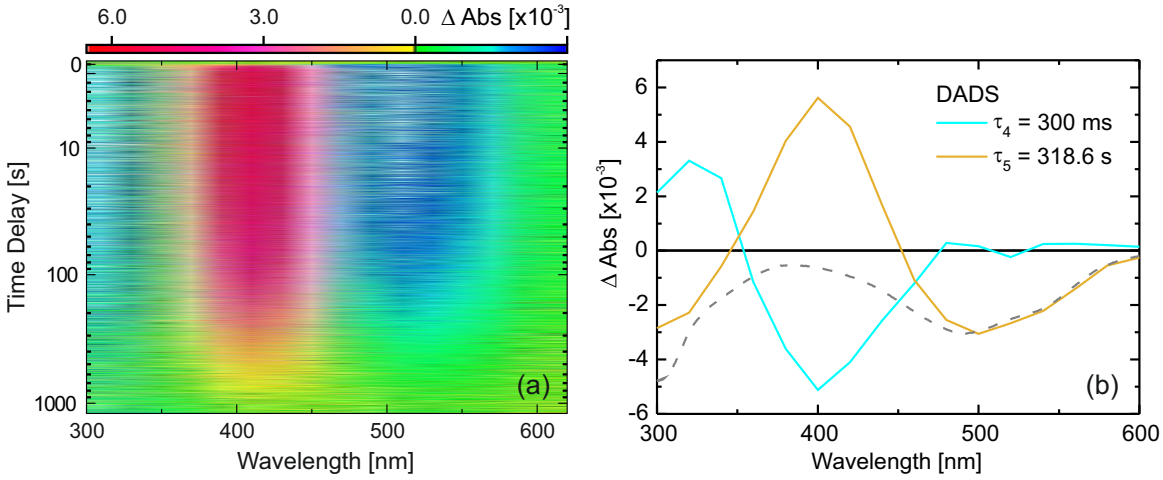

Figure A.12: (a) Transient absorption map of TPF in toluene after excitation with 520 nm light for 12.5 ms (LED1). (b) The corresponding DADS obtained from a biexponential global fit. The dashed gray line is the scaled and inverted spectrum of the solution in the dark.

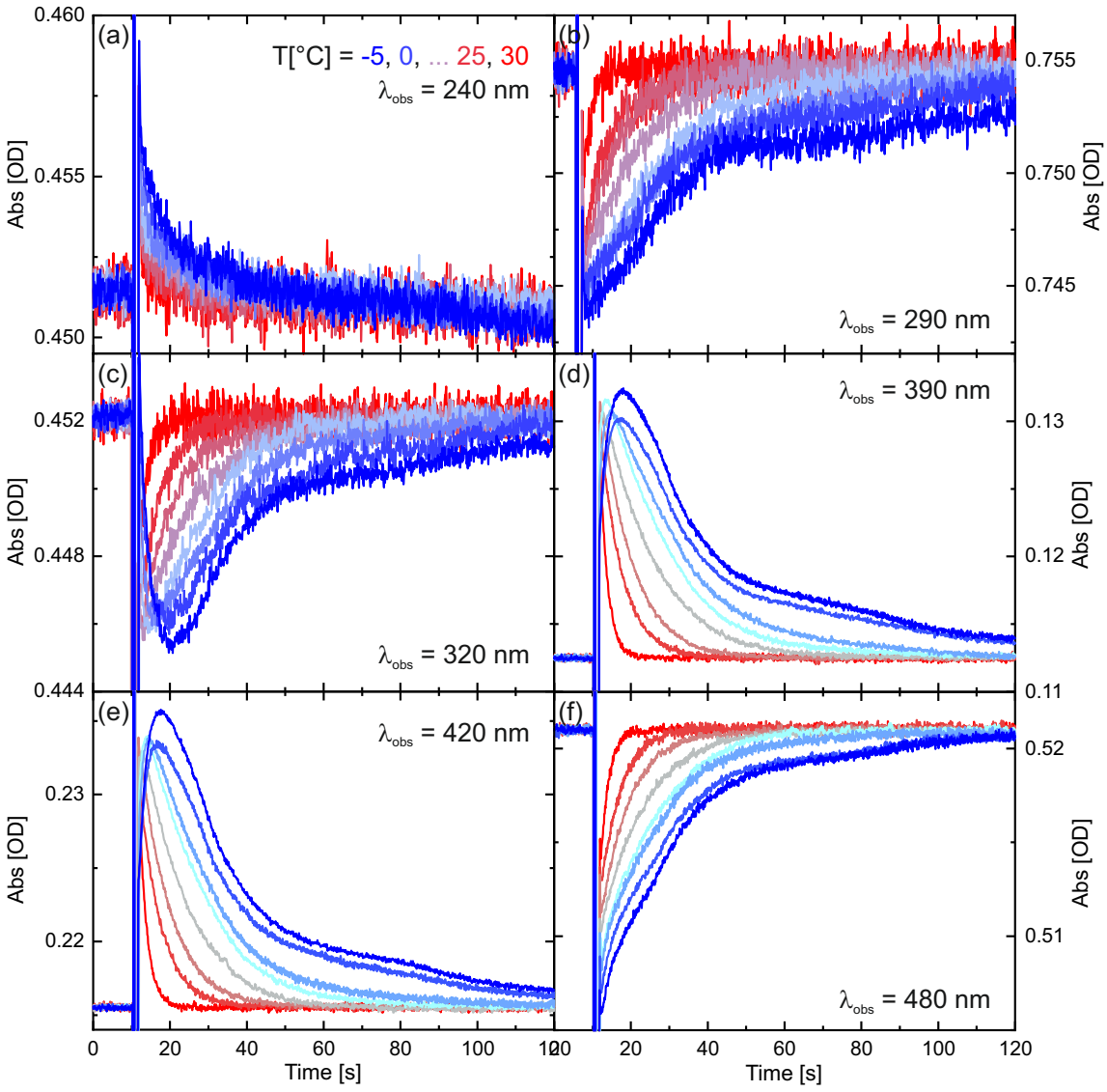

Figure A.13: Temperature-dependent decay kinetics after 530 nm excitation of TPF dissolved in methanol (Raw Data). The pulse length of the LED was set to 480 ms, according to the temporal resolution of the spectrometer. The kinetic traces were measured at six observation wavelength between -5°C and 30°C in 5°C steps. The here shown kinetic traces were spectral and temporal corrected, the pulse induced absorption changes were corrected and the data were weighted, before the data matrix at a distinct temperature was globally fitted. The longest decay time τ_5 was then used for an Arrhenius plot *via* the Arrhenius equation $k = A \cdot exp(-E_A/(RT))$ to calculate the activation barrier. Due to the high sample volume of 2-3 ml and an optical path of 10 mm, oscillations caused by diffusion effects are observable within the decay traces.

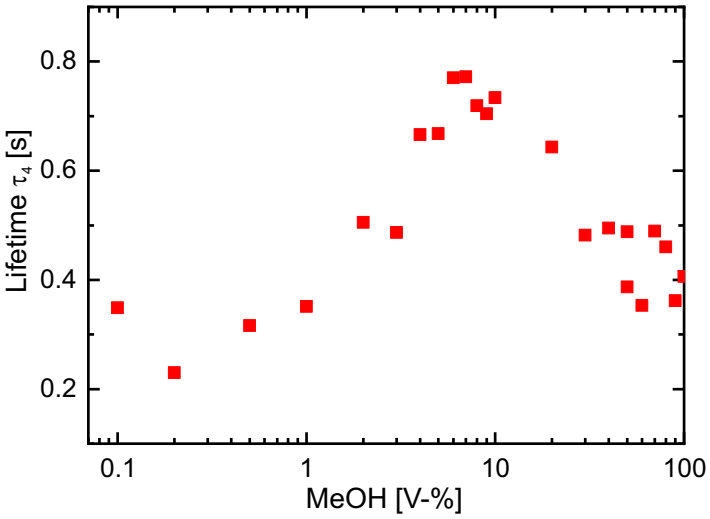

Figure A.14: Time constants τ_4 determined for the thermal isomerization from yellow I to red I after excitation with 520 nm light for 12.5 ms. The measured kinetic profiles and the lifetime τ_5 according to the slower dynamic are represented in dependence on the volume amount of methanol in toulene solution in Figure 3.17.

Quantum Chemical Calculations

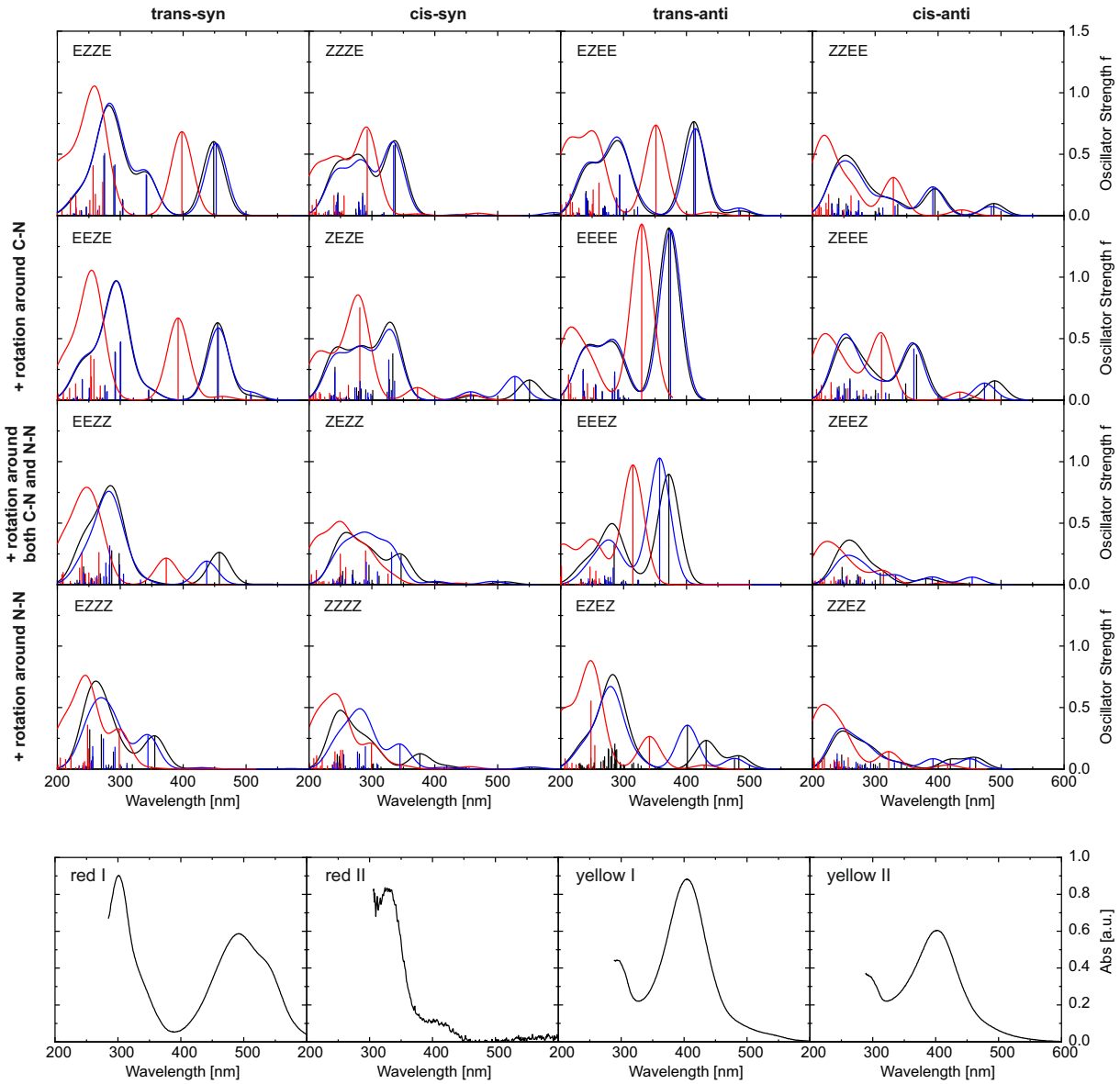

Figure A.15: Comparison of the calculated absorption spectra using B3LYP/def2-TZVP (black), B3LYP/def2-TZVP/D4 (blue) and CAM-B3LYP/def2-TZVP/D4 (red). The stick spectra were convoluted with Gaussians of 40 nm width at half maximum in all cases. The orientations with respect to the N=N and C=N double bonds are identical within each column, whereas the ones with respect to the C−N and N−N single bond are the same for each row. For the bottom row, refer to the description of the experimental spectra in the caption of Figure 3.11.

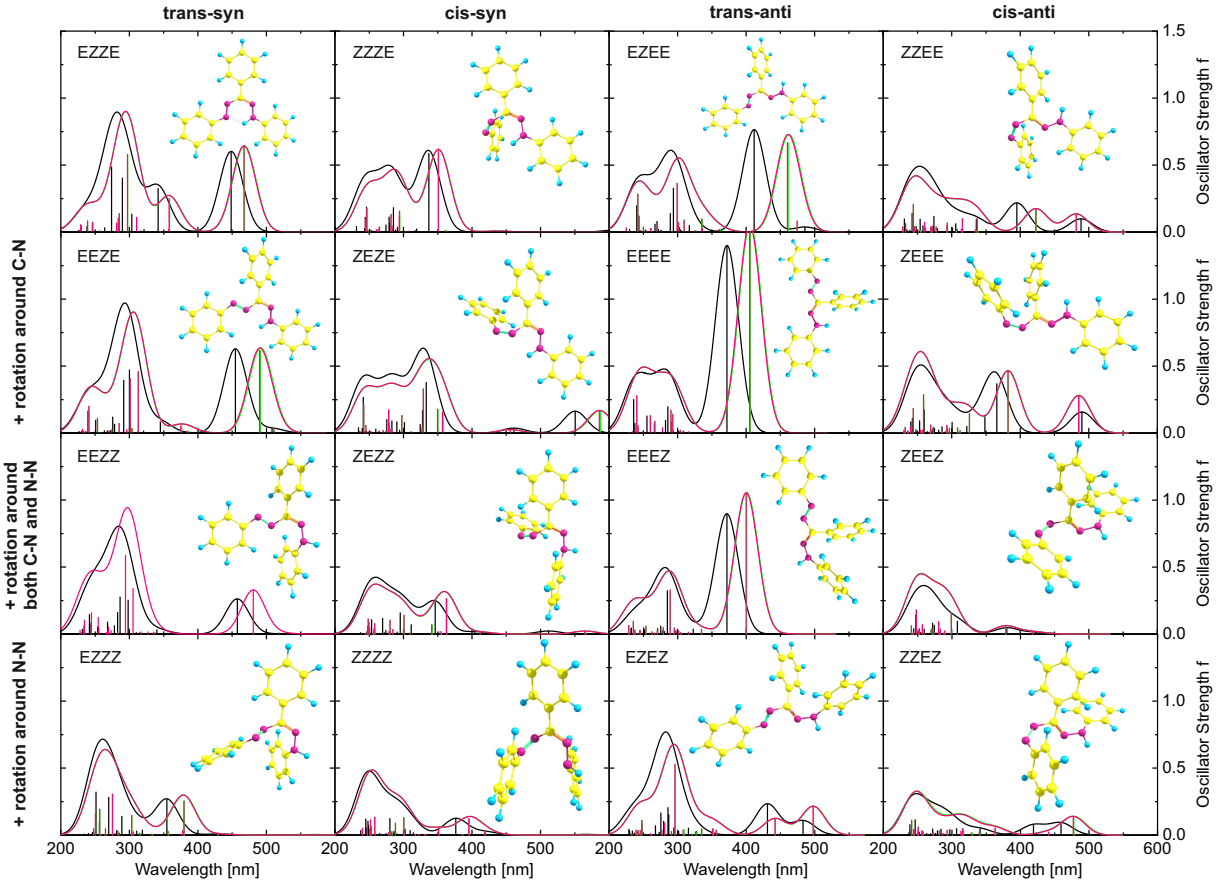

Figure A.16: Results from DFT (B3LYP/def2-TZVP; black = gas phase, magenta = CPCM(methanol); green = CPCM(acetonitrile)) calculations for the 16 isomers considered in this study. The optimized ground-state geometries are displayed together with the calculated absorption spectra (the oscillator strengths at the corresponding transition energies are given as stick spectrum convoluted each with a Gaussian of a 40 nm width at half maximum). The orientations with respect to the N=N and C=N double bonds are identical within each column, whereas the ones with respect to the C–N and N–N single bond are the same for each row.

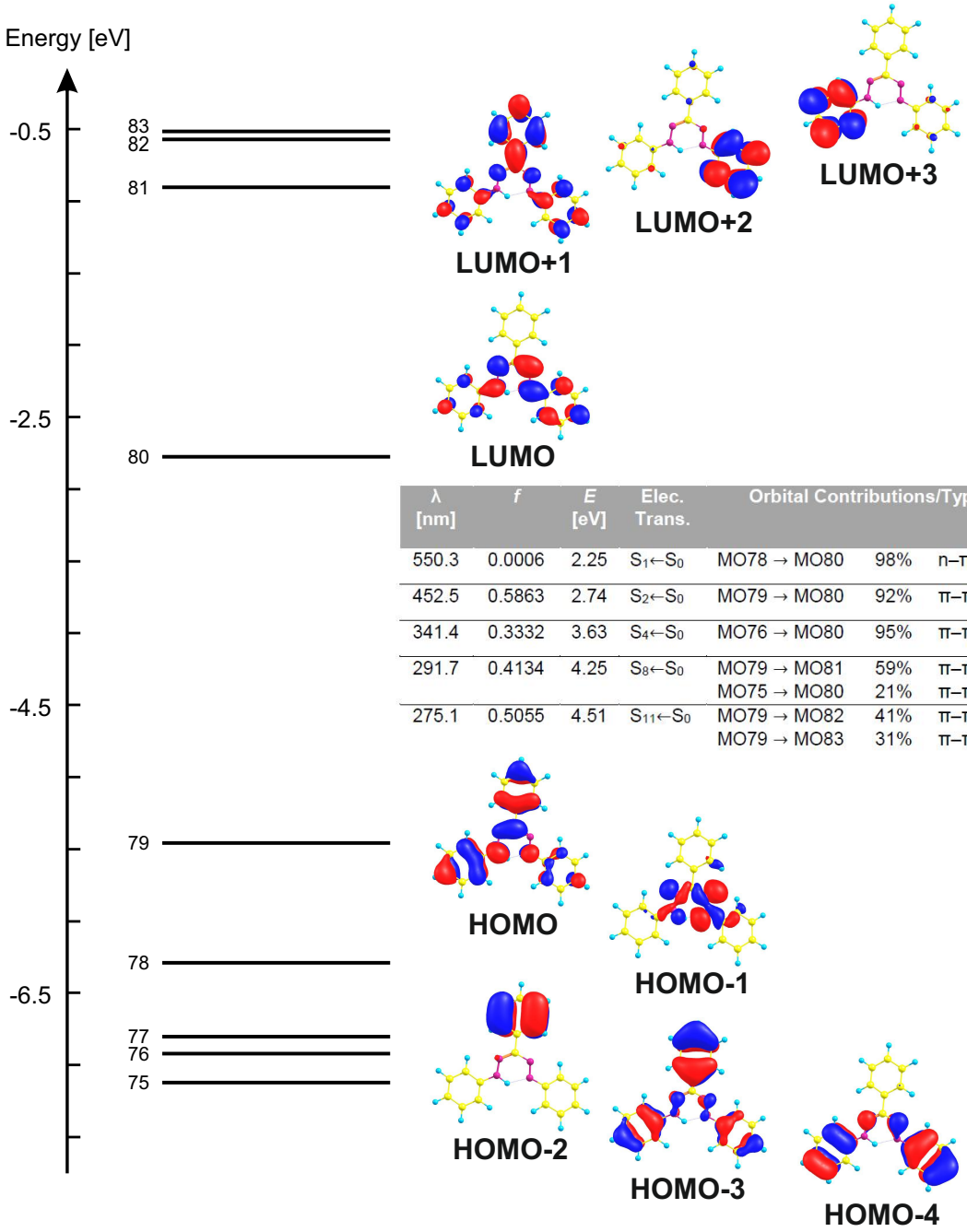

λ [nm]	*f*	*E* [eV]	Elec. Trans.	Orbital Contributions/Type		
550.3	0.0006	2.25	$S_1 \leftarrow S_0$	MO78 → MO80	98%	n–π*
452.5	0.5863	2.74	$S_2 \leftarrow S_0$	MO79 → MO80	92%	π–π*/CT
341.4	0.3332	3.63	$S_4 \leftarrow S_0$	MO76 → MO80	95%	π–π*
291.7	0.4134	4.25	$S_8 \leftarrow S_0$	MO79 → MO81	59%	π–π*
				MO75 → MO80	21%	π–π*
275.1	0.5055	4.51	$S_{11} \leftarrow S_0$	MO79 → MO82	41%	π–π*/CT
				MO79 → MO83	31%	π–π*/CT

Figure A.17: Molecular orbitals of the EZZE isomer based on TD-DFT calculations with B3LYP/def2-TZVP/D4 level of theory. The relevant highest occupied (HOMO) and lowest unoccupied molecular orbitals (LUMO) are represented as isosurface (contour value = 0.03). The table summarizes the calculated vertical transition energy, oscillator strength f, involved orbitals with contributions >10 %, and transition type of the four main transition bands of EZZE. Also the lowest electronic transition of n–π^* character is included.

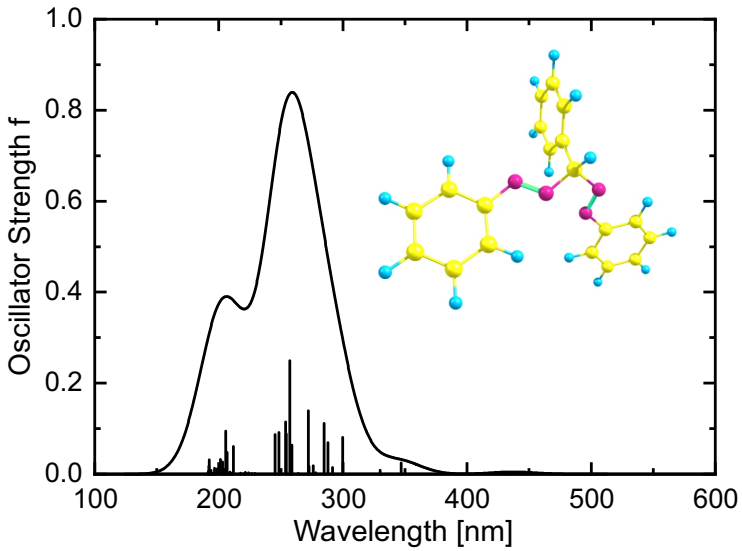

Figure A.18: Results from a DFT (B3LYP/def2-TZVP/D4) calculation for a structure where the hydrogen atom is bound to the carbon atom rather than to a nitrogen atom like in TPF, resulting in two azo groups instead of a combination of one azo and one hydrazone group as in TPF. The optimized ground-state geometry is displayed together with the calculated absorption spectrum (the oscillator strengths at the corresponding transition energies are given as stick spectrum convoluted with a Gaussian of a 40 nm width at half maximum).

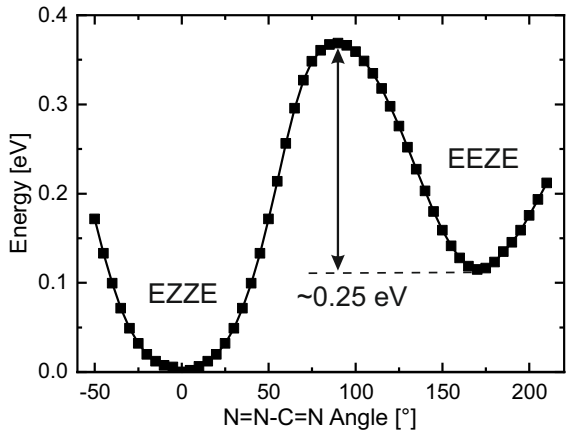

(a) rotation was monitored in 5° steps

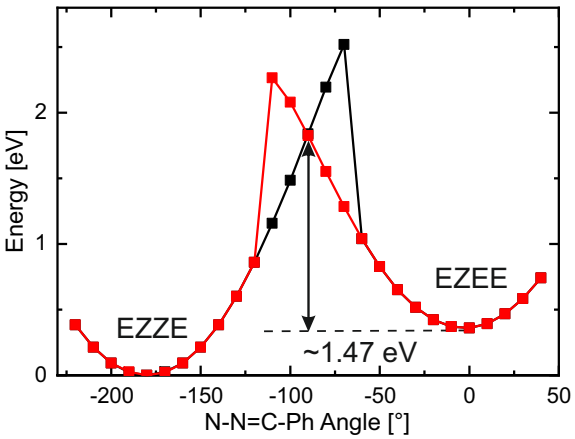

(b) Orca 4.2.1

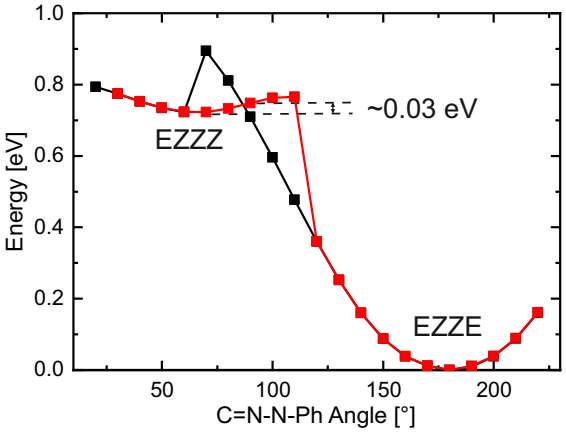

(c) -

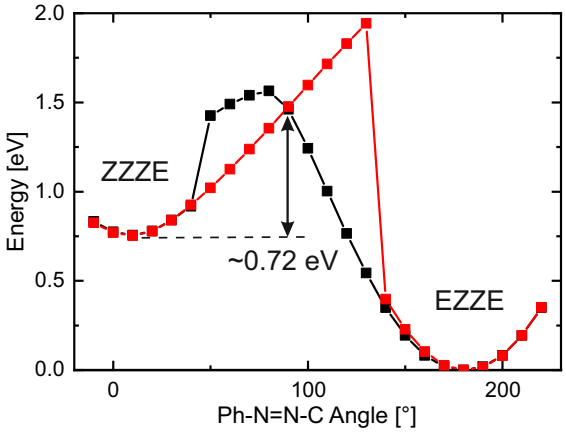

(d) Orca 4.2.1

N−N=C 121.36° FS
(Ph)C−N−N=C 73.9° BS

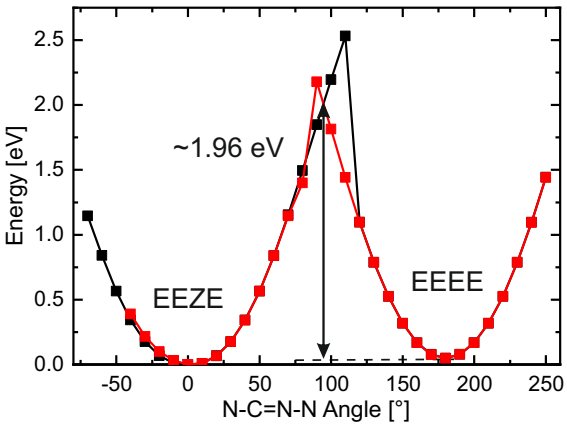

(e) -

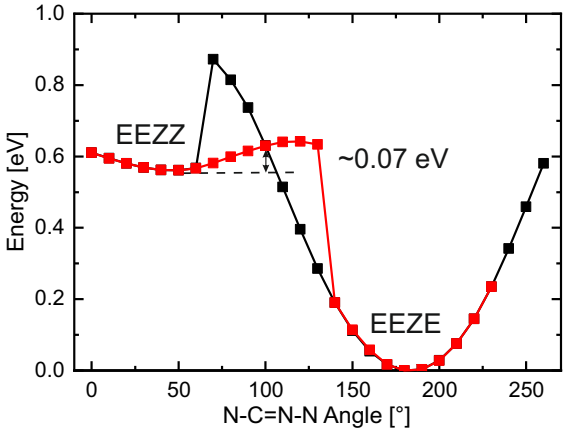

(f) -

Relaxed surface scan along a fixed torsional angle to estimate the barrier between different isomeric species of TPF. Additional constraints are mentioned in each subcaption. black: forward scan (FS), red: back scan (BS)

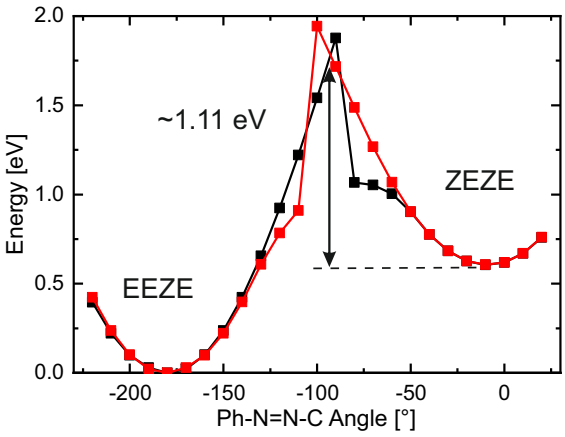

(g) C−N=N 120° FS / BS

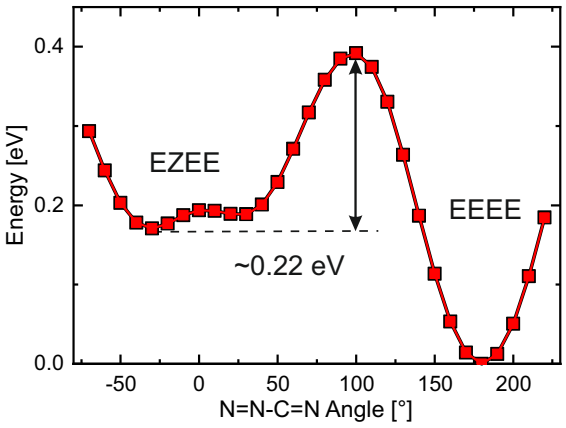

(h) -

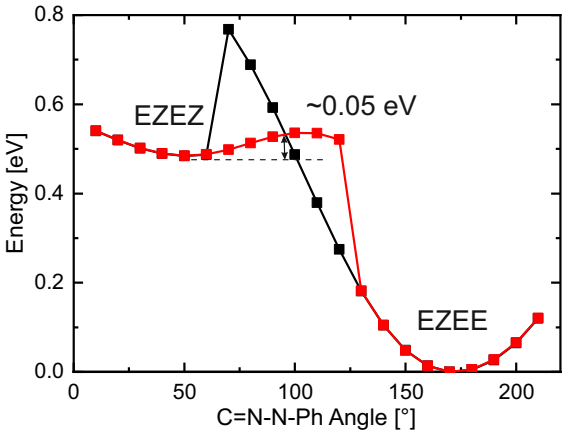

(i) -

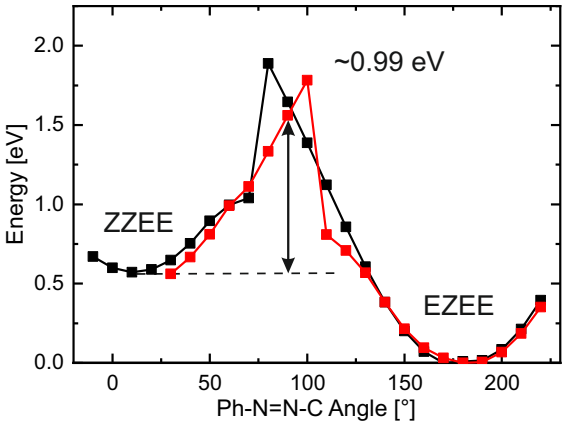

(j) C−N=N 125.551° BS

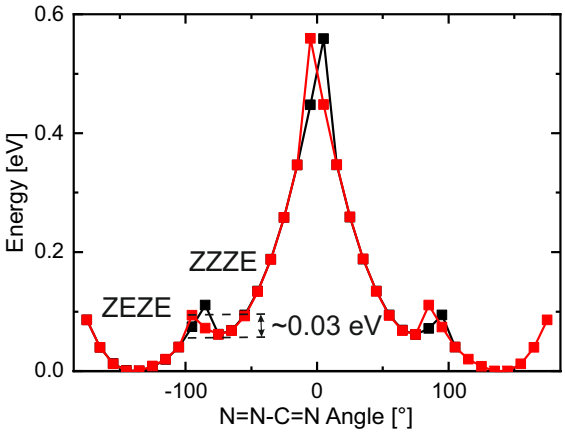

(k) -

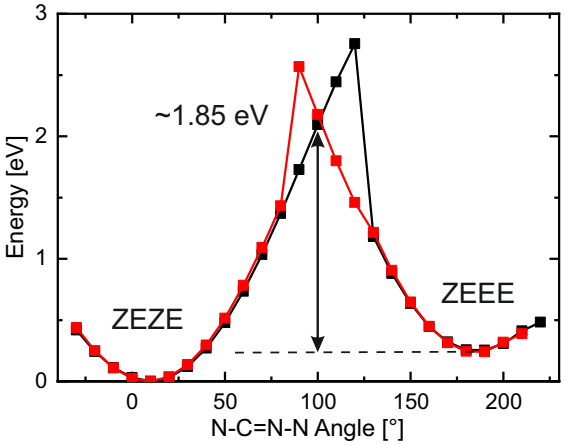

(l) C−N=N−C(Ph) 12° FS / BS
C=N−N 120° FS / BS
C−N=N 124° BS
C−N=N−H 1° BS

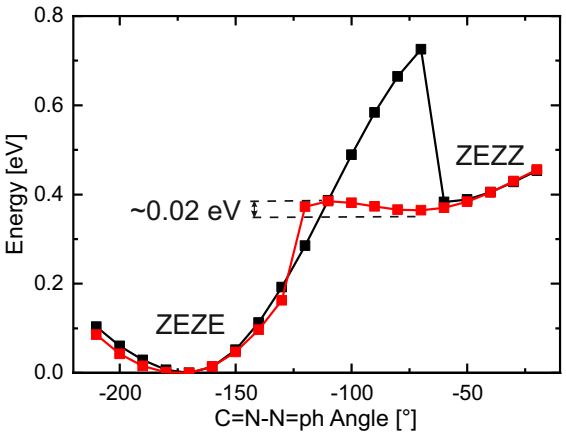

(m)

N=C−N=N	254°	FS

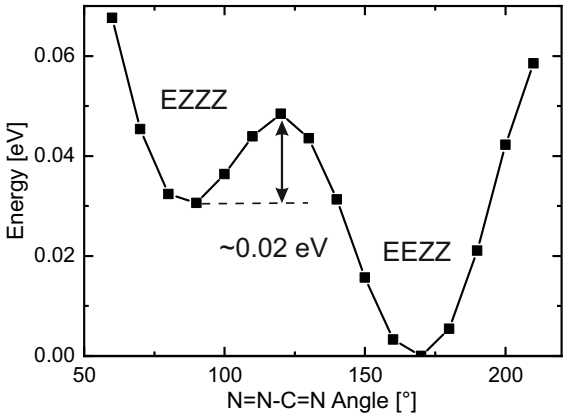

(n) -

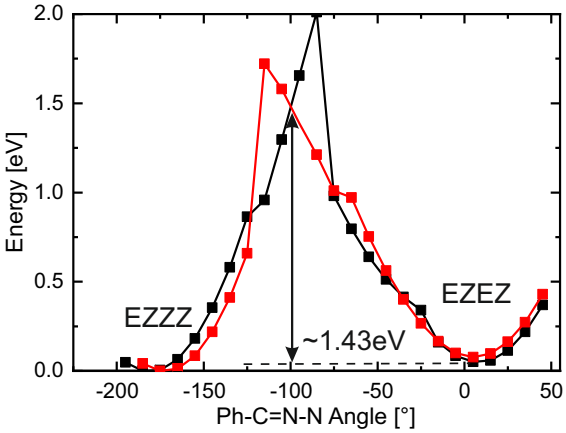

(o)

C=N−N	124°	FS
C=N−N−C(Ph)	50°	FS
C−N=N−C(Ph)	178°	FS / BS

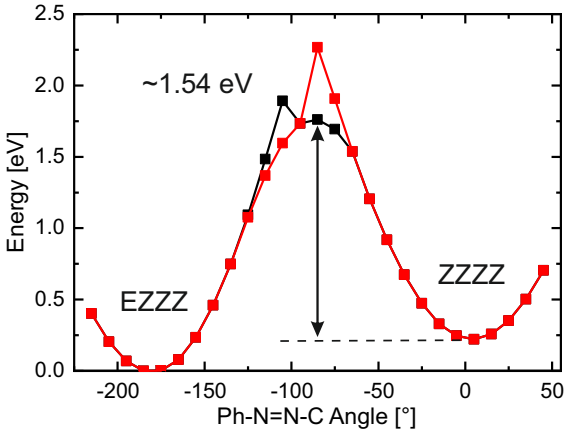

(p)

C=N−N−H	158°	FS
C−N=N	125°	FS
N=C−N=N	75°	FS
N=N−C(Ph)	123°	FS / BS

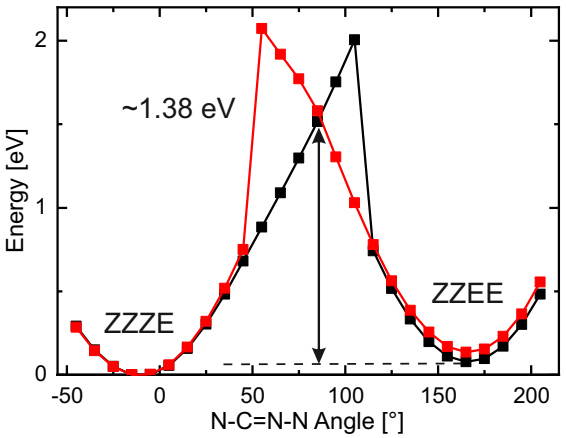

(q)

C=N−N	121°	FS
C−N=N	125°	FS / BS
C−N=N−C(Ph)	10°	FS / BS
N=N−C(Ph)−C(Ph)	30°	BS

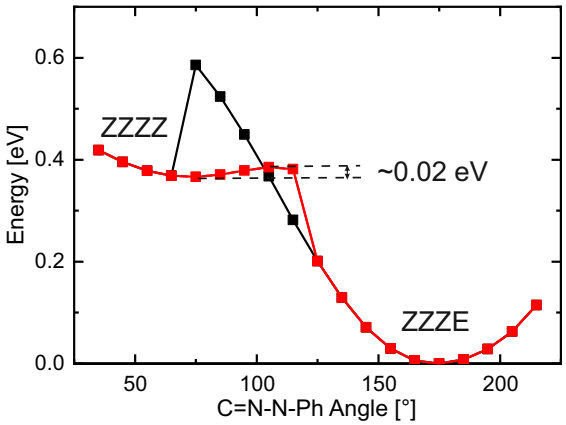

(r) -

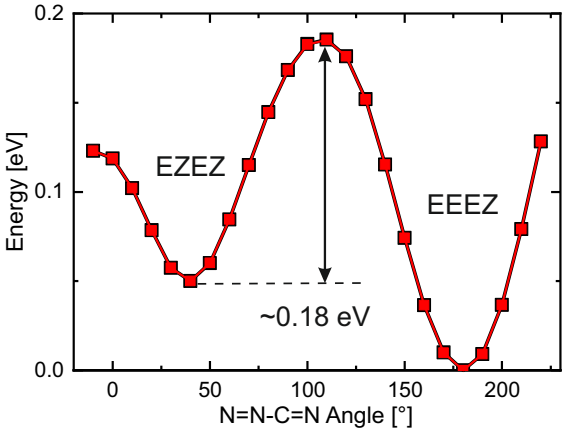

(s) -

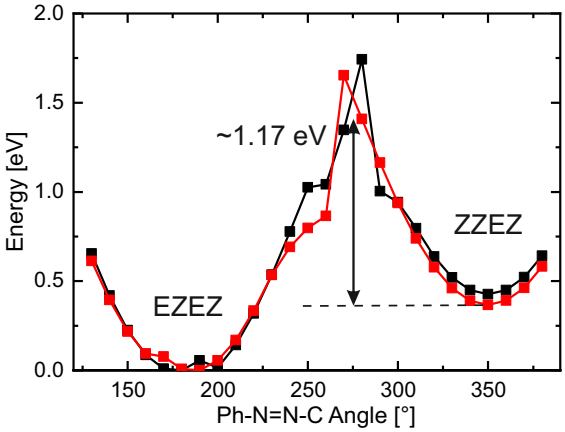

(t) C−N=N 124.787° BS

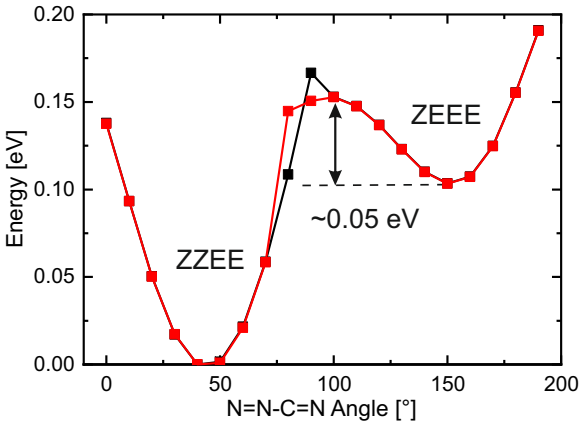

(u) -

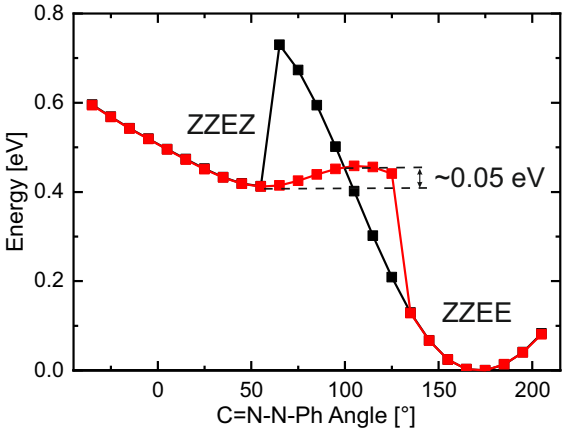

(v) -

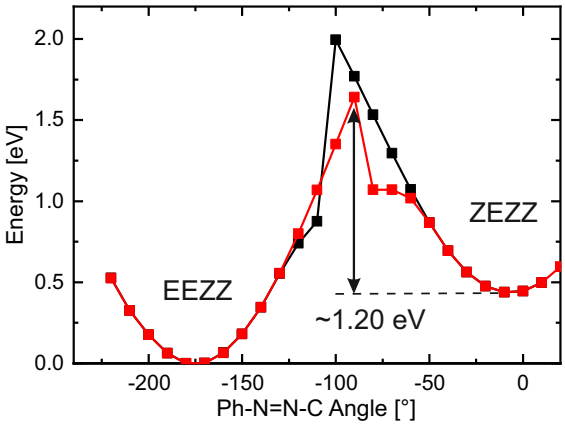

(w) C−N=N 120° FS
C=N−N−C(Ph) 40° FS / BS

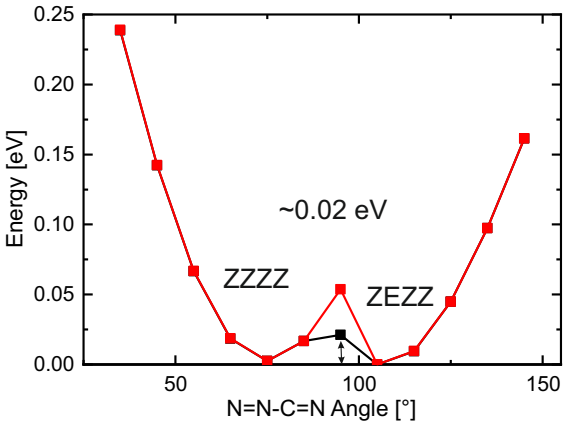

(x) C=N−N−C(Ph) 68.5° FS / BS

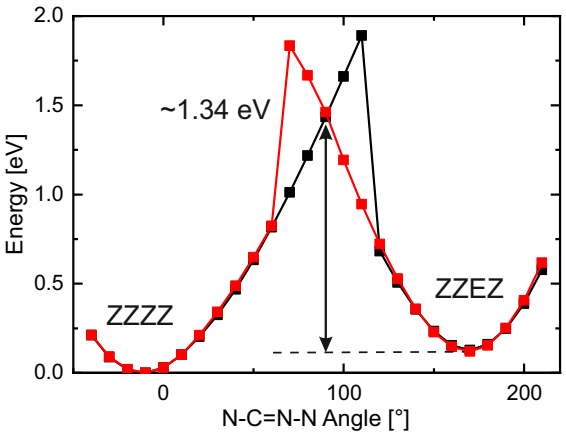

(y) N−C=N−N 8° FS
N−C=N−N 10° BS
C=N−N 122° FS
C−N=N 125° FS

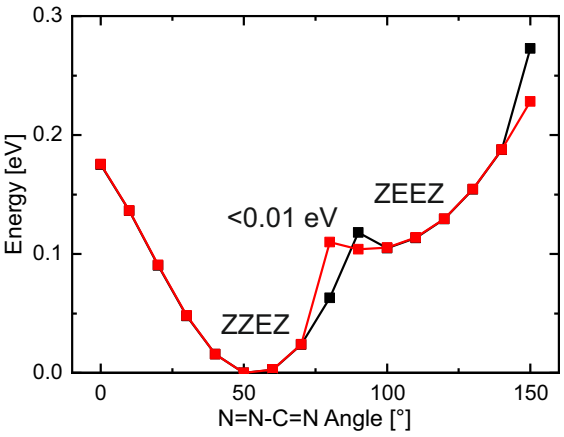

(z) -

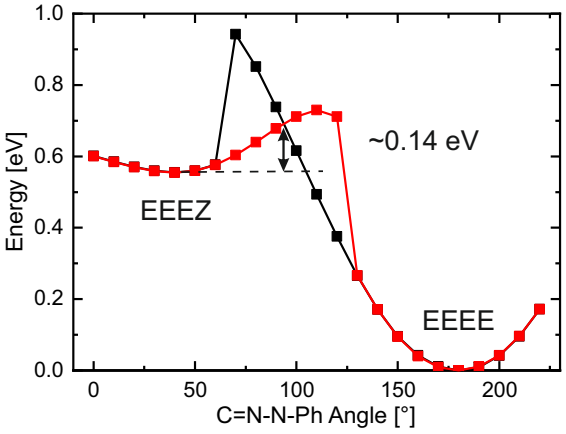

(aa) C=N−N−C(Ph) 179.8° FS / BS

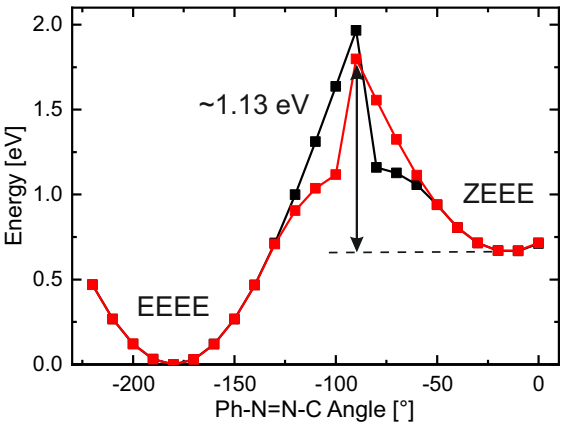

(ab) N=N−C(Ph) 124° FS / BS

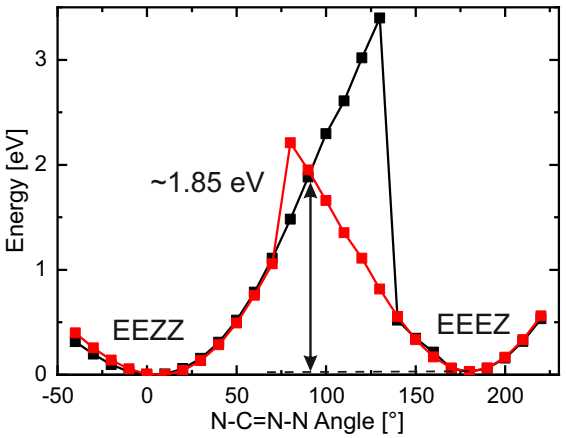

(ac) C=N−N−C(Ph) 41.120° FS
C=N−N−C(Ph) 40° BS
C=N−N 124.133° FS
N=C−N=N 180°

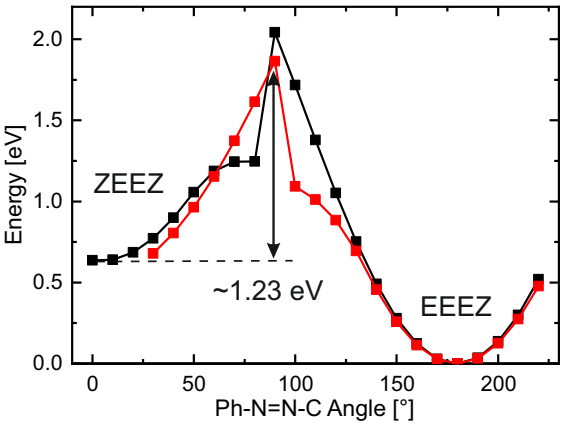

(ad) C−N=N 120° FS
C−N=N 120° BS
N=N−C(Ph) 123° FS

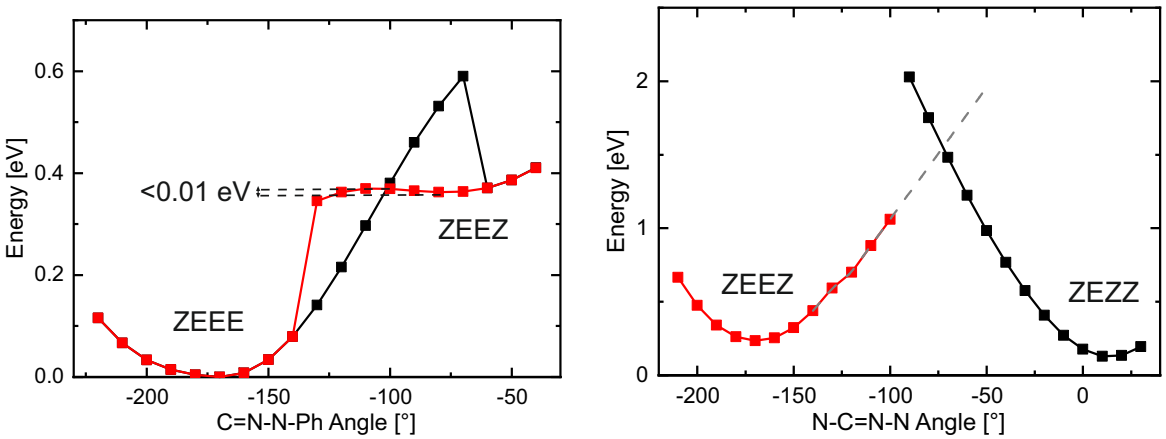

(ae) N=C−N=N 93° BS

(af) energy barrier only roughly estimated by extrapolation (gray dashed line) since the calculations did not converge;
N=C−N=N 254° FS
C=N−N 120° FS / BS

Figure A.19: Relaxed surface scan along a fixed torsional angle to estimate the barrier between different isomeric species of TPF. The calculations were carried out with Orca 5.0.1 (except where stated otherwise) at the UKS/B3LYP/def2-TZVP level of theory by optimizing all structural parameters except of the fixed torsional angle. The rotation was monitored in 10° steps from the energetically more stable to the energetically more unfavorable isomeric species (black) and vice versa (backscan [BS] red). Variations of the here described parameters are mentioned in the sub-caption of each individual scan.

APPENDIX B

Tropylium Salts

Steady-State Spectra

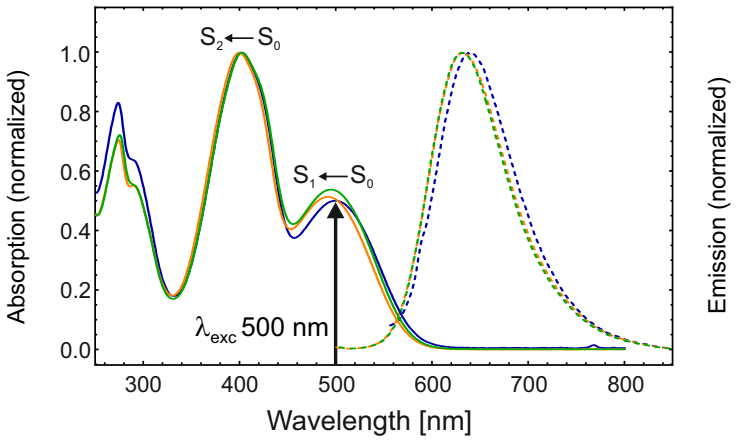

Figure B.1: Comparison of the normalized steady-state UV-Vis (solid curves) and emission spectra (dashed curves), recorded after 500 nm excitation, of the dyes $\mathbf{1}^+$ (blue), $\mathbf{2}^+$ (orange), and $\mathbf{3}^+$ (green).

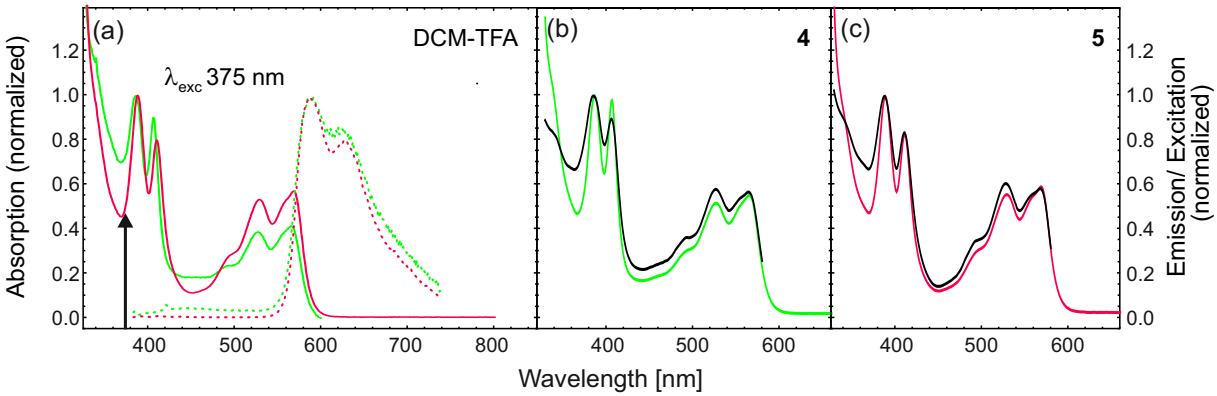

Figure B.2: Comparison of the normalized absorption (solid colored lines) and fluorescence spectra after excitation at 375 nm (dashed lines) of $\mathbf{4}^{+}$ (green) and $\mathbf{5}^{+}$ (pink), dissolved in a DCM-TFA mixtures, stabilizing their protonated species $\mathbf{4H}^{2+}$ and $\mathbf{5H}^{2+}$, respectively. The corresponding excitation spectra are included as solid black lines and are nearly equivalent for both emission bands around 525 nm and 565 nm.

ps-ns Time-Resolved Emission Spectroscopy – Streak Camera

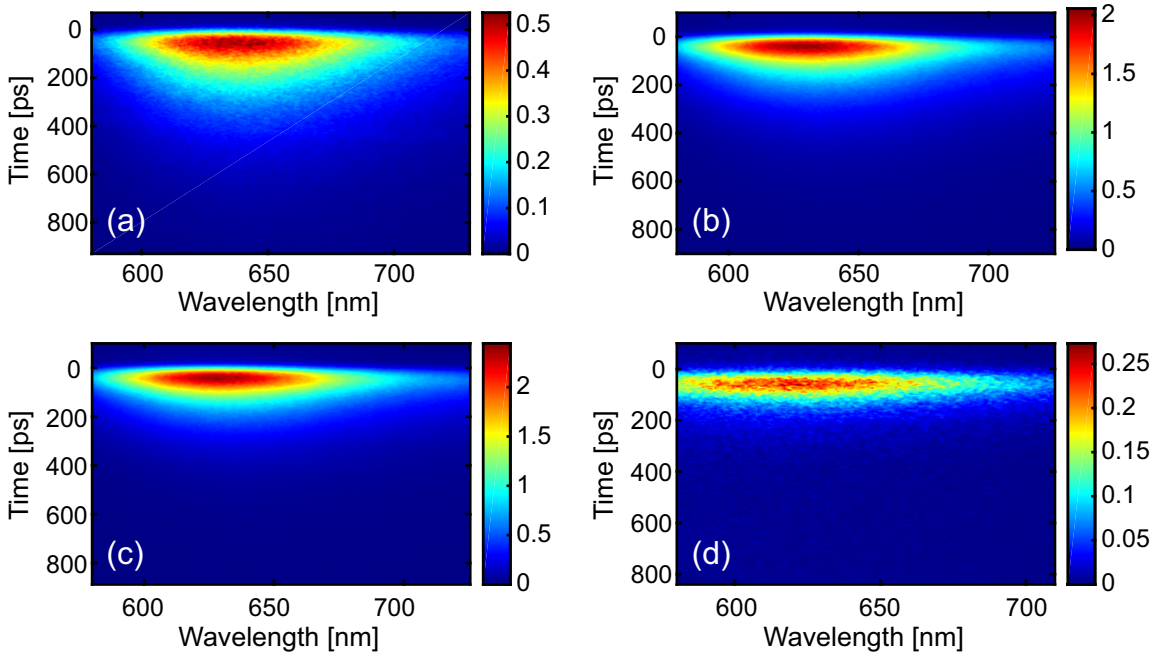

Figure B.3: Time-resolved fluorescence spectra of (a) $\mathbf{1}^{+}$,(b) $\mathbf{2}^{+}$, (c) $\mathbf{3}^{+}$ and (d) $\mathbf{4}^{+}$ after excitation at 405 nm in DCM.

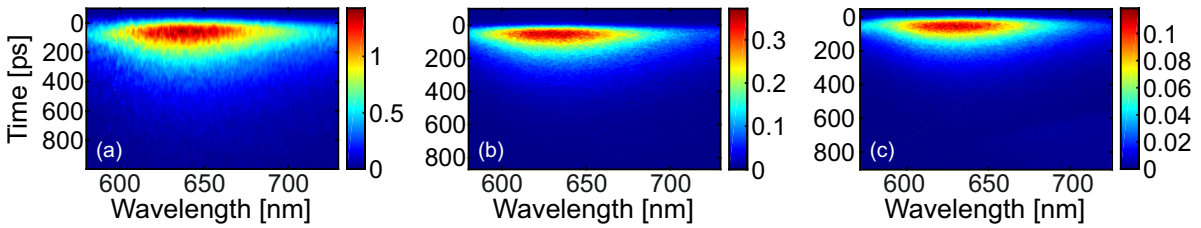

Figure B.4: Time-resolved fluorescence spectra of (a) $\mathbf{1}^{+}$,(b) $\mathbf{2}^{+}$, and (c) $\mathbf{3}^{+}$ after excitation at 266 nm in DCM.

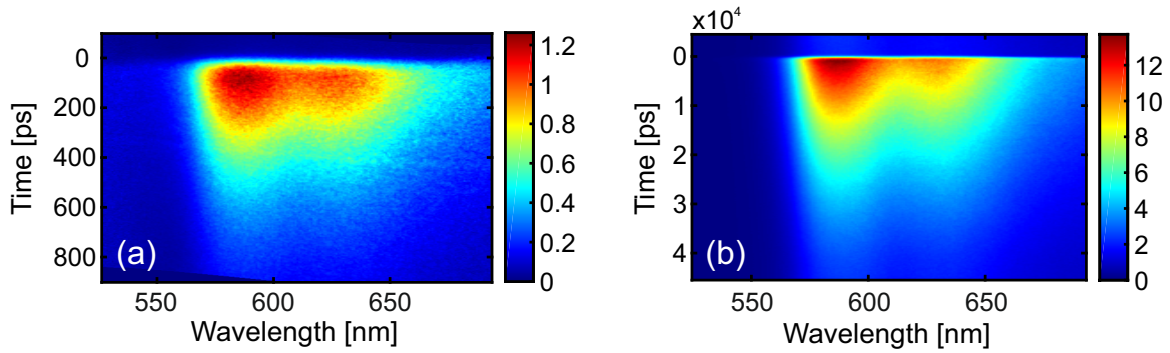

Figure B.5: Time-resolved fluorescence spectra detected after excitation at 405 nm of (a) $\mathbf{4H}^{2+}$ in DCM-TFA solution and (b) $\mathbf{5H}^{2+}$ in a freshly prepared DCM solution.

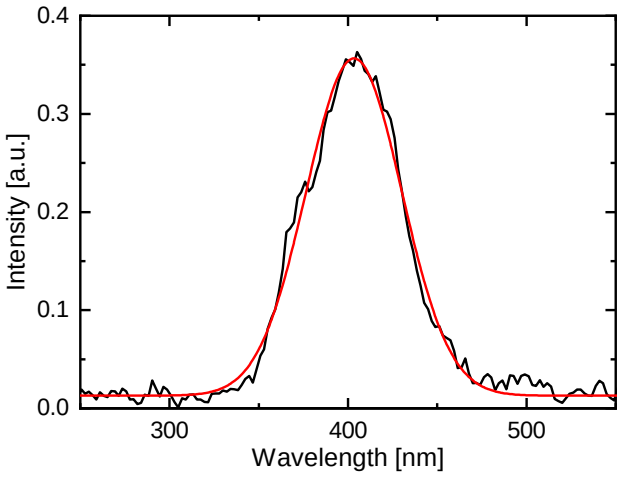

Figure B.6: Spectral profile of the 405 nm LED, used as excitation source within the ps-ns time-resolved emission setup with the streak camera (black). The IRF was determined by a Gaussian function fit to 54 ps (FWHM).

ns Time-Resolved Emission Spectroscopy – TCSPC

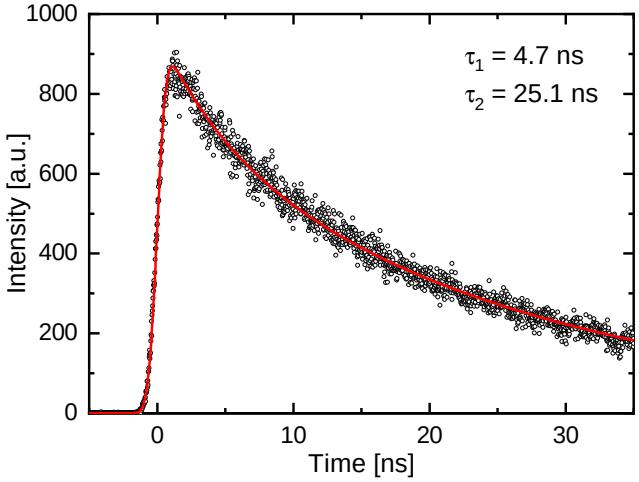

Figure B.7: Time-resolved fluorescence trace of $\mathbf{5H^{2+}}$ in DCM stabilized with 0.1 M TFA measured with the ns-TCSPC after excitation at 370 nm. The data were fitted biexponentially (red curve). Thereby τ_2 can be attributed to the emission of $\mathbf{5H^{2+}}$ and τ_1 might be caused by still unprotonated species $\mathbf{5^{+}}$.

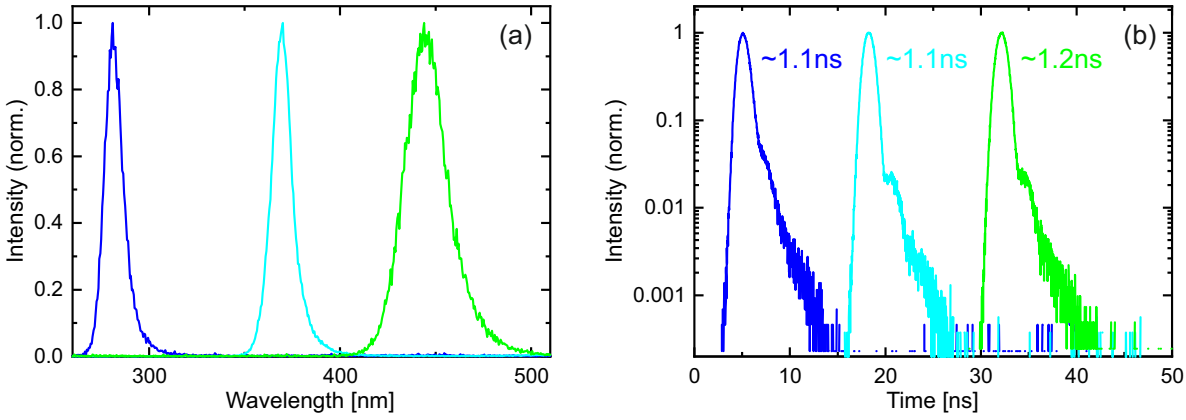

Figure B.8: Spectral and temporal characteristics of the available pulsed LEDs used within the ns-TCSPC setup. (a) Emission spectra and (b) pulse profile of the 280 nm- (blue), 370 nm- (cyan) and 445 nm-LED (green). The stated pulse width (FWHM) was determined with a Gaussian fit to the measured functions.

fs-ns Time-Resolved Emission Spectroscopy – Fluorescence Upconversion

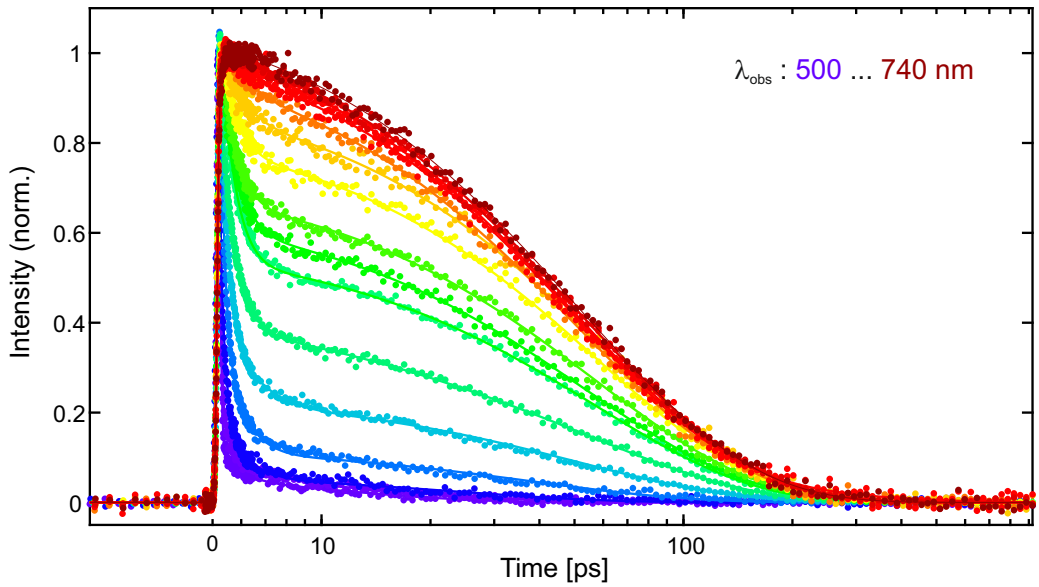

Figure B.9: Emission decays of $\mathbf{2}^{+}$ in DCM after excitation at 400 nm by fs-upconversion experiments. The data were analyzed by wavelength-dependent biexponential fit.

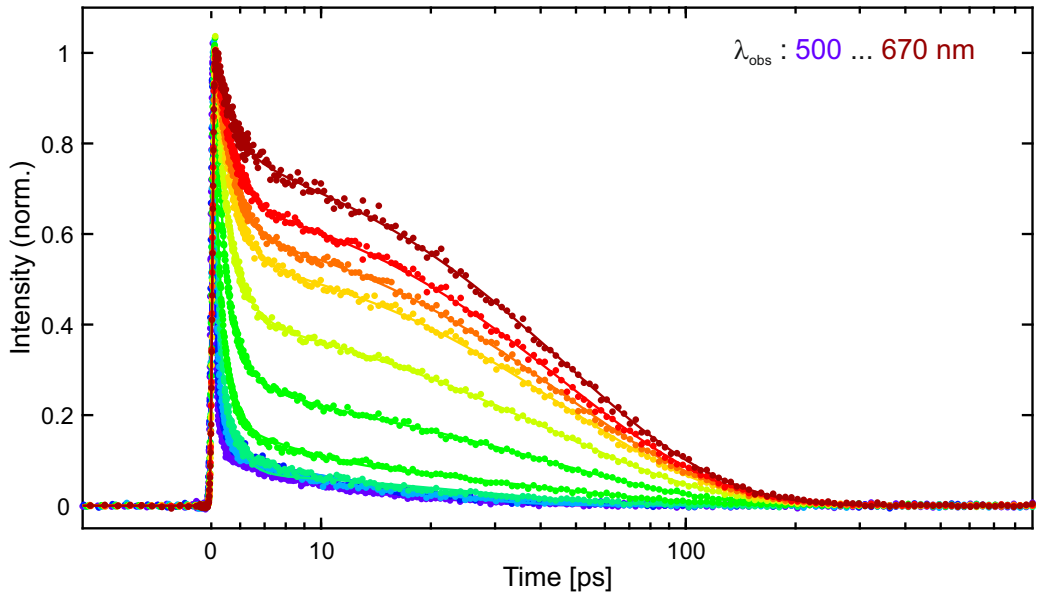

Figure B.10: Emission decays of $\mathbf{3}^{+}$ in DCM after excitation at 400 nm by fs-upconversion experiments. The data were analyzed by a wavelength-dependent biexponential fit.

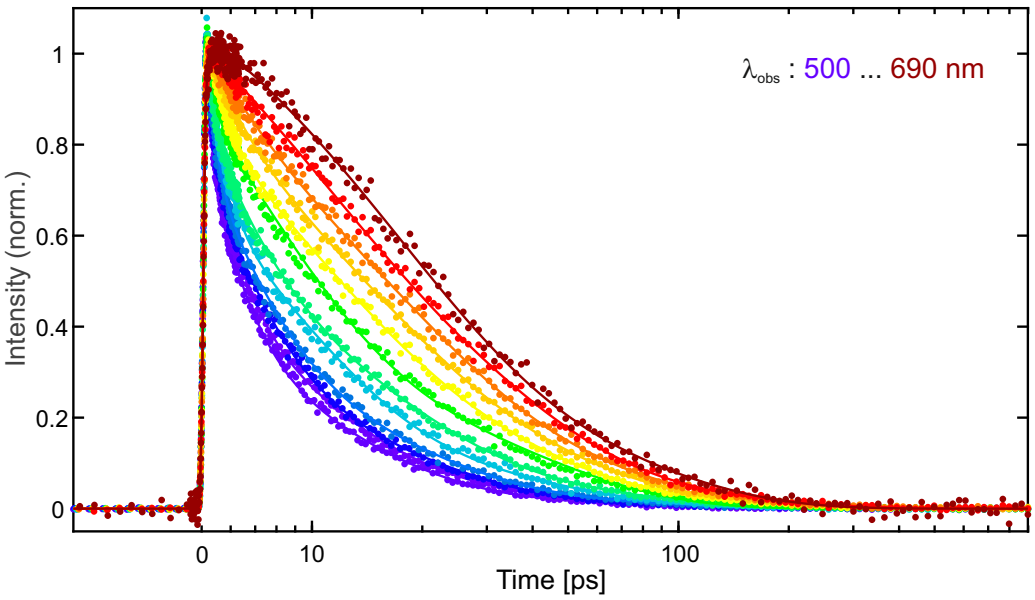

Figure B.11: Emission decays of $\mathbf{4}^{+}$ in DCM after excitation at 400 nm by fs-upconversion experiments. The data were analyzed by a wavelength-dependent biexponential fit.

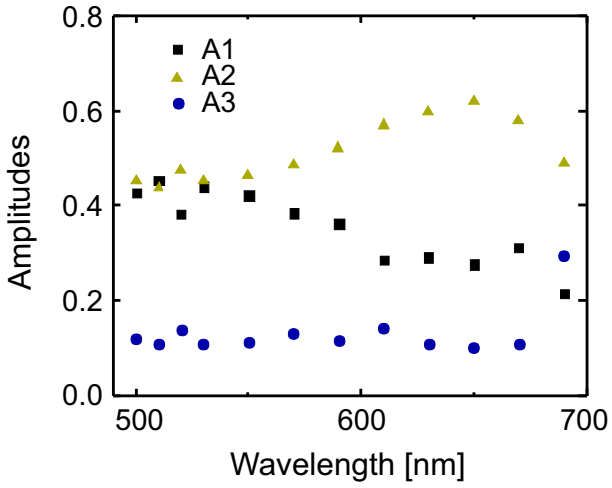

Figure B.12: Amplitudes of the three emission decays of dye $\mathbf{4}^{+}$ in DCM, obtained by a wavelength-dependent triexponential fitting model. The corresponding temporal fluorescence decays were recorded by time-resolved upconversion spectroscopy after excitation at 400 nm.

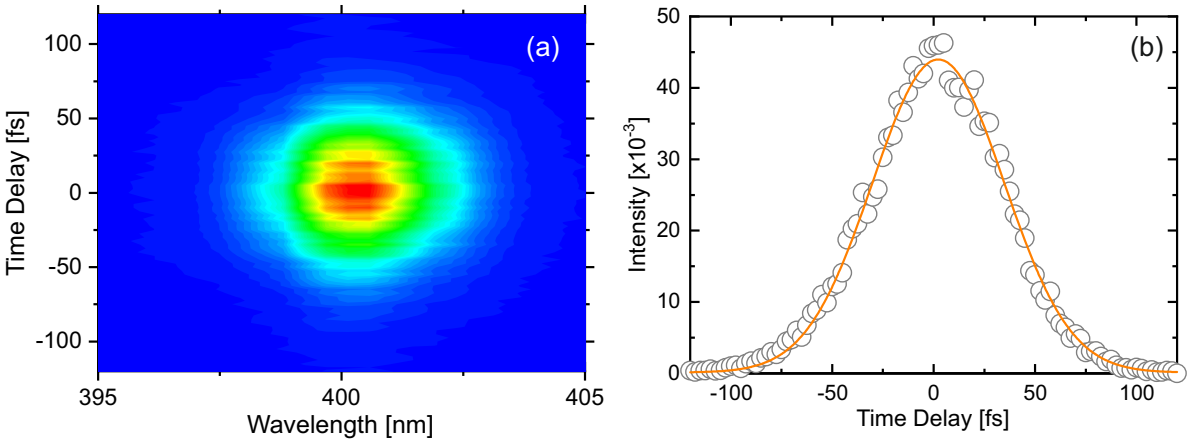

Figure B.13: (a) Measured SHG-FROG trace of the laser pulses generated by the Mira oscillator. Analysis with the program FROG[512;513] developed by Dr. Kenneth De Long yielded a temporal width of 72 fs (FWHM) and an autocorrelation width of 107 fs (FWHM). (b) Temporal profile of the recorded FROG trace at 400.6 nm with a Gaussian fit. Further information regarding the phase and the amplitude of the electric field of the short pulses generated by the Mira are reported in Ref. [514].

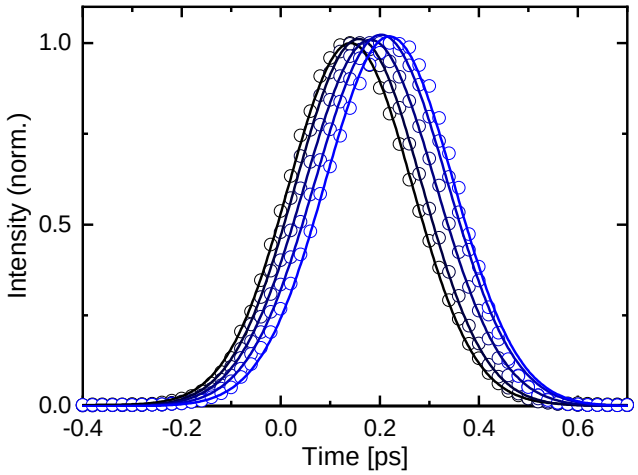

Figure B.14: IRFs of the fluorescence upconversion measured *via* the Raman band of H_2O after excitation at 400 nm, observed between 450 nm and 470 nm in 5 nm steps. The fitted Gaussian functions result in an IRF(FWHM) of ∼250 fs.

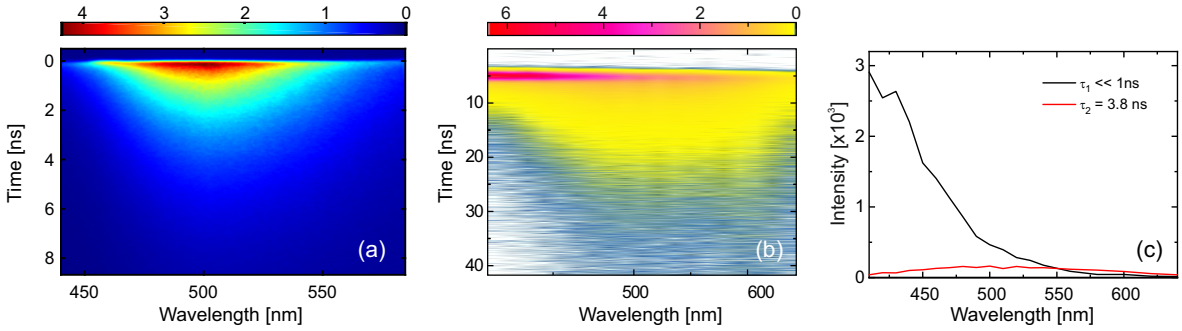

Figure B.15: (a) Time-resolved fluorescence of the 500 nm emission band of presumably **6-OH** in DCM detected after excitation at 405 nm with the ps-ns Streak Camera setup. Global lifetime analysis yielded a time constant of ∼3 ns. (b) Time-resolved fluorescence monitored with the ns-TCSPC setup after excitation at 370 nm of $\mathbf{6H^{2+}}$ in DCM-TFA solution. This map was reconstructed by several emission decay traces between 410 nm and 650 nm measured in 10 nm steps. A global lifetime analysis with two exponential functions results in the DADS shown in (c). The shorter dynamic falls below the IRF and corresponds to the emission signal of $\mathbf{6H^{2+}}$, while the longer dynamic with 3.8 ns presumably describes the emission decay of the still unknown 500 nm emitting species (equivalent to the spectra in (a)), which might be the **6-OH** adduct.

Quantum Chemical Calculations

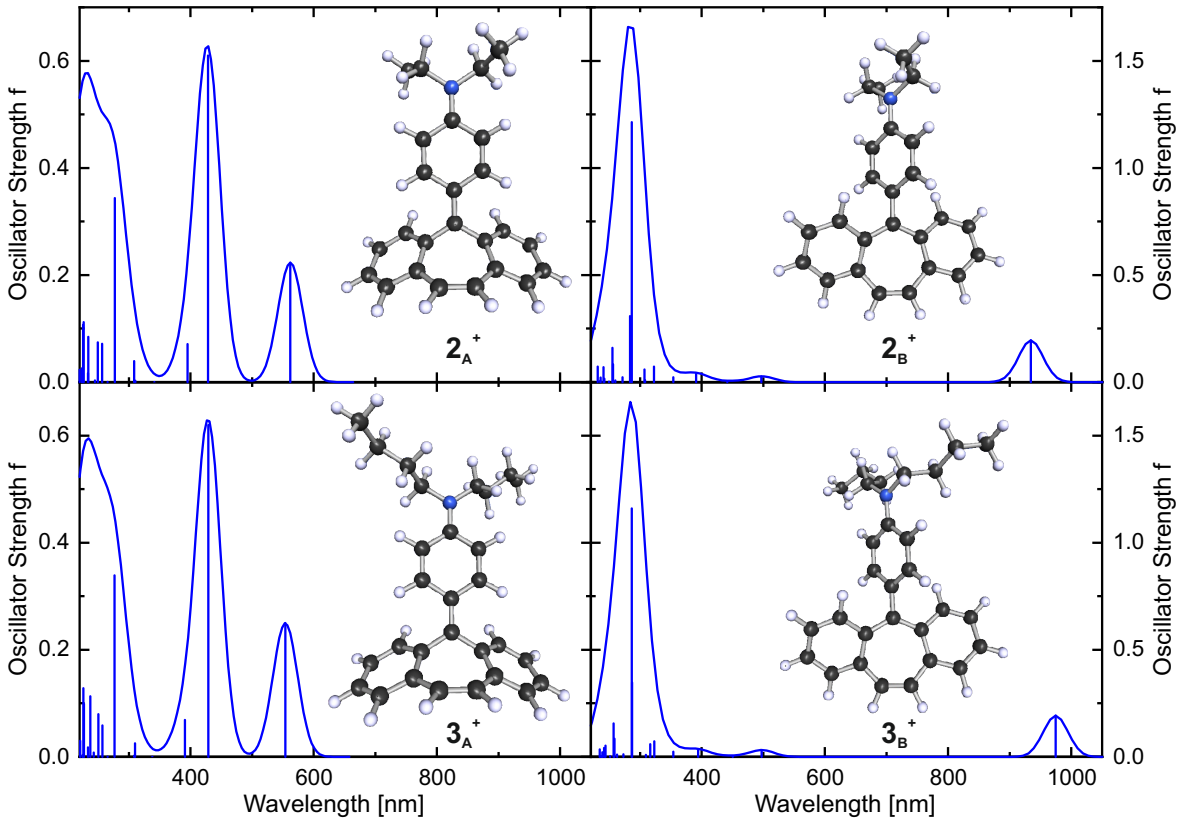

Figure B.16: Two stable ground state structures **A** and **B** were computationally found for $\mathbf{2}^{+}$ and $\mathbf{3}^{+}$ by DFT calculations on the B3LYP/def2-TZVP level of theory. For both optimized geometries, vertical excitation transitions without solvent environment were calculated (ADC2/aug-cc-pVDZ). Convolution of each oscillator strength corresponding to a distinct transition energy with a Gaussian of 20 nm width at half maximum results in the displayed UV-Vis spectra.

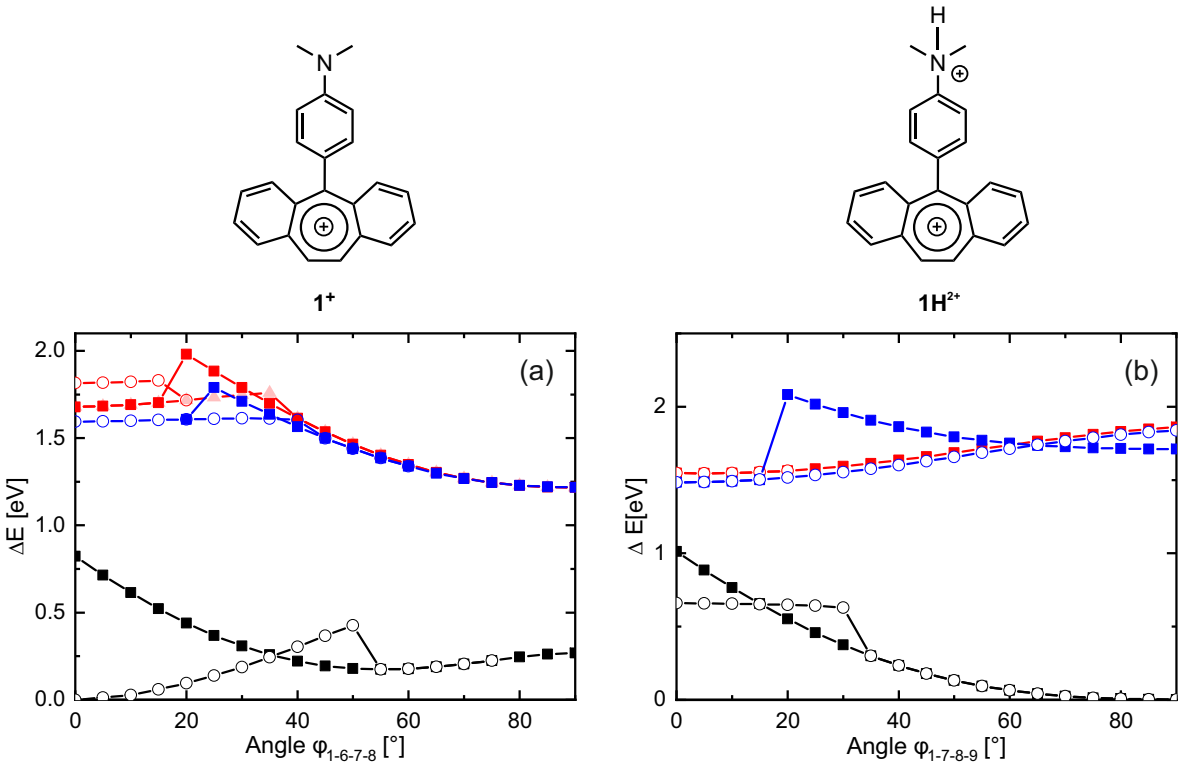

Figure B.17: Potential energy surface (PES) scans along the dihedral angle $C_1{-}C_7{-}C_8{-}C_9$, defining the twist between the DBTrop part and the DMA moiety of $\mathbf{1}^+$ (a) and $\mathbf{1H}^{2+}$ (b), in the ground state S_0 (black), the first excited singlet state S_1 (red) and the first triplet state T_1 (blue). Both potential energy surface scans were performed by starting from both conformers **A** (circles) and **B** (rectangles). However, for $\mathbf{1}^+$ in the excited singlet state S_1 an additional conformer $(\mathbf{1}^+_{\mathbf{A}})^*_{\mathbf{twisted}}$, characterized by a $\sim$90° twist within the aniline part, has to be considered (triangles). In the case of $\mathbf{1}^+$ there is no stable conformer **B** in the first excited state.

Table B.1: The twist angle φ of $\mathbf{1}^+$ is calculated from the two dihedral angles $\varphi_{6-7-8-13}$ and $\varphi_{1-7-8-9}$ *via* $\frac{1}{2}(\varphi_{6-7-8-13} + \varphi_{1-7-8-9})$.

Compound	**Conformer A**			**Conformer B**		
	$\varphi_{6-7-8-13}$	$\varphi_{1-7-8-9}$	φ	$\varphi_{6-7-8-13}$	$\varphi_{1-7-8-9}$	φ
$\mathbf{1}^+$	4.46	4.51	4.49	55.86	55.86	55.86
$\mathbf{2}^+$	4.32	4.16	4.24	54.27	54.28	54.28
$\mathbf{3}^+$	4.13	4.24	4.19	54.33	54.05	54.19
$\mathbf{4}^+$	1.51	1.66	1.59	68.01	68.03	68.02
$\mathbf{5}^+$	2.53	2.60	2.57	73.97	73.93	73.95

Table B.2: Molecular orbitals of conformer **A** of compound $\mathbf{1}^+$ based on calculations with ADC2/aug-cc-pVDZ level of theory. The relevant highest occupied (HOMO) and lowest unoccupied molecular orbitals (LUMO) are represented as isosurface (contour value = 0.03). The table summarizes the calculated vertical transition energy, oscillator strength f, involved orbitals with contributions > 10%, and transition type of the five main transition bands of $\mathbf{1}^+_{\mathbf{A}}$.

Elec. Trans.	Contribution	HOMO		LUMO	
581.6 nm f = 0.198 E = 2.13 eV $S_1 \leftarrow S_0$	95.4 %	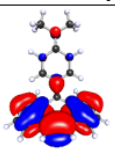	HOMO (MO82)	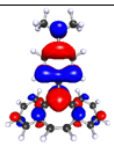	LUMO (MO83)
435.7 nm f = 0.564 E = 2.85 eV $S_2 \leftarrow S_0$	93.1 %	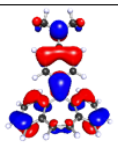	HOMO-1 (MO81)	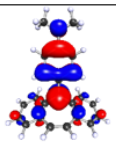	LUMO (MO83)
405.0 nm f = 0.076 E = 3.06 eV $S_3 \leftarrow S_0$	93.2 %	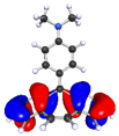	HOMO-2 (MO80)	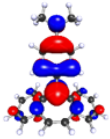	LUMO (MO83)
311.8 nm f = 0.035 E = 3.98 eV $S_6 \leftarrow S_0$	88.6 %	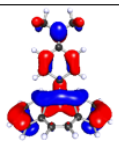	HOMO-4 (MO78)	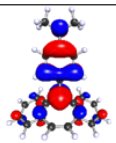	LUMO (MO83)
277.4 nm f = 0.349 E = 4.47 eV $S_7 \leftarrow S_0$	72.6 %	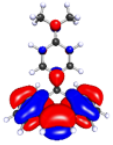	HOMO (MO82)	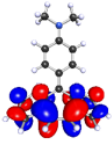	LUMO+5 (MO88)

Table B.3: Molecular orbitals of conformer **B** of compound $\mathbf{1}^+$ based on calculations with ADC2/aug-cc-pVDZ level of theory. The relevant highest occupied (HOMO) and lowest unoccupied molecular orbitals (LUMO) are represented as isosurface (contour value = 0.03). The table summarizes the calculated vertical transition energy, oscillator strength f, involved orbitals with contributions > 10%, and transition type of the five main transition bands of $\mathbf{1}_\mathbf{B}^+$.

Elec. Trans.	Contribution	HOMO	LUMO
876.8 nm f = 0.179 E = 1.41 eV $S_1 \leftarrow S_0$	91.9 %	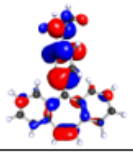 HOMO (MO82)	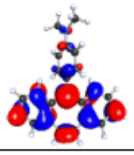 LUMO (MO83)
498.5 nm f = 0.026 E = 2.49 eV $S_2 \leftarrow S_0$	90.8 %	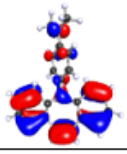 HOMO-1 (MO81)	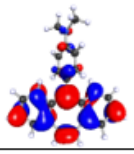 LUMO (MO83)
392.0 nm f = 0.045 E = 3.16 eV $S_4 \leftarrow S_0$	82.3 %	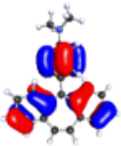 HOMO-2 (MO80)	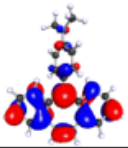 LUMO (MO83)
323.5 nm f = 0.067 E = 3.83 eV $S_8 \leftarrow S_0$	84.5 %	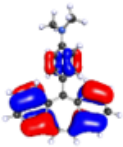 HOMO-4 (MO78)	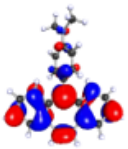 LUMO (MO83)
285.7 nm f = 1.252 E = 4.34 eV $S_9 \leftarrow S_0$	45.2 %	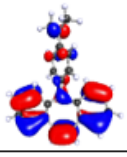 HOMO (MO81)	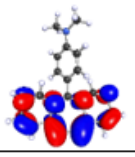 LUMO+1 (MO84)
	17.0 %	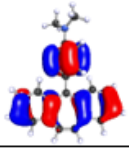 HOMO-3 (MO79)	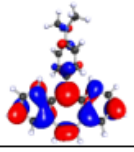 LUMO (MO83)
278.2 nm f = 0.248 E = 4.46 eV $S_{10} \leftarrow S_0$	32.6 %	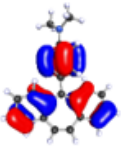 HOMO-2 (MO80)	LUMO+1 (MO84)
	26.2 %	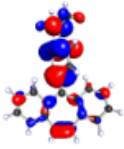 HOMO (MO82)	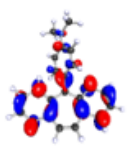 LUMO+14 (MO97)

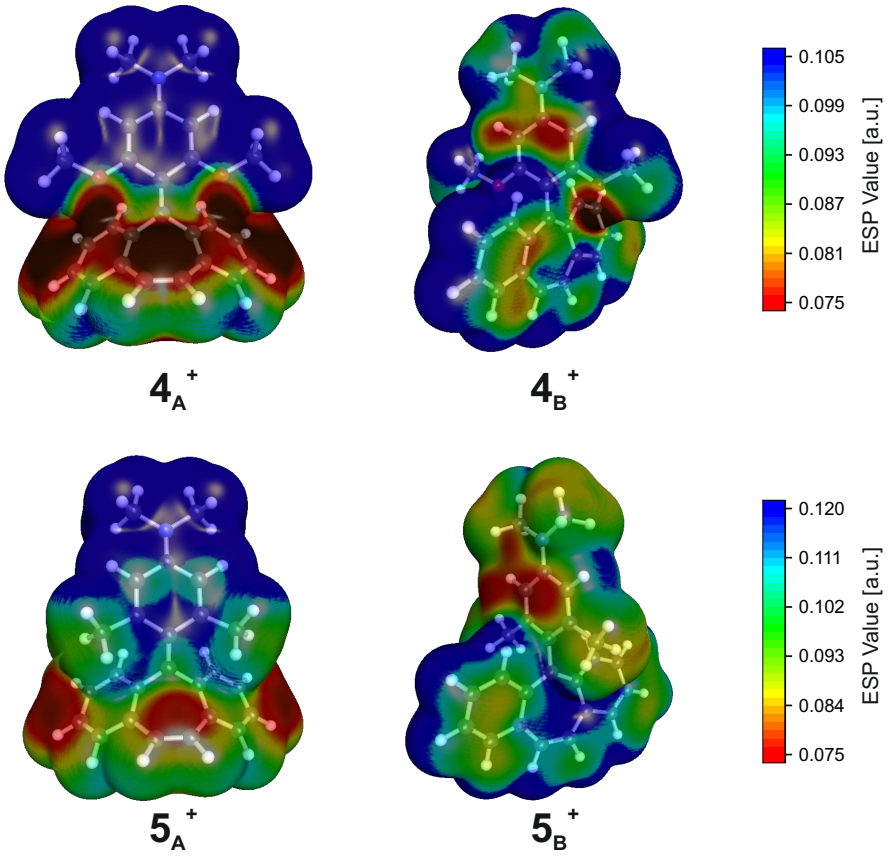

Figure B.18: Electrostatic potential surface (isovalue 0.001) of structures $\mathbf{4_A^+}$/$\mathbf{4_B^+}$ (upper panel) and $\mathbf{5_A^+}$/$\mathbf{5_B^+}$ (lower panel), plotted from DFT/B3LYP/def2-TZVP calculations.

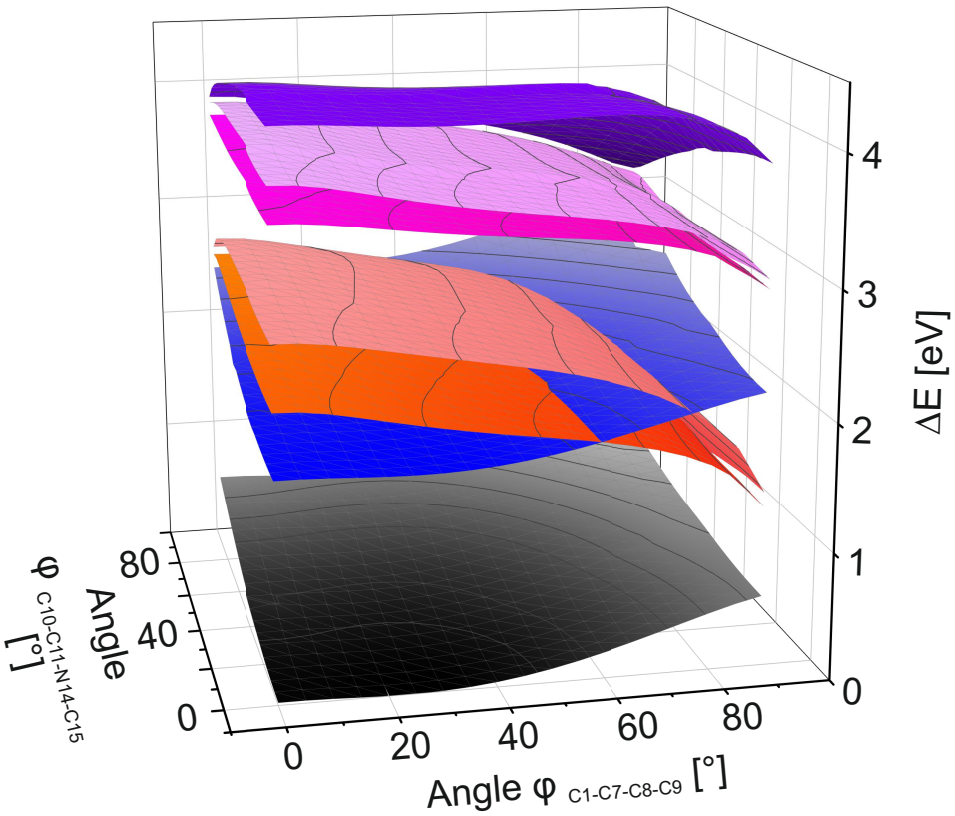

Figure B.19: Potential energy surface (PES) scans along both the dihedral angle $C_1{-}C_7{-}C_8{-}C_9$, defining the twist between the Trop and the DMA moiety, and the dihedral angle $C_{10}{-}C_{11}{-}N_{14}{-}C_{15}$, characterizing the twist between the benzene ring and the amino group within the DMA moiety of $\mathbf{6}^+$. The black PES describes the ground state S_0, while the reddish PESs characterize the excited singlet states S_1, S_2, S_3 and S_4 in ascending order. The bluey PESs correspond to the triplet states T_1 and T_2 also in ascending order. Those PESs were calculated by Roger Kutta, using ROHF-DFT/B3LYP/aug-cc-pVDZ for the S_0 optimization and RHF-TD-DFT/B3LYP/aug-cc-pVDZ for the transition energies.

APPENDIX C

Chiral Phosphoric Acid-Imine Complexes

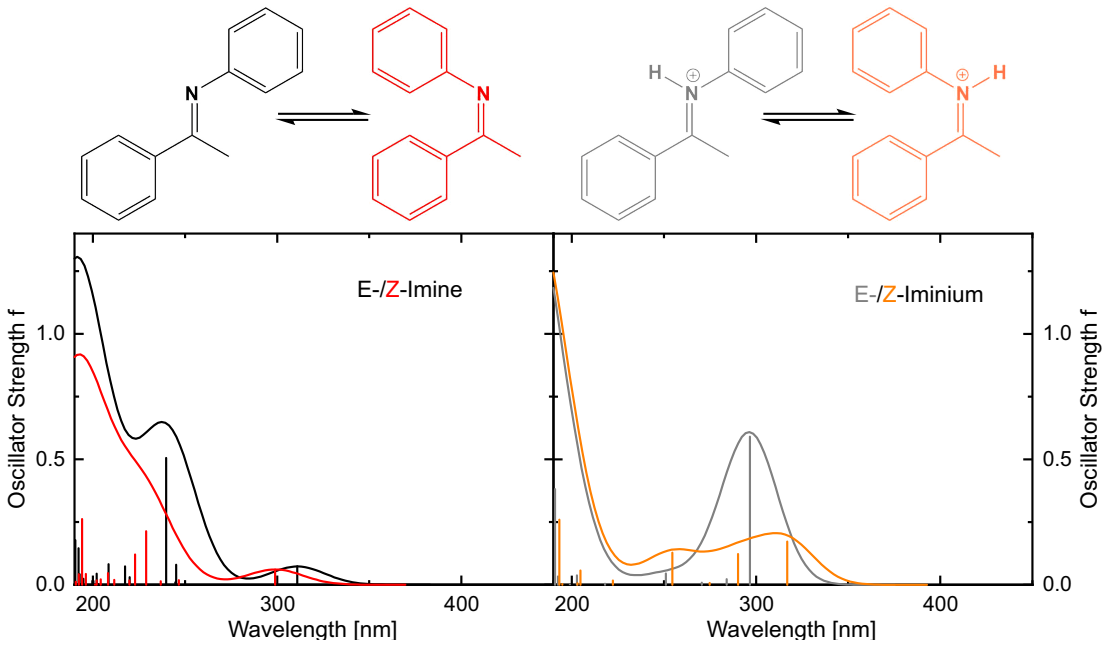

Figure C.1: Results of the TD-DFT/CAM-B3LYP/aug-cc-pVDZ calculations on (E/Z)-N,1-diphenylethan-1-imine (left) and their protonated analogues (right). The calculated oscillator strengths at the corresponding transition energies are given as stick spectrum convoluted each with a Gaussian of a 15 nm width at half maximum.

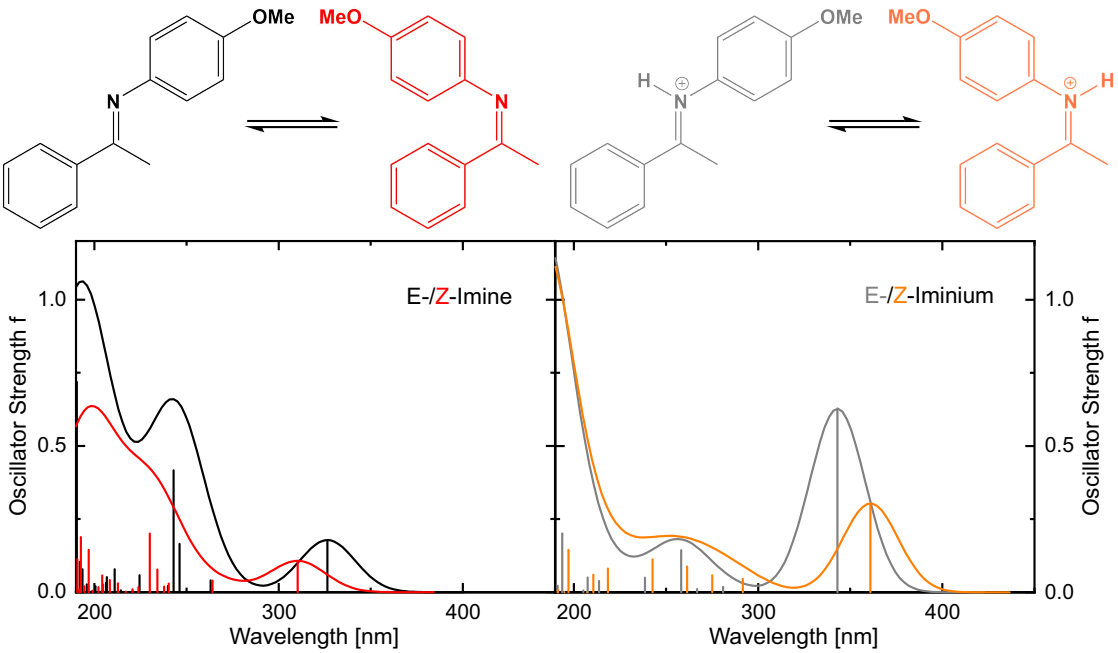

Figure C.2: Results of the TD-DFT/CAM-B3LYP/aug-cc-pVDZ calculations on (E/Z)-N,1-(4-methoxyphenyl)-1-phenylethanimine (left) and their protonated analogues (right). The calculated oscillator strengths at the corresponding transition energies are given as stick spectrum convoluted each with a Gaussian of a 15 nm width at half maximum.

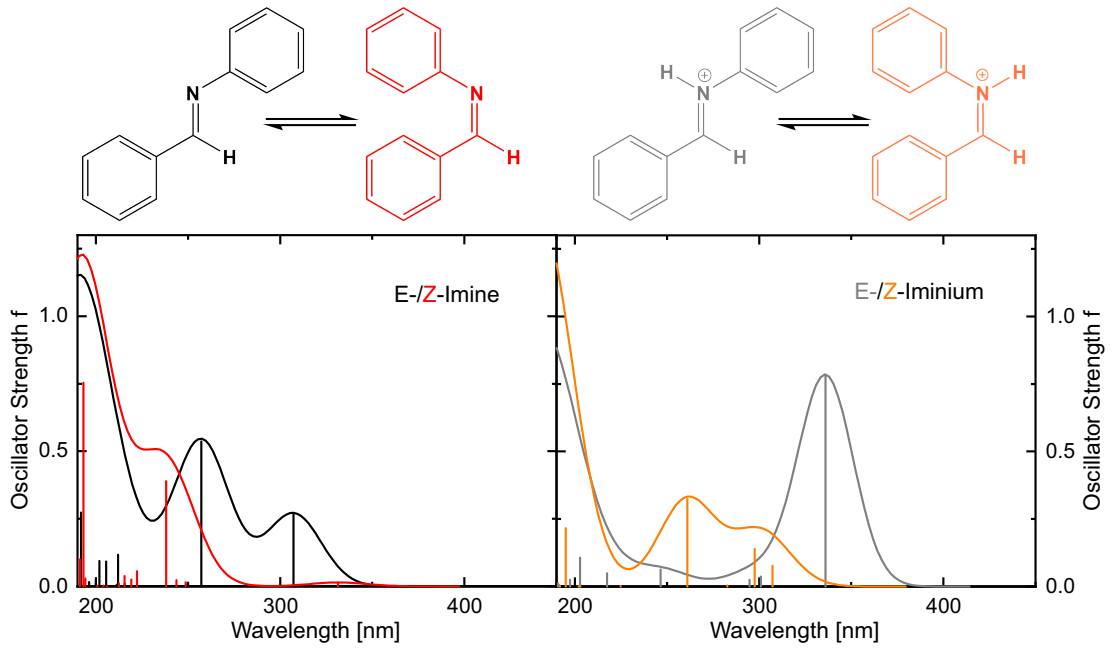

Figure C.3: Results of the TD-DFT/CAM-B3LYP/aug-cc-pVDZ calculations on (E/Z)-N,1-diphenylmethanimine (left) and their protonated analogues (right). The calculated oscillator strengths at the corresponding transition energies are given as stick spectrum convoluted each with a Gaussian of a 15 nm width at half maximum.

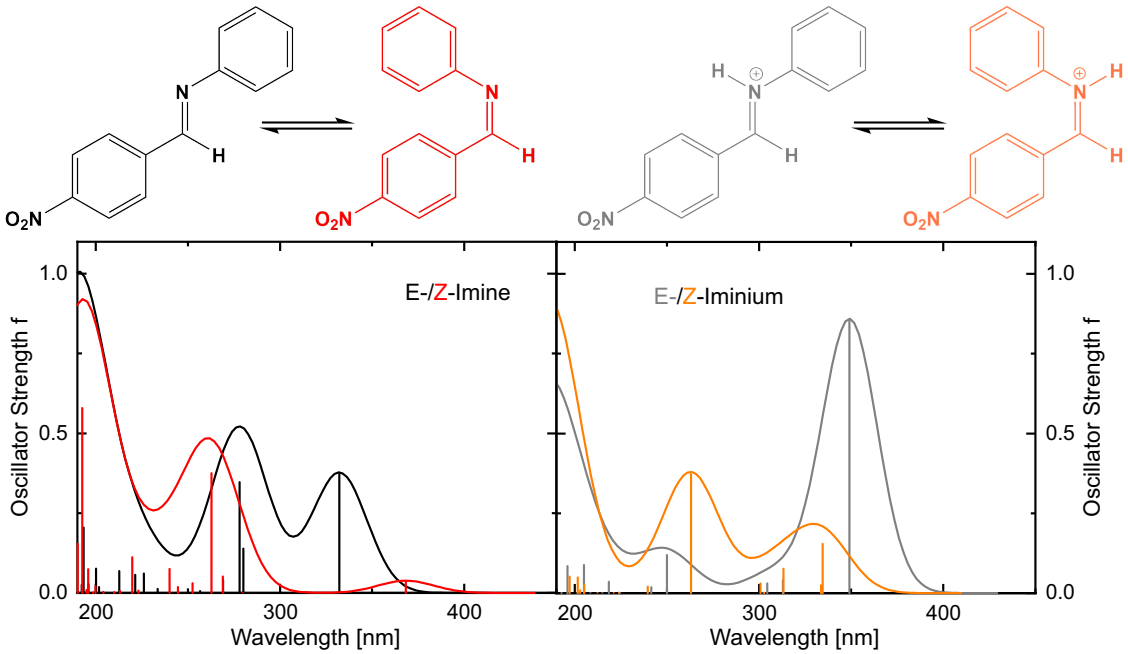

Figure C.4: Results of the TD-DFT/CAM-B3LYP/aug-cc-pVDZ calculations on (E/Z)-1-(4-nitrophenyl)-N-phenylmethanimine (left) and their protonated analogues (right). The calculated oscillator strengths at the corresponding transition energies are given as stick spectrum convoluted each with a Gaussian of a 15 nm width at half maximum.

Glossary of Abbreviations and Acronyms

ACN Acetonitrile [CH_3CN]

ADC Analog-to-Digital Converter

ADC2 Second-Order Algebraic Diagrammatic Construction

AIE Aggregation-Induced Emission

$BaSO_4$ Barium Sulfate

BBO β-Barium Borate [β-BaB_2O_4]

BF_4^- Tetrafluoroborate

BINOL 1,1'-Bi-2-naphthol [$C_{20}H_{14}O_2$]

CAS-SCF Complete Active Space Self-Consistent Field

CCD Charge-Coupled Device

CD Circular Dichroism

CGF Contracted Gaussian Function

CFD Constant Fraction Discriminator

CFT Constant Fraction Triggering

CI Conical Intersection

COSMO Conductor-like Polarizable Continuum Model

CPA Chiral Phosphoric Acid

CSM Continuum Solvation Model

cw Continuous Wave

DADS Decay-Associated Difference Spectrum

DAS Decay Associated Spectrum

DBA Dibuthylaniline Linker

DBTrop Dibenzotropylium Linker

DCM Dichloromethane [Cl_2CH_2]

DEA Diethylaniline Linker

DFG Difference-Frequency Generation

DFT Density Functional Theory

DM Dichroic Mirror

DMA Dimethylaniline Linker

DMF Dimethylformamide [$(CH_3)_2NC(O)H$]

DMSO Dimethyl sulfoxide [$(CH_3)_2SO$]

DOSY Diffusion Ordered Spectroscopy

EDS Electron Donor Strength

ESA Excited-State Absorption

ESIPT Excited-State Intramolecular Proton Transfer

fs Femtoseconds (10^{-15} s)

FWHM Full Width at Half Maximum

FLUP Fluorescence Upconversion

FROG Frequency-Resolved Optical Gating

GGA Generalized Gradient Approximation

GLA Global Lifetime Analysis

GSB Ground-State Bleach

GTO Gaussian-Type Orbitals

GVD Group Velocity Dispersion

HBD Hydrogen-Bond Donor

HE Hantzsch Ester

HF Hartree-Fock

HFIP Hexafluoroisopropanol [$(CF_3)_2CHOH$]

HOMO Highest Occupied Molecular Orbital

iPrOH Isopropyl alcohol, Propan-2-ol [$(CH_3)_2CHOH$]

IR Infrared

IRF Instrument Response Function

ISC Intersystem Crossing

KLM Kerr Lens Modelocking

LDA Local Density Approximation

LED Light-Emittin Diodes

LET Leading Edge Triggering

LUMO Lowest Unoccupied Molecular Orbital

MBPT Many-Body Perturbation Theory

MCA Multi Channel Analyzer

MCP Microchannel Plate

Me Methyl-Group

MeO Methoxy-Group

MeOH Methanol [CH_3OH]

MO Molecular Orbital

MP2 Second-Order M/oller Plesset Theory

MPPT Møller-Plesset Perturbation Theory

ms Milliseconds (10^{-3} s)

µs Microseconds (10^{-6} s)

NADH Reduced Form of Nicotinamide Adenine Dinucleotide

n.c. not converged

Nd:YAG Neodymium-Doped Yttrium Aluminum Garnet [Nd:$Y_3Al_5O_1$]

Nd:YVO_4 Neodym-Doped Yttrium Orthovanadate

NMR Nuclear Magnetic Resonance

NOPA Noncollinear Optical Parametric Amplifier

ns Nanoseconds (10^{-9} s)

o.A. Optical Axis

OD Optical Density

OFET Organic Field-Effect Transistors

OLED Organic Light-Emitting Diodes

OLET Organic Light-Emitting Transistor

OPO Optical Parametric Oscillator

PA Product Absorption

PES Potential Energy Surface

PFTB Perfluoro-tert-butanol [C_4HF_9O]

PGA Programmable Gain Amplifier

PMT Photomultiplier Tube

ps Picoseconds (10^{-12} s)

RHF Restricted Hartree–Fock

RM Removable Mirror

SCF Self-Consistent Field

SE Stimulated-Emission

SFG Sum-Frequency Generation

SH Second Harmonic

SHG Second Harmonic Generation

SPM Self-Phase Modulation

STO Slater-Type Orbitals

SVD Singular Value Decomposition

TA Transient Absrption

TAC Time-to-Amplitude Converter

TBAB Tetra-n-butylammonium tetrafluoroborate [$C_{16}H_{36}NBF_4$]

TC Time Calibrator

TCSPC Time-Correlated Single Photon Counting

TD-DFT Time-Dependent Density Functional Theory

TFA Trifluoroacetic acid [CF_3CO_2H]

TFE Trifluoroethanol

ThT Thioflavin T [$C_{17}H_{19}ClN_2S$]

TICT Twisted Intramolecular Charge Transfer

TiPSY *(R)*-3,3'-Bis(triphenylsilyl)-1,1'-binaphthyl-2,2'-diylhydrogenphosphat [$C_{56}H_{41}O_4PSi_2$]

Ti:Sa Titanium-Sapphire [Ti:Al_2O_3]

TPF 1,3,5-Triphenylformazan [$C_{19}H_{16}N_4$]

TRIP *(R)*-3,3'-Bis(2,4,6-triisopropylphenyl)-1,1'-binaphthyl-2,2'-diylhydrogenphosphat [$C_{50}H_{57}O_4P$]

TRIFP *(R)*-3,3'-Bis[3,5-bis(trifluoromethyl)phenyl]-1,1'-binaphthyl-2,2'-diylhydrogenphosphate [$C_{36}H_{17}F_{12}O_4P$]

Trop Tropylium

TTC 2,3,5-Triphenyltetrazolium Chloride [$C_{19}H_{15}ClN_4$]

UHF Unrestricted Hartree–Fock

UV Ultraviolet

VC Vibrational Cooling

Vis Visible

VR Vibrational Relaxation

WD Window Discriminator

WL White-Light

Xe Xenon

XPM Cross-Phase Modulation

XRD X-ray Diffraction

Bibliography

[1] S. Wortmann, S. Schloeglmann, P. Nuernberger, *The Journal of Organic Chemistry*, 2021, **87**, 1745–1755.

[2] S. Wortmann, R. J. Kutta, P. Nuernberger, *Frontiers in Chemistry*, 2022, **10**, 983342.

[3] S. Wortmann, R. J. Kutta, R. D. Crocker, F. Bergmeier, B. Geissler, D. J. M. Lyons, E. Riedle, T. V. Nguyen, N. P., To be submitted, 2023.

[4] S. Wortmann, R. J. Kutta, R. D. Crocker, F. Bergmeier, J. Poll, D. J. M. Lyons, E. Riedle, T. V. Nguyen, N. P., In preparation, 2024.

[5] I. M. Daubit, S. Wortmann, D. Siegmund, S. Hahn, P. Nuernberger, N. Metzler-Nolte, *Chemistry – A European Journal*, 2021, **27**, 6783–6794.

[6] N. Schubert, M. Vázquez-Hernández, J. W. Southwell, S. Wortmann, S. Schloeglmann, A.-K. Duhme-Klai, P. Nuernberger, J. E. Bandow, N. Metzler-Nolte, To be submitted, 2023.

[7] R. W. Schoenlein, L. A. Peteanu, R. A. Mathies, C. V. Shank, *Science*, 1991, **254**, 412–415.

[8] Q. Wang, R. W. Schoenlein, L. A. Peteanu, R. A. Mathies, C. V. Shank, *Science*, 1994, **266**, 422–424.

[9] Y. B. Tewari, *Applied Biochemistry and Biotechnology*, 1990, **23**, 187–203.

[10] S. H. Bhosale, M. B. Rao, V. V. Deshpande, *Microbiological Reviews*, 1996, **60**, 280–300.

[11] C. Dai, T. Miao, J. Hai, Y. Xiao, Y. Li, J. Zhao, H. Qiu, B. Xu, *BioMed Research International*, 2020, **2020**, 1–7.

[12] M. Andresen, M. C. Wahl, A. C. Stiel, F. Gräter, L. V. Schäfer, S. Trowitzsch, G. Weber, C. Eggeling, H. Grubmüller, S. W. Hell, S. Jakobs, *Proceedings of the National Academy of Sciences*, 2005, **102**, 13070–13074.

[13] M. Andresen, A. C. Stiel, S. Trowitzsch, G. Weber, C. Eggeling, M. C. Wahl, S. W. Hell, S. Jakobs, *Proceedings of the National Academy of Sciences*, 2007, **104**, 13005–13009.

[14] D. Bourgeois, V. Adam, *IUBMB Life*, 2012, **64**, 482–491.

[15] P. Dedecker, J.-i. Hotta, C. Flors, M. Sliwa, H. Uji-i, M. B. J. Roeffaers, R. Ando, H. Mizuno, A. Miyawaki, J. Hofkens, *Journal of the American Chemical Society*, 2007, **129**, 16132–16141.

[16] A. C. Stiel, S. Trowitzsch, G. Weber, M. Andresen, C. Eggeling, S. W. Hell, S. Jakobs, M. C. Wahl, *Biochemical Journal*, 2007, **402**, 35–42.

[17] D. A. Parthenopoulos, P. M. Rentzepis, *Science*, 1989, **245**, 843–845.

[18] B. L. Feringa, N. P. M. Huck, A. M. Schoevaars, *Advanced Materials*, 1996, **8**, 681–684.

[19] A. M. Schoevaars, W. Kruizinga, R. W. J. Zijlstra, N. Veldman, A. L. Spek, B. L. Feringa, *The Journal of Organic Chemistry*, 1997, **62**, 4943–4948.

[20] S. Kawata, Y. Kawata, *Chemical Reviews*, 2000, **100**, 1777–1788.

[21] D. A. Leigh, J. K. Y. Wong, F. Dehez, F. Zerbetto, *Nature*, 2003, **424**, 174–179.

[22] C. L. Ward, C. G. Elles, *The Journal of Physical Chemistry A*, 2014, **118**, 10011–10019.

[23] O. Watanabe, M. Tsuchimori, A. Okada, *Journal of Materials Chemistry*, 1996, **6**, 1487–1492.

[24] T. Nägele, R. Hoche, W. Zinth, J. Wachtveitl, *Chemical Physics Letters*, 1997, **272**, 489–495.

[25] Y.-C. Lu, C.-W. Chang, E. W.-G. Diau, *Journal of the Chinese Chemical Society*, 2002, **49**, 693–701.

[26] N. J. Dunn, W. H. Humphries IV, A. R. Offenbacher, T. L. King, J. A. Gray, *The Journal of Physical Chemistry A*, 2009, **113**, 13144–13151.

[27] K. N. Gherab, R. Gatri, Z. Hank, B. Dick, R. J. Kutta, R. Winter, J. Luc, B. Sahraoui, J.-L. Fillaut, *Journal of Materials Chemistry*, 2010, **20**, 2858–2864.

[28] G. S. Hammond, J. Saltiel, *Journal of the American Chemical Society*, 1962, **84**, 4983–4984.

[29] G. Hohlneicher, B. Dick, *Journal of photochemistry*, 1984, **27**, 215–231.

[30] R. Mohrschladt, J. Schroeder, D. Schwarzer, J. Troe, P. Vöhringer, *The Journal of Chemical Physics*, 1994, **101**, 7566–7579.

[31] W. Fuß, C. Kosmidis, W. E. Schmid, S. A. Trushin, *Angewandte Chemie International Edition*, 2004, **43**, 4178–4182.

[32] H. Görner, *Journal of Photochemistry*, 1982, **19**, 343–356.

[33] C. Gehrke, R. Mohrschladt, J. Schroeder, J. Troe, P. Vöhringer, *Chemical Physics*, 1991, **152**, 45–56.

[34] L.-Y. Yang, R. S. H. Liu, K. J. Boarman, N. L. Wendt, J. Liu, *Journal of the American Chemical Society*, 2005, **127**, 2404–2405.

[35] O. A. Krohn, M. Quick, S. M. Sudarkova, I. N. Ioffe, C. Richter, S. A. Kovalenko, *The Journal of Chemical Physics*, 2020, **152**, 224305.

[36] N. Ernsting, B. Dick, T. Arthen-Engeland, *Pure and Applied Chemistry*, 1990, **62**, 1483–1488.

[37] H. Görner, L. S. Atabekyan, A. K. Chibisov, *Chemical Physics Letters*, 1996, **260**, 59–64.

[38] A. K. Chibisov, H. Görner, *Journal of Photochemistry and Photobiology A: Chemistry*, 1997, **105**, 261–267.

[39] J. Buback, M. Kullmann, F. Langhojer, P. Nuernberger, R. Schmidt, F. Würthner, T. Brixner, *Journal of the American Chemical Society*, 2010, **132**, 16510–16519.

[40] J. Buback, P. Nuernberger, M. Kullmann, F. Langhojer, R. Schmidt, F. Würthner, T. Brixner, *The Journal of Physical Chemistry A*, 2011, **115**, 3924–3935.

[41] H. W. Mocker, R. J. Collins, *Applied Physics Letters*, 1965, **7**, 270–273.

[42] A. H. Zewail, *The Journal of Physical Chemistry A*, 2000, **104**, 5660–5694.

[43] A. H. Zewail, *Pure and Applied Chemistry*, 2000, **72**, 2219–2231.

[44] C. Wang, H. Dong, W. Hu, Y. Liu, D. Zhu, *Chemical Reviews*, 2012, **112**, 2208–2267.

[45] H. Dong, X. Fu, J. Liu, Z. Wang, W. Hu, *Advanced Materials*, 2013, **25**, 6158–6183.

[46] H. Sirringhaus, *Advanced Materials*, 2014, **26**, 1319–1335.

[47] H. Uoyama, K. Goushi, K. Shizu, H. Nomura, C. Adachi, *Nature*, 2012, **492**, 234–238.

[48] J.-X. Chen, W.-W. Tao, W.-C. Chen, Y.-F. Xiao, K. Wang, C. Cao, J. Yu, S. Li, F.-X. Geng, C. Adachi, *Angewandte Chemie*, 2019, **131**, 14802–14807.

[49] L. Hua, Y. Liu, H. Zhao, S. Chen, Y. Zhang, S. Yan, Z. Ren, *Advanced Functional Materials*, 2023, 2303384.

[50] D. Yuan, V. Sharapov, X. Liu, L. Yu, *ACS Omega*, 2019, **5**, 68–74.

[51] Z. Qin, H. Gao, H. Dong, W. Hu, *Advanced Materials*, 2021, **33**, 2007149.

[52] C. Pigot, G. Noirbent, D. Brunel, F. Dumur, *European Polymer Journal*, 2020, **133**, 109797.

[53] E. V. Verbitskiy, Y. A. Kvashnin, P. I. Bogdanov, M. V. Medvedeva, T. S. Svalova, A. N. Kozitsina, L. G. Samsonova, K. M. Degtyarenko, D. V. Grigoryev, A. E. Kurtcevich, et al., *Dyes and Pigments*, 2021, **187**, 109124.

[54] D. J. M. Lyons, R. D. Crocker, T. V. Nguyen, *Chemistry – A European Journal*, 2018, **24**, 10959–10965.

[55] M. L. Cano, M. N. Chrétien, H. Garcı'a, J. Scaiano, *Chemical Physics Letters*, 2001, **345**, 6409–414.

[56] M. Orda-Zgadzaj, V. Wendel, M. Fehlinger, B. Ziemer, W. Abraham, *European Journal of Organic Chemistry*, 2001, **2001**, 1549–1561.

[57] H. Mustroph, M. Stollenwerk, V. Bressau, *Angewandte Chemie International Edition*, 2006, **45**, 2016–2035.

[58] B. Breiten, I. Biaggio, F. Diederich, *Chimia*, 2010, **64**, 409–409.

[59] B.-G. Kim, K. Chung, J. Kim, *Chemistry – A European Journal*, 2013, **19**, 5220–5230.

[60] C.-P. Lee, R. Y.-Y. Lin, L.-Y. Lin, C.-T. Li, T.-C. Chu, S.-S. Sun, J. T. Lin, K.-C. Ho, *RSC Advances*, 2015, **5**, 23810–23825.

[61] T. V. Nguyen, A. Bekensir, *Organic Letters*, 2014, **16**, 1720–1723.

[62] S. Fukuzumi, K. Ohkubo, *Organic & Biomolecular Chemistry*, 2014, **12**, 6059–6071.

[63] L. Beverina, G. A. Pagani, *Accounts of Chemical Research*, 2014, **47**, 319–329.

[64] M. Gsänger, D. Bialas, L. Huang, M. Stolte, F. Würthner, *Advanced Materials*, 2016, **28**, 3615–3645.

[65] M. Gao, B. Z. Tang, *ACS Sensors*, 2017, **2**, 1382–1399.

[66] D. Lyons, R. Crocker, D. Enders, T. Nguyen, *Green Chemistry*, 2017, **19**, 3993–3996.

[67] J. W. Yang, M. T. Hechavarria Fonseca, B. List, *Angewandte Chemie International Edition*, 2004, **43**, 6660–6662.

[68] J. W. Yang, M. T. Hechavarria Fonseca, N. Vignola, B. List, *Angewandte Chemie International Edition*, 2005, **44**, 108–110.

[69] S. G. Ouellet, J. B. Tuttle, D. W. MacMillan, *Journal of the American Chemical Society*, 2005, **127**, 32–33.

[70] B. D. Sanwal, M. W. Zink, *Archives of Biochemistry and Biophysics*, 1961, **94**, 430–435.

[71] F. M. Dickinson, K. Dalziel, *Nature*, 1967, **214**, 31–33.

[72] M. Rueping, E. Sugiono, C. Azap, T. Theissmann, M. Bolte, *Organic Letters*, 2005, **7**, 3781–3783.

[73] M. Rueping, E. Sugiono, C. Azap, *Angewandte Chemie International Edition*, 2006, **45**, 2617–2619.

[74] M. Rueping, A. P. Antonchick, T. Theissmann, *Angewandte Chemie International Edition*, 2006, **45**, 3683–3686.

[75] T. Akiyama, J. Itoh, K. Yokota, K. Fuchibe, *Angewandte Chemie International Edition*, 2004, **43**, 1566–1568.

[76] S. G. Ouellet, A. M. Walji, D. W. MacMillan, *Accounts of Chemical Research*, 2007, **40**, 1327–1339.

[77] H. Kim, E. Sugiono, Y. Nagata, M. Wagner, M. Bonn, M. Rueping, J. Hunger, *ACS Catalysis*, 2015, **5**, 6630–6633.

[78] N. Sorgenfrei, J. Hioe, J. Greindl, K. Rothermel, F. Morana, N. Lokesh, R. M. Gschwind, *Journal of the American Chemical Society*, 2016, **138**, 16345–16354.

[79] T. H. Maiman, *Nature*, 1960, **187**, 493–494.

[80] B. E. Saleh, M. C. Teich, *Grundlagen der Photonik 2nd ed.*, John Wiley & Sons, 2008.

[81] P. Franken, A. E. Hill, C. Peters, G. Weinreich, *Physical Review Letters*, 1961, **7**, 118.

[82] R. W. Boyd, J. J. Maki, J. E. Sipe, *Nonlinear Optics 1st ed.*, Academic Press, San Diego (USA), 1992.

[83] Y.-R. Shen, *Principles of Nonlinear Optics*, Wiley-Interscience, New York, NY, USA, 1984.

[84] G. S. He, *Nonlinear Optics and Photonics*, OUP Oxford, 2014.

[85] E. Hanamura, Y. Kawabe, A. Yamanaka, *Quantum Nonlinear Optics*, Springer Science & Business Media, 2007.

[86] D. Meschede, *Optik, Licht und Laser 3rd ed.*, Springer-Verlag, 2009.

[87] E. Hecht, *Optik 3rd ed.*, De Gruyter, 1994.

[88] P. Rentzepis, *Chemical Physics Letters*, 1968, **2**, 117–120.

[89] K. B. Eisenthal, *Accounts of Chemical Research*, 1975, **8**, 118–124.

[90] R. M. Hochstrasser, H. Lutz, G. W. Scott, *Chemical Physics Letters*, 1974, **24**, 162–167.

[91] M. Kullmann, S. Ruetzel, J. Buback, P. Nuernberger, T. Brixner, *Journal of the American Chemical Society*, 2011, **133**, 13074–13080.

[92] R. J. Kutta, K. Magerl, U. Kensy, B. Dick, *Photochemical & Photobiological Sciences*, 2015, **14**, 288–299.

[93] P. K. Verma, A. Steinbacher, A. Schmiedel, P. Nuernberger, T. Brixner, *Structural Dynamics*, 2016, **3**, 023606.

[94] F. Brandl, S. Bergwinkl, C. Allacher, B. Dick, *Chemistry – A European Journal*, 2020, **26**, 7946–7954.

[95] A. H. Zewail, *The Journal of Physical Chemistry A*, 2000, **104**, 5660–5694.

[96] D. E. Spence, P. N. Kean, W. Sibbett, *Optics Letters*, 1991, **16**, 42–44.

[97] A. H. Zewail, *Science*, 1988, **242**, 1645–1653.

[98] R. R. Alfano, S. Shapiro, *Physical Review Letters*, 1970, **24**, 584–587.

[99] R. R. Alfano, S. Shapiro, *Physical Review Letters*, 1970, **24**, 592–595.

[100] R. R. Alfano, *The Supercontinuum Laser Source*, Springer, 1984.

[101] S. A. Kovalenko, A. L. Dobryakov, J. Ruthmann, N. P. Ernsting, *Physical Review A*, 1999, **59**, 2369.

[102] R. Huber, H. Satzger, W. Zinth, J. Wachtveitl, *Optics Communications*, 2001, **194**, 443–448.

[103] F. Träger, *Springer Handbook of Lasers and Optics*, *Vol. 2*, Springer, 2012.

[104] A. Maciejewski, R. Naskrecki, M. Lorenc, M. Ziolek, J. Karolczak, J. Kubicki, M. Matysiak, M. Szymanski, *Journal of Molecular Structure*, 2000, **555**, 1–13.

[105] S. Wortmann, Focal Point Practical Report, Ruhr-Universität Bochum, 2018.

[106] J. M. Hollas, *Modern Spectroscopy*, John Wiley & Sons, 2004.

[107] P. Nuernberger, S. Ruetzel, T. Brixner, *Angewandte Chemie International Edition*, 2015, **54**, 11368–11386.

[108] K. Wynne, R. Hochstrasser, *Chemical Physics*, 1995, **193**, 211–236.

[109] A. L. Dobryakov, S. A. Kovalenko, N. P. Ernsting, *The Journal of Chemical Physics*, 2003, **119**, 988–1002.

[110] M. Rasmusson, A. N. Tarnovsky, E. Åkesson, V. Sundström, *Chemical Physics Letters*, 2001, **335**, 201–208.

[111] M. Lorenc, M. Ziolek, R. Naskrecki, J. Karolczak, J. Kubicki, A. Maciejewski, *Applied Physics B*, 2002, **74**, 19–27.

[112] B. Akhremitchev, C. Wang, G. C. Walker, *Review of Scientific Instruments*, 1996, **67**, 3799–3805.

[113] B. Dietzek, T. Pascher, V. Sundström, A. Yartsev, *Laser Physics Letters*, 2006, **4**, 38–43.

[114] K. Ekvall, P. van der Meulen, C. Dhollande, L.-E. Berg, S. Pommeret, R. Naskrecki, J.-C. Mialocq, *Journal of Applied Physics*, 2000, **87**, 340–2352.

[115] Q. Hong, J. Durrant, G. Hastings, G. Porter, D. Klug, *Chemical Physics Letters*, 1993, **202**, 183–185.

[116] S. A. Kovalenko, N. P. Ernsting, J. Ruthmann, *Chemical Physics Letters*, 1996, **258**, 445–454.

[117] R. Stolen, A. Ashkin, *Applied Physics Letters*, 1973, **22**, 294–296.

[118] P. Ho, R. R. Alfano, *Physical Review A*, 1979, **20**, 2170–2187.

[119] R. A. Fisher, P. Kelley, T. Gustafson, *Applied Physics Letters*, 1969, **14**, 140–143.

[120] U. Megerle, I. Pugliesi, C. Schriever, C. F. Sailer, E. Riedle, *Applied Physics B*, 2009, **96**, 215–231.

[121] H. Mahr, M. D. Hirsch, *Optics Communications*, 1975, **13**, 96–99.

[122] T. Damen, J. Shah, *Applied Physics Letters*, 1988, **52**, 1291–1293.

[123] M. L. Horng, J. A. Gardecki, A. Papazyan, M. Maroncelli, *The Journal of Physical Chemistry*, 1995, **99**, 17311–17337.

[124] R. Schanz, S. Kovalenko, V. Kharlanov, N. Ernsting, *Applied Physics Letters*, 2001, **79**, 566–568.

[125] S. Wortmann, Master Thesis, Ruhr-Universität Bochum, 2018.

[126] C. Reichardt, T. Welton, *Solvents and Solvent Effects in Organic Chemistry*, John Wiley & Sons, 2011.

[127] J. R. Lakowicz, *Principles of Fluorescence Spectroscopy 3rd ed.*, Springer, 2006.

[128] C. Reichardt, *Chemical Society Reviews*, 1992, **21**, 147–153.

[129] L. Bollinger, G. E. Thomas, *Review of Scientific Instruments*, 1961, **32**, 1044–1050.

[130] J. Demas, *Excited state lifetime measurements*, Elsevier, 2012.

[131] D. O'Connor, *Time-Correlated Single Photon Counting*, Academic Press, 2012.

[132] J. Karolczak, D. Komar, J. Kubicki, T. Wróżowa, K. Dobek, B. Ciesielska, A. Maciejewski, *Chemical Physics Letters*, 2001, **344**, 154–164.

[133] T. Bolze, J.-L. Wree, F. Kanal, D. Schleier, P. Nuernberger, *ChemPhysChem*, 2018, **19**, 138–147.

[134] J. Knorr, N. Sülzner, B. Geissler, C. Spies, A. Grandjean, R. J. Kutta, G. Jung, P. Nuernberger, *Photochemical & Photobiological Sciences*, 2022, **21**, 2179–2192.

[135] Hamamatsu, *Guide to Streak Cameras*, 2008.

[136] H. Shiraga, N. Miyanaga, M. Heya, M. Nakasuji, Y. Aoki, H. Azechi, T. Yamanaka, K. Mima, *Review of Scientific Instruments*, 1997, **68**, 745–749.

[137] L. Gao, J. Liang, C. Li, L. V. Wang, *Nature*, 2014, **516**, 74–77.

[138] H. Shiraga, M. Heya, A. Fujishima, O. Maegawa, K. Shimada, Y. Kato, T. Yamanaka, S. Nakai, *Review of Scientific Instruments*, 1995, **66**, 722–724.

[139] R. J. Kutta, T. Langenbacher, U. Kensy, B. Dick, *Applied Physics B*, 2013, **111**, 203–216.

[140] H. Hertz, *Annalen der Physik*, 1887, **267**, 983–1000.

[141] W. Hallwachs, *Annalen der Physik*, 1888, **270**, 731–734.

[142] P. Lenard, *Annalen der Physik*, 1900, **307**, 359–375.

[143] R. J. Kutta, Dissertation, Universität Regensburg, 2013.

[144] M. Wolf, *Physik in unserer Zeit*, 1981, **12**, 90–95.

[145] M. Ito, H. Kume, K. Oba, *IEEE Transactions on Nuclear Science*, 1984, **31**, 408–412.

[146] W. H. Sachs, *Acta Chemica Scandinavica*, 1971, **25**, 762–764.

[147] I. H. van Stokkum, D. S. Larsen, R. Van Grondelle, *Biochimica et Biophysica Acta (BBA)-Bioenergetics*, 2004, **1657**, 82–104.

[148] K. M. Mullen, I. H. van Stokkum, *Journal of Statistical Software*, 2007, **18**, 1–46.

[149] W. Kessler, *Multivariate Datenanalyse: Für die Pharma, Bio-und Prozessanalytik*, John Wiley & Sons, 2011.

[150] C. B. Talbot, J. Lagarto, S. Warren, M. A. Neil, P. M. French, C. Dunsby, *Journal of Fluorescence*, 2015, **25**, 1169–1182.

[151] R. G. D. Steel, J. H. Torrie, et al., *Principles and Procedures of Statistics*, McGraw-Hill Book Company, Inc., New York, Toronto, London, 1960.

[152] R. O. M. Born, *Annalen der Physik*, 1927, **389**, 457–484.

[153] E. Schrödinger, *Annalen der Physik*, 1926, **385**, 437–490.

[154] I. Ramanchandran, G. Deepa, K. Nambori, *Computational Chemistry and Molecular Modeling*, Springer, Coimbatore, 2008.

[155] W. Koch, M. C. Holthausen, *A Chemist's Guide to Density Functional Theory*, John Wiley & Sons, 2015.

[156] D. Püschner, *Quantitative Rechenverfahren der Theoretischen Chemie*, Springer, 2017.

[157] W. Pauli, *Zeitschrift für Physik*, 1925, **31**, 765–778.

[158] J. C. Slater, *Physical Review*, 1930, **35**, 210–211.

[159] J. C. Slater, *Physical Review*, 1951, **81**, 385–390.

[160] D. R. Hartree, *Mathematical Proceedings of the Cambridge Philosophical Society*, 1928, **24**, 89–110.

[161] V. Fock, *Zeitschrift für Physik*, 1930, **61**, 126–148.

[162] A. R. Leach, *Molecular Modelling: Principles and Applications*, Pearson Education, 2001.

[163] A. Szabo, N. S. Ostlund, *Modern Quantum Chemistry: Introduction to Advanced Electronic Structure Theory*, Courier Corporation, 2012.

[164] L. H. Thomas, *Mathematical Proceedings of the Cambridge Philosophical Society*, 1927, **23**, 542–548.

[165] E. Fermi, *Zeitschrift für Physik*, 1928, **48**, 73–79.

[166] P. Hohenberg, W. Kohn, *Physical Review*, 1964, **136**, B864–B871.

[167] R. G. Parr, W. Yang, *Annual Review of Physical Chemistry*, 1995, **46**, 701–728.

[168] W. Kohn, L. J. Sham, *Physical Review*, 1965, **140**, A1133–A1138.

[169] L. W. S. H. Vosko, M. Nusair, *Canadian Journal of Physics*, 1980, **58**, 1200 – 1211.

[170] J. P. Perdew, Y. Wang, *Physical Review B*, 1992, **45**, 13244–13249.

[171] A. D. Becke, *Physical Review A*, 1988, **38**, 3098–3100.

[172] J. P. Perdew, *Physical Review B*, 1986, **33**, 8822–8824.

[173] C. Lee, W. Yang, R. G. Parr, *Physical Review B*, 1988, **37**, 785–789.

[174] J. P. Perdew, K. Burke, M. Ernzerhof, *Physical Review Letters*, 1996, **77**, 3865–3868.

[175] A. D. Becke, *The Journal of Chemical Physics*, 1993, **98**, 1372–1377.

[176] S. F. Boys, *Proceedings of the Royal Society of London. Series A. Mathematical and Physical Sciences*, 1950, **200**, 542–554.

[177] J. C. Slater, *Physical Review*, 1930, **36**, 57.

[178] T. Kato, *Communications on Pure and Applied Mathematics*, 1957, **10**, 151–177.

[179] N. March, *Physical Review A*, 1986, **33**, 88–89.

[180] E. Besalú, R. Carbó-Dorca, *Journal of Mathematical Chemistry*, 2011, **49**, 1769–1784.

[181] A. L. Magalhaes, *Journal of Chemical Education*, 2014, **91**, 2124–2127.

[182] S. Grimme, *Journal of Computational Chemistry*, 2004, **25**, 1463–1473.

[183] S. Grimme, J. Antony, S. Ehrlich, H. Krieg, *The Journal of Chemical Physics*, 2010, **132**, 154104.

[184] J. Tomasi, B. Mennucci, R. Cammi, *Chemical Reviews*, 2005, **105**, 2999–3094.

[185] B. Mennucci, *The Journal of Physical Chemistry Letters*, 2010, **1**, 1666–1674.

[186] E. Runge, E. K. Gross, *Physical Review Letters*, 1984, **52**, 997–1000.

[187] M. A. Marques, N. T. Maitra, F. M. Nogueira, E. K. Gross, A. Rubio, *Fundamentals of Time-Dependent Density Functional Theory*, *Vol. 837*, Springer, 2012.

[188] C. Møller, M. S. Plesset, *Physical Review*, 1934, **46**, 618–622.

[189] K. Brueckner, *Physical Review*, 1955, **100**, 36–45.

[190] J. Goldstone, *Proceedings of the Royal Society of London. Series A. Mathematical and Physical Sciences*, 1957, **239**, 267–279.

[191] R. T. Pu, E. S. Chang, *Physical Review*, 1966, **151**, 31–40.

[192] H. J. Silverstone, M.-L. Yin, *The Journal of Chemical Physics*, 1968, **49**, 2026–2030.

[193] S. Huzinaga, C. Arnau, *Physical Review A*, 1970, **1**, 1285–1288.

[194] R. J. Bartlett, D. M. Silver, *The Journal of Chemical Physics*, 1975, **62**, 3258–3268.

[195] D. Cremer, *Wiley Interdisciplinary Reviews: Computational Molecular Science*, 2011, **1**, 509–530.

[196] J. C. Slater, *Physical Review*, 1929, **34**, 1293–1322.

[197] E. Condon, *Physical Review*, 1930, **36**, 1121–1133.

[198] P.-O. Löwdin, *Physical Review*, 1955, **97**, 1474–1489.

[199] R. J. Bartlett, D. M. Silver, *International Journal of Quantum Chemistry*, 1974, **8**, 271–276.

[200] J. A. Pople, J. S. Binkley, R. Seeger, *International Journal of Quantum Chemistry*, 1976, **10**, 1–19.

[201] J. Schirmer, *Physical Review A*, 1982, **26**, 2395–2416.

[202] F. A. Neugebauer, *Angewandte Chemie International Edition*, 1973, **12**, 455–464.

[203] O. M. Polumbrik, *Russian Chemical Reviews*, 1978, **47**, 767–785.

[204] L. N. Ganyuk, N. F. Guba, V. D. Pokhodenko, *Theoretical and Experimental Chemistry*, 1983, **18**, 321–324.

[205] A. R. Katritzky, S. A. Belyakov, H. D. Durst, R. Xu, N. S. Dalal, *Canadian Journal of Chemistry*, 1994, **72**, 1849–1856.

[206] G. N. Lipunova, T. G. Fedorchenko, O. N. Chupakhin, *Russian Journal of General Chemistry*, 2019, **89**, 1225–1245.

[207] L. Hunter, C. B. Roberts, *Journal of the Chemical Society*, 1941, 823–826.

[208] B. Hirsch, *Justus Liebigs Annalen der Chemie*, 1960, **637**, 167–172.

[209] R. Price, *Journal of the Chemical Society A: Inorganic, Physical, Theoretical*, 1971, 3379–3385.

[210] O. E. Sherif, Y. M. Issa, M. E. M. Hassouna, S. M. Abass, *Monatshefte für Chemie*, 1993, **124**, 627–635.

[211] H. Tezcan, E. Uzluk, *Dyes and Pigments*, 2008, **76**, 733–740.

[212] G. I. Sigeikin, G. N. Lipunova, I. G. Pervova, *Russian Chemical Reviews*, 2006, **75**, 885–900.

[213] J. B. Gilroy, E. Otten, *Chemical Society Reviews*, 2020, **49**, 85–113.

[214] H. V. Pechmann, P. Runge, *Berichte der Deutschen Chemischen Gesellschaft*, 1894, **27**, 2920–2930.

[215] I. Hausser, D. Jerchel, R. Kuhn, *Chemische Berichte*, 1949, **82**, 195–199.

[216] A. W. Nineham, *Chemical Reviews*, 1955, **55**, 355–483.

[217] B. Jámbor, *Tetrazoliumsalze in der Biologie*, Gustav Fischer, Jena, Germany, 1960.

[218] F. A. Neugebauer, G. A. Russell, *The Journal of Organic Chemistry*, 1968, **33**, 2744–2746.

[219] K. Umemoto, *The Chemical Society of Japan*, 1985, **58**, 2051–2055.

[220] M. C. Gonzalez, E. San Roman, *The Journal of Physical Chemistry*, 1989, **93**, 3536–3540.

[221] F. Kanal, D. Schleier, P. Nuernberger, *ChemPhysChem*, 2015, **16**, 3143–3146.

[222] T. Bolze, J.-L. Wree, F. Kanal, D. Schleier, P. Nuernberger, *ChemPhysChem*, 2018, **19**, 138–147.

[223] A. Kovács, L. Wojnárovits, W. L. McLaughlin, S. E. E. Eid, A. Miller, *Radiation Physics and Chemistry*, 1996, **47**, 483–486.

[224] I. Hausser, D. Jerchel, R. Kuhn, *Chemische Berichte*, 1949, **82**, 515–527.

[225] R. Kuhn, H. M. Weitz, *Chemische Berichte*, 1953, **86**, 1199–1212.

[226] U. W. Grummt, H. Langbein, *Journal of Photochemistry*, 1981, **15**, 329–334.

[227] H. Ziegler, *Zeitschrift für Naturforschung B*, 1953, **8**, 662–667.

[228] T. Mosmann, *Journal of Immunological Methods*, 1983, **65**, 55–63.

[229] M. V. Berridge, P. M. Herst, A. S. Tan in *Biotechnology Annual Review*, *Vol. 11*, Elsevier, 2005, pp. 127–152.

[230] G. Lakon, *Berichte der Deutschen Botanischen Gesellschaft*, 1942, **60**, 299–305.

[231] F. E. Smith, *Science*, 1951, **113**, 751–754.

[232] A. M. Mattson, C. O. Jensen, *Analytical Chemistry*, 1950, **22**, 182–185.

[233] J. Carmichael, W. G. DeGraff, A. F. Gazdar, J. D. Minna, J. B. Mitchell, *Cancer Research*, 1987, **47**, 936–942.

[234] M. C. Alley, D. A. Scudiere, A. Monks, M. L. Hursey, M. J. Czerwinski, D. L. Fine, B. J. Abbott, J. G. Mayo, R. H. Shoemaker, M. R. Boyd, *Cancer Research*, 1988, **48**, 589–601.

[235] D. A. Scudiere, R. H. Shoemaker, K. D. Paul, A. Monks, S. Tierney, T. H. Nofziger, M. J. Currens, D. Seniff, M. R. Boyd, *Cancer Research*, 1988, **48**, 4827–4833.

[236] J. B. Gilroy, E. Otten, *Chemical Society Reviews*, 2020, **49**, 85–113.

[237] J. Zhao, B. Zhang, J. Li, Y. Liu, W. Wang, *Chemical Communications*, 2016, **52**, 11595–11598.

[238] J. Zhao, R. Zhu, X. Zhang, B. Zhang, Y. Liu, Y. Li, W. Wang, D. L. Phillips, *Physical Chemistry Chemical Physics*, 2021, **23**, 3761–3770.

[239] G. Turkoglu, H. Berber, I. Kani, *New Journal of Chemistry*, 2015, **39**, 2728–2740.

[240] D. Creangă, C. Nădejde, *Chemical Papers*, 2014, **68**, 260–271.

[241] O. E. Sherif, *Monatshefte für Chemie*, 1997, **128**, 981–990.

[242] C. Nădejde, D. Creangă, E. Filip, D.-O. Dorohoi, *Romanian Journal of Physics*, 2009, **54**, 649–657.

[243] S. Kumar, R. Sharma, S. Kumar, Nitika, *Chemical Science Transactions*, 2014, **3**, 919–928.

[244] D. Schulte-Frohlinde, *Justus Liebigs Annalen der Chemie*, 1959, **622**, 47–53.

[245] O. E. Sherif, *International Journal of Electrochemical Science*, 2015, **10**, 9751–9765.

[246] G. Gökce, Z. Durmuş, H. Tezcan, E. Kiliç, Y. H, *Analytical Sciences*, 2005, **21**, 685–688.

[247] U. W. Grummt, H. Langbein, R. Nöske, G. Röbisch, *Journal of Photochemistry*, 1984, **24**, 53–63.

[248] L. S. Atabekyan, V. A. Barachevskii, S. A. Melkozerov, G. N. Lipunova, I. G. Perova, I. N. Lipunov, G. I. Sigeikin, *High Energy Chemistry*, 2011, **45**, 52–56.

[249] G. Buemi, F. Zuccarello, P. Venuvanalingam, M. Ramalingam, S. Salai Cheettu Ammal, *Journal of the Chemical Society, Faraday Transactions*, 1998, **94**, 3313–3319.

[250] G. Buemi, F. Zuccarello, *Journal of Molecular Structure: Theochem*, 2002, **581**, 71–85.

[251] R. A. King, B. Murrin, *The Journal of Physical Chemistry A*, 2004, **108**, 4961–4965.

[252] H. Tezcan, N. Tokay, *International Journal of Quantum Chemistry*, 2010, **110**, 2140–2146.

[253] C. Schiele, *Berichte der Bunsengesellschaft für Physikalische Chemie*, 1965, **69**, 308–318.

[254] W. Otting, F. A. Neugebauer, *Zeitschrift für Naturforschung B*, 1968, **23**, 1064–1071.

[255] W. Otting, F. A. Neugebauer, *Chemische Berichte*, 1969, **102**, 2520–2529.

[256] J. W. Lewis, C. Sandorfy, *Canadian Journal of Chemistry*, 1983, **61**, 809–816.

[257] H. Hiura, H. Takahashi, *Journal of Molecular Structure*, 1989, **212**, 221–233.

[258] H. Hiura, H. Takahashi, *Journal of Molecular Structure*, 1989, **212**, 235–245.

[259] H. Tezcan, N. Ozkan, *Dyes and Pigments*, 2003, **56**, 159–166.

[260] G. Arnold, C. Schiele, *Spectrochimica Acta Part A: Molecular Spectroscopy*, 1969, **25**, 661–669.

[261] H. Langbein, *Journal für Praktische Chemie*, 1979, **321**, 655–664.

[262] Y. Sueishi, N. Nishimura, *The Chemical Society of Japan*, 1983, **56**, 2598–2604.

[263] C. Veas-Arancibia, Dissertation, Louisiana State University, Baton Rouge, LA, 1986.

[264] G. H. Brown, *Photochromism*, Wiley-Interscience, New York, 1971.

[265] T. Wilhelm, J. Piel, E. Riedle, *Optics Letters*, 1997, **22**, 1494–1496.

[266] A. Dobryakov, S. A. Kovalenko, A. Weigel, J. L. Pérez-Lustres, J. Lange, A. Müller, N. Ernsting, *Review of Scientific Instruments*, 2010, **81**, 113106.

[267] S. Schott, A. Steinbacher, J. Buback, P. Nuernberger, T. Brixner, *Journal of Physics B: Atomic, Molecular and Optical Physics*, 2014, **47**, 124014.

[268] B. Dick, U. Kensy, R. J. Kutta, *Physical Sciences Reviews*, 2019, **4**, 1–18.

[269] F. Neese, *The ORCA program system, WIREs Comput. Mol. Sci. 2 (2012) 73–78.*

[270] F. Neese, *Software update: the ORCA program system, version 4.0. WIREs Comput Mol Sci 8 (1): e1327*, 2018.

[271] F. Weigend, M. Häser, H. Patzelt, R. Ahlrichs, *Chemical Physics Letters*, 1998, **294**, 143–152.

[272] F. Weigend, R. Ahlrichs, *Physical Chemistry Chemical Physics*, 2005, **7**, 3297–3305.

[273] G. V. Avramenko, B. I. Stepanov, *Zhurnal Obshchei Khimii (Journal of General Chemistry of the USSR)*, 1974, **44**, 1298–1302.

[274] E. Wilhite, Dissertation, United States: Louisiana State University, 1991.

[275] H. Satzger, S. Spörlein, C. Root, J. Wachtveitl, W. Zinth, P. Gilch, *Chemical Physics Letters*, 2003, **372**, 216–223.

[276] H. Satzger, C. Root, M. Braun, *The Journal of Physical Chemistry A*, 2004, **108**, 6265–6271.

[277] T. Pancur, F. Renth, F. Temps, B. Harbaum, A. Krüger, R. Herges, C. Näther, *Physical Chemistry Chemical Physics*, 2005, **7**, 1985–1989.

[278] M. Quick, A. Dobryakov, M. Gerecke, C. Richter, F. Berndt, I. Ioffe, A. Granovsky, R. Mahrwald, N. Ernsting, S. Kovalenko, *The Journal of Physical Chemistry B*, 2014, **118**, 8756–8771.

[279] A. Nenov, R. Borrego-Varillas, A. Oriana, L. Ganzer, F. Segatta, I. Conti, J. Segarra-Marti, J. Omachi, M. Dapor, S. Taioli, et al., *The Journal of Physical Chemistry Letters*, 2018, **9**, 1534–1541.

[280] R. Siewertsen, J. B. Schönborn, B. Hartke, F. Renth, F. Temps, *Physical Chemistry Chemical Physics*, 2011, **13**, 1054–1063.

[281] C. Slavov, C. Yang, L. Schweighauser, C. Boumrifak, A. Dreuw, H. A. Wegner, J. Wachtveitl, *Physical Chemistry Chemical Physics*, 2016, **18**, 14795–14804.

[282] L. Grimmelsmann, A. Marefat Khah, C. Spies, C. Hättig, P. Nuernberger, *The Journal of Physical Chemistry Letters*, 2017, **8**, 1986–1992.

[283] C. T. Middleton, B. Cohen, B. Kohler, *The Journal of Physical Chemistry A*, 2007, **111**, 10460–10467.

[284] R. Ghosh, A. K. Mora, S. Nath, *The Journal of Physical Chemistry B*, 2019, **123**, 4408–4414.

[285] D. Veierov, T. Bercovici, E. Fischer, Y. Mazur, A. Yogev, *Journal of the American Chemical Society*, 1977, **99**, 2723–2729.

[286] A. Kobayashi, M. Yamaji, S. Nakajima, K. Akiyama, S. Tero-Kubota, S.-i. Kato, Y. Nakamura, *Chemical Physics Letters*, 2013, **555**, 101–105.

[287] S. Xu, S. T. Park, J. S. Feenstra, R. Srinivasan, A. H. Zewail, *The Journal of Physical Chemistry A*, 2004, **108**, 6650–6655.

[288] L. Poisson, P. Roubin, S. Coussan, B. Soep, J.-M. Mestdagh, *Journal of the American Chemical Society*, 2008, **130**, 2974–2983.

[289] P. K. Verma, F. Koch, A. Steinbacher, P. Nuernberger, T. Brixner, *Journal of the American Chemical Society*, 2014, **136**, 14981–14989.

[290] P. K. Verma, A. Steinbacher, F. Koch, P. Nuernberger, T. Brixner, *Physical Chemistry Chemical Physics*, 2015, **17**, 8459–8466.

[291] D. L. Beveridge, H. Jaffe, *Journal of the American Chemical Society*, 1966, **88**, 1948–1953.

[292] A. A. Beharry, G. A. Woolley, *Chemical Society Reviews*, 2011, **40**, 4422–4437.

[293] P. Hamm, S. Ohline, W. Zinth, *The Journal of Chemical Physics*, 1997, **106**, 519–529.

[294] J. Wachtveitl, B. Puell, W. Zinth, M. Krüger, S. Rudolph-Böhner, D. Oesterhelt, L. Moroder, *Journal of Photochemistry and Photobiology A: Chemistry*, 1997, **105**, 283–288.

[295] F. Koller, C. Sobotta, T. Schrader, T. Cordes, W. Schreier, A. Sieg, P. Gilch, *Chemical Physics*, 2007, **341**, 258–266.

[296] J. Bahrenburg, F. Renth, F. Temps, F. Plamper, W. Richtering, *Physical Chemistry Chemical Physics*, 2014, **16**, 11549–11554.

[297] L. Grimmelsmann, V. Schuabb, B. Tekin, R. Winter, P. Nuernberger, *Physical Chemistry Chemical Physics*, 2018, **20**, 18169–18175.

[298] A. M. Khah, L. Grimmelsmann, J. Knorr, P. Nuernberger, C. Hättig, *Physical Chemistry Chemical Physics*, 2018, **20**, 28075–28087.

[299] C. J. Otolski, A. M. Raj, V. Ramamurthy, C. G. Elles, *The Journal of Physical Chemistry Letters*, 2019, **10**, 121–127.

[300] C. Slavov, C. Yang, A. H. Heindl, H. A. Wegner, A. Dreuw, J. Wachtveitl, *Angewandte Chemie International Edition*, 2020, **59**, 380–387.

[301] H. S. M. Coxeter, *Regular polytopes*, Methuen & Co., Ltd., London, 1948.

[302] H. Maehara, *Journal of Geometry*, 2016, **107**, 567–577.

[303] R. H. Hammack, P. C. Kainen, *The American Mathematical Monthly*, 2021, **128**, 352–359.

[304] P. Fischer, B. Kaul, H. Zollinger, *Helvetica Chimica Acta*, 1968, **51**, 1449–1451.

[305] A. T. Hutton, H. M. Irving, *Journal of the Chemical Society, Chemical Communications*, 1980, **16**, 763–765.

[306] A. T. Hutton, H. M. Irving, *Journal of the Chemical Society, Perkin Transactions 2*, 1982, **9**, 1117–1121.

[307] A. F. Hegarty, F. L. Scott, *Chemical Communications*, 1966, **17**, 622–623.

[308] A. F. Hegarty, F. L. Scott, *The Journal of Organic Chemistry*, 1967, **32**, 1957–1963.

[309] N. Agmon, *Chemical Physics Letters*, 1995, **244**, 456–462.

[310] T. Miyake, M. Rolandi, *Journal of Physics: Condensed Matter*, 2015, **28**, 023001.

[311] E. M. Adams, H. Hao, I. Leven, M. Rüttermann, H. Wirtz, M. Havenith, T. Head-Gordon, *Angewandte Chemie International Edition*, 2021, **60**, 25419–25427.

[312] E. S. Stoyanov, I. V. Stoyanova, C. A. Reed, *Chemistry – A European Journal*, 2008, **14**, 3596–3604.

[313] A. Fujii, N. Sugawara, P.-J. Hsu, T. Shimamori, Y.-C. Li, T. Hamashima, J.-L. Kuo, *Physical Chemistry Chemical Physics*, 2018, **20**, 14971–14991.

[314] Z. Long, A. O. Atsango, J. A. Napoli, T. E. Markland, M. E. Tuckerman, *The Journal of Physical Chemistry Letters*, 2020, **11**, 6156–6163.

[315] C. Reichardt, T. Welton, *Solvents and Solvent Effects in Organic Chemistry 4th ed.*, Wiley-VCH, 2010.

[316] M. J. Kamlet, L. M. Abboud, M. H. Abraham, R. W. Taft, *Journal of Organic Chemistry*, 1983, **48**, 2877–2887.

[317] M. B. Smith, J. March, *March's Advanced Organic Chemistry*, John Wiley & Sons, Inc., Hoboken, NJ, USA, 2006.

[318] D. A. Cram, *Fundamentals of Carbanion Chemistry*, Academic Press, New York, NY, 1965.

[319] R. G. Pearson, R. L. Dillon, *Journal of the American Chemical Society*, 1953, **75**, 2439–2443.

[320] K. J. Klabunde, D. J. Burton, *Journal of the American Chemical Society*, 1972, **94**, 5985–5990.

[321] P. Ballinger, F. A. Long, *Journal of the American Chemical Society*, 1960, **82**, 795–798.

[322] J. T. Muckerman, J. H. Skone, M. Ning, Y. Wasada-Tsutsui, *Biochimica et Biophysica Acta (BBA) - Bioenergetics*, 2013, **1827**, 882–891.

[323] W. S. Matthews, J. E. Bares, J. E. Bartmess, F. G. Bordwell, F. J. Cornforth, G. E. Drucker, Z. Margolin, R. J. McCallum, G. J. McCollum, N. R. Vanier, *Journal of the American Chemical Society*, 1975, **97**, 7006–7014.

[324] I. Colomer, A. E. R. Chamberlain, M. B. Haughey, T. J. Donohoe, *Nature Reviews Chemistry*, 2017, **1**, 0088.

[325] B. Dereka, E. Vauthey, *Chemical Science*, 2017, **8**, 5057–5066.

[326] R. Filler, R. M. Schure, *The Journal of Organic Chemistry*, 1967, **32**, 1217–1219.

[327] L. Eberson, *Journal of the Chemical Society, Perkin Transactions 2*, 1995, 1735–1744.

[328] J. Ortega, C. Ràfols, E. Bosch, M. Rosés, *Journal of the Chemical Society, Perkin Transactions 2*, 1996, **7**, 1497–1503.

[329] P. Jacques, *Chemical Physics Letters*, 1990, **171**, 353–356.

[330] S. Gupta, S. Rafiq, M. Kundu, P. Sen, *The Journal of Physical Chemistry B*, 2012, **116**, 1345–1355.

[331] R. K. Saini, K. Das, *The Journal of Physical Chemistry B*, 2012, **116**, 10357–10363.

[332] R. K. Saini, K. Das, *Journal of Luminescence*, 2013, **144**, 169–175.

[333] R. K. Saini, K. Das, *Journal of Luminescence*, 2014, **145**, 832–837.

[334] Y.-H. Wang, P. Wan, *Photochemical & Photobiological Sciences*, 2013, **12**, 1571–1588.

[335] N. Barman, K. Sahu, *RSC Advances*, 2014, **4**, 58299–58306.

[336] L. R. Santin, S. C. dos Santos, D. L. R. Novo, D. Bianchini, A. P. Gerola, G. Braga, W. Caetano, L. M. Moreira, E. L. Bastos, A. P. Romani, *Dyes and Pigments*, 2015, **119**, 12–21.

[337] D. Das Mahanta, S. I. Islam, S. Choudhury, D. K. Das, R. K. Mitra, A. Barman, *Journal of Molecular Liquids*, 2019, **290**, 111194.

[338] J. Knorr, P. Sokkar, S. Schott, P. Costa, W. Thiel, W. Sander, E. Sanchez-Garcia, P. Nuernberger, *Nature Communications*, 2016, **7**, 1–8.

[339] J. Knorr, P. Sokkar, P. Costa, W. Sander, E. Sanchez-Garcia, P. Nuernberger, *The Journal of Organic Chemistry*, 2019, **84**, 11450–11457.

[340] L. Eberson, M. P. Hartshorn, O. Persson, F. Radner, *Chemical Communications*, 1996, **18**, 2105–2112.

[341] M. Burdisso, R. Gandolfi, L. Toma, R. Oberti, *Tetrahedron*, 1991, **47**, 6725–6736.

[342] A. Berkessel, J. A. Adrio, D. Hüttenhain, J. M. Neudörfl, *Journal of the American Chemical Society*, 2006, **128**, 8421–8426.

[343] M. O. Ratnikov, V. V. Tumanov, W. A. Smit, *Angewandte Chemie*, 2008, **120**, 9885–9888.

[344] J. Hankache, D. Hanss, O. S. Wenger, *The Journal of Physical Chemistry A*, 2012, **116**, 3347–3358.

[345] A. M. Arnold, A. Pöthig, M. Drees, T. Gulder, *Journal of the American Chemical Society*, 2018, **140**, 4344–4353.

[346] P. F. McGarry, S. Jockusch, Y. Fujiwara, N. A. Kaprinidis, N. J. Turro, *The Journal of Physical Chemistry A*, 1997, **101**, 764–767.

[347] Z. Yuan, Q. Tang, K. Sreenath, J. T. Simmons, A. H. Younes, D.-e. Jiang, L. Zhu, *Photochemistry and Photobiology*, 2015, **91**, 586–598.

[348] G. Palla, G. Predieri, P. Domiano, C. Vignali, W. Turner, *Tetrahedron*, 1986, **42**, 3649–3654.

[349] S. Müller, B. List, *Angewandte Chemie International Edition*, 2009, **48**, 9975–9978.

[350] S. M. Landge, E. Tkatchouk, D. Benítez, D. A. Lanfranchi, M. Elhabiri, W. A. Goddard, I. Aprahamian, *Journal of the American Chemical Society*, 2011, **133**, 9812–9823.

[351] S. Müller, M. J. Webber, B. List, *Journal of the American Chemical Society*, 2011, **133**, 18534–18537.

[352] M. de Gracia Retamosa, E. Matador, D. Monge, J. M. Lassaletta, R. Fernández, *Chemistry – A European Journal*, 2016, **22**, 13430–13445.

[353] I. Aprahamian, *Chemical Communications*, 2017, **53**, 6674–6684.

[354] I. Cvrtila, H. Fanlo-Virgós, G. Schaeffer, G. Monreal Santiago, S. Otto, *Journal of the American Chemical Society*, 2017, **139**, 12459–12465.

[355] S. Mader, M. S. Maji, I. Atodiresei, M. Rueping, *Organic Chemistry Frontiers*, 2022, **9**, 4466–4471.

[356] M. Žabka, R. M. Gschwind, *European Journal of Organic Chemistry*, 2022, **2022**, e202200048.

[357] E. Hückel, *Zeitschrift für Physikalische Chemie*, 1931, **70**, 204–286.

[358] W. von E. Doering, L. Knox, *Journal of the American Chemical Society*, 1954, **76**, 3203–3206.

[359] W. von E. Doering, L. Knox, *Journal of the American Chemical Society*, 1957, **79**, 352–356.

[360] G. Berti, *The Journal of Organic Chemistry*, 1957, **22**, 230–230.

[361] G. Naville, H. Strauss, E. Heilbronner, *Helvetica Chimica Acta*, 1960, **43**, 1243–1254.

[362] M. E. Vol'pin, *Russian Chemical Reviews*, 1960, **29**, 129–160.

[363] D. Lloyd, *Carbocyclic Non-Benzenoid Aromatic Compounds*, Elsevier, Amsterdam, 1966.

[364] G. D. Kolomnikova, Z. N. Parnes, *Russian Chemical Reviews*, 1967, **36**, 735–753.

[365] S. V. Krivun, O. Alferova, S. V. Sayapina, *Russian Chemical Reviews*, 1974, **43**, 835–850.

[366] G. A. Olah, G. Liang, *The Journal of Organic Chemistry*, 1975, **40**, 2108–2116.

[367] Y. Takahashi, S. Sankararaman, J. K. Kochi, *Journal of the American Chemical Society*, 1989, **111**, 2954–2967.

[368] J. Henninger, H. Mayr, M. Patz, M. D. Stanescu, *Liebigs Annalen*, 1995, **1995**, 2005–2009.

[369] M. Feldman, S. Winstein, *Journal of the American Chemical Society*, 1961, **83**, 3338–3339.

[370] T. Beaumont, K. Davis, *Journal of the Chemical Society B: Physical Organic*, 1970, 592–595.

[371] T. Beaumont, K. Davis, *Nature*, 1970, **225**, 632–632.

[372] K. Okamoto, K. Komatsu, M. Fujimori, S. Yasuda, *Bulletin of the Chemical Society of Japan*, 1974, **47**, 2426–2430.

[373] K. Okamoto, K. Komatsu, O. Sakaguchi, *Bulletin of the Chemical Society of Japan*, 1974, **47**, 2431–2436.

[374] K. Takeuchi, K. Komatsu, K. Yasuda, K. Okamoto, *Tetrahedron Letters*, 1976, **17**, 3467–3470.

[375] K. Takeuchi, T. Kurosaki, Y. Yokomichi, Y. Kimura, Y. Kubota, H. Fujimoto, K. Okamoto, *Journal of the Chemical Society, Perkin Transactions 2*, 1981, 670–674.

[376] C. A. Bunton, K. Lal, W. E. Watts, *Journal of Organometallic Chemistry*, 1983, **247**, c14–c16.

[377] K. Komatsu, *The Chemical Record*, 2015, **15**, 160–174.

[378] S. Gronowitz, B. Yom-Tov, U. Michael, *Acta Chemica Scandinavica*, 1973, **27**, 2257–2270.

[379] T. Liljefors, U. Michael, B. Yom-Tov, S. Gronowitz, *Acta Chemica Scandinavica*, 1973, **27**, 2485–2494.

[380] N. S. Mills, F. E. Cheng, J. M. Baylan, C. Tirla, J. L. Hartmann, K. C. Patel, B. J. Dahl, S. P. McClintock, *The Journal of Organic Chemistry*, 2011, **76**, 645–653.

[381] C. Jutz, F. Voithenleitner, *Chemische Berichte*, 1964, **97**, 29–48.

[382] G. Hohlneicher, R. Kiessling, H. Jutz, P. Straub, *Berichte der Bunsengesellschaft für Physikalische Chemie*, 1966, **70**, 60–73.

[383] P. Schuster, D. Vedrilla, O. E. Polansky, *Monatshefte für Chemie*, 1969, **100**, 1–27.

[384] W. Abraham, M. Kupfer, C. Raetz, U. Tietz, D. Kreysig, *Polish Journal of Chemistry*, 1979, **53**, 737–740.

[385] W. Abraham, B. Dreher, K. Buck, D. Kreysig, *Journal für Praktische Chemie*, 1982, **324**, 925–932.

[386] B. Dreher, W. Abraham, F. Pragst, *Journal für Praktische Chemie*, 1983, **325**, 104–112.

[387] W. Abraham, B. Dreher, D. Kreysig, N. Sadovskij, M. Kuzmin, *Journal für Praktische Chemie*, 1987, **329**, 569–578.

[388] D. Jacobi, W. Abraham, *Tetrahedron Letters*, 1996, **37**, 7493–7496.

[389] V. Wendel, W. Abraham, *Tetrahedron Letters*, 1997, **38**, 1177–1180.

[390] D. Jacobi, W. Abraham, U. Pischel, L. Grubert, W. Schnabel, *Journal of the Chemical Society, Perkin Transactions 2*, 1999, 1241–1248.

[391] D. Jacobi, W. Abraham, U. Pischel, L. Grubert, R. Stösser, W. Schnabel, *Journal of the Chemical Society, Perkin Transactions 2*, 1999, 1695–1702.

[392] D. Jacobi, W. Abraham, U. Pischel, R. Stößer, W. Schnabel, *Journal of Photochemistry and Photobiology A: Chemistry*, 1999, **128**, 75–83.

[393] V. Kharlanov, W. Abraham, W. Rettig, *Journal of Photochemistry and Photobiology A: Chemistry*, 2001, **143**, 109–117.

[394] W. Abraham, *Journal of Inclusion Phenomena and Macrocyclic Chemistry*, 2002, **43**, 159–174.

[395] V. Kharlanov, W. Abraham, U. Pischel, *Journal of Photochemistry and Photobiology A: Chemistry*, 2004, **162**, 213–223.

[396] M. Fehlinger, W. Abraham, *Journal of Inclusion Phenomena and Macrocyclic Chemistry*, 2007, **58**, 263–274.

[397] W. Abraham, L. Grubert, *Molecular Encapsulation: Organic Reactions in Constrained Systems*, 2010, 327–360.

[398] D. Bethell, P. Clare, *Journal of the Chemical Society, Perkin Transactions 2*, 1972, 1464–1471.

[399] H. Mayr, K.-H. Müller, A. R. Ofial, M. Bühl, *Journal of the American Chemical Society*, 1999, **121**, 2418–2424.

[400] R. Childs, V. Taguchi, *Journal of the Chemical Society D: Chemical Communications*, 1970, 695–696.

[401] V. Fornés, H. García, M. A. Miranda, F. Mojarrad, M.-J. Sabater, N. N. Suliman, *Tetrahedron*, 1996, **52**, 7755–7760.

[402] K. Asai, A. Fukazawa, S. Yamaguchi, *Chemistry – A European Journal*, 2016, **22**, 17571–17575.

[403] K. Asai, A. Fukazawa, S. Yamaguchi, *Angewandte Chemie*, 2017, **129**, 6952–6956.

[404] L. Frish, M. O. Vysotsky, S. E. Matthews, V. Böhmer, Y. Cohen, *Journal of the Chemical Society, Perkin Transactions 2*, 2002, 88–93.

[405] N. Song, T. Kakuta, T.-a. Yamagishi, Y.-W. Yang, T. Ogoshi, *Chem*, 2018, **4**, 2029–2053.

[406] D. J. Lyons, R. D. Crocker, M. Blümel, T. V. Nguyen, *Angewandte Chemie International Edition*, 2017, **56**, 1466–1484.

[407] U. P. Tran, G. Oss, D. P. Pace, J. Ho, T. V. Nguyen, *Chemical Science*, 2018, **9**, 5145–5151.

[408] G. Oss, S. D. de Vos, K. N. Luc, J. B. Harper, T. V. Nguyen, *The Journal of Organic Chemistry*, 2018, **83**, 1000–1010.

[409] G. Oss, J. Ho, T. V. Nguyen, *European Journal of Organic Chemistry*, 2018, **2018**, 3974–3981.

[410] R. D. Crocker, D. P. Pace, B. Zhang, D. J. Lyons, M. M. Bhadbhade, W. W. Wong, B. K. Mai, T. V. Nguyen, *Journal of the American Chemical Society*, 2021, **143**, 20384–20394.

[411] C. Empel, T. V. Nguyen, R. M. Koenigs, *Organic Letters*, 2021, **23**, 548–553.

[412] D. J. Lyons, A. H. Dinh, N. N. Ton, R. D. Crocker, B. K. Mai, T. V. Nguyen, *Organic Letters*, 2022, **24**, 2520–2525.

[413] N. N. Ton, B. K. Mai, T. V. Nguyen, *The Journal of Organic Chemistry*, 2021, **86**, 9117–9133.

[414] S. H. Doan, M. A. Hussein, T. V. Nguyen, *Chemical Communications*, 2021, **57**, 8901–8904.

[415] S. H. Doan, T. V. Nguyen, *Green Chemistry*, 2022, **24**, 7382–7387.

[416] H. Yamamoto, W. Muramatsu, *Synfacts*, 2022, **18**, 0342.

[417] A. Anchi, S. M. Sutar, R. G. Kalkhambkar, G. L. Borosky, K. K. Laali, *ChemistrySelect*, 2022, **7**, e202202791.

[418] Rekha, S. Sharma, G. Singh, R. Vijaya Anand, *ACS Organic & Inorganic Au*, 2021, **2**, 186–196.

[419] Y. Hayashi, S. Suzuki, T. Suzuki, Y. Ishigaki, *Journal of the American Chemical Society*, 2023, **145**, 2596–2608.

[420] J. S. Mann, B. K. Mai, T. V. Nguyen, *ACS Catalysis*, 2023, **13**, 2696–2701.

[421] K.-H. Hong, Y. S. Lee, C. H. Nam, *Optics Communications*, 2007, **271**, 169–177.

[422] Y. Hong, J. W. Lam, B. Z. Tang, *Chemical Society Reviews*, 2011, **40**, 5361–5388.

[423] Y. Cai, L. Du, K. Samedov, X. Gu, F. Qi, H. H. Sung, B. O. Patrick, Z. Yan, X. Jiang, H. Zhang, *Chemical Science*, 2018, **9**, 4662–4670.

[424] *Operator's Manual: The Coherent Mira Model 900-B Laser*, Coherent Inc., 1993.

[425] R. Ahlrichs, M. Bär, M. Häser, H. Horn, C. Kölmel, *Chemical Physics Letters*, 1989, **162**, 165–169.

[426] *TURBOMOLE V7.4 2019, a development of University of Karlsruhe and Forschungszentrum Karlsruhe GmbH, 1989-2007, TURBOMOLE GmbH, since 2007; available from* `http://www.turbomole.com`.

[427] J. Thom H. Dunning, *Journal of Chemical Physics*, 1989, **90**, 1007–1023.

[428] R. A. Kendall, T. H. Dunning Jr, R. J. Harrison, *The Journal of Chemical Physics*, 1992, **96**, 6796–6806.

[429] D. E. Woon, T. H. Dunning Jr, *The Journal of Chemical Physics*, 1993, **98**, 1358–1371.

[430] G. Fleming, *Chemical Applications of Ultrafast Spectroscopy*, Oxford University Press, New York, 1986.

[431] T. Fiebig, M. Chachisvilis, M. Manger, A. Zewail, A. Douhal, I. Garcia-Ochoa, A. de La Hoz Ayuso, *The Journal of Physical Chemistry A*, 1999, **103**, 7419–7431.

[432] H. Wang, H. Zhang, O. Abou-Zied, C. Yu, F. Romesberg, M. Glasbeek, *Chemical Physics Letters*, 2003, **367**, 599–608.

[433] J. Xu, J. R. Knutson, *Methods in Enzymology*, 2008, **450**, 159–183.

[434] H. Lemmetyinen, N. V. Tkachenko, B. Valeur, J.-i. Hotta, M. Ameloot, N. P. Ernsting, T. Gustavsson, N. Boens, *Pure and Applied Chemistry*, 2014, **86**, 1969–1998.

[435] A. A. Maskevich, V. I. Stsiapura, V. A. Kuzmitsky, I. M. Kuznetsova, O. I. Povarova, V. N. Uversky, K. K. Turoverov, *Journal of Proteome Research*, 2007, **6**, 1392–1401.

[436] V. I. Stsiapura, A. A. Maskevich, V. A. Kuzmitsky, K. K. Turoverov, I. M. Kuznetsova, *The Journal of Physical Chemistry A*, 2007, **111**, 4829–4835.

[437] S. Freire, M. H. de Araujo, W. Al-Soufi, M. Novo, *Dyes and Pigments*, 2014, **110**, 97–105.

[438] Z. R. Grabowski, K. Rotkiewicz, W. Rettig, *Chemical Reviews*, 2003, **103**, 3899–4032.

[439] O. Kwon, S. Barlow, S. A. Odom, L. Beverina, N. J. Thompson, E. Zojer, J.-L. Brédas, S. R. Marder, *The Journal of Physical Chemistry A*, 2005, **109**, 9346–9352.

[440] D. Pace, R. Crocker, W. Kendrick, B. Zhang, W. Wong, M. Bhadbhade, T. Schmidt, T. V. Nguyen, 2023, https://doi.org/10.26434/chemrxiv-2023-s9l13.

[441] J. A. Hirsch, *Topics in Stereochemistry*, 1967, **1**, 199–222.

[442] G. Berti, *Gazzetta Chimica Italiana*, 1957, **87**, 293–309.

[443] A. Siemiarczuk, J. Koput, A. Pohorille, *Zeitschrift für Naturforschung A*, 1982, **37**, 598–606.

[444] N. Sülzner, B. Geissler, A. Grandjean, G. Jung, P. Nuernberger, *ChemPhotoChem*, 2022, **6**, e202200041.

[445] W. Abraham, H. Otto, D. Kreysig, *Journal of Photochemistry*, 1981, **16**, 261–266.

[446] J.-H. Choi, H. R. Choi, J. Jeon, M. Cho, *The Journal of Chemical Physics*, 2017, **147**, 154107.

[447] J.-H. Choi, M. Cho, *The Journal of Chemical Physics*, 2016, **145**, 174501.

[448] R. I. Storer, D. E. Carrera, Y. Ni, D. W. MacMillan, *Journal of the American Chemical Society*, 2006, **128**, 84–86.

[449] S. Hoffmann, A. M. Seayad, B. List, *Angewandte Chemie*, 2005, **117**, 7590–7593.

[450] M. Mahlau, B. List, *Angewandte Chemie*, 2013, **125**, 540–556.

[451] M. Terada, *Synthesis*, 2010, 1929–1982.

[452] D. Uraguchi, M. Terada, *Journal of the American Chemical Society*, 2004, **126**, 5356–5357.

[453] M. Yamanaka, J. Itoh, K. Fuchibe, T. Akiyama, *Journal of the American Chemical Society*, 2007, **129**, 6756–6764.

[454] X. Xu, Y. Qian, L. Yang, W. Hu, *Chemical Communications*, 2011, **47**, 797–799.

[455] E. P. Avila, R. M. Justo, V. P. Goncalves, A. A. Pereira, R. Diniz, G. W. Amarante, *The Journal of Organic Chemistry*, 2015, **80**, 590–594.

[456] K. Shen, X. Liu, Y. Cai, L. Lin, X. Feng, *Chemistry – A European Journal*, 2009, **15**, 6008–6014.

[457] S. Saha, C. Schneider, *Chemistry – A European Journal*, 2015, **21**, 2348–2352.

[458] C. Gharui, S. Singh, S. C. Pan, *Organic & Biomolecular Chemistry*, 2017, **15**, 7272–7276.

[459] H. Liu, L.-F. Cun, A.-Q. Mi, Y.-Z. Jiang, L.-Z. Gong, *Organic Letters*, 2006, **8**, 6023–6026.

[460] Q. Kang, Z.-A. Zhao, S.-L. You, *Journal of the American Chemical Society*, 2007, **129**, 1484–1485.

[461] Y.-X. Jia, J. Zhong, S.-F. Zhu, C.-M. Zhang, Q.-L. Zhou, *Angewandte Chemie*, 2007, **119**, 5661–5663.

[462] G. Li, G. B. Rowland, E. B. Rowland, J. C. Antilla, *Organic Letters*, 2007, **9**, 4065–4068.

[463] M. Terada, K. Sorimachi, *Journal of the American Chemical Society*, 2007, **129**, 292–293.

[464] M. Terada, S. Yokoyama, K. Sorimachi, D. Uraguchi, *Advanced Synthesis & Catalysis*, 2007, **349**, 1863–1867.

[465] M. J. Wanner, R. N. van der Haas, K. R. de Cuba, J. H. van Maarseveen, H. Hiemstra, *Angewandte Chemie International Edition*, 2007, **46**, 7485–7487.

[466] Q. Kang, Z.-A. Zhao, S.-L. You, *Organic Letters*, 2008, **10**, 2031–2034.

[467] K. Saito, T. Akiyama, *Chemical Communications*, 2012, **48**, 4573–4575.

[468] V. N. Wakchaure, P. S. Kaib, M. Leutzsch, B. List, *Angewandte Chemie International Edition*, 2015, **54**, 11852–11856.

[469] C. Min, D. Seidel, *Chemical Society Reviews*, 2017, **46**, 5889–5902.

[470] T. Marcelli, P. Hammar, F. Himo, *Chemistry – A European Journal*, 2008, **14**, 8562–8571.

[471] J. P. Reid, J. M. Goodman, *Journal of the American Chemical Society*, 2016, **138**, 7910–7917.

[472] A. Milo, A. J. Neel, F. D. Toste, M. S. Sigman, *Science*, 2015, **347**, 737–743.

[473] R. Maji, S. C. Mallojjala, S. E. Wheeler, *Chemical Society Reviews*, 2018, **47**, 1142–1158.

[474] J. P. Reid, L. Simón, J. M. Goodman, *Accounts of Chemical Research*, 2016, **49**, 1029–1041.

[475] L. Simón, J. M. Goodman, *The Journal of Organic Chemistry*, 2011, **76**, 1775–1788.

[476] C. B. Santiago, J.-Y. Guo, M. S. Sigman, *Chemical Science*, 2018, **9**, 2398–2412.

[477] G. Li, Y. Liang, J. C. Antilla, *Journal of the American Chemical Society*, 2007, **129**, 5830–5831.

[478] J. H. An, K. D. Kim, J. H. Lee, *The Journal of Organic Chemistry*, 2021, **86**, 2876–2894.

[479] M. Sickert, F. Abels, M. Lang, J. Sieler, C. Birkemeyer, C. Schneider, *Chemistry – A European Journal*, 2010, **16**, 2806–2818.

[480] M. Fleischmann, D. Drettwan, E. Sugiono, M. Rueping, R. M. Gschwind, *Angewandte Chemie*, 2011, **123**, 6488–6493.

[481] W. Tang, S. Johnston, J. A. Iggo, N. G. Berry, M. Phelan, L. Lian, J. Bacsa, J. Xiao, *Angewandte Chemie*, 2013, **125**, 1712–1716.

[482] J. Greindl, J. Hioe, N. Sorgenfrei, F. Morana, R. M. Gschwind, *Journal of the American Chemical Society*, 2016, **138**, 15965–15971.

[483] M. Melikian, J. Gramüller, J. Hioe, J. Greindl, R. M. Gschwind, *Chemical Science*, 2019, **10**, 5226–5234.

[484] N. Lokesh, J. Hioe, J. Gramüller, R. M. Gschwind, *Journal of the American Chemical Society*, 2019, **141**, 16398–16407.

[485] D. Jansen, J. Gramüller, F. Niemeyer, T. Schaller, M. C. Letzel, S. Grimme, H. Zhu, R. M. Gschwind, J. Niemeyer, *Chemical Science*, 2020, **11**, 4381–4390.

[486] J. Gramüller, P. Dullinger, D. Horinek, R. M. Gschwind, *Chemical Science*, 2022, **13**, 14366–14372.

[487] M. Franta, J. Gramüller, P. Dullinger, S. Kaltenberger, D. Horinek, R. M. Gschwind, *Angewandte Chemie*, 2023, e202301183.

[488] L. Simón, J. M. Goodman, *Journal of the American Chemical Society*, 2008, **130**, 8741–8747.

[489] L. Simón, J. M. Goodman, *Journal of the American Chemical Society*, 2009, **131**, 4070–4077.

[490] L. Simón, J. M. Goodman, *The Journal of Organic Chemistry*, 2010, **75**, 589–597.

[491] T. Marcelli, P. Hammar, F. Himo, *Advanced Synthesis & Catalysis*, 2009, **351**, 525–529.

[492] T. Yanai, D. P. Tew, N. C. Handy, *Chemical Physics Letters*, 2004, **393**, 51–57.

[493] D. Xiao, M. Premont-Schwarz, E. T. Nibbering, V. S. Batista, *The Journal of Physical Chemistry A*, 2012, **116**, 2775–2790.

[494] J. Ferguson, L. W. Reeves, W. G. Schneider, *Canadian Journal of Chemistry*, 1957, **35**, 1117–1136.

[495] H. Maeda, T. Maeda, K. Mizuno, *Molecules*, 2012, **17**, 5108–5125.

[496] R. Masrat, M. Maswal, A. A. Dar, *Journal of Hazardous Materials*, 2013, **244**, 662–670.

[497] I. Minkov, F. Gel'mukhanov, R. Friedlein, W. Osikowicz, C. Suess, G. Öhrwall, S. L. Sorensen, S. Braun, R. Murdey, W. R. Salaneck, *The Journal of Chemical Physics*, 2004, **121**, 5733–5739.

[498] D. Wang, Q. Liu, B. Chen, L. Zhang, C. Tung, L. Wu, *Chinese Science Bulletin*, 2010, **55**, 2855–2858.

[499] N. A. Pizarro-Urzúa, L. J. Núñez-Vergara, *Journal of Photochemistry and Photobiology A: Chemistry*, 2005, **175**, 129–137.

[500] W. Huang, X. Cheng, *Synlett*, 2017, **28**, 148–158.

[501] H. R. Memarian, M. M. Sadeghi, A. R. Momeni, D. Döpp, *Monatshefte für Chemie*, 2002, **133**, 661–667.

[502] H. R. Memarian, M. Bagheri, D. Döpp, *Monatshefte für Chemie*, 2004, **135**, 833–838.

[503] X.-x. Wang, H. Fu, D.-m. Du, Z.-y. Zhou, A.-g. Zhang, C.-f. Su, K.-s. Ma, *Chemical Physics Letters*, 2008, **460**, 339–342.

[504] F. R. Dutra, C. d. S. Silva, R. Custodio, *The Journal of Physical Chemistry A*, 2020, **125**, 65–73.

[505] R. N. Goldberg, N. Kishore, R. M. Lennen, *Journal of Physical and Chemical Reference Data*, 2002, **31**, 231–370.

[506] P. Christ, A. G. Lindsay, S. S. Vormittag, J.-M. Neudörfl, A. Berkessel, A. C. O'Donoghue, *Chemistry – A European Journal*, 2011, **17**, 8524–8528.

[507] S. Niziński, M. Wendel, M. F. Rode, D. Prukała, M. Sikorski, S. Wybraniec, G. Burdziński, *RSC Advances*, 2017, **7**, 6411–6421.

[508] M. F. Rode, A. L. Sobolewski, *The Journal of Physical Chemistry A*, 2010, **114**, 11879–11889.

[509] H. Böhnke, J. Bahrenburg, X. Ma, K. Röttger, C. Näther, M. F. Rode, A. L. Sobolewski, F. Temps, *Physical Chemistry Chemical Physics*, 2018, **20**, 2646–2655.

[510] J. Jankowska, M. F. Rode, J. Sadlej, A. L. Sobolewski, *ChemPhysChem*, 2014, **15**, 1643–1652.

[511] K. Artmann, C. H. Pollok, C. Merten, P. Nuernberger, *Physical Chemistry Chemical Physics*, 2022, **24**, 30017–30026.

[512] R. Trebino, K. W. DeLong, D. N. Fittinghoff, J. N. Sweetser, M. A. Krumbügel, B. A. Richman, D. J. Kane, *Review of Scientific Instruments*, 1997, **68**, 3277–3295.

[513] *DeLong, K. FROG (Frequency-Resolved Optical Gating) software for measuring ultrafast laser pulses. https://github.com/kenwdelong/frog, 2016.*

[514] T. Rittner, Master Thesis, Universität Regensburg, 2021.

Acknowledgment

At this point, I want to express my gratitude to all supervisors, referees, sponsors, cooperation partners, colleagues, friends and family members, who supported and helped me during my PhD time. It has been a pleasure to work with you on the here presented research topics. Therefore, I would like to take this opportunity to express my gratitude for the successful collaboration and teamwork on which this thesis and the joint publications are based.

First of all, I want to thank **Prof. Dr. Patrick Nürnberger** for the opportunity to spend my time as a PhD student in his group. I am very grateful for the awesome supervision and the valuable ideas and discussions regarding my research projects. I thank you for the great promotion of not only my scientific expertise but also my personality development by affording the participation at several scientific and also non-scientific conferences, workshops, and further educational training courses. It was impressive that you always took the time for answering my questions, discussing the challenges within my projects and collecting new ideas.

I also want to express my gratitude to **Prof. Dr. Bernhard Dick** for the very helpful scientific discussions, his expert advice and for being the second referee. Furthermore, I enjoyed the varied stories and wisdoms regarding every condition of life.

I am very thankful to **Dr. Roger Kutta** for welcoming me in Regensburg, showing me the laboratories and explaining the basics, discussing my results, providing new ideas, and giving an introduction to the world of computational chemistry. Thank you for the continuous support, your contribution to several parts of this thesis and for providing your LabView programs.

Furthermore, I would like to acknowledge **Prof. Dr. Alkwin Slenczka** for always having a friendly ear and a perfect advice even if not directly involved in my research projects.

My gratitude also goes to **Prof. Dr. Julia Rehbein** and **Prof. Dr. Oliver Tepner** for the willingness to support me as third referee and as chair of my doctoral committee, respectively.

I also want to thank **Prof. Dr. Ruth Gschwind** for the opportunity to be part of the RTG2620,

whereby I got the possibility to attend several conferences, retreats and workshops which supported my personal development in addition to inspiring scientific conversations. Furthermore, I am grateful for the excellent scientific cooperation with Prof. Dr. Ruth Gschwind and **Christian Scholtes**, whose ideas and experiences have greatly enriched the CPA/imine-project.

I am also thankful to **Prof. Dr. Eberhard Riedle** for his educational lessons and for sharing his long-term experience regarding optics and ultrafast spectroscopy. Moreover, I would like to thank Prof. Dr. Eberhard Riedle and **Ferdinand Bergmeier** for the extraordinary cooperation leading to great scientific discussions and a promising paper draft regarding the spectroscopic characterization of the tropylium dyes.

Even though the results are not shown in this work, I am grateful for the fabulous cooperation and the valuable scientific exchange with **Prof. Dr. Nils Metzler-Nolte**, **Dr. Isabelle Daubit**, and **Dr. Nicole Schubert**, resulting in great scientific contributions about organic/organometallic compounds with biological applications.

My gratitude goes also to **Prof. Dr. Vinh Nguyen and his group members** for the great cooperation with excellent scientific discussions despite the time difference. They always created a friendly working atmosphere especially due to their extraordinary patience when the project progress went more slowly because of moving from Bochum to Regensburg.

Furthermore, I am thankful to the chemistry students **Sylvia Schlöglmann**, **Jonas Poll**, and **Matthias Kawalek**, who helped me with my research during their practical courses. An additional gratitude goes to Sylvia for staying in our group as research assistant and thus, further promoting my scientific projects.

I would also like to thank all of my colleagues in Regensburg **Niklas Gessner**, **Stephan Muth**, **Dr. Kevin Artmann**, **Gabriel Mayer**, **Carina Allacher**, **Daniel Grenda**, **Thomas Rittner**, **Christina Graf**, **Sophie Chisholm**, **Sebastian Bösl-Bichlmeier**, **Marcel Fischer**, **Dr. Sebastian Bergwinkl**, **Johannes Fischer** and **Florian Schlaghaufer** for the scientific discussions, the help in the lab, the entertaining game nights full of fun and for becoming a great team during the last years. Furthermore, I would like to acknowledge the alumni of the physical chemistry group **Fabian Brandl**, **Dr. Uwe Faltermeier**, **Dr. Stefan Fuchs**, **Magdalena Luger**, **Dr. Marsel Shavikov** and **Dr. Rafal Czerwieniec**, who introduced me into the Bavarian customs.

Additionally, I want to thank the technicians **Madlene von Sanden**, **Birte Höing** and **Gabriele Alder** for taking care of the chemistry lab and **Klaus Ziereis** for keeping the IT infrastructure

running. The structured and reliable preparation of chemicals by Madlene made the chemistry lab course for physicists much easier.

I also want to express my gratitude to **Andrea Nömeier** for managing the administrative stuff in our group and always knowing an answer to my bureaucratic problems.

Furthermore, I would also like to thank my former colleagues from Bochum **Dr. Johannes Knorr**, **Dr. Lena Grimmelsmann**, **Dr. Bastian Geißler**, **Niklas Gessner**, **Dr. Kevin Artmann**, **Dr. Niklas Sülzner**, **Dr. Christian Spies** and **Dr. Tom Bolze**, who taught me a lot about nonlinear optics and time-resolved spectroscopy, found always the time to answer my questions or to help me with technical problems.

I also would like to acknowledge the **Deutsche Forschungsgemeinschaft** for funding since April 2021 within the project RTG2620 with the topic "Ion Pair Effects in Molecular Reactivity". Thus, I got the opportunity to attend at several national and international conferences and advanced educations, where I could present and discuss my recent scientific results, where I could further develop my personality, and where I made new friends.

I am also very grateful for a lot of friendships that have developed during my chemistry studies. I would like to thank **Dr. Till Eckhard**, **Simon Zerulla**, **Kevin Profita**, **Marcel Schmickler**, **Dr. Dina Zakgeym**, **Dr. Nils Weißing**, **Dr. Fabio Caló**, **Dr. Niklas Sülzner** and **Julien Rowen** for the fun times, the good team spirit and the support during my studies. Without all of you, I would have had only half of the fun during the last ten years.

In addition to his expertise and support as group member, I want to thank **Kevin Artmann** for his extraordinary patience and help regarding LaTeX problems, for discussing my research results and his encouragement, especially during the last year of my PhD.

And finally, a special gratitude goes to my parents **Bernd and Brigitte Wortmann**, and my little brother **Sören Wortmann** for their entire love, their continuous support and encouragement without I would never have got to this point. Thanks for being my Family!

Permissions

Publication [1]:

Reused and reprinted with permission from S. Wortmann, S. Schloeglmann, and P. Nuernberger. Sensitivity of Isomerization Kinetics of 1,3,5-Triphenylformazan on Cosolvents Added to Toluene. *J. Org. Chem.* **2021**, 87, 1745-1755, doi:10.1021/acs.joc.1c01928. **Copyright 2021 American Society.** https://pubs.acs.org/doi/10.1021/acs.joc.1c01928

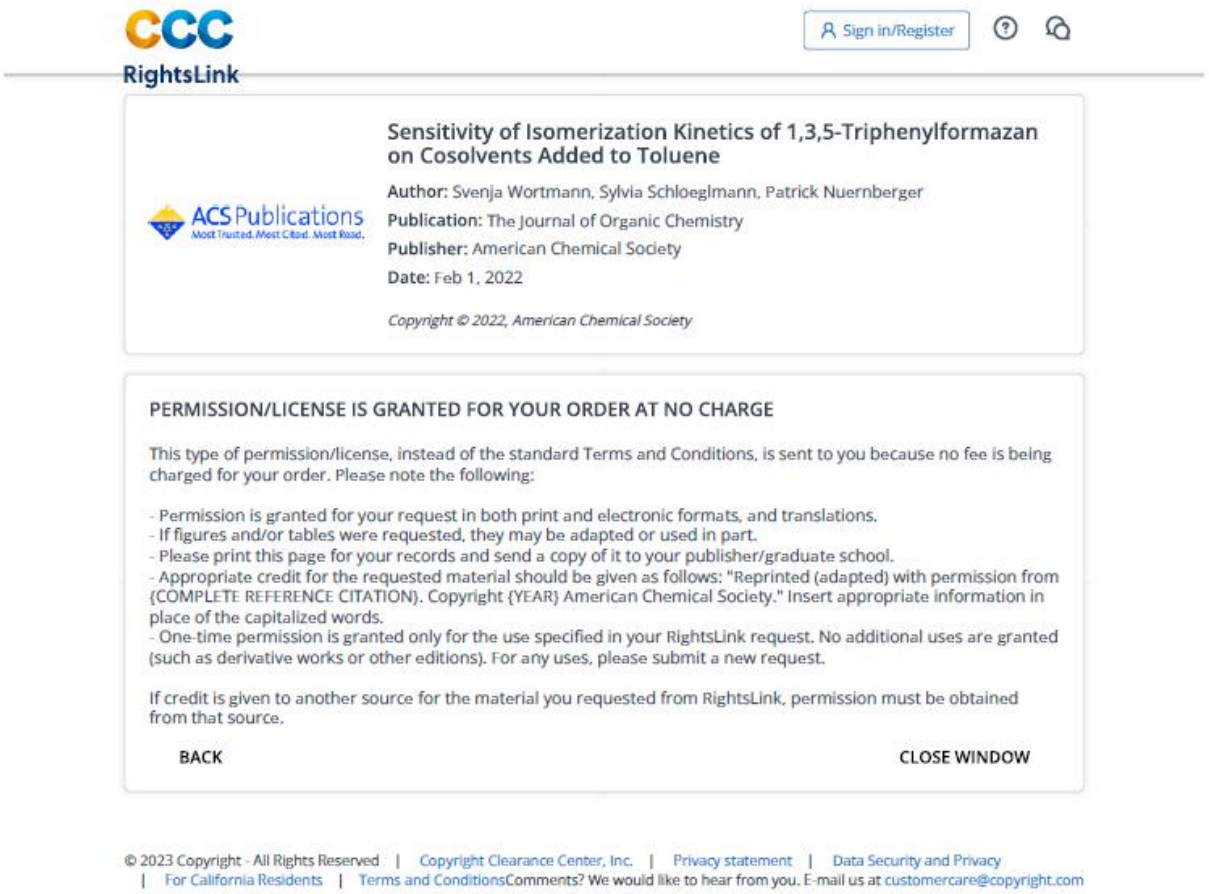

Publication [2]:

Reused and reprinted with permission from S. Wortmann, R.J. Kutta, and P. Nuernberger.
Monitoring the photochemistry of a formazan over 15 orders of magnitude in time. *Front. Chem.* **2022**, 10, 983342, doi: 10.3389/fchem.2022.983342
https://www.frontiersin.org/articles/10.3389/fchem.2022.983342/full

This work is used under the Creative Commons Attribution 4.0 International License (CC BY 4.0) with proper attribution to the original source. The original publication is available at the provided link.

Copyright © 2022 Wortmann, Kutta and Nuernberger. This is an open-access article distributed under the terms of the Creative Commons Attribution License (CC BY). The use, distribution or reproduction in other forums is permitted, provided the original author(s) and the copyright owner(s) are credited and that the original publication in this journal is cited, in accordance with accepted academic practice. No use, distribution or reproduction is permitted which does not comply with these terms.